ECOLOGICAL ENGINES: FINESCALE HYDRODYNAMIC AND CHEMICAL CUES, ZOOPLANKTON BEHAVIOR, AND IMPLICATIONS FOR NEARSHORE MARINE ECOSYSTEMS

A Thesis
Presented to
The Academic Faculty

by

Aaron Conway True

In Partial Fulfillment
of the Requirements for the Degree
Doctor of Philosophy in the
School of Civil and Environmental Engineering

Georgia Institute of Technology
August, 2014

ECOLOGICAL ENGINES: FINESCALE HYDRODYNAMIC AND CHEMICAL CUES, ZOOPLANKTON BEHAVIOR, AND IMPLICATIONS FOR NEARSHORE MARINE ECOSYSTEMS

Approved by:

Dr. Donald R. Webster, Advisor
School of Civil and Environmental Engineering
Georgia Institute of Technology

Dr. Philip J. W. Roberts
School of Civil and Environmental Engineering
Georgia Institute of Technology

Dr. Jeannette Yen
School of Biology
Georgia Institute of Technology

Dr. Kevin A. Haas
School of Civil and Environmental Engineering
Georgia Institute of Technology

Dr. Marc J. Weissburg
School of Biology
Georgia Institute of Technology

Date Approved: June 2014

Dedicated to my Brother

Brit James Johnson (1977 - 2004)

Curious Adventurer, Engineer, Jesus-lover, People-lover

ACKNOWLEDGEMENTS

There are numerous people without whom this work would never have happened and I am truly grateful to all of them. Jesus: I know where I would be without you and it's not here; the joy, strength, and revelation you give me by your Holy Spirit have sustained me and produced this work! To my advisor Dr. Donald R. Webster: for the past 6 years you've truly been a friend, mentor, and advocate and I am quite positive I wouldn't still be here today without your guidance and support, thank you. To my (co) advisor, Dr. Jeannette Yen, I admire your pure curiosity about the natural world around us, thank you for your invaluable contributions, your infectious enthusiasm, and for plugging me into the community; you are a master of pulling strings! To my committee member Dr. Marc Weissburg, thanks for helpful statistics contributions; you've also made my life significantly more difficult, but I know your motivation is good science, and for that I am grateful. To my committee members Dr. Philip Roberts and Dr. Kevin Haas, thank you for always having open doors and for taking the time to engage in my work, as ecological as it may be, and for dealing with me (and accepting my 300 page thesis a week before my defense), thank you.

To my current and former lab mates in both the Webster and Yen labs at GT for friendship, camaraderie, and encouragement: David Murphy (I'll never forget going through Quals together, and then you went and graduated and left me), Rachel Lasley-Rasher (for many heart to hearts), Ann Larson (for making me jealous with all your pictures of Sweden), David Young (I don't need anymore chocolate or caffeine David!), Celio Beiring (who graciously tracked copepods for me in a time crunch on top of his own work load), John Jung (who has a seemingly infinite fount of motivation and energy), Anna Skipper (the sassiest undergrad I ever TA'ed), Larisa

Pender-Healy, and Kathy Nagel. Also, to an army of undergraduate researchers who digitized zooplankton trajectories for hours on end: John Jung, Anna Skipper, Julia Wang, Pureum Kim, Matt Lynch, Joanna Wright, and Clara Choi. Also to two excellent undergraduate researchers in the Yen lab, Aakanksha Angra and Brooke Beaulieu, who maintained and counted phytoplankton cultures. Thanks also to the Hay lab at GT for giving me access to the centrifuge.

To all the folks at the Skidaway Institute of Oceanography for helping me greatly in various ways during the summer of 2012 (after almost arresting me for camping on the dock at Priest's Landing), thank you! Thank you also to Kate Ruck and Debbie Steinberg for collecting and sending the Antarctic krill used here! Thanks to Phoebe Jekielek at University of Maine for graciously collecting and sending copepods.

To Andy Udell for patient (mostly) help and guidance while fabricating experimental gear (and stepping in when I almost cut my finger off) as well as for friendship and excellent conversation (homebrewing, projects du jour, etc.); you've taught me a heap of practical skills and knowledge, thank you. Thanks also to Mike Sorensen in the CEE shop. To the CEE GT Staff (Mike Anderson, Dennis, and Winston in IT, business/student services office, etc.) for constant logistical support over the years, thank you for always being eager to help.

To my wife Ellen, you are amazing and I love you; you've been a constant companion and you have vastly improved the quality of this work, I look forward to a new season of life together! And to my daughter Ada, you are a huge joy and blessing; I can't wait to see you learn and grow and teach you to be nerd like your parents :).

To my Mom and Dad, my brother Keter (and Lael), my sister Hannah (and Eric), and my sister Tova, I love you all, thank you for instilling in me a love of life, Jesus, and people. Mom and Dad, you're sacrifices and perpetual support laid the foundation for the path I'm on, thank you. All of my siblings have contributed in both seen and unseen ways to my success, thank you all.

To the numerous friends who loved me, kept me grounded, and provided healthy outlets: Kip Tyler (and family), Steve Dollar (and the whole Dollar family), Brandon Bradley, Nathan and Terrie Johnson, Adam Balcom, John and Sarah Burke, Trace Copeland (and Angie), the Gunters and Martzes, lots of Trinity and Midtown church folks, Howell Station folks, and numerous others at various times over the years. Thank you all.

To the National Science Foundation, you funded this work and will ensure that the results are put to use! Thanks taxpayers.

"And wherever the river goes, every living creature that swarms will live, and there will be very many fish."

Ezekiel 47:9

"Trust in the Lord with all your heart, and lean not on your own understanding. In all your ways acknowledge Him and He will direct your path."

Proverbs 3:5-6

TABLE OF CONTENTS

LIST OF TABLES

LIST OF FIGURES

NOMENCLATURE

C	Local Concentration.
C_o	Source Concentration.
δ_j	Jet Half-width.
d_j	Jet Slot Width.
e_{ij}	Strain Rate Tensor.
$F2D$	Two-Dimensional Path Fractal Dimension.
μ	Mean Behavioral Response.
μ	Dynamic Viscosity.
N	Buoyancy Frequency.
$NGDR$	Net-to-Gross-Displacement Ratio.
ν	Kinematic Viscosity.
p	Significance Level.
Pe	Péclet Number.
PRT	Proportional Residence Time.
PVT	Proportional Vicinity Time.
Re	Reynold's Number.
Re_j	Jet Reynold's Number.
ρ	Fluid Density.
Ri	Richardson number.
r_{ij}	Rotation Tensor.
σ	Standard Deviation of Behavioral Response.
TF	Turn Frequency.
U_j	Jet Exit Velocity.
U_o	Jet Centerline Velocity.
$VNGDR$	Vertical Net-to-Gross-Displacement Ratio.

SUMMARY

Dynamic and ephemeral resource patches (on fine temporal and spatial scales) are fundamental to the life success of plankton populations - and thus to the overall health and vitality of coastal marine ecosystems. Here we have employed various tools from experimental fluid mechanics to recreate ecologically-relevant hydrodynamic and chemical conditions in a recirculating flume system for zooplankton behavioral assays. A laminar, planar free jet (the Bickley jet) is employed to create finescale free shear layers and thin, sharp-edged layers of both beneficial and toxic phytoplankton exudates. Planar particle image velocimetry (PIV) and laser-induced fluorescence (LIF) are used to quantify the concentration and velocity fields allowing us to fine-tune experimental parameters to match chemical and fluid mechanical conditions reported *in situ*. Subsequent behavioral assays with a variety of zooplankton species, each with unique morphologies, ecologies, and life histories, consistently reveal statistically significant changes in behavior. We seek to understand how individual behavioral responses of zooplankton to various sensory cues on the finescale ($<1\ m$) potentially drive ecological processes in the coastal ocean on the submesoscale ($<1\ km$).

In the first part of this study, we investigated how dispersed estuarine crab larvae can potentially optimize long term (habitat selection) and short term (foraging) behavioral needs by sensing and exploiting the information contained in multi-directional free shear flows. Analyses of digitized trajectories from free-swimming *Panopeus herbstii* (the Atlantic mud crab) megalopae established orientation-specific behavioral shear strain rate thresholds (0.04 s^{-1} upwelling flow, 0.07 s^{-1} downwelling flow, 0.1 s^{-1} horizontal flow). These thresholds are seen to significantly influence

larval behavior through changes in path kinematics (relative swimming speed, turn frequency) and gross path characteristics (net-to-gross-displacement ratio, $NGDR$, vertical-net-to-gross-displacement ratio, $VNGDR$, and proportional residence time, PRT). These larval responses are likely associated with foraging and sampling behaviors in the region surround shear layers in which the coherent shear flows acts as a cue to restrict search volume in hopes of exploiting some coincident or nearby cue and/or resource patch, typical features in fronts and clines. The exploitation of sensory cues contained in finescale patches is likely an important means by which dispersed larvae can couple behavioral needs and processes operating on disparate time and space scales (i.e. foraging and finding suitable settlement habitat) and has important implications for structuring coastal marine ecosystems.

In the second part of this study, thin layers of toxic phytoplankton (cryptic blooms) were modeled for behavioral assays with calanoid copepods to examine the effects of dissolved toxins, copepod species, and sympatry versus allopatry in behavioral response trends. The sympatric (geographically co-occurring) *Acartia tonsa* and the allopatric (geographically separate) *Temora longicornis* were exposed to thin layers of algal exudates from the toxic dinoflagellate *Karenia brevis* (equivalent cell concentration: 1 - 10,000 $cells/mL$). Behavioral response trends with increasing *K. brevis* concentration revealed extreme avoidance behaviors for both species. Trajectories of the sympatric *A. tonsa* became more diffuse and erratic, whereas trajectories of the allopatric *T. longicornis* became more linear and ballistic, on average. As trophic mediators linking primary producers and higher trophic levels, copepods can significantly influence harmful algal bloom (HAB) dynamics and modulate large scale ecological effects through their behavioral interactions with toxic blooms.

Finally, in the last part of this study, we investigated how finescale hydrodynamic and chemical cues commonly associated with thin planktonic layers affect individual behavioral processes in Antarctic krill (*Euphausia superba*). Analyses of digitized

trajectories revealed a behavioral shear strain rate threshold of 0.02 s^{-1} that is seen to significantly influence krill behavior through changes in path kinematics. Slight increases in proportional time spent in the shear layer and significant increases in time spent in the phytoplankton layer suggest that finescale hydrodynamic and chemical cues associated with thin layers enable krill to hone in on a particular resource patch with greater effectiveness and are likely a potential mechanism generating patchiness in krill populations. We have shown that individual behavioral processes could help explain higher frequency variability in krill population dynamics.

CHAPTER I

INTRODUCTION

The patchy nature of primary and secondary productivity in coastal marine ecosystems has been well-known and documented for the past 50 years. Oceanographic fronts have long been known as ecological hotspots of enhanced productivity, with cascading ecological effects (Largier 1993). Similarly, rapid advances in acoustic and optical instrumentation have recently revealed vertically-thin, high-density plankton layers, which are most often associated with hydrographic structure (pycnocline, thermocline, etc.), dubbed *thin layers* (Cowles et al. 1993, Dekshenieks et al. 2001, McManus et al. 2003). It is the unique coupling of physical forcing and individual plankton behavior across vast spatiotemporal scales that create highly patchy plankton distributions and govern spatiotemporal patch dynamics (Tiselius 1992; Woodson et al. 2005; Durham and Stocker 2012). Dynamic and ephemeral resource patches with distinct hydrodynamic and biochemical cue signatures are exploited by crustacean zooplankton with a wide variety of unique morphologies, ecologies, and life histories to optimize life success and thus have profound ecological (and often economic) consequences. These regions of enhanced productivity are truly ecological engines, veritable marine oases supporting the health and vitality of nearshore marine ecosystems. Elucidating and quantifying various mechanisms influencing patchiness in nearshore ecosystems is fundamental to sustainable modeling and managing of marine fishery resources.

One of the most ubiquitous sources of patchiness in coastal marine ecosystems is *thin layers*. Thin layers are one of the most ecologically significant and research-inspiring subjects that have risen out of the interdisciplinary study of oceanographic

processes in the past 20 years. The term thin layer in the context of biological and physical oceanography is more or less synonymous with biophysical coupling and has come to be defined as spatially coherent plankton patches (marine snow, bacteria, phytoplankton, zooplankton, icthyoplankton) in which biomass can be several orders of magnitude greater than the water column immediately above or below the layer. Thin layers range in thickness from a few centimeters to a few meters vertically, span up to square kilometers horizontally, and can persist for days (Benoit-Bird et al. 2010; Moline et al. 2010). Thin layers most often correspond with structure in the ocean associated with vertical gradients of physical, chemical and biological properties in the water column (Dekshenieks et al. 2001). They are a widespread phenomenon occurring in virtually all marine environments where conditions are favorable including fjords, river mouths, continental shelves, and shelf basins (McManus et al. 2003). The extremely dense aggregation of biomass in thin layers has profound implications on the health and vitality of marine ecosystems, specifically through its linkage of fine scale ($< 1\ m$) individual behavioral processes and submesoscale (10s to 100s m) processes that underlay the spatiotemporal distribution of marine fishery productivity.

The first part of this thesis addresses behavioral response of *Panopeus herbstii* megalops (the Atlantic mud crab) to fine scale velocity gradient cues. Selective tidal stream transport (STST) is a behavioral adaptation common to many nearshore fish and invertebrate species in which dispersed planktonic larvae exploit vertical gradients of horizontal velocity during various migrations (ontogenetic, tidally-synchronized, diel, etc.) to control the extent of horizontal dispersion, thus optimizing the dispersal trajectory (e.g. Cronin and Forward 1986, Eggleston et al. 1998, Forward et al. 2001, Forward et al. 2004). By swimming vertically down during ebb tide and up during flood tide, larvae gain net transport shoreward, or vice-a-versa, depending on the goals of the particular larval stage. What remains relatively unstudied and unknown is the extent to which foraging behaviors, informed by individual behavioral responses

to finescale hydrodynamic cues, can influence dispersal trajectories (as discussed by Woodson and McManus 2007). Larval dispersal has important implications for population connectivity and the overall structuring of coastal marine ecosystems (e.g. Queiroga and Blanton 2005) and thus quantifying the role of short-term foraging behaviors in modifying long-term dispersal trajectories is of critical importance.

The second part of this thesis addresses copepod behavioral response to thin layers of exudates of toxic phytoplankton. Harmful Algal Blooms (HABs), "red tides", are associated with dense blooms of phytoplankton known to produce toxic compounds in both fresh and marine waters. HAB events are often associated with massive fish and marine mammal kills and human neurological poisoning by consumption of filter feeding shellfish, coral reef fishes, or even aerosol exposure in extreme events (Dolah 2000). The frequency, intensity, and geographic distribution of HAB events worldwide have been increasing in the past two decades, with associated adverse effects on human and economic health (Wang 2008, Anderson 1989, Smayda 1990, Hallegraeff 2005). The total estimated annual cost to the United States alone from HAB economic impact on commercial fisheries, public health, recreation/tourism, and monitoring/management is $87 million (Hoagland and Scatasta 2006). In their role as trophic mediators who collectively compose the largest biomass on the planet (Mauchline 1998), copepods link primary producers and higher order trophic levels; thus they can significantly influence harmful algal bloom dynamics and modulate large-scale ecological effects through their physiological and behavioral interactions with toxic blooms.

The third part of this thesis addresses Antarctic krill (*Euphausia superba*) response to thin layers of velocity shear and beneficial phytoplankton. Antarctic krill are a critical link in the Southern Ocean ecosystem. As direct consumers of primary producers and crucial prey for a variety of predators including whales, seals, sea birds and squid, krill are a vital trophic link in the (very short) Antarctic food

chain (Everson 2000). They are also the subjects of a valuable commercial fishery (Nicol and Endo 1999) and are the focus of numerous research studies (Siegel 2005). And yet, there are still significant holes in our basic understanding of krill ecology, particularly with respect to behavioral processes on short time scales and fine spatial scales (Nicol and Brierley 2010). We hypothesize that behavior response to finescale hydrodynamic and chemical cues commonly associated with thin planktonic layers may help explain higher frequency variability in population dynamics. Quantifying changes in individual behavior for this ecologically and economically valuable species is fundamental to building tools for modeling and managing a sustainable krill fishery (e.g. via biophysically-coupled individual-based models (IBM), Cresswell et al. 2009).

The approach of the present study is to build a laboratory model of a thin layer, one of the most ubiquitous sources of patchiness in coastal marine ecosystems, with hydrodynamic (shear) and chemical (beneficial and potentially toxic) conditions faithful to reported *in situ* values. Zooplankton behavioral assays will allow us to assess the potential of individual and interactive effects to produce population-scale phenomena. Resolving the relevant process linkages and extrapolating from individual zooplankton behavior to population scale phenomena will ultimately shed light on the factors regulating the spatiotemporal distribution of productivity in coastal marine ecosystems. Further, quantifying the role of individual behavioral processes influencing nearshore productivity dynamics provides a crucial tool for accurately modeling and managing sustainable fisheries for generations to come.

CHAPTER II

LITERATURE REVIEW

This study is concerned with various physical, chemical, and biological factors influencing the formation, maintenance, and dispersal of observed high-density plankton patches in the marine environment, called *thin layers*. Thus, the topics reviewed here are chosen to provide the necessary physical and biological background as well as the relevant ecological context: biophysical coupling and thin layer dynamics, zooplankton sensory ecology, and some useful methods in experimental fluid mechanics.

2.1 Thin Layers: Biophysical Coupling in Plankton Patches

Thin layers are one of the most ecologically significant and research-inspiring subjects that have risen out of the interdisciplinary study of oceanographic processes in the past 15 years. The term *thin layer* in the context of biological and physical oceanography is more or less synonymous with biophysical coupling and has come to be defined as spatially coherent plankton patches (marine snow, bacteria, phytoplankton, zooplankton, icthyoplankton) in which biomass can be several orders of magnitude greater than the water column immediately above or below the layer. Thin layers range in thickness from a few centimeters to a few meters vertically, span up to square kilometers horizontally, and can persist for days. Thin layers most often correspond with structure in the ocean associated with vertical gradients of physical, chemical and biological properties in the water column (Dekshenieks et al. 2001). They are a widespread phenomenon occurring in virtually all marine environments where conditions are favorable including fjords, river mouths, continental shelves, and shelf basins (McManus et al. 2003). The extremely dense aggregation of biomass in thin layers has profound implications on the health and vitality of marine ecosystems,

specifically through its linkage of fine scale ($< 1\ m$) individual behavioral processes and submesoscale (10s to 100s m) processes that underlay the spatiotemporal distribution of marine fishery productivity.

2.1.1 Thin Layer Dynamics: Formation, Maintenance, and Dispersion

In order to quantify thin layer dynamics, it is helpful to apply a control volume type approach when considering the physical, chemical, and biological factors that regulate the formation, maintenance, and dissipation of thin layers. In general, these factors can be considered convergent (they encourage layer formation) or divergent (they encourage dispersion), and conditions are considered favorable for thin layer development if the convergent mechanisms outweigh the divergent mechanisms (Sullivan et al. 2010, McManus et al. 2003, Stacey et al. 2007). Similarly, thin layers will be maintained when convergence and divergence are in balance, and they can be either locally or entirely dispersed when divergence outweighs convergence (Birch et al. 2008, Stacey et al. 2007).

Generally speaking, physical processes (vertical shear, turbulent mixing, stratification, internal wave packets) set the stage for the formation of thin layers, and biological and chemical processes (passive settling of phytoplankton along isopycnals, active migration and swimming behavior, behavioral responses to chemical and physical cues, foraging) are increasingly seen as the regulators of maintenance and dispersion. For these reasons and considering that thin layers almost without exception form in the pycnocline (Dekshenieks et al. 2001, McManus et al. 2003), the Richardson number has arisen as a baseline indicator of whether thin layer formation is feasible or not given the present *in situ* hydrographic conditions. From fluid mechanics, the Richardson number, Ri, is defined as follows:

$$Ri = \frac{N^2}{\left(\frac{\partial u}{\partial z}\right)^2} \tag{2.1}$$

where the Brunt-Väisälä or buoyancy frequency N is defined as

$$N = \sqrt{-\frac{g}{\rho_o}\frac{\partial \rho}{\partial z}} \tag{2.2}$$

Ri represents the ratio of the stabilizing effect of vertical density stratification characterized by N to the destabilizing effect of vertical shear (Kundu and Cohen 2004). Field studies indicate that when Ri is less than 0.25, thin layers do not exist (Dekshenieks et al. 2001, Velo-Suarez et al. 2010). Somewhat unsurprisingly, the critical value of the Richardson number for a continuously stratified flow with vertical shear as derived from the normal modes linear stability analysis is precisely 0.25 (Drazin and Reid 1981). Thus, we see close biophysical coupling in the necessity of turbulent mixing to be suppressed and stratification maintained ($Ri > 0.25$) to promote thin layer formation.

Assuming that the Richardson number criteria for the formation of a thin layer ($Ri > 0.25$) is met, various convergence mechanisms can act in concert to encourage the formation of a thin layer. For a comprehensive overview of proposed thin layer formation mechanisms summarized below, see Cheriton et al. (2009). Several authors have highlighted the importance of the ability of phytoplankton to self-regulate buoyancy and thus maintain vertical position along a given isopycnal in the formation of thin layers (Derenbach et al. 1979, Franks 1992, Alldredge et al. 2002). Additionally, various mechanisms that generate vertical shear such as current jets, the passage of internal waves, and horizontal intrusions can act to vertically compress and thin an existing plankton layer (Franks 1995, Ryan et al. 2008). More recently, Durham et al. (2009) proposed a biophysical mechanism by which the combination of phytoplankton motility and vertical shear can trigger thin layer formation in what they termed *gyrotactic trapping*. A major biophysical/biochemical mechanism important in thin layer formation is motile plankton actively aggregating in response to physical and chemical cues in the ecological context of foraging, mate-seeking, and predator-avoidance (Leising 2001, Dekshenieks et al. 2001, McManus et al. 2003, Woodson et al. 2005,

2007; Woodson and McManus 2007, Benoit-Bird et al. 2010, Moline et al. 2010). Finally, purely biological mechanisms such as *in situ* phytoplankton blooms, differential grazing, and swimming behavior can also play important roles in thin layer formation (Cowles et al. 1998, Alldredge et al. 2002, Holliday et al. 2003).

Once a thin layer is formed, a complex balance between the competing convergent and divergent physical, biological, and chemical processes plays out across a wide range of spatiotemporal scales. Gallager et al. (2004) found that plankton aggregations were sustained only when the Motility Number ($Mn = U_{swim}/U_{rms}$ = plankton swimming speed / RMS of turbulent velocity fluctuations) was greater than 3, which essentially shows that plankton swimming behavior must dominate physical forcing for thin layers to be maintained. Similarly, Steinbuck et al. (2009) found that high dinoflagellate swimming speed was required to overcome the effects of turbulent mixing during thin layer formation, but once the layer was formed reduced swimming speed was required for layer maintenance. Benoit-Bird et al. (2009) and Benoit-Bird et al. (2010) showed the importance of predation on shaping thin layer thickness, edge shape, and intensity. Finally, Cheriton et al. (2009) document the importance of internal wave propagation in the convergence (thinning) and divergence (thickening) of an existing thin layer structure. Thus, it is clear that biophysical interactions in thin layer maintenance are complex and diverse, and a holistic understanding of these internal linkages can only be gained through systematic laboratory studies that isolate and quantify the effects of various interactions over the correct spatial and temporal scales.

At some point, organism behavior and turbulent mixing act together to dissipate a thin layer structure. Shoaling and vertical displacement of the thermocline/pycnocline, animal migration out of the layer, turbulent mixing, and intense predation can bring about the end of a thin layer structure. Additionally, large scale changes in water column shear and stratification, as well as smaller scale events such

as the passage of internal wave packets can act to partially or entirely dissipate a thin layer (Sullivan et al. 2010).Various modeling studies have sought to quantify the dynamic balance between convergent and divergent mechanisms (Stacey et al. 2007, Birch et al. 2008).

In summary, formation, persistence, and dispersion of thin layers lie at the intersection of physical forcing and plankton behavioral responses to discontinuities in the water column associated with physical and chemical gradients. High-resolution, biologically-physically coupled field studies documenting various aspects of thin layer structures *in situ* abound in the literature (Derenbach et al. 1979, Cowles et al. 1998, Dekshenieks et al. 2001, McManus et al. 2003, Sutor et al. 2005, Cheriton et al. 2007, Cheriton et al. 2009, Benoit-Bird et al. 2009, Moline et al. 2010), and have highlighted the importance of understanding the correct biological (growth, predation, cue sensing, foraging, etc.) and physical (thermocline and pycnocline dynamics, internal waves, vertical shear, turbulent mixing) mechanisms at the *correct spatial and temporal scales*. However, there is still a decided lack of well-designed laboratory studies which have the potential to extrapolate the ecological implications of thin layer phenomena to the fisheries scale.

2.1.2 Ecological Implications of Thin Layer Phenomena

Well-designed laboratory studies isolate various biological and physical factors important in thin layer dynamics and quantify the potential of these effects to ripple up through the trophic system. Quantifying zooplankton behavioral responses to individual and combined factors such as velocity gradients (shear strain rate), density gradients (salinity, temperature), and chemical gradients (phytoplankton, chemical exudates, etc.) typical of *in situ* conditions is undoubtedly fundamental to our understanding of thin layer dynamics. This information provides the crucial connection between individual behavioral processes and ecological processes on the submesoscale,

which drive marine ecosystem productivity. A few key studies, which have highlighted the ecological importance of thin layer dynamics, are considered below.

Early work by Tiselius (1992) utilized weak density stratification to create finescale patches of a diatom, *Thalassiosira weissflogii*, and to assess behavioral responses of a calanoid copepod *Acartia tonsa*. Animal trajectories were recorded and evaluated for response time, net-to-gross displacement ratio, and frequency of feeding. He found that *A. tonsa* can utilize density differences and/or phytoplankton chemical exudates to perform area-restricted searches and remain in the high density phytoplankton patch.

Bochdansky and Bollens (2004) investigated changes in the spatial distribution and physiological processes of the calanoid copepod *Acartia hudsonica* in response to differing spatial and temporal distributions of a thin layer of the diatom *Skeletonema costatum*. The study found that the distribution of copepods showed a significant, but ephemeral change in response to thin diatom layers. The copepods, given a choice, will preferentially swim through the layer of diatoms rather than around. Also, the thin layer significantly influenced the depth at which the copepods were distributed. The authors note that the aggregative force of the thin layers on the copepods could be the result of an area-restricted search strategy where the copepods increase their turn angles and decrease their hop size to maintain their position in the food patch, which is consistent with previous research (Tiselius 1992). These experimental results further established that copepod behavioral responses toward food patchiness are species-, food type-, and feeding history-dependent.

The same laboratory setup from the previous study was also used by Clay et al. (2004) to determine if the vertical distributions of 5 and 10 day old Pacific herring (*Clupea pallasi*) larvae are affected by thin layers of highly concentrated rotifers (*Brachionus plicatilis*) and density stratification. They found that the peak abundance of herring larvae occurred at the thin layer when density stratification was present.

This suggests that thin layers, which by nature include a physical signature (density jump, shear strain rate, etc.), drive the vertical distribution of larvae rather than just food patches in general.

Both of the previous two studies suggested further laboratory modeling over relevant spatial and temporal scales, in which individual and combined biological, chemical, and physical cues can be presented with the resulting zooplankton behavioral responses quantified. Further laboratory studies should specifically investigate how organisms orient themselves within thin layers, specific environmental cues, and individual behavioral responses that act as mechanisms for the aggregation at and the formation of thin layers.

Along these lines, Ignoffo et al. (2005) examined the effect of food patches and stratification on the behavior of the rotifer *Brachionus plicatilis*. They found that the rotifers aggregated around food patches and dispersed once the patch was depleted. Furthermore, rotifers selectively chose thin layers based the type of food present and aggregated at density gradients without food presence. Again, this suggests the importance of not only biological cues (food) but physical cues in producing zooplankton aggregations, the combination of which is found in thin layers.

Perhaps the most exhaustive and quantitative thin layer laboratory study to date was conducted by Woodson et al. (2005, 2007); Woodson and McManus (2007). Using a laminar planar jet in a recirculating flume, the behavioral effects of isolated and combined velocity and density gradients, thin phytoplankton layers, and thin phytoplankton exudate layers were quantified for two calanoid copepods, *Acartia tonsa* and *Temora longicornis*. Copepods were exposed to both isolated and combined cues and the behavioral responses of the copepods to each treatment scenario were quantified in terms of relative swimming speed and turn frequency pre- and post-contact with the treatment layer, as well as proportional residence time (PRT = time spent in the treatment layer / total time of observation). They found that both species increased

swimming speed and turn frequency for the velocity gradient and chemical exudates treatments in order to remain in the thin layer, thus increasing PRT. These results are consistent with an excited area-restricted search mechanism found in previous studies (e.g., Tiselius 1992). Additionally, they showed that strong density gradients act as barriers to vertical migrations. Thus, a cue hierarchy can be established where velocity gradients act as an initial cue for decreasing search area, and additional cues such as chemical exudates increase the aggregative effect. The fully quantified, interactive effects of various physical and biological cues in this study on a species-specific basis make it particularly useful in understanding the complex biophysical interactions in thin layers, and in extrapolating these results to the ecosystem level with relevance.

In summary, it is the unique combination of biochemical gradients and physical structure in thin layers that combine to produce these high-biomass drivers of coastal marine productivity. Individual organisms exploiting the highly concentrated, coincident sensory information can produce population scale aggregations with profound trickle up trophic consequences.

2.1.3 A Case Study in Thin Layers: Harmful Algal Blooms (HABs)

2.1.3.1 What are HABs and Why are they Important?

Harmful Algal Blooms (HABs) are often referred to as "red tides" and are associated with dense blooms of phytoplankton in both fresh and marine waters, most commonly due to dinoflagellates and diatoms, which are known to produce toxic compounds. HAB events are often associated with massive fish and marine mammal kills and human neurological poisoning by consumption of filter feeding shellfish, coral reef fishes, or even aerosol exposure in extreme events (Dolah 2000). The frequency, intensity, and geographic distribution of HAB events worldwide have been increasing in the past two decades, with associated adverse effects on human and economic health (Wang 2008, Anderson 1989, Smayda 1990, Hallegraeff 2005). Anthropogenic

causes are quite often, though not always, directly linked to HAB events, specifically due to injection of inorganic and organic nutrients into coastal marine ecosystems (coastal development, aquaculture, industrial waste, etc.) leading to eutrophication and monospecific domination (Verity 2010). The total estimated annual cost to the United States alone from HAB economic impact on commercial fisheries, public health, recreation/tourism, and monitoring/management is $87 million (Hoagland and Scatasta 2006).

As of 1990, there were approximately 20 phytoplankton genera known to have toxic strains (Smayda 1997). The variety of toxins produced, of which the known varieties continue to increase, manifest themselves in two basic toxicological groups: neurotoxins and heptatoxins. Five major neurotoxic seafood poisoning syndromes due to dinoflagellates alone have been identified, each with characteristic symptoms: paralytic shellfish poisoning (PSP), neurotoxic shellfish poisoning (NSP), amnesic shellfish poisoning (ASP), diarrheic shellfish poisoning (DSP), and ciguatera fish poisoning (CFP) (Wang 2008). These neurotoxins bind themselves to neurotransmitter receptors, or voltage-sensitive ion channels, which control contraction of muscles, secretion of hormones, environmental sensing, and signal processing in the brain in vertebrates (organisms with centralized nervous systems) (Catterall et al. 2007). When these processes are interfered with, symptoms including the following can result in death: tickling sensations, numbness in extremities, breathing difficulties, paralysis, cardiovascular shock, nausea, severe muscular pain, and gastrointestinal problems (Wang 2008). The route that these neurotoxins take from the primary producer (dinoflagellate and diatom) to vertebrate victims and the associated accumulation of toxicity along the way has been the subject of much research in the past 20 years. Obviously, there are massive implications for human health and economics as well as public policy (Turner and Tester 1997).

Understanding the relevant, coupled biological, chemical, and physical processes

at the correct spatiotemporal scales is critical for building accurate early detection and predictive management tools (coupled biophysical Individual-Based Models, e.g. Milroy et al. 2008, Janowitz et al. 2008).

2.1.3.2 Biophysical Coupling in HABs

The mechanisms governing the formation, maintenance, and dispersal of HAB events is a relevant and growing field. The interaction of biological and ecological influences (algal growth dynamics, chemical defenses, zooplankton grazing and mating, etc.) with physical influences (nutrient injection by vertical mixing from breaking internal waves, upwelling systems, the onset of stratification, etc.) reveals some of the complexities of the underlying processes that have only recently begun to be examined.

Harmful algal blooms, like all phytoplankton blooms, are best incubated under nutrient-rich, low turbulent mixing (high stratification) conditions (Miller 2004, Mann and Lazier 2006). As in thin layer dynamics, the physical structure of the water column sets the stage for a HAB event, whereas physiological and behavioral responses to environmental cues determine the persistence and potential ecological impact (Donaghay and Osborn 1997). Figure 2.1 shows the patchiness of a harmful algal bloom across multiple scales owing to large scale circulation patterns and localized biophysical interactions.

Relatively recent research has begun to highlight the importance of meso- and submesoscale physical oceanographic processes in creating a landscape favorable for HAB development. Donaghay and Osborn (1997) discuss the preferential location for HAB incubation along the pycnocline (i.e. in thin layers) and the potential for breaking internal waves to lead to surface expression of a HAB event through strong vertical mixing. Ryan et al. (2009) documented the influence of upwelling dynamics in the incubation, retention, spreading, and dispersal of a HAB event in Monterey Bay off the California coast. Upwelling favorable winds draw up nutrient-rich waters and

Figure 2.1: A bloom of the toxic phytoplankton *Lingulodinium polyedrum* off the California coast (Photo by Kai Schumann, California Department of Public Health).

also pull in new water masses into the bay from offshore. These conditions favored the onset of the bloom, which was subsequently spread out by the upwelling-induced circulation in the bay. When upwelling-favorable winds reversed, an intrusion of warm offshore water dispersed much of the bloom. Finally, favorable winds resumed and new circulation further dispersed the bloom and flushed the bay. Pitcher et al. (2010) discuss the importance of coastline shape and bottom topography in influencing circulation patterns in various upwelling systems with respect to HAB incubation, retention, and dispersal. These are but a few of the numerous physical mechanisms at work in HAB dynamics.

Once the physical stage is set (nutrient-rich waters, stable stratification), HAB species employ various means by which to gain an initial advantage and then proceed to dominate the local phytoplankton taxa. Kubanek et al. (2005) document the ability of a red tide dinoflagellate, *Karenia brevis*, to use allelopathy to outcompete other co-occuring non-toxic phytoplankton on a species-specific basis. This gives *K. brevis* a competitive advantage and could promote the onset of a monospecific HAB event. Following the onset of the bloom, toxic anti-grazing deterrents act to

lower predation rates and sustain the bloom (Buskey and Hyatt 1995, Waggett et al. 2008, Graham and Strom 2010), whereas active remote prey-selection by chemical or fluid mechanical cues enhances or dampens the effect (Sole et al. 2006, Schultz and Kiørboe 2009). These factors, on a species-specific basis, can act in concert to produce preferential vectors by which toxins accumulate at higher and higher trophic levels: the accumulation of toxicity. Turner et al. (2012) show that toxins accumulate disproportionately in the copepod *Calanus finmarchicus*, later shown by Leandro et al. 2010 to be due to a lack of active prey selection by which to reject toxic cells that are morphologically similar to non-toxic cells. Gannon et al. (2009) discuss the effect of HABs on nearshore fish communities through reduced fish abundance and health as well as changes in community structure. The effects may be due to neurotoxic influence that cause zooplankton to act erratically and thus become conspicuous prey items and preferential vectors for toxin trophic transfer.

Perhaps most interesting is the large number of HAB species that have recently been identified in thin layers (Rines et al. 2002, McManus et al. 2008, Sullivan et al. 2010). McManus et al. (2008) found enhanced concentrations of *Pseudo-nitzschia spp.* in a thin layer in Monterey Bay and proposed that thin layers may conceal a HAB event until the effects are evident in massive fish kills (a "cryptic bloom"). Thus, sampling regimes aimed at early detection of HAB events must resolve thin layers *at the appropriate temporal and spatial scales.* More generally, this means that all of the biophysical mechanisms pertaining to thin layer formation, maintenance, and dispersal are equally applicable to HABs. *Therefore, HABs could be considered another biochemical effect in the dynamics and ecology of thin layers.*

In summary, the current HAB literature has highlighted the importance of biophysical coupling at a variety of spatial and temporal scales in the formation, maintenance, and dispersal of blooms. However, as in the thin layer literature, there is a

decided lack of laboratory studies that have isolated and quantified the effects of single and combined biochemical (HAB species, toxicity, cell concentrations, etc.) and physical (density stratification, shear strain rate, internal waves) cues on zooplankton behavior. This information is crucial in quantifying the potential human health and economic impact of a particular HAB event, as well as to build early detection and predictive management tools.

2.1.3.3 HABs and Copepod Ecology

The effects of toxic phytoplankton blooms on copepod ecology range from the physiological (fecundity, overall fitness: Prince et al. 2006, Waggett et al. 2012) and behavioral (swimming speeds, fractal characteristics of trajectory, sampling, feeding and mating behaviors: Cohen et al. 2007, Breier and Buskey 2007, Schultz and Kiørboe 2009, Hong et al. 2012) to the evolutionary (species success: Jiang et al. 2011), spanning a wide spectrum of relevant temporal scales.

Many chemical compounds (e.g. domoic acid, paralytic shellfish poison, dimethyl sulfide: e.g. Prince et al. 2010) associated with HAB species are known to have deleterious effects on copepod fitness (Jiang et al. 2009) not only because of toxicity-related responses but also from typical low nutritional values. Among studies of copepod grazers fed harmful algae, decreased grazing and fecundity are the most common results, though the causes of decreased grazing (physiological incapacitation, behavioral avoidance or lack of stimulation) and/or decreased fecundity (toxic versus nutritional effect) vary among studies (Breier and Buskey 2007). Prince et al. (2006) looked at the effects of toxic *Karenia brevis* on fitness for the copepod *Acartia tonsa*, and found that on diets rich in *K. brevis*, copepods experienced decreased survivorship and decreased egg production per female, but the percentage of eggs that hatched was unaffected. Similarly, egg production rates of *A. tonsa* fed toxic *K. brevis* strains were similar to those of starved copepods, while those of copepods fed

non-toxic strains along with beneficial *Rhodomonas salina* were significantly higher (Waggett et al. 2012). Jiang et al. (2011) found an interesting physiological response with evolutionary implications in the copepod *A. tonsa* responding to the harmful dinoflagellate *Cochlodinium polykrikoides*: a rapid gain and loss of evolutionary toxin resistance as a population. After four generations of chronic exposure to toxic phytoplankton, copepods had evolved toxin resistances 3 times higher than pre-exposure generations; within two generations lacking exposure, all increased toxin resistance was lost. This suggests that copepods can rapidly adapt to dissolved toxic compounds and likely play a critical role in implementing some form of top-down grazer control on toxic phytoplankton blooms. These findings also highlight how algal toxins may influence copepod feeding behavior and alter top-down control exerted by copepod grazers.

The idea of top-down grazer control (or the modification of it) is consistent in the literature. Hong et al. (2012) used digital holographic cinematography to compare feeding behavior of free-swimming copepods, *A. tonsa*, on nutritional prey (*Storeatula major*) to that occurring during exposure to toxic and non-toxic strains of *K. brevis* and *Karlodinium veneficum*. They found two different beating modes of the copepods feeding appendagesa sampling beating of short durations and a longer duration grazing beating that generates feeding currents as well as a variety of behavioral regimes corresponding to the presence, absence, or combination of beneficial and harmful algal cells. This modification of top-down grazer control was also seen by Waggett et al. (2012) whose data indicate that *K. brevis* influences copepod grazer populations via multiple synergistic mechanisms: (1) decreased ingestion rates, (2) decreased egg production, and (3) increased mortality of copepods through a combination of toxicity and nutritional inadequacy. Cohen et al. (2007) conducted grazing and mortality experiments with *K. brevis* cells and brevetoxins, establishing routes of toxicity for the copepods *A. tonsa*, *Temora turbinata* and *Centropages typicus*. *A. tonsa* exhibited

minimal sublethal behavioral responses; however, there were significant effects on the swimming and photobehavior of *T. turbinata* and *C. typicus* at the lowest sublethal concentrations tested (105 *K. brevis* cells/L), suggesting very low behavioral response thresholds. Their data suggest that sublethal effects of *K. brevis* and its brevetoxins on copepod behavior occur on a species-specific basis. Similarly, Schultz and Kiørboe (2009) found that *A. tonsa* was capable of incredible selective feeding behaviors by remotely identifying and rejecting toxic cells based on associated hydrodynamic or chemical signatures whereas Leandro et al. (2010) found that a lack of remote prey selection lead to the copepod *Calanus finmarchicus* becoming a preferential trophic vector for toxin accumulation, likely due to a lack of ability to remotely characterize toxic cells. Species-specific selective feeding behavior (or lack thereof) through active, remote prey selection can enhance or dampen bloom growth dynamics thus modulating ecological impacts on other trophic levels (Sole et al. 2006, Schultz and Kiørboe 2009).

During toxic bloom conditions, anti-grazing deterrents act to lower predation rates by copepod grazers and sustain the bloom (Buskey and Hyatt 1995, Kubanek et al. 2005, Waggett et al. 2008, Graham and Strom 2010). Teegarden et al. (2003) showed that even though sloppy copepod grazing was effective at dispersing toxins to low concentration levels by aiding environmental advection and turbulent diffusion, toxins were still seen to bio-accumulate in copepods, acting as a preferential toxin accumulation vector. Extrapolating trophically, Gannon et al. (2009) examined the effect of HABs on nearshore fish communities through reduced fish abundance and health as well as changes in community structure. The effects are likely due to neurotoxic influences that cause zooplankton to act erratically and thus become conspicuous prey items and preferential vectors for trophic transfer of dissolved toxic compounds. These factors, on a species-specific basis, can act in concert to produce preferential

vectors by which toxins accumulate at higher and higher trophic levels: the accumulation of toxicity.

Changes in copepod feeding and swimming behavior caused by toxic compounds can significantly influence predator, prey, and mate encounter rates by altering the fracticality (diffuseness or volume-fillingness, e.g. Seuront 2011) of a copepods trajectory. Erratic, hydrodynamically conspicuous, diffuse swimming behavior (high path fractal dimensions) and inconspicuous, ballistic, steady swimming behavior (low path fractal dimensions) each have their ecological place for copepods; however, too much of one or the other can have deleterious effects on copepod life success (e.g. by decreasing mate or prey encounters or increasing conspicuity to predators). Changes in individual copepod behaviors are quickly extrapolated to population scale phenomena with important implications for HAB dynamics (intensity/toxicity, duration, trophic transfer, etc.) and overall ecological effects.

Finally, HABs are intricately linked to fronts and clines and thus to copepod ecology; dissolved toxic compounds should (often) be considered as another biochemical factor in the trophic and biogeochemical dynamics of fronts (Stumpf et al. 2008, Ryan et al. 2009) and clines (Donaghay and Osborn 1997, Rines et al. 2002, McManus et al. 2008, Sullivan et al. 2010). There are numerous biological (phyto-, zoo-, and icthyo-plankton species, algal growth dynamics, zooplankton grazing), chemical (toxic compound, toxicity levels), and physical (hydrography, advection, turbulent and molecular diffusion) factors coupled over wide spatiotemporal scales that affect HAB dynamics and determine overall ecological impacts. They are additive and complicated, but one thing is clear: ecological effects and trophic implications are highly species-specific and dependent on toxicity level, mode of action, morphology, and monospecificity of a particular toxic algal species and its associated toxic compounds. In addition, species-specific copepod physiological and behavioral responses (fitness,

foraging, grazing, sampling, mating, etc.) as well as local physics (turbulence, stratification, surface waves, internal waves, tides, etc.) play significant roles influencing the duration, density, toxicity, and overall ecological impacts of a particular HAB event.

2.2 Zooplankton Sensory Ecology

Zooplankton, like all plankton, live in an aquatic environment in which their primary goals are three-fold: to eat, to not be eaten, and to reproduce, each being mediated by fluid mechanical and chemical sensory cues. Thus, the ability of an organism to detect and respond to the highly dynamic transport of mass, momentum, and heat in the ocean over various spatial and temporal scales will absolutely dictate the life success of that organism.

The present study seeks to quantify the behavioral responses of a diverse group of zooplankters to isolated and combined physical (shear strain rate, internal waves, density stratification) and chemical (layers of beneficial and toxic phytoplankton exudates) cues common in thin layers. Thus, the subjects reviewed in this section give a brief overview of zooplankton sensory ecology as well as a few illustrative examples in the zooplankton. Mechanosensing and chemosensing in the zooplankton are reviewed before examining how they play out in the life trajectories of calanoid copepods, decapod crab larvae, and mysids. The life histories and morphology of each are briefly discussed before special attention is given to the sensory ecology; that is, what is known about the way that these organisms gather and respond to the physical and chemical cues in their marine environments.

2.2.1 Mechanosensing: The Velocity Gradient Tensor

In any flow field there are multiple fluid mechanical cues a zooplankter could sense, namely acceleration, vorticity, and deformation (e.g. Kundu and Cohen 2004). A general three-dimensional velocity gradient, $\partial u_i/\partial x_j$, can be decomposed into rotational

and irrotational components, the strain rate tensor, e_{ij}, and the rotation tensor, r_{ij}, where i and j are the three coordinate directions, as:

$$\frac{\partial u_i}{\partial x_j} = e_{ij} + \frac{1}{2} r_{ij} \tag{2.3}$$

with the strain rate tensor given as

$$e_{ij} = \frac{1}{2}\left(\frac{\partial u_i}{\partial x_j} + \frac{\partial u_j}{\partial x_i}\right) = \begin{vmatrix} \frac{\partial u_1}{\partial x_1} & \frac{1}{2}\left(\frac{\partial u_2}{\partial x_1} + \frac{\partial u_1}{\partial x_2}\right) & \frac{1}{2}\left(\frac{\partial u_3}{\partial x_1} + \frac{\partial u_1}{\partial x_3}\right) \\ \frac{1}{2}\left(\frac{\partial u_2}{\partial x_1} + \frac{\partial u_1}{\partial x_2}\right) & \frac{\partial u_2}{\partial x_2} & \frac{1}{2}\left(\frac{\partial u_3}{\partial x_2} + \frac{\partial u_2}{\partial x_3}\right) \\ \frac{1}{2}\left(\frac{\partial u_3}{\partial x_1} + \frac{\partial u_1}{\partial x_3}\right) & \frac{1}{2}\left(\frac{\partial u_3}{\partial x_2} + \frac{\partial u_2}{\partial x_3}\right) & \frac{\partial u_3}{\partial x_3} \end{vmatrix} \tag{2.4}$$

and the rotation tensor given as

$$r_{ij} = \frac{\partial u_i}{\partial x_j} - \frac{\partial u_j}{\partial x_i} = -\varepsilon_{ijk}\omega_k = \begin{vmatrix} 0 & -\left(\frac{\partial u_2}{\partial x_1} - \frac{\partial u_1}{\partial x_2}\right) & -\left(\frac{\partial u_3}{\partial x_1} - \frac{\partial u_1}{\partial x_3}\right) \\ \left(\frac{\partial u_2}{\partial x_1} - \frac{\partial u_1}{\partial x_2}\right) & 0 & -\left(\frac{\partial u_3}{\partial x_2} - \frac{\partial u_2}{\partial x_3}\right) \\ \left(\frac{\partial u_3}{\partial x_1} - \frac{\partial u_1}{\partial x_3}\right) & \left(\frac{\partial u_3}{\partial x_2} - \frac{\partial u_2}{\partial x_3}\right) & 0 \end{vmatrix} \tag{2.5}$$

The strain rate tensor can be thought of as the relative velocity due to pure deformation and can itself be decomposed into the normal strain rate terms (diagonal terms) and the shear strain rate terms (twice the off-diagonal terms). The rotation tensor can be thought of as the relative velocity due to fluid rotation, which can be succinctly described by the vorticity vector ω_k as in Equation 2.5. Thus, any three-dimensional velocity field can be thought of as the superposition of rotational and deformational flow components, and the ability of a zooplankter to distinguish between flow components allows it to distinguish say the suction force from a predator (Holzman and Wainwright 2009) versus the fluid mechanical signature of a phytoplankton cell entrained in its own feeding current (Strickler and Balazsi 2007). The

type of flow component most important in triggering behavioral responses in various zooplankton species is an important piece of quantitative data that allows for the coupling of hydrodynamically characterized environments and individual and population scale zooplankton behavior.

A large body of quantitative literature on mechanosensing in crustacean zooplankton exists for calanoid copepods. Copepods, and many crustacean zooplankton, are able to sense spatial gradients of flow via an array of mechanosensory hairs, or setae, which are located along the entire body but are most highly concentrated on the antennules (Yen et al. 1992, Fields et al. 2002) (see Figure 2.2). Bending or deformation of setae caused by fluid flow relative to the body generates neural signals, providing the bridge between hydromechanical signal and behavioral response (Fields et al. 2002). Thus, for a copepod to gain useful information about the hydrodynamic environment around it there must be relative fluid motion around the copepod (i.e. it cannot be simply passively advected in uniform flow). The focus of the review provided here is the vast literature on copepod mechanosensing. The morphological similarities between calanoid copepods and other crustacean zooplankton, such as decapod crab larvae and mysids, as well as the overwhelming circumstantial evidence in the literature, make a strong case for the generalization of *qualitative* findings from the copepod mechanosensory literature to these other crustacean zooplankton as well.

Early work by Yen et al. (1992) laid the foundation for quantifying the effects of fluid mechanical cues on zooplankton behavior. The calanoid copepods *Labidocera madurae* and *Acartia fossae* were exposed to controlled mechanical stimuli via a waveform generator. Via monitoring neural activity, both copepods were found to be extremely sensitive to small displacements and sensitivity increased with increasing stimuli frequency. Displacements as small as 10 nm and displacement velocities as small as 20 $\mu m/s$ were enough to trigger neural responses. They concluded that copepod setae may be explicitly velocity sensors; they are capable of sensing closely

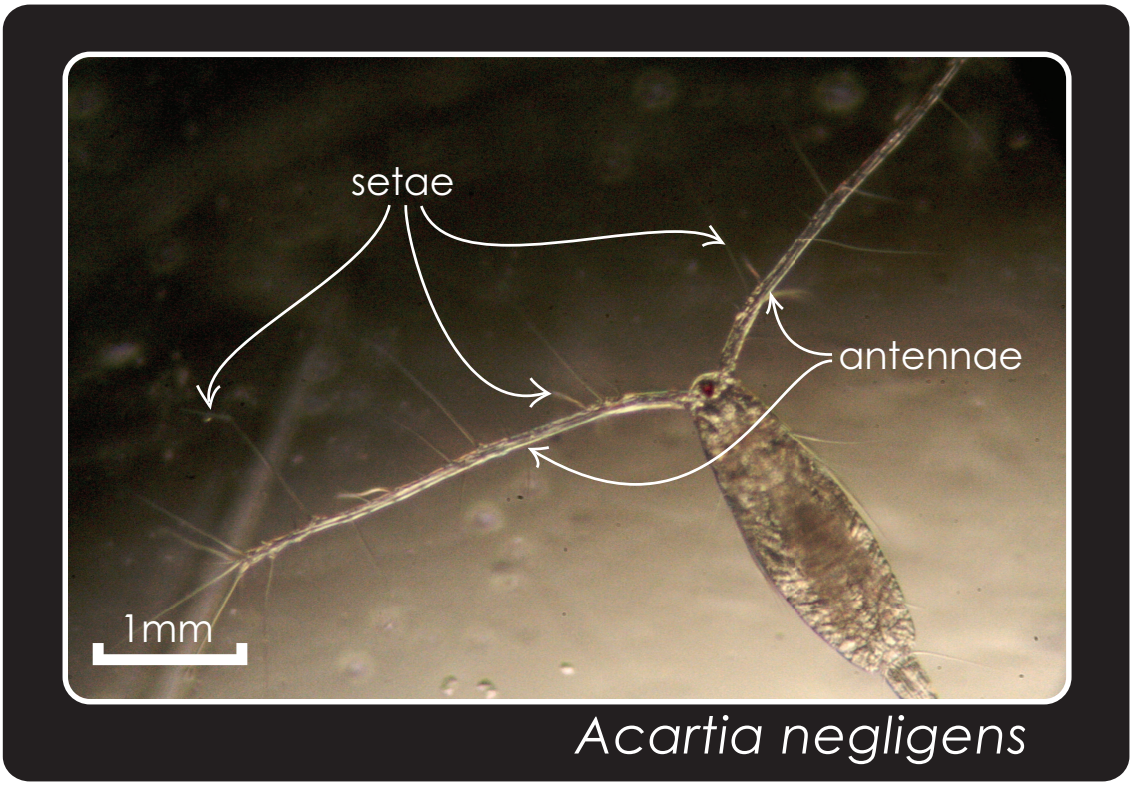

Figure 2.2: Mechanosensitive setae distributed along the antennae of *Acartia negligens*.

spaced stimuli; responses are dependent upon stimuli frequency and duration: and receptors can supply directional information. Since this foundational study, much effort has gone into understanding the bridge between neural and behavioral thresholds as well as identifying the most behaviorally important fluid mechanical cue.

In detailed experiments by Kiørboe and Visser (1999) and Kiørboe et al. 1999, the copepod *Acartia tonsa* was systematically exposed to each isolated fluid mechanical cue (deformation rate, vorticity, and acceleration) and behavioral responses were gauged. Acceleration and vorticity were determined to be largely unimportant cues, with more intense focus warranted for the importance of deformation rate in eliciting behavioral responses from copepods. Threshold escape behavioral responses to pure deformation ranged from 1.19 to 2.49 s^{-1}. These studies largely focused the ensuing literature to investigations of the effects of threshold fluid deformation rates in eliciting escape responses. Table 2.1 summarizes quantitative threshold deformation rates that elicit copepod escape responses reported in the literature.

The threshold deformation rates reported in Table 2.1 elicit *escape* responses in copepods. Another ecologically-relevant and practically unstudied response is a simple behavioral response. Strickler and Balazsi (2007) found that copepods were capable of distinguishing the source of a hydrodynamic disturbance (prey, predator, mate, etc.) based on the information contained in the signal. This suggests that different types of behavioral responses to different types and magnitudes of various hydrodynamic signals are likely in the zooplankton. Manifestations of other behavioral responses to a threshold deformation rate could include increased turn frequency and swimming speed consistent with area-restricted foraging behavior. This was shown by Woodson et al. (2005) with species-specific behavioral strain thresholds ranging from 0.015 - 0.06 s^{-1} for the calanoid copepods *Acartia tonsa* and *Temora longicornis*.

Table 2.1: Threshold deformation rates reported for escape response in various copepod species.

Species	Threshold Deformation(s^{-1})	Study
Calanus finmarchicus	0.40	Haury et al. (1980)
Polyathra remata, Rotifer	2.0 – 3.1	Kirk and Gilbert (1988)
Acartia hudsonica	0.80	Yen and Fields (1992)
Euchaeta rimana	2.4	Fields and Yen (1997a)
Pleuromamma xiphias	4.6	Fields and Yen (1997a)
Labidocera madurae	6.3	Fields and Yen (1997a)
Acartia tonsa, Adult	0.38	Fields and Yen (1997a)
Acartia tonsa, Nauplii	0.38	Fields and Yen (1997a)
Oithona spp.	3.8	Fields and Yen (1997a))
Eurytemora affinis	1.9	Viitasalo et al. (1998)
Acartia tonsa	1.19 – 2.49	Kiørboe et al. (1999)
Temora longicornis, Nauplii	2.78 – 3.96	Titelman (2001)
Eurytemora affinis	1.88 – 2.65	Titelman and Kiørboe (2003)
Euterpina acuftifrons	1.92 – 4.25	Titelman and Kiørboe (2003)
Calanus helgolandicus	0.52 – 3.24	Titelman and Kiørboe (2003)
Centropages typicus	2.60 – 2.79	Titelman and Kiørboe (2003)

Importantly, these threshold values are one to two orders of magnitude lower than thresholds that induce escape responses and one to two orders of magnitude higher than neural response thresholds (Yen et al. 1992).

Other important findings in the copepod mechanosensory literature have highlighted the effects of animal size and setal sensitivity (Kiørboe et al. 1999), the importance of resolving fluid signals at the *setal* location (Jiang et al. 2002), and the effects of body orientation with respect to the fluid mechanical signal (Fields 2010).

2.2.2 Chemosensing: Diffusion, Advection-Diffusion, and Turbulence

Chemosensing and chemical signals play a vast and complex role in structuring interactions within marine environments. Intraspecific signaling, host-parasite interactions, allelopathy, predator-prey and mate interactions, predation defenses, and prey and mate tracking and capture are all directly mediated by chemical signaling within the aquatic environment. Release of both beneficial and toxic chemicals

in the marine environment most often takes the form of highly soluble ($\Gamma \sim 10^{-5}$ cm^2/s) compounds including amino acids, proteinaceous compounds, nucleic-acid related compounds, glycerolipids, and pheromones (Carr 1988, Dusenbery 1992, Yen et al. 1998, Zimmer and Butman 2000, Lide 2008, Poulson et al. 2009). The means of emission and the hydrodynamically-regulated advection and diffusion of a chemical signal all determine the amount and specificity of information conveyed (Yen et al. 1998, Webster and Weissburg 2009). The focus here will be on the biophysical coupling concerning the emission of chemical cues, the subsequent hydrodynamic transport and diffusion, and finally the cue perception and implications for behavioral responses as reviewed in Webster and Weissburg (2009). Further attention is paid to the ecological ramifications of chemosensing in individual zooplankters from diverse habitats in the subsections below.

The two most important parameters that define the appropriate regimes of fluid flow and chemical transport in any aquatic environment are the Reynolds number,

$$Re = \frac{\rho U L}{\nu} \tag{2.6}$$

and the Péclet number,

$$Pe = \frac{U L}{\Gamma} \tag{2.7}$$

where U is the characteristic velocity, L is the characteristic length scale, ρ is the fluid density, and μ and ν are the dynamic and kinematic viscosities, respectively. Re represents the ratio of inertial to viscous forces acting in a flow, whereas Pe describes the ratio of advective to diffusive effects acting on a passive scalar in a flow field. Low Re flows are dominated by laminar advective transport and likewise small Pe

flows signify that molecular diffusion dominates the spreading of a chemical cloud. Alternately, high Re and large Pe flows introduce random turbulent fluctuations of chemical concentration (turbulent diffusion) in the advection-dominated spreading of the chemical cloud. Thus, the combination of these two parameters properly defines the length and time scales of concentration fluctuations for a chemical released into a given hydrodynamic environment. This forms the basis for a quantitative understanding of the relevant transport processes as well the probable concentration magnitudes and frequencies of fluctuation likely to be experienced by the signal recipient somewhere downstream (Webster and Weissburg 2009). Thus, the ability of an organism to make life-altering choices based on a chemical signal is highly coupled to the ambient hydrodynamic environment.

The spread of chemicals emitted into a stagnant fluid environment is governed by classical Fickian diffusion in which chemical flux q is proportional to the concentration gradient as

$$\mathbf{q} = -\Gamma \nabla c \tag{2.8}$$

and the Fickian diffusion equation is given as

$$\frac{\partial c}{\partial t} = \Gamma \nabla^2 c \tag{2.9}$$

where c is the concentration of the chemical. Time scales in pure molecular diffusion are extremely long and gradients of chemical solute develop slowly.

A small, but ecologically-important, step away from pure molecular diffusion is chemical transport and diffusion in low Re laminar flow governed by the advection-diffusion equation,

$$\frac{\partial c}{\partial t} + \mathbf{u} \cdot \nabla c = \Gamma \nabla^2 c \tag{2.10}$$

and the chemical flux q is now given as

$$\mathbf{q} = \mathbf{u}c - \Gamma \nabla c \tag{2.11}$$

Thus, in addition to chemical transport due to molecular diffusion (concentration gradients), there is chemical flux due to hydrodynamic advection. The added benefit (or detriment depending on the ecological perspective) of chemical flux due to advection versus pure diffusion can be expressed by the non-dimensional Sherwood number,

$$Sh = \frac{hL}{\rho \Gamma} \tag{2.12}$$

where h is the overall mass transfer coefficient. Sh describes the relative importance of the additional advective chemical flux over pure molecular diffusion and could be used to quantify adaptations used by organisms to enhance or conceal transmission of chemical signals in an aquatic environment (Webster and Weissburg 2009).

Finally, chemical flux in high Re turbulent flows is additionally influenced by random velocity fluctuations that deviate from the mean flow. The turbulent time-averaged flux of a chemical solute $\bar{\mathbf{q}}$ is now given as

$$\bar{\mathbf{q}} = \bar{\mathbf{u}}\bar{c} - \Gamma \nabla \bar{c} + \overline{\mathbf{u}'c'} \tag{2.13}$$

revealing the additional turbulent flux term corresponding to the covariance of the velocity and concentration fluctuations about the mean. The time-averaged concentration field is now governed by the Reynolds-averaged advection-diffusion equation as

$$\frac{\partial \bar{c}}{\partial t} + \bar{\mathbf{u}} \cdot \nabla \bar{c} = \Gamma \nabla^2 \bar{c} - \nabla \cdot (\overline{\mathbf{u}' c'}) \tag{2.14}$$

The ecological ramifications for plankton due to chemical transport and diffusion in each of these regimes are significant and are overviewed in Webster and Weissburg (2009).

2.2.3 A Closer Look at a Few Zooplankters

A theme in the sensory ecology literature is the idea of a cue hierarchy in triggering changes in behavior (Tumlinson et al. 1993, Vet 1999). A cue hierarchy explains the relative importance of various types of sensory cues (physical and chemical) in triggering behavioral responses in relation to one another. For example, Woodson et al. (2007) found that velocity gradients (shear) act as an initial cue to restrict search area in a foraging copepod, and chemical cues then allow the copepod to hone in on a particular resource patch with greater effectiveness. The idea of a cue hierarchy is ever present in the life cycle of a zooplankter and is particularly helpful when considering zooplankton sensory ecology. The three zooplankters considered below are particularly relevant to the present study and illustrate the use of cue hierarchies in a variety of habitats as a means of adaptive life strategy.

2.2.3.1 Calanoid Copepods: Life History and Morphology

Crustaceans of the subclass Copepoda are collectively the most numerous multicellular organisms on earth, ranging in size from 0.5 - 12 mm. There are ten orders of

copepods with 200 families, 1650 genera, and some 11,500 known species (Mauchline 1998). Perhaps the best-known and most studied family is Calanoida, primarily pelagic marine copepods.

Calanoid copepods reproduce sexually before hatching from eggs and going through a series of larval stages that culminate in the final adult stage. Almost all calanoid copepods hatch into the first nauplius stage (NI) and molt five times into the NVI stage. Following the NVI stage, calanoids enter the initial copepodid juvenile stage (CI), which, after five more molts, results in the adult stage (CVI) (Mauchline 1998). Adult calanoid copepods have bodies that are made up of three main regions: the urosome (tail), the five-segmented metasome (body), and the cephalosome (head). Paired appendages along the body aid swimming, prey detection and capture, and mating, whereas antennae and antennules emanating from the head region are covered in mechanosensitive setae responsive to displacements on the nm scale (Yen et al. 1992, Mauchline 1998). Additionally, chemosensors are distributed along the cephalic appendages (Paffenhöfer 1998). Various species of calanoids can be distinguished by differences in body and appendage morphology and swimming behavior as illustrated in Figures 2.3 and 2.4.

As the largest collective of multicellular organisms on earth and direct consumers of primary producers, copepods are an integral component of the marine ecosystem and are critical in understanding the spatiotemporal distribution of productivity in the world's oceans.

2.2.3.2 Calanoid Copepod Sensory Ecology

"The Paradox of the Plankton" as proposed by Hutchison (1961) asked how a number of similar species competing for similar, limited resources in an isotropic, homogeneous environment could survive. The answer is they do not, the environment is in fact patchy at finescales ($< m$), and plankton use cue hierarchies in locating isolated

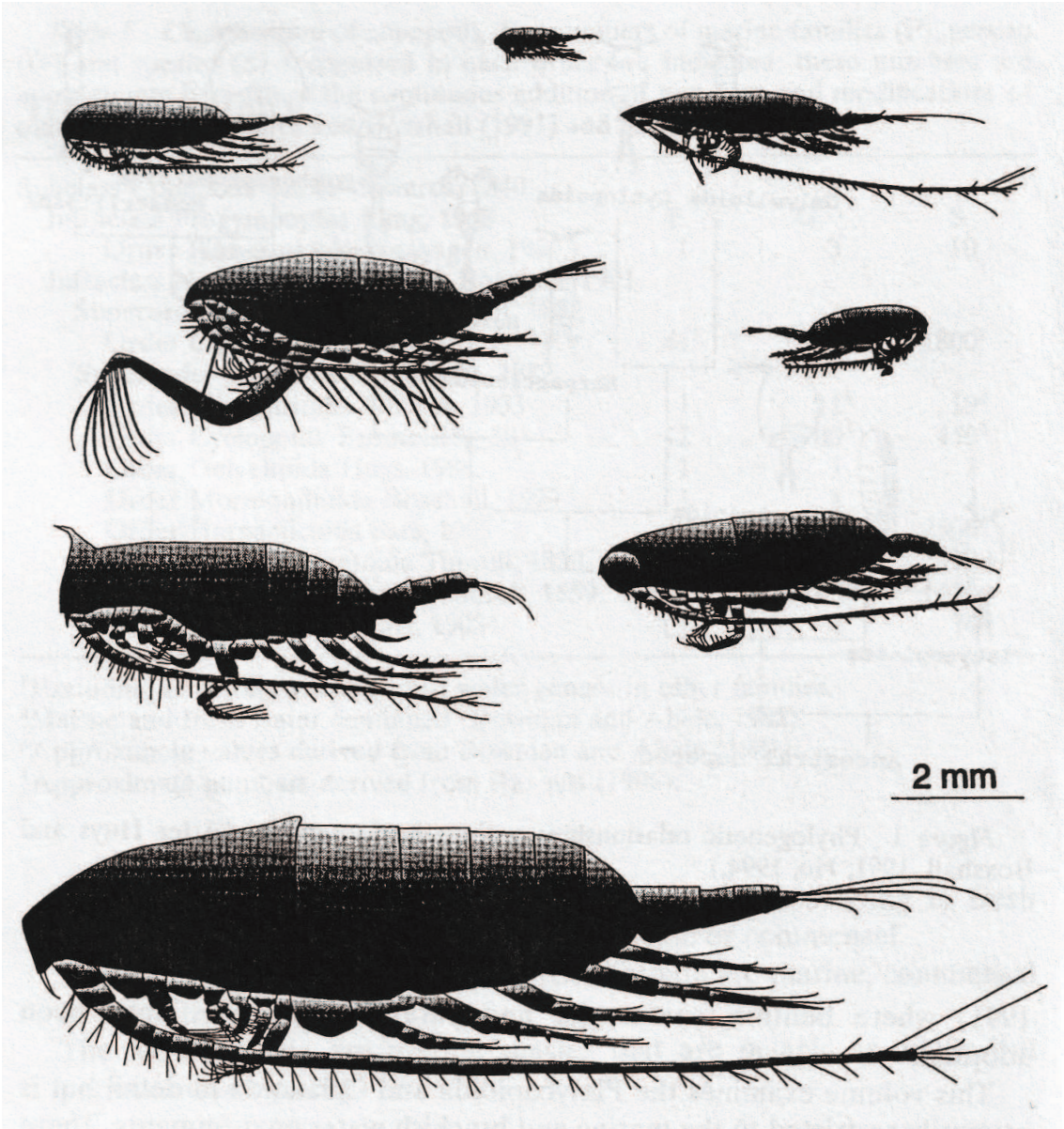

Figure 2.3: Various calanoid morphologies from Mauchline (1998).

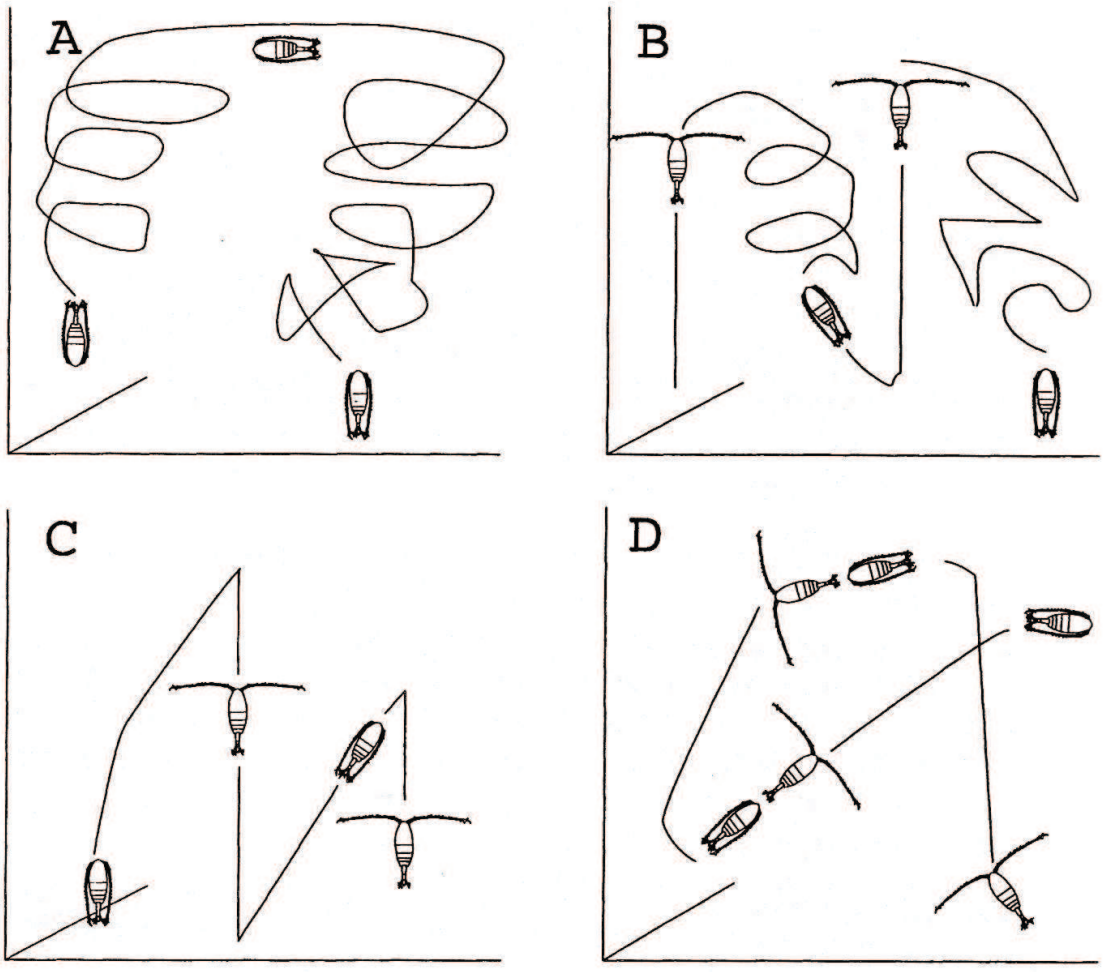

Figure 2.4: Various calanoid swimming styles from Mauchline (1998).

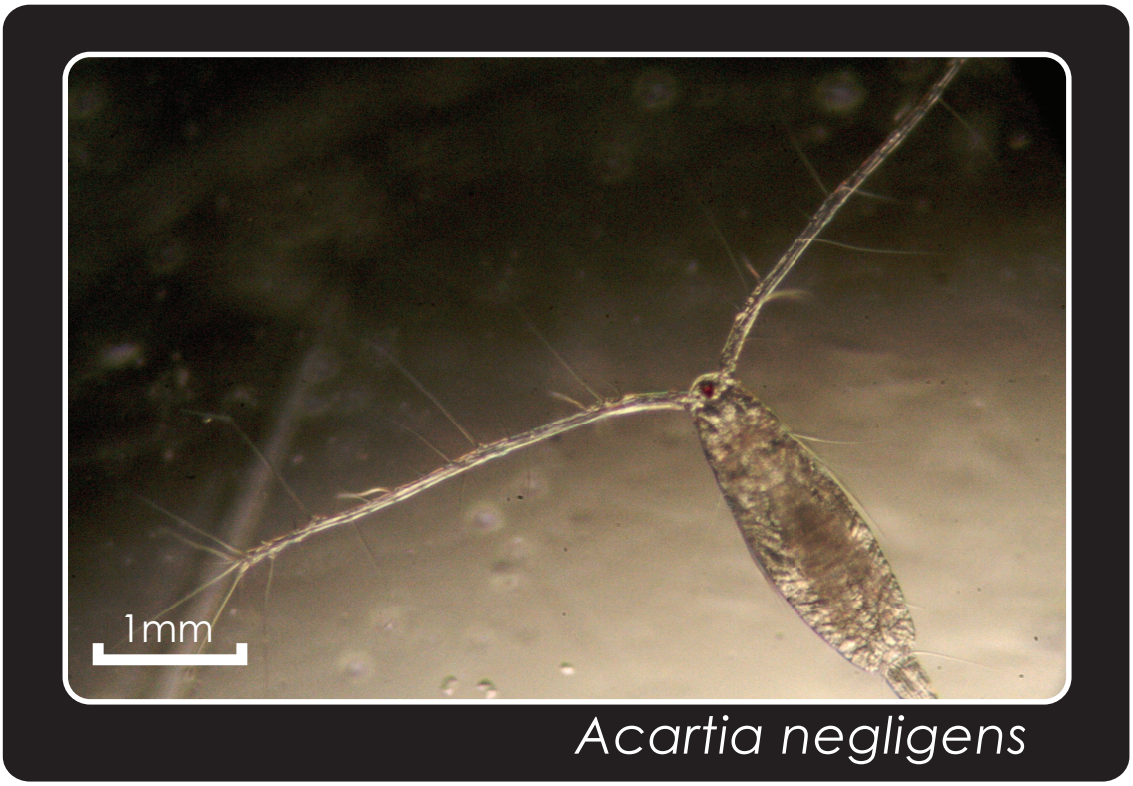

Figure 2.5: *Acartia negligens* collected in the Gulf of Aqaba, Red Sea, Eilat, Israel (photo by Ellen True).

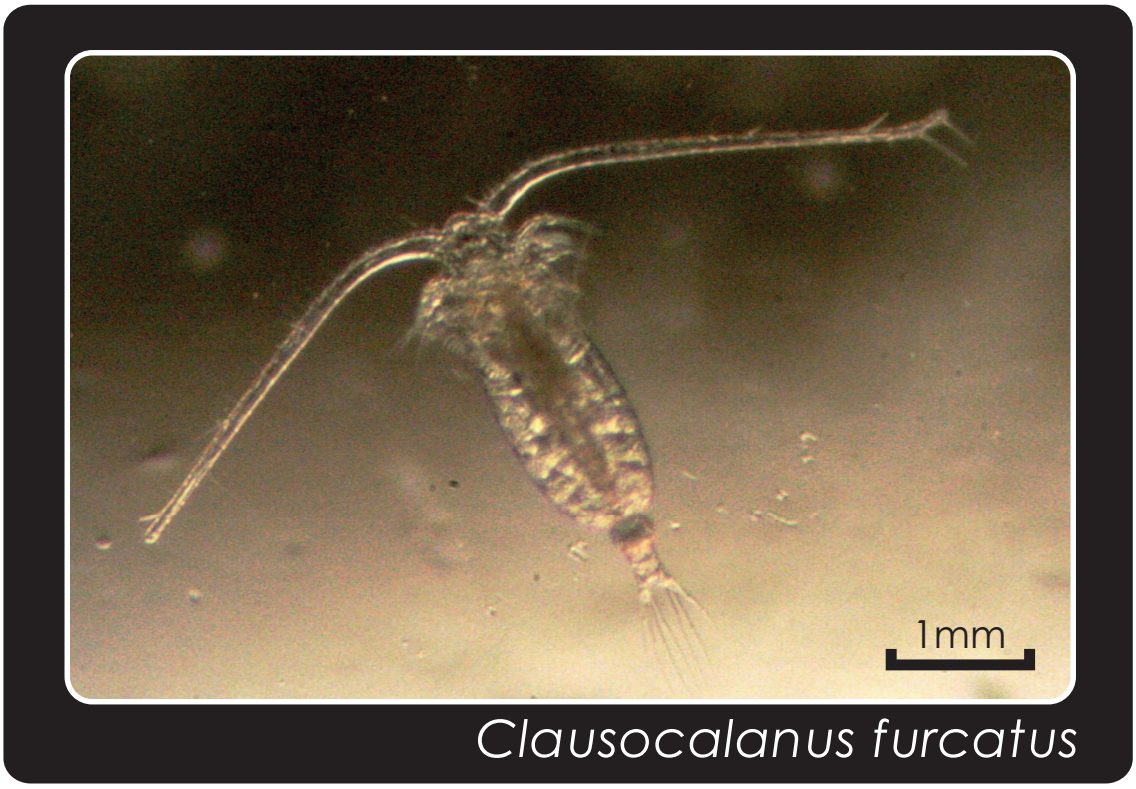

Figure 2.6: *Clausocalanus furcatus* collected in the Gulf of Aqaba, Red Sea, Eilat, Israel (photo by Ellen True).

resource patches. For calanoids, foraging and feeding behavior are driven by mechano- and chemoreception in an effort to locate resource patches. Field studies by Mullin and Brooks (1976) found that the copepod *Calanus pacificus* would not be able to survive in the water column except at a preferential depth with concentrated food resources. Similarly, Daro (1988) found that a dominant copepod species was food limited at most depths and that minimum concentrations necessary for survival (200 $mg\ cm^{-3}$) were only found in one narrow depth range between 20 and 30 m. Furthermore, massive *in situ* evidence for microscale patchiness (Derenbach et al. 1979, Cowles et al. 1993, Jaffe et al. 1998) shows that often limited food resources inhibit copepod growth and thus copepods must be able to actively locate and exploit isolated resource patches in order to survive. Indeed, the idea of area-restricted search behavior (Tinbergen et al. 1967) in individuals through decreased swimming speed and increased turn frequency can often produce population scale aggregations. Many species of copepod including *Pseudocalanus minutus* (Buskey 1984), *Temora longicornis* and *Pseudocalanus elongans* (Tiselius and Jonsson 1990), and *Acartia tonsa* (Tiselius 1992), are observed to decrease swimming speed (or hop frequency) when encountering food patches. Leising et al. (2005) also note predation risks for a foraging copepod exploiting different portions of the water column, and modeling studies by Leising and Franks (2000) and Leising and Franks (2002) examined the effect of food concentrations and patchiness on copepod swimming behavior and found behavior consistent with area-restricted foraging.

In addition to habitat partitioning, prey capture and predator detection and avoidance behaviors are also stimulated by a variety of chemical and fluid mechanical cues. While there are many types of feeding behavior (Kiørboe 2011), one option is for copepods to set up a complex three-dimensional feeding current to entrain remote phytoplankton cells (Malkiel et al. 2003) and through sensing the hydrodynamic (Kiørboe and Visser 1999) and chemical (Paffenhöfer 1998) signals accept or reject incoming

particles. Fields and Yen (1997a) and Fields and Yen (1997b) quantified threshold shear strain rate values that triggered escape responses in various calanoid copepods (Table 2.1). Viitasalo et al. (1998) examined the effect of predator foraging technique and copepod sensitivity in the hydrodynamic signal perception of an ensuing strike, whereas Holzman and Wainwright (2009) performed a quantitative PIV analysis of suction forces and signal perception in fish feeding on copepods.

Another important behavior mediated by the generation and perception of chemical and fluid mechanical signals is reproductive and mating behaviors. Yen et al. (1998) observed male calanoids tracking pheromone trails left by females. They discuss the importance of chemical and fluid mechanical signal persistence by quantifying diffusivities for the chemical cue. In fact, the low Re and low Pe regime was found to be significantly important in the success of the male in locating the female. Similarly, Bagøien and Kiørboe (2005a,b) observed mating behavior in two calanoid copepods. In *Acartia tonsa*, a hop-sink swimmer, mating appeared to be controlled by fluid mechanical signals as a series of 7 - 8 synchronized hops often ended in mating (Bagøien and Kiørboe 2005a). On the other hand, for *Centropages typicus*, a cruiser, mating appeared to be chemically-mediated, as males were observed to accelerate and zig-zag across the females pheromone trail (Bagøien and Kiørboe 2005b). Thus, individual species of copepods with different morphologies can best exploit their own sensing abilities to optimize the mating process.

Finally, habitat partitioning through diel vertical migration (DVM) and behavioral responses to fluid mechanical, chemical, and phototactic cues can have significant trophic consequences. Many calanoid copepods, like many other zooplankters, are diel vertical migrators, i.e. they exhibit large changes in depth on a diel cycle driven by photactic cues (Enright and Hamner 1967). When vertical migratory behavior is superimposed on the physical structure of the water column and coupled with individual behavioral responses to patchy cues, population-scale, high-density aggregations can

results. Early experiments by Harder (1968) on a variety of zooplankton showed that almost every species tested aggregated at salinity and/or temperature interfaces (i.e. the pycnocline). Field work by Mackas et al. (1993) showed multiple species of copepods aggregating in the layer just above the permanent halocline. Interestingly, depth-distribution was species-segregated. Bollens et al. (1994) tested the effects of a variety of mechanical, chemical, and visual cues in producing patchy aggregations of the copepod *Acartia hudsonica*. Genin et al. (2005) acoustically tracked over 375,000 zooplankters over a coral reef in the Red Sea and observed active behavioral choices to swim against vertical flows and thus maintain depth that on a population scale could lead to dense aggregations. Finally, Pierson et al. (2009) documented that copepods make periodic forays into deeper waters throughout the night, suggesting a higher frequency component to classical conceptualization of DVM.

In summary, every aspect of a calanoid copepod's life is dominated by behavioral responses to hydrodynamic (Jiang et al. 2002), chemical (Poulet and Ouellet 1982), and phototactic (Bollens et al. 1994) cues. The way in which behavioral responses change when multiple cues are combined leads to the idea of a cue hierarchy and provides a basic tool for quantifying the ecological implications of individual behavior.

2.2.3.3 Brachyuran Crab Larvae: Life History and Morphology

Decapod crustaceans of the infraorder Brachyura are common crabs that inhabit a variety of aquatic ecosystems. There are 93 families of Brachyuran crabs and at least 6,793 individual species. Different species are distinguished by variations in external morphology, sexual dimorphism, and larval developmental stages. Brachyuran crabs reproduce sexually, after which larvae are dispersed to feed in surface waters as a planktonic stage during which they progress through a number of zoeal stages. Following the final zoeal stage, larvae molt into the megalopa stage after which they

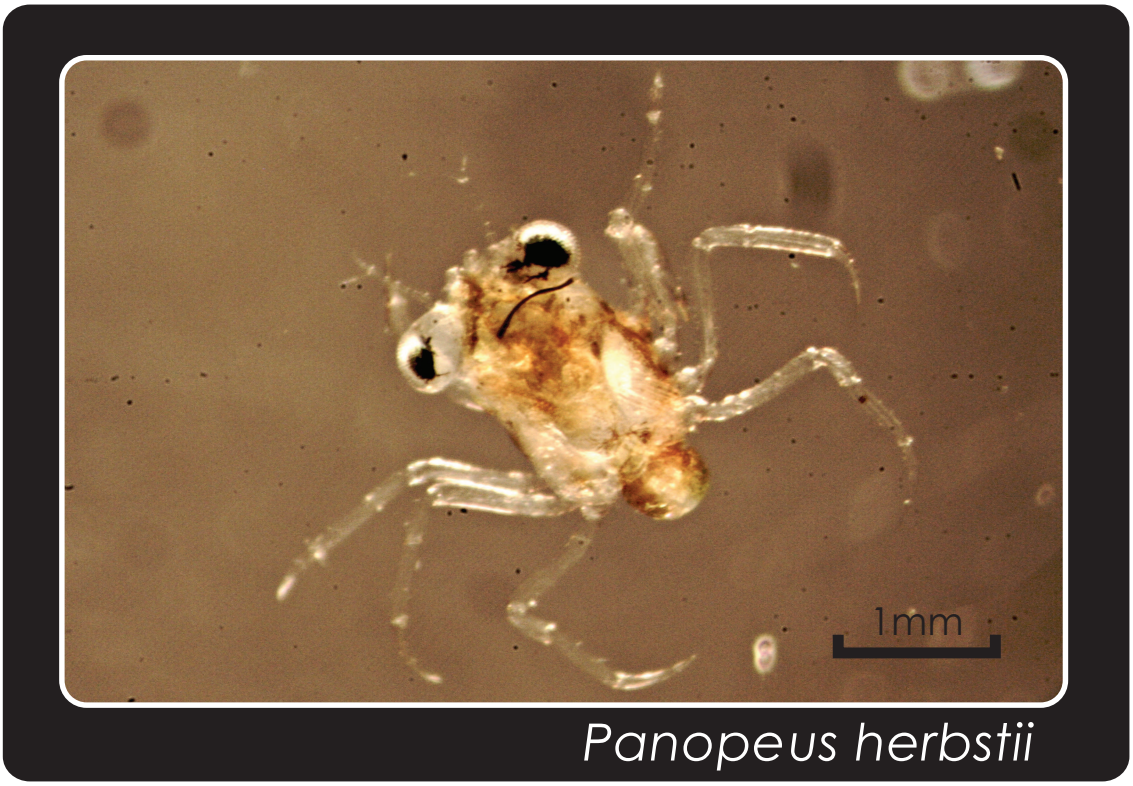

Figure 2.7: *Panopeus herbstii* collected in Wassaw Sound, Skidaway Island, GA, USA (Photo by Ellen True).

settle out to the benthic stage and molt again into the first crab (juvenile) stage (Forward et al. 2001). Thus, these crabs are mandatory ontogenetic migrators, that is the vertical distribution of the population is life-stage dependent. Ontogenetic, diel, and tidal vertical migration, along with higher frequency behavioral responses to physical and chemical cues, superimposed on the ambient hydrodynamic environment lead to complex larval dispersal trajectories and have important implications for structuring coastal marine ecosystems (Queiroga and Blanton 2005).

There is vast literature on the ways in which individual behavioral responses to various physical and chemical cues combine with physical forcing mechanisms to regulate dispersal and metamorphosis in planktonic larval stages (Ott and Forward 1976, Queiroga and Blanton 2005, Lecchini et al. 2010). The two species most likely to be employed in this study are the estuarine Atlantic mud crab, *Panopeus herbstii*, and

the estuarine Atlantic blue crab, *Callinectes sapidus*, and thus the focus here will be on understanding the interactions of estuarine hydrodynamic forcing and individual behavioral processes in regulating dispersal and settling in the planktonic larval stages of these two, and similar, Brachyuran crabs.

2.2.3.4 Brachyuran Crab Larvae Sensory Ecology

The manner in which crab larvae interact with their estuarine environments is an incredibly complex subject owing to behavioral variability among and within larval stages (Shanks 1986, Jamieson and Phillips 1988, Hobbs and Botsford 1992), a wide variety of physical forcings (Officer 1976), and relevant length and time scales spanning many orders of magnitude (Queiroga and Blanton 2005). The literature is vast, and there are two major recurring biophysical themes. The first is the ability of crab larvae to exploit vertical gradients of horizontal velocity during various vertical migrations (ontogenetic, tidally-synchronized, diel, etc.) to control the extent of horizontal dispersion (e.g. Cronin and Forward 1986, Eggleston et al. 1998, Forward et al. 2004). The second is the role of physical and chemical cues in delaying or inducing larval metamorphosis and settling (e.g. Forward et al. 2001, Houser and Epifanio 2009).

Brachyuran crab larvae are some of the strongest swimmers in the zooplankton and are capable of sustaining swimming velocities from 0.2 - 8.3 cm/s, though most measurements fall in the range from 0.5 - 2 cm/s (Mileikovsky 1973, Sulkin et al. 1979, Forward 1989a, Forward 1989b). Larvae can effectively navigate vertically throughout the water column during ontogenetic, tidal, and diel migrations, but their swimming capabilities are generally insufficient to counteract displacement by horizontal currents for an extended amount of time (Chia et al. 1984, Young 1995). Furthermore, competent larval stages have mechanosensing setae distributed along the appendages capable of sensing spatial gradients of flow (Santana et al. 2004, Kornienko et al. 2008). Thus, larvae can sense vertical gradients of horizontal velocity to effectively

maintain position or induce shoreward or shelfward transport depending on the goals of that particular larval stage. Hill (1991a,b) noted that vertical migration must extend into the bottom boundary layer for larvae to escape high tidal velocities and thus displacements. Olmi (1994) and Queiroga (1998) document how high vertical shear during tidal exchange in shallow estuaries can be exploited by larvae to influence their own transport. By swimming vertically down during ebb tide and up during flood tide, larvae gain net transport shoreward. This effect is aptly named Selective Tidal Stream Transport (STST) and describes the means by which larvae can exploit vertical gradients of horizontal velocity to control the extent of horizontal dispersion (Forward et al. 2001, Forward et al. 2003b). It should be noted that the term *Selective Tidal Stream Transport* refers specifically to tidal cyclic migrations that exploit vertical shear for optimal horizontal transport, but the idea of larval behavioral responses to fluid mechanical shear strain rate can be considered a generalization of this behavior (Queiroga and Blanton 2005) and is an ecologically-important adaptation in practically all species.

Whereas shear strain rate sensing and vertical migrations are dominant behaviors in Brachyuran larvae, other environmental variables can also act to regulate and modify larval behavior. Sulkin (1984) modeled the negative feedback effects of pressure and gravity on larval behavior and found depth-keeping behavior, though there is considerable variability in the effects of barokinesis and geotaxis in different larval stages. Various studies have found positive phototaxis to directional light, again with changes in effects with larval stage and the presence of other sensory cues (Forward 1974, Sulkin 1975, Sulkin et al. 1980). Depth-keeping seems to be regulated by negative geotaxis in darkness and changes in phototaxis combined with a sinking response above a threshold light level (Queiroga and Blanton 2005). Another interesting interaction among cues occurs when larvae exposed to increasing pressure respond by swimming vertically up. However, this effect is dampened in the presence

of high light levels (Tankersley et al. 1995). Increasing salinity levels were observed to trigger vertical migrations upwards and the process was noted to be rate dependent (Forward 1989a), whereas high temperatures have been observed to reverse geotactic behavior from negative to positive in zoeae of *Rhithropanopeus harrisii* (Ott and Forward 1976). Changes in turbulent kinetic energy levels up to a saturation level of 1.1 $cm^2 s^{-2}$ triggered exited swimming behavior in *Callinectes sapidus* (Welch et al. 1999). Finally, chemical cues play an important role in inducing or delaying metamorphoses between larval stages and in site selection for settlement. In general, positive cues that accelerate metamorphosis include adult habitat substrate, aquatic vegetation, conspecific odors, estuarine water, odor of a related crab species, and prey odor. Negative cues that delay metamorphosis include ammonium and ammonia, hypoxia, predator odor, and extreme temperatures and salinities. Cues found to have no effect are clean seawater, clean structural material, and odor of other non-related species (Forward et al. 2001 and the references therein).

The effects of various interacting physical and chemical cues on larval behavior are certainly complicated and case dependent. Nevertheless, it is clear that behavioral responses to changing physical variables (light, temperature, salinity, current velocity) associated with tidal fluctuations have the potential to significantly modify vertical migratory behavior and ultimately larval dispersal trajectories. Additionally, chemical cues play an important role in dictating larval behavior, and most importantly it is the superposition of these interacting effects (behavioral responses, vertical migrations, physical forcing) that dictates the dispersal trajectories of planktonic Brachyuran crab larvae.

2.2.3.5 Antarctic Krill: Life History and Morphology

Antarctic krill (*Euphausia superba*) inhabit the peninsular region off the northwest coast of the Antarctic continent. Krill populations range from the Antarctic Continental Shelf break to the Antarctic Polar Frontal Zone, with regions of enhanced biomass and krill density associated with the interaction of the Antarctic Coastal and Antarctic Circumpolar Currents. As direct consumers of primary producers and a crucial prey item for a variety of predators from whales and seals to sea birds and squid, Antarctic krill are the lynch-pin of Southern Ocean ecology. They are also the subjects of a valuable commercial fishery and are responsible for a significant body of scientific literature.

After sexual reproduction of adult krill, fertilized eggs are laid and sink continually for approximately 10 days to depths of up to 2000 meters, after which they hatch as nauplii and begin an ontogentic migration towards surface waters. During this ontogenetic ascent, larvae metamorphose through multiple stages, molting both within and between stages, which include the following: nauplius, metanauplius, calyptopus, and furcilia. Furcilia develop into juvenile krill (body lengths 4 - 10 mm) during feeding in surface waters by the end of the first winter, and finally reach sexual maturity as adults at two years of age (Everson 2000, Hamner and Hamner 2000, Nicol 2006).

Antarctic krill would most commonly be described as shrimp-like in morphology. A calcified exoskeleton, or carapace, has two main segments: the cephalothorax, from which emanate a pair of highly-developed compound eyes, antennules, antennae (coated in mechanosensitive setae), and six pairs of thoracic appendages (which collectively form the feeding basket apparatus) and the abdomen, from which emanates five forked swimming appendages, or pleopods. The abdomen terminates in the fan-shaped tail, or telson, which plays an important role in directing the propulsive jet generated by the drag-based, metachronal beating of the abdominal pleopods

(Alben et al. 2010; Murphy et al. 2011, 2013). Multiple bioluminescent photophores are distributed along the body as well chemoreceptors which play a crucial role in foraging behaviors. Adult krill range in size from 5 to 6.5 cm long and can live for up to nine years, though typically two to seven. Adults display sexual dimorphism in which females are slightly larger and males are more elongated, have larger eyes, and longer antennae.

Antarctic krill are omnivorous, feeding on ice algae, pelagic algal blooms, copepods, other krill, and/or molted exoskeletons. They feed by forming a water-tight feeding basket with their six pairs of thoracic appendages. Prey items contained in the encapsulated water volume are then filtered out by compression-filtration of the basket, which expels water laterally through finely spaced setae (Hamner et al. 1983; Hamner 1988). Feeding behavior is initiated by the presence of dissolved chemical cues such as amino acids or other metabolites.

2.2.3.6 Antarctic Krill Ecology

Following the final larval metamorphosis from the final furcilia stage to the juvenile stage, Antarctic krill are obligate schoolers and do not break formation except to mate, forage, molt, or engage in associated behaviors (Hamner and Hamner 2000). Aggregations are diverse and dynamic, ranging from schools and swarms to super-swarms and extensive layers, with hydrodynamic, chemical and visual cues playing important roles in the spatiotemporal structuring of population-scale aggregations (body alignment, nearest-neighbor distance, overall density, etc.). Understanding and quantifying the spatiotemporal dynamics of krill populations is fundamental to sustainable modeling and managing of the rich Southern Ocean ecosystem.

Of primary interest in the literature are krill behavioral biology (Price 1989; Strand and Hamner 1990; Hamner and Hamner 2000; Zhou and Dorland 2004; Johnson and Tarling 2008), biomechanics and energetics (Kils 1981; Swadling et al. 2005;

Catton et al. 2011; Murphy et al. 2011, 2013), larval recruitment and retention (Wiebe et al. 2011), the mechanics, characteristics, and competitive advantages of schools and swarms (Grunbaum 1998; Watkins and Murray 1998; Patria and Wiese 2004; Tarling et al. 2009; Nowacek et al. 2011; Krafft et al. 2012, and spatiotemporal population dynamics in relation to environmental factors (Daly and Macaulay 1991; Trathan et al. 1993; Ward et al. 2002; Lawson et al. 2008; Ianson et al. 2011; Wiebe et al. 2011). If anything in the literature is clear, it is this: each of these important topics is highly variable with krill state (size, sex, maturity, predation stress, satiation level, etc.), season, and year. Nevertheless, important findings are being implemented into individual-based ecosystem models in an effort to sustainably manage this valuable ecological and economic resource.

2.2.4 Fractal Analysis: A Useful Tool for Analyzing and Quantifying Zooplankton Trajectory Characteristics

The term *fractal geometry* was coined by Mandelbrot (1977, 1982) in a quantitative effort to develop a unified means of describing the highly complex, irregular, and fragmented nature of the natural world. Traditional or Euclidean geometry often lacks the means to describe nested irregularities and *scale invariance* so often found in the geometries of plants, turbulence, and organisms swimming trajectories as well as a myriad of other natural phenomena (Seuront 2009). Somewhat counterintuitive, scale invariance means that an observed nested structure is unchanged under magnification or contraction and thus is *scale dependent* because it cannot be fully characterized by a single scale. It is precisely the ability of a fractal analysis to reveal multiple *scaling regimes*that make it a highly valuable and worthwhile endeavor in the present study and in marine ecology in general, where biophysical processes are so intimately linked across a vast continuum of spatio-temporal scales.

A *self-similar* fractal by definition may be written as a union of rescaled copies of itself, with the rescaling being isotropic. However, natural objects do not display

exact (statistical) self-similarity as do mathematical fractals. They do, however, often exhibit self-similarity over some finite range of spatial or temporal scales, and often over multiple ranges. These scaling regimes are separated by transition zones, which physically indicate scales at which environmental parameters (e.g. thermal, saline, shear, photic fields) impose constraints or induce changes in organism behavior. Thus, the use of a given power law to describe scale-dependent features and the extent of its validity (i.e. scaling range) inherently identifies characteristic scales of organization for organism behavior or environmental processes. Furthermore, enforcing statistical validity in the identification of scaling ranges ensures correct interpretation of the results of a *behavioral fractal analysis*.

The basic mathematical foundation of a fractal analysis begins with a quantity measured at some scale δ. For each measurement scale δ we ignore irregularities at sub-δ scales, but we are interested in how our measured quantity, $M(\delta)$, behaves as $\delta \to 0$. For example, in the present study we are examining a plane curve representing the discretization of an organisms swimming trajectory. Our measured quantity, $M(\delta)$, may be the number of steps of a finite length, δ, required to traverse the entire path. That is, as $\delta \to 0$, $M(\delta) \to \infty$. In the case of a fractal, the relationship between the measured quantity and measurement scale must follow a power law given by:

$$M(\delta) = k\delta^{-\phi} \tag{2.15}$$

where k and ϕ are empirical constants and ϕ is the *scaling exponent*. The convenience of the fractal analysis reveals itself here. Taking the logarithm of both sides, plotting the results on a log-log scale, and performing a regression analysis reveals the scaling parameter as the slope of the curve. In reality, there may be multiple scaling regions in which fractal behavior is observed, but which break down when a transition or break point is reached. The statistically-valid identification of these regions is of utmost importance to the revelation of the multifractal behavioral responses of the

zooplankton examined in this study. The specific methodology and statistical verification used in applying a behavioral fractal analysis to the present study is described in depth below.

A survey of zooplankton behavioral studies from 1964-2004 (Seuront et al. 2004) revealed 88 studies, of which only 12 made use of a behavioral fractal analysis to describe zooplankton swimming behavior. However, from 2004-2013 that number seems to be growing rapidly. The unique ability of a behavioral fractal analysis to provide scale-independent behavioral metrics that elucidate various types of behavior over a wide range of spatial and temporal scales is unmatched and provides a crucial unifying platform for the literature.

Traditional metrics used to quantify zooplankton swimming behavior, such as path length, move length and duration, swimming speed, turning angle and rate, and $NGDR$ are scale dependent (Seuront et al. 2004). That is, because different values of these metrics will be obtained when measured at different spatial and temporal scales, it would appear that there is no single, unambiguous scale at which swimming paths can be described. This is where the scale invariant nature of the fractal dimension becomes of utmost importance, providing a crucial reference framework for analyzing and interpreting behavioral data. In the present study, the path fractal dimension has been computed, as well as some traditional metrics, in order to facilitate both scale dependent and scale independent comparisons to the literature.

There are numerous methodologies for computing the fractal dimension, each with its particular flavor, which lend themselves preferentially to various types of analyses. In the present study, the *box-count method* is employed for computational ease and statistical validity. In this method, the fractal dimension, D, is computed by superimposing a grid of boxes, or pixels, of length λ on the path and counting the number of occupied boxes, $N(\lambda)$. This procedure is repeated for a range of pixel sizes dictated by the spatial measurement scale and temporal resolution. As

discussed previously, the number of occupied boxes will increase with decreasing box size, leading to a power law relationship, characteristic of a fractal:

$$N(\lambda) = k\lambda^{-D} \tag{2.16}$$

where λ is box size, $N(\lambda)$ is the number of boxes occupied by the path at a given λ, k is a constant, and D is the box-counting fractal geometry. More in depth information concerning the box-count algorithm is given in the subsection below. Taking the logarithm of the data, plotting on log-log scales, and performing a regression analysis reveals the path fractal dimension as the slope of the curve. Physically, D provides a measure of the path complexity, lying somewhere between linear ($D = 1$) and Brownian ($D = 2$) motion. Changes in zooplankton swimming behavior as indicated by statistically-significant changes in path fracticality (diffuseness or volume-fillingness) can significantly influence predator, prey, and mate encounter rates.

In order to ensure that observed fractal behavior is indeed statistically sound over the whole range of available scales, and to test for the existence of multiple scaling regimes, the R^2-SSR procedure (Seuront 2009, 2010) is applied to all fractal data sets obtained through application of the box-counting method. This eliminates any implicit assumption of linear behavior in the log-log plots, and thus statistical significance of the fractal dimension being dependent upon the R^2 value obtained during the regression. Conveniently, the R^2-SSR procedure simultaneously tests for breakpoints or transition zones between different scaling regimes, thus revealing any multiscaling behavior.

Application of the R^2-SSR procedure is simple and powerful. Regression windows of varying width, from 5 data points (the minimum number for a statistically valid regression analysis) to the entire data set, are slid along the entire data set one point at a time. Within all windows and for every window width a least squares regression is performed and the coefficient of determination (R^2) and the sum of the squared

residuals (SSR) are computed. Finally, only values of box width (λ) which minimize the total SSR and maximize R^2 are selected to define the scaling regime and thus provide the fractal dimension. Again this procedure conveniently tests for both the existence of fractal behavior as well as the possibility of multiple scaling regimes.

Two dimensional zooplankton trajectory fractal dimensions (F_{2D}) were computed using a custom box-count algorithm written in MATLAB (R2012b) following the recommendations of Liebovitch and Toth (1989), Buczkowski et al. (1998), Uttieri et al. (2005), and Seuront (2009). A variety of factors are known to significantly affect the accuracy and statistical validity of fractal dimensions computed algorithmically, each of which was addressed in the custom box-count algorithm written here. These include the following: grid positioning with respect to the digitized trajectory data (i.e. origin location), the upper and lower limit of box sizes used as it relates to the overall resolution of the optical system, the mathematical sequence of box sizes, and the regression analyses used to extract F_{2D}) from the resulting log-log plot of $N(\lambda)$ vs. λ.

Digitized trajectory data (x, y, t) were first shifted to a new origin located at the intersection of two tangent lines originating at the two trajectory points containing the minimum x and y values of the trajectory set, respectively (Buczkowski et al. 1998). Using a standardized grid origin with respect to the trajectory data ensures optimal embedding and alleviates the possibility of differing grid locations resulting in different computed fractal dimensions (Uttieri et al. 2005). Next, a dyadic sequence (2^n or powers of two) of box sizes was chosen, as this mathematical sequence always yields an integer number of boxes and alleviates potential border problems Buczkowski et al. 1998). The lower cutoff for the box size sequence was chosen as 2^1 pixels to avoid saturation problems typical of single pixel box sizes, whereas the upper cutoff was taken as $2^8 = 256$, the power of 2 closest to half the minimum optical resolution of the system (e.g. for the camera used here, the CCD sensor is 480 x 720 pixels, 480/2

$= 240 \rightarrow$ upper cutoff $= 256$). These procedures are somewhat standard in the fractal analysis/box-count algorithm literature (Liebovitch and Toth 1989, Buczkowski et al. 1998, Uttieri et al. 2005). Finally, the digitized trajectory image is converted into a binary (or logical) array for each grid of box sizes and the sum of all nonzero elements (i.e. boxes occupied by the trajectory) is taken as the number of boxes occupied for that particular grid size. Lastly, linear, least-squares regression analysis is used on the resulting data set ($N(\lambda)$ vs. λ) to extract F_{2D}. The R^2-SSR procedure (Seuront 2009), described in detail above, is employed to ensure a statistically valid and an accurate description of the zooplankton trajectory fractal characteristics.

Validation and calibration of the custom box-count algorithm were performed by computing the fractal dimensions of pure two-dimensional linear motion (theoretical $F_{2D} = 1$) and pure two-dimensional Brownian motion, or random walk (theoretical $F_{2D} = 2$). Values computed for each of these two cases were 0.9982 and 1.9982, respectively, revealing a constant correction factor of +0.0018, which was applied to all path fractal dimensions computed with this algorithm.

2.3 Experimental Methods in Fluid Mechanics

In this study we aim to reproduce ecologically-relevant physical and chemical cues commonly reported in thin layers. Importantly, we need to fully quantify the cue structure to ensure that conditions replicated in the lab are indeed what a zooplankter would experience *in situ*. This section reviews several methods that will be employed in the proposed study. Specifically, the Bickley jet can produce repeatable and continuous shear strain rate fields as well as high density phytoplankton layers via advection through the observation region, internal waves simulate oscillations of the thermocline and pycnocline associated with thin layer dynamics, particle image velocimetry (PIV) fully resolves to the two-dimensional velocity and shear strain rate fields, and planar laser-induced fluorescence (PLIF) fully resolves the spatial structure

of chemical concentrations.

2.3.1 Planar Laser-Induced Florescence (PLIF)

Planar laser-induced fluorescence (PLIF) is a widely-used, non-invasive technique for measuring scalar concentration fields in a variety of flow conditions. The flow of interest is illuminated with a sheet of laser light (in the two dimensional or planar case), and a fluorescent dye acting as a proxy for the scalar is excited and emits light of a slightly different wavelength. With proper system design and image post-processing techniques, the intensity of the fluoresced light is linearly proportional to the concentration field (Ferrier et al. 1993). Through careful selections of digital camera, dye, laser, and optical setup, PLIF can be quantitatively applied to a vast spectrum of flows from turbulent plumes in open channel flow (Webster et al. 2003) to stratified flows (Daviero et al. 2001) to internal waves (Troy and Koseff 2005) to biologically-generated flows (Monismith et al. 1990, Koehl et al. 2001, Crimaldi et al. 2002, Mead et al. 2003). Here we will consider some of the theory, hardware, and sources of error common in many aqueous PLIF applications, as reviewed by Crimaldi (2008).

2.3.1.1 Basic Florescence Theory

Assuming that the local excitation intensity is much less than the saturation intensity ($I << I_{sat}$), the local fluorescence, F, is linearly proportional to the product of the local excitation intensity, I, and the local concentration, C, as

$$F \propto IC \tag{2.17}$$

I is usually unknown and varies spatially and temporally along any given ray path in an instantaneous concentration field according to the well-known Beer-Lambert Law

as

$$\frac{dI}{I} = -\epsilon C dr \tag{2.18}$$

where ϵ is an absorption or extinction coefficient (Walker 1987). Thus, Equation 2.18 tells us that a ray of light with intensity I passing an infinitesimal distance dr through a local concentration C will experience a change in intensity. Integrating Equation 2.18 over the length that a given ray travels from point $r = r_o$ to $r = r_1$ through a dye field gives

$$I(r_1) = I(r_o) exp[-\epsilon \int_{r_o}^{r_1} C(r) dr] \tag{2.19}$$

Light attenuation (changes in intensity) along a given path can be considered negligible if

$$\epsilon \int_{r_o}^{r_1} C(r) dr << 1 \tag{2.20}$$

PLIF systems with dye concentration fields and optical paths that satisfy the condition of Equation 2.20 are considered "optically thin" by Melton and Lipp (2003) and the post-processing analyses are greatly simplified. Finally, the quantum efficiency of the fluorescent dye, Φ, is the ratio of the light energy emitted to the light energy absorbed and leads to a differential statement of Equation 2.17 along a given ray path as

$$dF = -\Phi \epsilon I C dV \tag{2.21}$$

in a differential volume dV for finite laser sheet thickness. Finally, Equation 2.21 can be applied to a typical PLIF system in which a laser sheet is emitted radially to give the total volumetric fluorescence. If we assume that no emitted light is reabsorbed along a given ray path, the fluorescence intensity at any given pixel location (i, j) in polar coordinates (r, θ) is given as

$$I_F(i,j) = \beta(i,j)\frac{F}{\Delta A} = \alpha(i,j)a(r,\theta)C \tag{2.22}$$

where ΔA is the imaged area, $\beta(i, j)$ is the flux of fluorescence onto the camera optics at any given pixel location, $\alpha(i, j)$ is a collection of constants independent of concentration with units $[\frac{I}{C}]$, and $a(r, \theta)$ is the dimensionless attenuation due to absorption along radial ray paths and is often designed to be close to unity (Walker 1987, Ferrier et al. 1993, Crimaldi 2008).

2.3.1.2 The Hardware: Cameras, Dyes, Lasers, and Optics

A properly designed PLIF system requires a laser and fluorescent dye combination to match. The wavelength of incoming laser light excites the dye by lying in at least a portion of the dye absorption band (Crimaldi 2008). Continuous wave (CW) Argon-ion lasers (488 nm, 514.5 nm) and pulsed Nd:YAG lasers (532 nm) are by far the most commonly used in the literature. Ion lasers typically have superior beam quality than Nd:YAG lasers (i.e. Gaussian beam cross-sections) but are also much less powerful. For this reason, scanning mirrors have been used to generate laser sheets from a ion laser beam as a means of maximizing sheet intensity with the lower characteristic laser power. Alternatively, a cylindrical lens could be used to generate the laser sheet at the cost of sheet intensity, which is typically not a problem in Nd:YAG lasers, especially

when considering possible errors due to excitation saturation (i.e. photobleaching, Larsen and Crimaldi 2006). Each optical solution for producing laser sheets can lead to distortions of scalar structure in the imaged flow; however, these effects can be mitigated by matching certain non-dimensional parameters that combine advection and scalar structure length scales as well as by properly factoring in CCD exposure time (Crimaldi 2008).

There are a variety of organic and synthetic fluorescent dyes that can be used in PLIF depending on the flow application and the desired data. Three of the most commonly used are flourescein (Karasso and Mungal 1997), Rhodomine WT (Melton and Lipp 2003), and Rhodomine 6G (Shan et al. 2004), which have been shown to produce linear relationships between fluorescence and concentration even well above saturation intensities, although there is slight dependence on temperature. Table 2.2 summarizes fluorescence characteristics of three commonly used dyes in aqueous applications.

Lastly, matching camera specifications to experimental needs usually involves a balance of three main parameters: pixel count, bit-depth, and frame rate. The bit-depth, n, determines the maximum intensity resolution as the total number of resolved concentrations levels (2^n). The pixel count and frame rate obviously set the spatial and temporal resolutions of the system. Another important camera parameter to consider is the spectral sensitivity as it relates to the wavelengths of the exciting laser light and the fluoresced dye emission. By nature PLIF requires a camera to focus on a single plane and thus flat-field lenses are needed to correct for aperture and depth of field distortions (Crimaldi and Koseff 2001). Finally, optical filters (high, low, band-pass) are employed to ensure imaging of only fluoresced light.

Table 2.2: Fluorescence characteristics of dyes commonly used in aqueous applications, adapted from Crimaldi (2008).

Dye	$\lambda_{abs}(nm)$	$\lambda_{em}(nm)$	$\epsilon(cmM^{-1})$	$\Gamma(cm^2/s)$
Fluor.	490	515	8.5 E 4 (@ 488 nm)	5.1 E -6
Rhodo. 6G	525	555	1.1 E 5 (@ 514.5 nm)	1.2 E -6
Rhodo. B	555	580	8.6 E 4 (@ 514.5 nm)	3.7 E -6

2.3.1.3 Image Processing and Error Mitigation

As in nearly all digital imaging applications, post-processing of raw PLIF images is required to correct for error, calibrate, and ultimately extract the desired information (the passive scalar field). The algorithm described below is representative of typical, robust PLIF codes as used by Crimaldi and Koseff (2001) and others.

The dye concentration present in the n^{th} image, $C_n(i,j)$, can be decomposed into the uniform background concentration at the imaging time, b_n, and the desired concentration scalar structure, $c_n(i,j)$, as

$$C_n(i,j) = c_n(i,j) + b_n \tag{2.23}$$

The decomposition allows the total attenuation coefficient in polar coordinates for a radial laser sheet $a(r,\theta)$ to be given as the product of $a_c(r,\theta)$ and $a_b(r)$, the local attenuations due to the desired scalar structure c_n and the background dye concentration b_n, respectively. Similarly, the total fluorescence intensity of the uniform background concentration $B_n(i,j)$ can itself be decomposed into contributions from the background attenuation and the camera dark response $D(i,j)$ as

$$B_n(i,j) = \alpha(i,j)a_b(r)b_n + D(i,j) \tag{2.24}$$

The dark response is simply the average of a number of images taken with the lens cap on and is typically temperature dependent. The recorded image fluorescence intensity $I_n(i,j)$ in the n^{th} image for a flow with uniform background and additional scalar structure is then given as

$$I_n(i,j) = \alpha(i,j)a_c(r,\theta)a_b(r)[c_n(i,j) + b_n] + D(i,j) \tag{2.25}$$

Combining Equations 2.25 and 2.24 and assuming that the recorded intensity I_n is much greater than the difference between the background intensity and dark response ($I_n >> B_n - D$) yields the final equation that guides algorithm development for error correction and concentration calculation as

$$c_n(i,j) \approx \frac{b_n}{a_c(r,\theta)} \frac{I_n(i,j) - B_n(i,j)}{B_n(i,j) - D(i,j)} \tag{2.26}$$

where $a_c(r)$ is of order unity. Thus we see that there are three major step to the correction and computation algorithm. First, the raw images are "flat-fielded, that is the scalar structure intensity is normalized by the difference between the background and dark response intensities as in the (I_n - B_n)/(B_n - D) term. Next, the images are dimensionalized through scaling by b_n. Lastly, the images are corrected for attenuation via division by $a_c(r,\theta)$. A set of calibration images of multiple known concentrations can provide a functional relationship between pixel intensity and dimensional concentration (Karasso and Mungal 1996, Unger and Muzzio 1999) for computations.

Finally, as in any experimental design, there are various common sources of error as well as methods of minimizing and mitigating these errors. Table 2.3 provides a summary of error sources to be aware of in PLIF experimental design.

Table 2.3: Common error sources and remediations in PLIF spplications. Adapted from Crimaldi and Koseff (2001) and Crimaldi (2008).

Error Source	Error Type	Mitigation
Dye	Fluorescence from Background Dye	Eqn. 2.26
Dye	Fluorescence Sensitivity to pH and Temperature	Eqn. 2.26
Dye	Fluorescence Saturation (over-excitation)	Eqn. 2.26
Dye	Photobleaching	Typically not a problem in common PLIF applications
Excitation	Spatial Variation in Light Sheet	Eqn. 2.26
Excitation	Laser Attenuation from Background Dye Field	Eqn. 2.26
Excitation	Laser Attenuation from Instantaneous Dye Field	Low Dye Concentrations and Short Ray Paths
Excitation	Shot-to-shot Power Variation	CW lasers in Closed-Loop Operation
Optics	Refraction through Walls or Interfaces	Grid Image (Ferrier et al. 1993)
Optics	Lens Vignette	2.26
CCD	Pixel-to-pixel Offsets (Dark-response)	Eqn. 2.26
CCD	Pixel-to-pixel Gain Variations	Eqn. 2.26

Lastly, particle image velocimetry (PIV), like PLIF, is a well-known, non-invasive flow measurement technique employed widely in the fluid mechanics research community. In PIV, the flow of interest is seeded with small, neutrally-buoyant particles that are passively advected with the flow. The flow is then illuminated with laser light and the light scattered from the seeding particles is filmed digitally. The images are post-processed to compute particle displacements between successive frames. With a known temporal resolution, the velocity fields can be fully resolved in space and time (Raffel et al. 1998). It should also be noted here, that many of the same considerations concerning optics, lasers, and cameras in PLIF are directly applicable to considerations in PIV.

2.3.2 Free Shear Flows and the Bickley Jet

By definition, free shear flows are characterized by unrestricted spatial gradients of fluid velocity and commonly include jets, wakes, and shear layers (Kundu and Cohen 2004). Shear flows are a ubiquitous feature in the marine environment and most often take one of two forms as an artifact of the prevalent density stratification in many coastal marine environments: a plane jet (fluid intrusion) and/or a shear layer. A plane jet is characterized by a maximum velocity on the centerline of the jet with gradual decrease towards the stagnant layers above and below, whereas shear layers are characterized by a gradually changing velocity profile linking two layers of differing horizontal velocity (Figure 2.8). Field observations of thin layers (e.g. McManus et al. 2003, Velo-Suarez et al. 2010) document the co-occurrence of thin layers with physical structure in the water column, specifically the pycnocline and/or thermocline that essentially demarks an interface between two fluid layers. Thus, an appropriate model for a laboratory thin layer could be based on a free shear flow design. The Bickley jet is a laminar planar free jet (with known analytical solutions) that can be fine-tuned to produce ecologically-relevant gradients of velocity (shear strain rate). We will consider more closely the governing equations and analytical solutions for the Bickley jet as well as some considerations concerning hydrodynamic instabilities and implications for nozzle design.

2.3.2.1 The Bickley Jet: Governing Equations and Analytical Solution

Following the analysis of Bickley (1937), we consider a steady, incompressible, two-dimensional flow generated by a viscous jet issuing from a long narrow orifice into a fluid body at rest. Assuming the Prandtl boundary layer equations provide a good approximation to the free jet and noting that pressure is invariant in the streamwise, x, and transverse, y, directions, the flow is governed by the continuity equation,

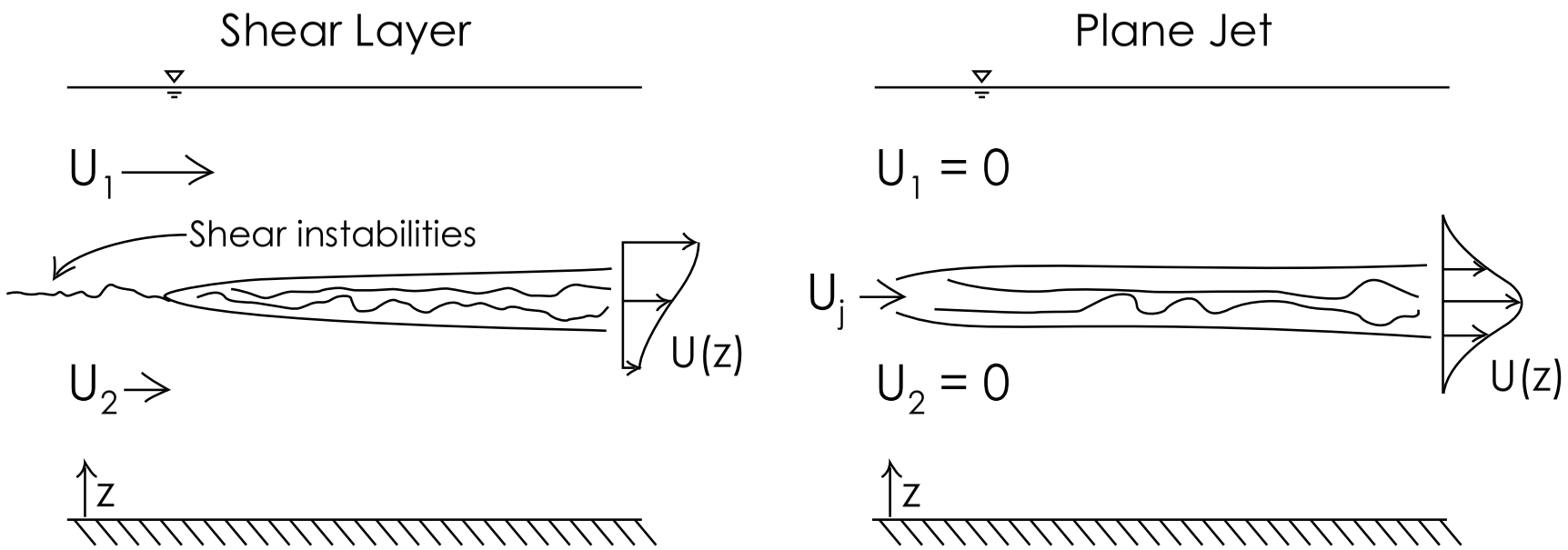

Figure 2.8: Typical free shear flows in the marine environment (adapted from Woodson 2005).

$$\frac{\partial u}{\partial x} + \frac{\partial v}{\partial y} = 0 \tag{2.27}$$

and the x momentum equation,

$$u\frac{\partial u}{\partial x} + v\frac{\partial u}{\partial y} = \nu\frac{\partial^2 u}{\partial y^2} \tag{2.28}$$

where u and v are the x and y components of velocity, respectively, and ν is the kinematic viscosity. The flow is subject to the following three boundary conditions concerning symmetry about the jet centerline, purely parallel flow, and boundedness in the transverse direction:

$$\frac{\partial u}{\partial y} = 0 \tag{2.29}$$

$$v = 0 \; at \; y = 0 \tag{2.30}$$

$$u \to 0 \; as \; y \to \infty \tag{2.31}$$

Finally, the total x momentum, M, is conserved such that

$$M = \rho \int_{-\infty}^{\infty} u^2 dy = Initial \; Jet \; Momentum \; Flux \tag{2.32}$$

Following the solution method of Schlichting (1933) and presenting the results per Sato and Sakao (1964), the non-dimensional analytical velocity field results as

$$\frac{u}{u_o} = \text{sech}^2\left(\frac{ay}{\delta}\right) \tag{2.33}$$

where $a = 0.88136$. The maximum, or centerline velocity, u_o, deceases with distance downstream due to entrainment of low momentum fluid as

$$u_o = \left(\frac{3M^2}{32\nu x}\right)^{1/3} \tag{2.34}$$

and the jet half-width δ (based on the velocity field) is given as

$$\delta = a\left(\frac{48\nu^2 x^2}{M}\right)^{1/3} \tag{2.35}$$

It is clear that the centerline velocity is singular at $x = 0$ and this has given rise to the idea of a virtual origin to account for a non-zero nozzle width as the x location of a point source of momentum from which the jet can be considered to emanate (Andrade 1939, Revuelta et al. 2002, Peacock et al. 2004).

Andrade (1939) noted that the "plane jet is difficult to realize experimentally", but was able to reproduce the Bickley solution in the neighborhood of an orifice if the flow was considered to emanate from a virtual origin a small distance upstream of the orifice. Sato (1960), however, was unable to reproduce the self-similar profiles of Bickley precisely because the plane jet is difficult to experimentally operate. The reasons for these difficulties are considered below as well as some design precautions.

2.3.2.2 Hydrodynamic Instabilities and Design Considerations

To gain a better understanding of the stability characteristics of the Bickley jet and the critical parameters, it is useful to consider the linear stability analysis. As for all parallel shear flows, the hydrodynamic stability of the viscous Bickley jet is governed by the Orr-Sommerfeld Equation via normal modes analysis as

$$(i\alpha Re)^{-1}\left(\frac{\partial^2}{\partial y^2}-\alpha^2\right)^2\Phi=(U-c)\left(\frac{\partial^2}{\partial y^2}-\alpha^2\right)\Phi-\frac{\partial^2 U}{\partial y^2}\Phi \tag{2.36}$$

where α is the perturbation wavenumber, c is the perturbation wave celerity, U is the base flow velocity distribution in the y direction, and Φ is the eigenfunction of the perturbation streamfunction. This equation is essentially a linearized equation of motion (conservation of mass and momentum) for small perturbations superposed on the base flow. With a known base flow and set boundary conditions, α can be varied and the behavior of c observed. Various numerical and expansion solution techniques have been proposed (Tatsumi and Kakutani 1958, Sato 1960, Drazin and Reid 1981) that yield the marginal stability curves. Experimental results by Sato (1960) observed two sinusoidal instability modes that manifest as velocity fluctuations symmetric and antisymmetric about the jet centerline.

The marginal stability curves in Figure 2.9 were derived by Peacock et al. (2004) using a Newton-Raphson relaxation scheme to numerically solve the Orr-Sommerfeld Equation for the Bickley jet base flow. It is clearly seen that for a given ω, the symmetric and antisymmetric modes are unstable at different Reynolds numbers. The critical Re for the antisymmetric mode is extremely small for virtually all frequencies of perturbation, ≈ 4, whereas the symmetric mode is stable to most perturbation frequencies until $Re \approx 80$. Thus, the critical experimental parameter governing jet stability is revealed as the jet Re

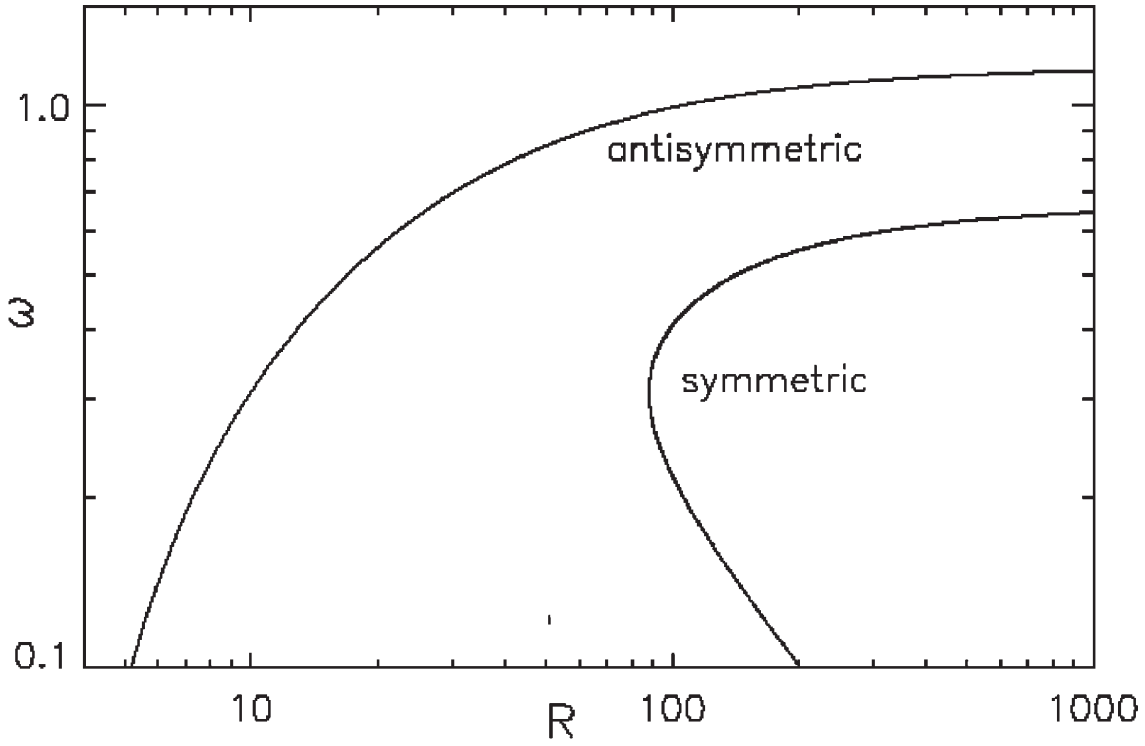

Figure 2.9: The Bickley jet marginal stability curve. ω is the non-dimensional perturbation frequency and R is the local Reynolds number based on the centerline velocity and the velocity half-width. Source: Peacock et al. (2004).

$$Re_j = \frac{u_j d_j}{\nu} \tag{2.37}$$

that describes the ratio of the destabilizing momentum forces to the stabilizing effect of shear. Sato and Sakao (1964) experimentally investigated instabilities in the Bickley jet based on Re_j and found good agreement with linear stability theory for $Re_j \geq 10$ (Table 2.4). For smaller Re_j, the theory does not account for the streamwise variation of the base flow through entrainment and spreading of the momentum distribution, i.e. the *local* Reynolds number, Re_o, which is a function of the downstream distance x.

Considering the inherent instabilities in free shear flows and the particularly fickle behavior of the Bickley jet, a few main design considerations for reducing instabilities and producing the desired flow field have arisen from experimental studies of both laminar and turbulent planar jets. Many modern experimental studies suggest honeycomb and wire mesh baffles and a fifth-order polynomial contraction upstream of the nozzle exit to prevent flow separation and ensure a top-hat exit velocity profile (Mehta and Bradshaw 1979, Hussein 1994). Deo et al. (2007a) suggested a criteria for ensuring a top-hat profile as the ratio of the nozzle radius of curvature just upstream of the jet entrance, r, to the nozzle width, d_j, as $r/d \rightarrow 3.6$. Similarly, Deo et al. (2007b) suggested that a statistically two-dimensional mean velocity field is only achievable in turbulent jets aspect ratios greater than or equal to 20. Finally, Alnahhal and Panidis (2009) discuss the effect of sidewalls and found statistically different flow fields with and without sidewalls. There is a trade-off between boundary layer growth downstream, which acts as a lateral momentum sink (sidewalls), and lateral entrainment causing departure from two-dimensional mean flow. Each of these design considerations have been incorporated in the nozzle design here.

Re_j	Jet Behavior
$12 < Re_j < 20 \sim 30$	The jet is entirely laminar with possible periodic instabilities in limited regions
$20 \sim 30 < Re_j < 40 \sim 60$	Pseudo-steady periodic instabilities, found in a wide region of the jet, are dampened before transitioning to highly irregular instabilities
$40 \sim 60 < Re_j$	Periodic fluctuations transition to highly irregular instabilities downstream

Table 2.4: Jet stability characteristics as a function of Re_j from Sato and Sakao (1964).

CHAPTER III

BEHAVIORAL RESPONSE OF *PANOPEUS HERBSTII* MEGALOPAE TO COHERENT SHEAR FLOWS

3.1 Abstract

Behavioral assays with megalopae of the common Atlantic mud crab (*Panopeus herbstii* were performed in a laboratory mimic of hydrodynamic structure associated with fronts and clines. A laminar, planar free jet apparatus was employed to mimic finescale, coherent hydrodynamic structure associated with upwelling, downwelling, and horizontal free shear flows. The velocity and shear strain rate fields were quantified via particle image velocimetry (PIV). Analyses of digitized trajectories from free-swimming megalopae established orientation-specific behavioral shear strain rate thresholds (0.04 s^{-1} upwelling flow, 0.07 s^{-1} downwelling flow, 0.1 s^{-1} horizontal flow). Relative swimming speeds were statistically smaller post-contact and out-of-layer and turn frequency was statistically larger out-of-layer. Differences in average path kinematics revealed an area-restricted search behavior in the vicinity of horizontal shear flows (swimming slower on average, swimming slower post-contact and out-of-layer, and greater turn frequency out-of-layer) and an excited area-restricted search behavior in the vicinity of both vertical shear flows (swimming faster on average, swimming slower post-contact and out-of-layer, and greater turn frequency out-of-layer), although not in the layers themselves. Significant reduction in the net-to-gross displacement ratio ($NGDR$) and the vertical-net-to-gross displacement ratio ($VNGDR$) with respect to control (stagnant) conditions indicate that larval trajectories become more sinuous and larvae enhance depth-keeping behaviors under all shear flow orientations. Collectively, these shear-induced behavioral responses are

likely to produce megalopal aggregations in the vicinity of coherent shear flows, although there is explicit avoidance of both vertical layers themselves (↓ proportional residence time). These responses are likely associated with foraging and sampling behaviors in which the coherent shear flow acts as a cue to restrict search volume in hopes of exploiting some coincident or nearby cue and/or resource patch that are typical in fronts and clines. The exploitation of sensory cues contained in finescale patches is likely an important means by which dispersed larvae can couple behavioral needs and processes operating on disparate time and space scales (i.e. foraging and finding suitable settlement habitat).

3.2 Introduction

Selective tidal stream transport (STST) is a behavioral adaptation common to many nearshore fish and invertebrate species in which dispersed planktonic larvae exploit vertical gradients of horizontal velocity during various migrations (ontogenetic, tidally-synchronized, diel, etc.) to control the extent of horizontal dispersion, thus optimizing the dispersal trajectory (e.g. Cronin and Forward 1986, Eggleston et al. 1998, Forward et al. 2001, Forward et al. 2004). In general, larval dispersal is a complex function of numerous coupled biological, chemical, and physical processes operating over a wide spectrum of relevant space and time scales (Queiroga and Blanton 2005). Larvae can gain net transport shoreward by swimming vertically down during ebb tide and up during flood tide (or depending on the goals of the particular larval stage they can gain net transport seaward with the opposite behavior). Behavioral variability among and within larval stages (Shanks 1986, Jamieson and Phillips 1988, Hobbs and Botsford 1992) in combination with a wide variety of physical forcing mechanisms (Officer 1976) and the ever-present need to forage, create complex and somewhat stochastic dispersal trajectories.

There are a variety of tidally-modulated physical and biochemical cues known

to influence larval behavioral and thus overall dispersal trajectories in Brachyuran crabs (Ott and Forward 1976, Queiroga and Blanton 2005, Lecchini et al. 2010). A key behavioral response to tidally-modulated cues enabling larval STST behaviors is depth-keeping. The interaction of barokinesis (pressure-change induced behavioral responses) and geotaxis (gravity-induced behavioral responses) has been shown to produce depth-keeping behavior in brachyuran crab larvae (Sulkin 1984). However, there is considerable variability in the effects of pressure and gravity in different larval stages (Sulkin 1984), likely an artifact of different goals at various larval stages. Depth-keeping seems to be regulated by negative geotaxis in darkness and changes in phototaxis combined with a sinking response above a threshold light level (Queiroga and Blanton 2005). Various studies have found positive phototaxis to directional light, again with changes in effects with larval stage and the presence of other sensory cues (Forward 1974, Sulkin 1975, Sulkin et al. 1980). Larvae exposed to increasing pressure respond by swimming vertically up (i.e. on a flood tide); however, this effect is dampened in the presence of high light levels (Tankersley et al. 1995). Increasing salinity levels trigger vertical migrations upwards and the process was noted to be dependent on the rate of salinity increase (Forward 1989a), whereas high temperatures have been observed to reverse geotactic behavior from negative to positive in certain larval stages (Ott and Forward 1976).

Competent decapod megalopae are equipped with advanced mechano- and chemosensitive morphologies (e.g. Santana et al. 2004; Queiroga and Blanton 2005; Kornienko et al. 2008) that allow them to exploit tidally-modulated signals and dissolved chemical cues to maintain position, induce selective transport (Olmi 1994, Queiroga 1998), and/or effectively forage/sample the local environment. The ability to sense spatial gradients of fluid velocity and exploit that information is a fundamental ability megalopae require in order to navigate complex estuarine and nearshore hydrodynamic environments and ultimately find suitable settlement habitat, the final selection of which

is chemically-mediated (Forward et al. 2001). While many studies have examined the effects of chemical cues on larval metamorphoses (e.g. Rodriguez and Epifanio 2000; Andrews et al. 2001), habitat selection (e.g. Lecchini et al. 2010; Tapia-Lewin and Pardo 2014), and to a lesser extent swimming behaviors (e.g. Forward et al. 2003a; Houser and Epifanio 2009), there is a surprising lack of studies establishing behavioral (and physiological) response thresholds to hydrodynamic cues. Hydrodynamic cues are fundamental to many larval behavioral processes related to both STST and foraging/sampling. For example, changes in turbulent kinetic energy (TKE) levels up to a saturation level triggered exited swimming behavior in blue crab *Callinectes sapidus* larvae (Welch et al. 1999). More generally, larval behavioral responses to hydrodynamic cues are ubiquitous and an ecologically-important adaptation in practically all species (Queiroga and Blanton 2005).

In addition to the STST context, tidally-modulated cues influence larval behavior in foraging, larval metamorphoses, and benthic settling (e.g. Rodriguez and Epifanio 2000, Forward et al. 2001, Houser and Epifanio 2009). In general, positive cues that accelerate metamorphosis include adult habitat substrate, aquatic vegetation, conspecific odors, estuarine water, odor of a related crab species, and prey odor. Negative cues that delay metamorphosis include ammonium, ammonia, hypoxia, predator odor, extreme temperatures, and extreme salinities. Cues found to have no effect are clean seawater, clean structural material, and odor of other non-related species (Forward et al. 2001 and the references therein). The effects of various interacting physical and chemical cues on larval behavior are certainly complicated and case dependent. Nevertheless, it is clear that behavioral responses to changing physical cues (light, temperature, salinity, hydrodynamics) associated with tidal fluctuations have the potential to significantly modify vertical migratory behavior and ultimately larval dispersal trajectories. Additionally, chemical cues play an important role in dictating larval behavior, and most importantly it is the superposition of these interacting

effects (behavioral responses, vertical migrations, physical forcing) that dictates the dispersal trajectories of planktonic Brachyuran crab larvae.

It has been well-established that ambient turbulence levels play a fundamental role as an environmental cue that triggers competent larval behavioral responses linked to STST (e.g. Welch et al. 1999, Queiroga and Blanton 2005). High turbulent kinetic energy (TKE) levels are associated with highly unsteady, anisotropic flow conditions that act to homogenize a larva's environment (e.g. by mixing dissolved chemicals/heat, creating a flow field that has no innate directionality to it, etc.). In absence of other sensory cues to inform and/or structure larval behavior, it is disadvantageous to remain in such a region. In contrast to the effects of turbulence, the role of persistent flow structure often associated with fronts (e.g. the Estuarine Transition Zones) and clines (e.g. tidally-modulated vertical shear structure) has been relatively unstudied, particularly in the context of STST behavioral phenomena despite the fact that such structure is likely to be ecologically relevant. Finescale structure in the water column often is associated with enhanced productivity (Largier 1993; McManus et al. 2003) and thus raises fundamental questions about the role of sensory cues in affecting larval behavior and in particular what role does larvae foraging behavior play in and around thin layers?

In the present study we examine whether behavior of the imminently-settling megalop of the common Atlantic mud crab *Panopeus herbstii* is influenced by persistent, finescale shear flow commonly associated with fronts and clines. We hypothesize that regions of high TKE (highly unsteady and anisotropic flows), which are exploited as a fundamental cue for STST behaviors (e.g. Welch et al. 1999; Criales et al. 2013), are temporarily trumped by regions of psuedo-steady, spatially-coherent flow that often contain other coincident sensory cues and/or resources. This intermittent injection of a dominating sensory cue causing foraging behaviors may cause temporary departures from typical STST behaviors and significantly influence larval dispersal

trajectories (Woodson and McManus 2007).

3.3 Methods

A laminar, planar free jet (the Bickley jet) was employed in a recirculating flume system to mimic finescale, coherent hydrodynamic structure for behavioral assays with *Panopeus herbstii* megalops in upwelling, downwelling, and horizontal free shear layers. Planar particle image velocimetry (PIV) quantified the spatiotemporal flow structure allowing for quantitative correlation of larval behavioral responses to coincident hydrodynamic cues. Assays were conducted in a custom flume (Figure 3.1) in which acrylic walls allowed for undistorted optical access and video observation of two-dimensional free-swimming larval trajectories under infra-red illumination. A 10 cm x 10 cm observation window was centered in a $\sim$ 25 L volume, beginning 5 cm downstream of the physical jet origin; a custom baffle at the downstream end of the volume was designed to stabilize the free shear flow. Free-swimming larval trajectories were digitized under control (stagnant water) and laminar shear layer conditions to correlate changes in swimming kinematics and gross trajectory characteristics to coincident hydrodynamic cues.

3.3.1 Laminar Jet Flume and Flow Characterization

Larval behavioral assays were conducted in a recirculating flume system that employs a laminar, planar free jet (the Bickley jet) to create steady, finescale shear layers in upwelling, downwelling, or horizontal flow configurations (Figure 3.1, left panel). The main flume (1 m x 25 cm x 30 cm) is constructed of clear acrylic for optical access and can be aligned parallel or perpendicular to the gravity vector for laminar jet layer assays under various flow configurations. An elevated constant head tank (28 L, US Plastics) with a free surface overflow drives flow through a rotameter (Dwyer Instruments) and through a slot jet nozzle (316 SS, jet opening 1 cm x 25 cm) to create a laminar, planar free jet in the main test section. A 12:1 area ratio contraction

was employed with a 5th-order polynomial contraction to prevent flow separation and to minimize turbulent fluctuations in the upstream section. Stainless steel mesh (50% open area) and a layer of high porosity polypropylene sponge inside the main body of the nozzle further dampen turbulent fluctuations and distribute fluid momentum across the width of the nozzle opening. These design features ensure a uniform (top-hat) velocity profile at the nozzle exit and produce a laminar, steady match to the analytical velocity field immediately downstream in the observation section (Bickley 1937, Mehta and Bradshaw 1979, Hussein 1994, Woodson et al. 2005). The jet flow in the main test section flows through an acrylic flow conditioner to prevent recirculation, flow instability, and exit geometry effects. Finally, the flow continues via a free surface overflow to the bottom receiving reservoir (28 L, US Plastics) where it is pumped through a 4 diaphragm, positive displacement pump (JABSCO Model 31801-1305) to the constant head tank in a closed loop.

During all larval behavioral assays a volumetric flowrate of 16.8 cm^3/s (16 gph) was selected to produce a well-defined and ecologically-relevant laminar flowfield. A flowrate of 16.8 cm^3/s (16 gph) for the given nozzle geometry results in a maximum jet exit velocity, U_j, of 6.7 mm/s and a jet Reynolds number ($Re_j = U_j d/\nu$) of $\sim$50, which is in the transitionally stable, laminar flow regime. The velocity and strain rate profiles vary in the transverse directions producing ecologically-relevant velocity and shear strain rate fields throughout the observation window.

The flow fields produced by all laminar jet flow configurations were characterized with a time-resolved planar particle image velocimetry (PIV) system. PIV is a non-intrusive flow characterization technique commonly employed in experimental fluid mechanics in which the flow of interest is seeded with neutrally-buoyant particles and illuminated with a sheet (in the planar case) of laser light. A series of high frequency images of light scattered from the seeding particles is post-processed to compute particle displacement fields between successive frames and thus flow velocity fields

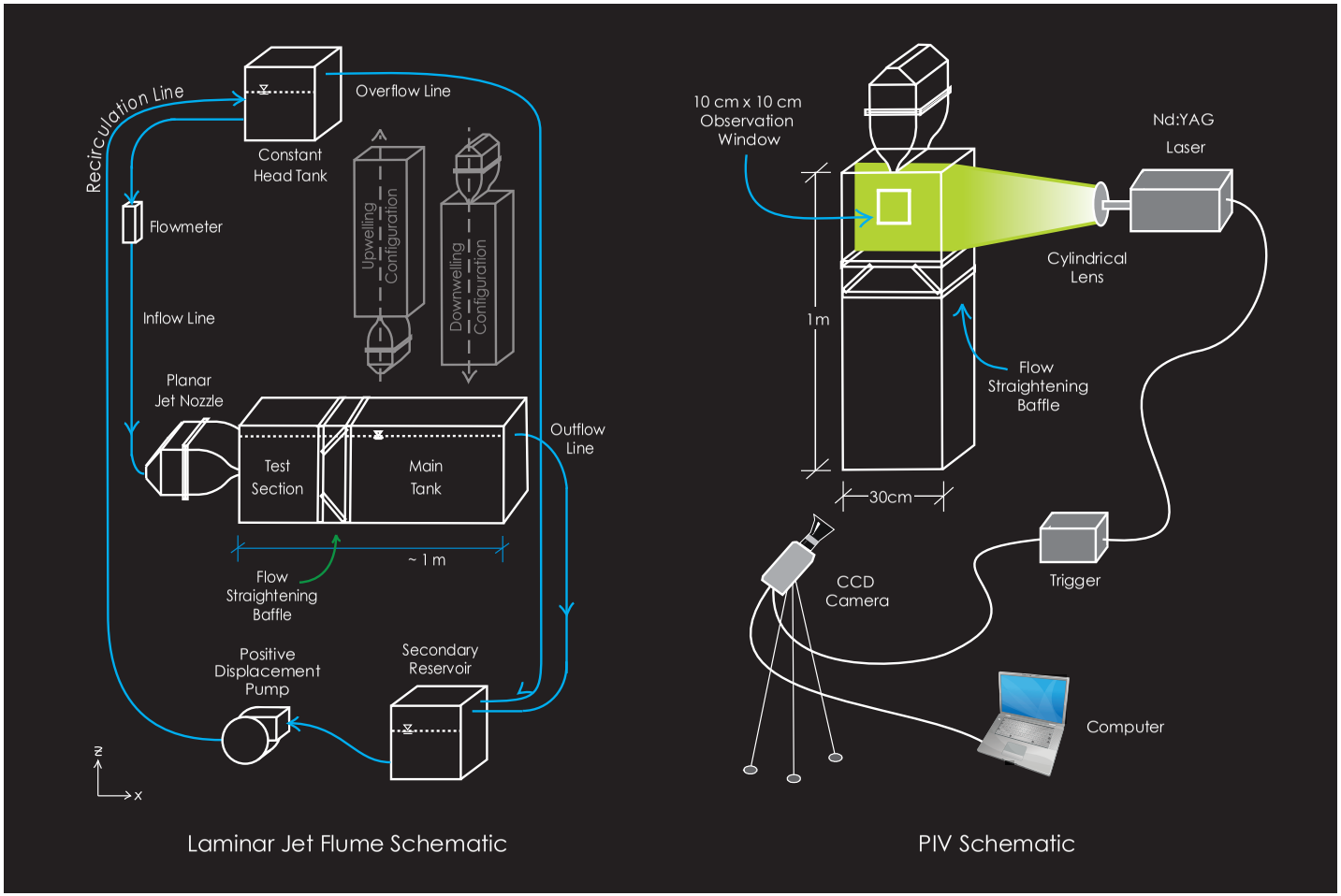

Figure 3.1: Left panel: Recirculating laminar jet flume schematic, main flume section can be oriented in upwelling, downwelling, or horizontal flow configurations. Right panel: Schematic of electro-optical components of the planar particle image velocimetry (PIV) system.

(e.g. Raffel et al. 1998). Here, the flow is illuminated with a planar sheet of laser light from a pair of pulsed Nd:YAG lasers (New Wave Research Gemini, 532 nm, 125 $mJ/pulse$) (Figure 3.1, right panel). The laser beam was first focused with a 1 m focal length spherical lens and then expanded with a -12.6 mm cylindrical lens resulting in a thin sheet of laser light in the observation region. In this study, the flow was seeded with titanium dioxide particles of diameter less than or equal to 5 μm.

Data capture was controlled using an eight-channel pulse generator (Berkeley Nucleonics Model 500D), which triggered coordinated firing of the laser heads with the shutter of a CCD camera (Kodak Megaplus ES 1.0, 1 MP, 8-bit monochrome). The camera was equipped with a 105 mm lens (Nikon AF Micro Nikkor) and interfaced with a desktop PC running Windows XP via a Coreco Image Capture board. Hardware communication and image sequence capturing were achieved using Video Savant 3.0 software (IO Industries). Raw image pair sequences of the light scattered from the seeding particles was captured at 15 Hz for approximately 30 s, resulting in a 450 image sequence. Images were postprocessed using in-house software (Dasi 2004) based on standard PIV algorithms (Cowen and Monismith 1997, Wereley and Meinhart 2001, Gui and Wereley 2002). The algorithm first subtracts the average background illumination to enhance particle contrast and overall signal strength. Each image is then divided into 16 pixel square interrogation subwindows and a two-dimensional spatial cross-correlation is performed in wavenumber space between successive images for each interrogation subwindow. Particle displacement between successive frames is estimated by the location of the cross-correlation peak. A Gaussian peak fit analysis is employed to determine the displacement vector in all interrogation windows to subpixel accuracy. The displacement vectors are then divided by the time delay between laser pulses (0.05 s) to produce the instantaneous two-dimensional velocity field, from which the shear strain rate field is easily computed (via central-differences).

3.3.2 Behavioral Assays and Data Analyses

Panopeus herbstii larvae were collected in June of 2010 from Wassaw Sound at Priest Landing (Skidaway Institute of Oceanography) on Skidaway Island near Savannah, GA, USA. A light trap was constructed and deployed from the dock at Priest Landing between 10 pm and midnight (slack tide) for two consecutive nights. The light trap consisted of a large plastic jar (approximately 5 L Nalgene) with an inverted funnel at the wide mouth, designed to increase plankton retention in the trap. A dive light was secured to the bottom of the jar in order to attract phototactic larvae into the trap. The jar was suspended horizontally between a weighted mooring device on the bed and a float on the water surface. The trap was retrieved after a two hour deployment, and larvae were taken to the laboratory to be processed. Crab larvae were immediately sorted out and kept in recirculating seawater, while being fed copepod nauplii (*Acartia tonsa*), before being transported to the Georgia Institute of Technology for behavioral assays. At Georgia Tech, larvae were kept in well-oxygenated artificial seawater (Instant Ocean) at estuarine conditions (30 ppt, 28 $^{\circ}C$) and fed copepod nauplii (*A. tonsa*) and brine shrimp nauplii (*Artemia spp.*) over the 1 week duration in which all behavioral assays were conducted. Larvae were not feed in the 24 hours prior to each behavioral assay.

3.3.2.1 Behavioral Assays and Trajectory Digitization

Two hour behavioral assays were conducted between 8 p.m. and midnight under horizontal, upwelling, and downwelling flow configurations (separately) in which a group of 40 mixed-sex, stage-specific (megalopa) larvae were introduced to the main test section and allowed to acclimate for one hour prior to the experiment. During this period the laminar jet layer flow was started and allowed to reach steady state and larvae were aggregated away from the jet layer with a point source of white light. Two replicates of each jet layer configuration were conducted in addition to a one

hour control experiment in which larvae swim freely in a stagnant tank. In all cases, one trajectory of each larva was filmed in the 10 cm x 10 cm observation window, centered on the jet centerline, beginning 5 cm downstream from the jet origin. The observance of typical larval trajectories that interacted with the jet only once and typical aggregation of larvae downstream of the main test section at the end of an assay reduced the likelihood of larval resampling (psuedo-replication).

Optical elements mounted behind the main test section allowed for visualization of larval swimming trajectories via shadowgraph observation (Figure 3.2). An infrared (IR) fiber-coupled diode (CVI Melles Griot, 57 PNL 054/P4/S, 660 nm, 22 mW) was collimated via a 15.24 cm spherical mirror (Edmunds Optics, NT32-845, effective focal length 1524 mm) and reflected at 45° via a planar mirror perpendicularly into the rear of the tank. This method provides uniform illumination through the depth of the tank. The back illumination projects a silhouette of the swimming animals onto the front surface of the tank, on which is placed a sheet of film paper (Sam Flax), resulting in a crisp, high contrast shadow. The shadowgraph trajectories produced over the course of each two hour behavioral assay were recorded via a CCD video camera (Pulnix, 745i, 768 x 494 pixels) linked to a digital video recorder (mini dv tapes). All experiments were recorded at 30 frames per second (fps), the maximum temporal resolution of the camera.

Mini dv tapes containing raw trajectory data were digitized as a series of uncompressed avi (Audio-Video Interleave) clips at 15 fps using iMovie HD (Apple Inc). The reduction in temporal resolution was warranted to reduce memory requirements (order of 1 TB for all assays), and this frame rate is sufficient to resolve all larval swimming behaviors. For example, larvae exhibited bouts of behavior with maximum swimming speeds up to 2 cm/s. Hence, at a typical magnification of 500 $pixels/10$ cm, or 0.2 $mm/pixel$, a swimming speed of 2 cm/s results in a displacement of 100 $pixels/s$. When considering a typical larval carapace length of 2 mm (10

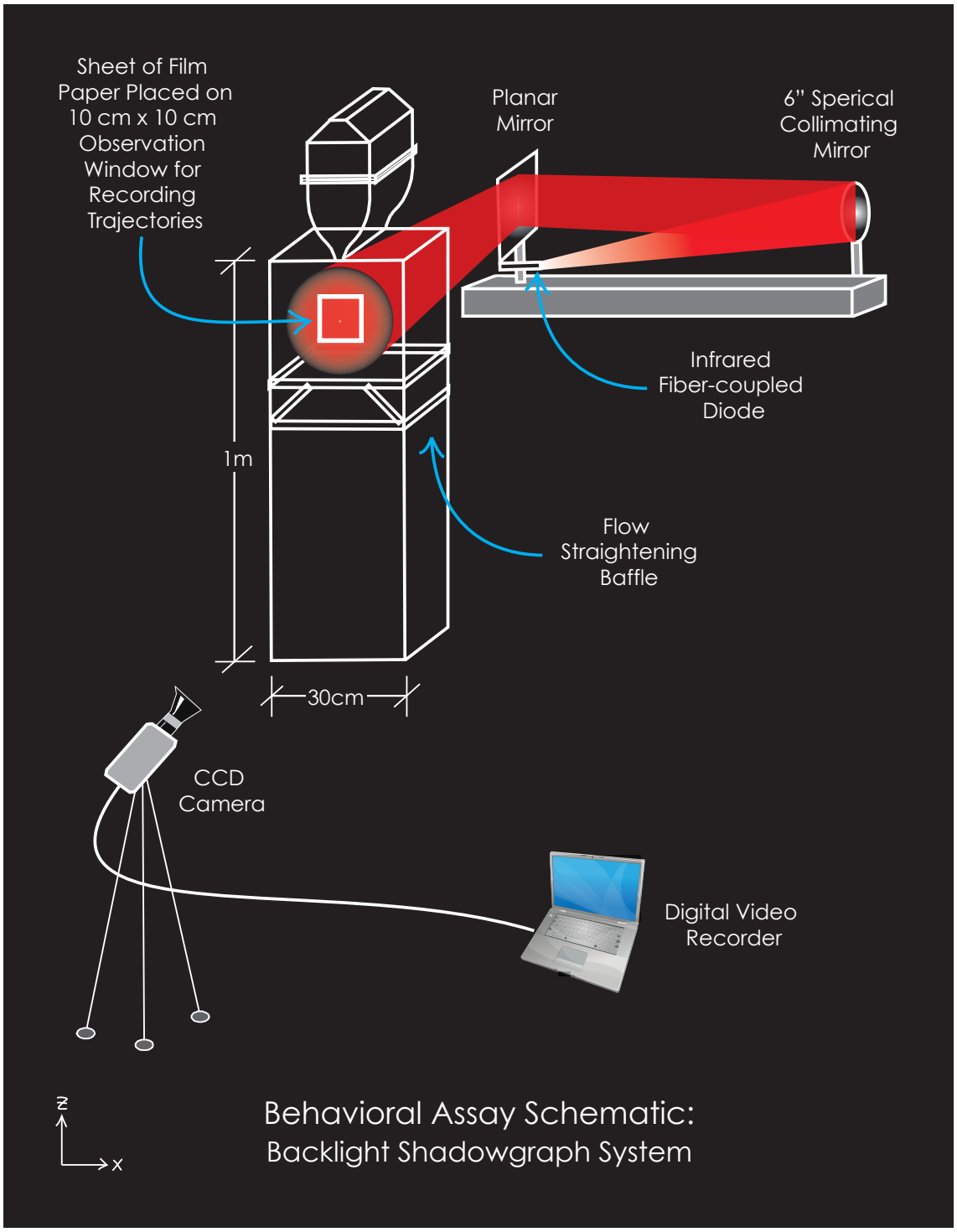

Figure 3.2: Electro-optical equipment configuration for larval behavioral assays.

pixels), the corresponding displacement is only 10 body lengths per second, or 2/3 body length per frame. Thus, 15 Hz is a sufficient temporal resolution to accurately resolve displacement of the body centroid. Larval swimming trajectories were digitized using LabTrack (BioRAS) software. The resulting raw trajectory data sets (x, z, t) were analyzed using a suite of custom MATLAB codes.

3.3.2.2 Kinematic and Threshold Shear Strain Rate Analyses

The first analysis determined a threshold shear strain rate (described below) value that elicits significant larval behavioral responses. The second analysis examined path kinematic parameters for portions of each trajectory in-layer and out-of-layer (boundaries defined by the threshold shear strain rate level), as well as pre-contact and post-contact with the threshold level. The path kinematics computed in this study are relative swimming speed (the swimming speed of the animal minus the local fluid velocity from the PIV results) and turn frequency (where a turn is defined as a change of direction of 15° or more). Additionally, the following gross trajectory parameters are computed to examine the net effect of changes in larval behavior on macroscale trajectory characteristics: net-to-gross-displacement ratio ($NGDR$ = net displacement/gross displacement), the vertical net-to-gross-displacement ratio ($VNGDR$ = net vertical displacement/gross vertical displacement), and the proportional residence time (PRT = time spent in-layer/total time in observation window). These gross path parameters elucidate the effects of shear-induced changes in path kinematics on macroscale larval trajectories by bridging the gap between high frequency changes in path kinematics and lower frequency behavioral phenomena. This provides a platform for understanding the full meaning of behavioral responses in the context of foraging, larval aggregations, and STST phenomena. The $VNGDR$ can be viewed as a spectrum of depth-keeping behavior, where low values ($\rightarrow 0$) indicate trajectories with low net vertical transport and thus strong depth-keeping behavior.

In contrast, high $VNGDR$ values ($\rightarrow 1$) indicate trajectories with high net vertical transport and thus weak depth-keeping behavior. To alleviate potential dependence of $NGDR$ (and $VNGDR$) values on trajectory duration (Tiselius 1992), $NGDR$ was consistently computed for two second duration segments of a given trajectory and ensemble averaged.

Figure 3.3 shows a hypothetical larval trajectory in the experimental domain as a useful visualization of the shear layer/treatment region in relation to the spatial scales of path kinematic responses which are computed by location (in-layer versus out-of-layer) and exposure (pre-contact versus post-contact). While there is some overlap in insight provided (e.g. portions of the trajectory post-contact can have both in-layer and out-of-layer components), behavioral response trends computed by location and exposure provide unique insights into larval responses. In particular, responses by location are associated with the spatial scale of the layer itself and short time scales. Similarly, responses by exposure are associated with the spatial scale of the vicinity of the layer as well as the layer itself (the encompassing volume) and relatively longer time scales.

The examination of larval kinematic responses both by location and exposure is warranted for multiple reasons because of the unique insights they each provide. For example, high swimming speeds typical of megalopae (on the order of $\sim cm/s$) and the likelihood of some phase lag between shear sensing and behavioral response necessitate the use of both by-exposure and by-location analyses to fully capture shear-induced behavioral responses. Also, the division of the experimental domain into in-layer and out-of-layer regions (by the threshold shear strain rate level, see full presentation below) is not a binary division into "full shear" and "zero shear" zones. In other words, even though a larvae may be out-of-layer (pre-contact or post-contact), there is still a coherent, physiologically sensible hydrodynamic cue that can potentially inform larval behavior (Figure 3.14).

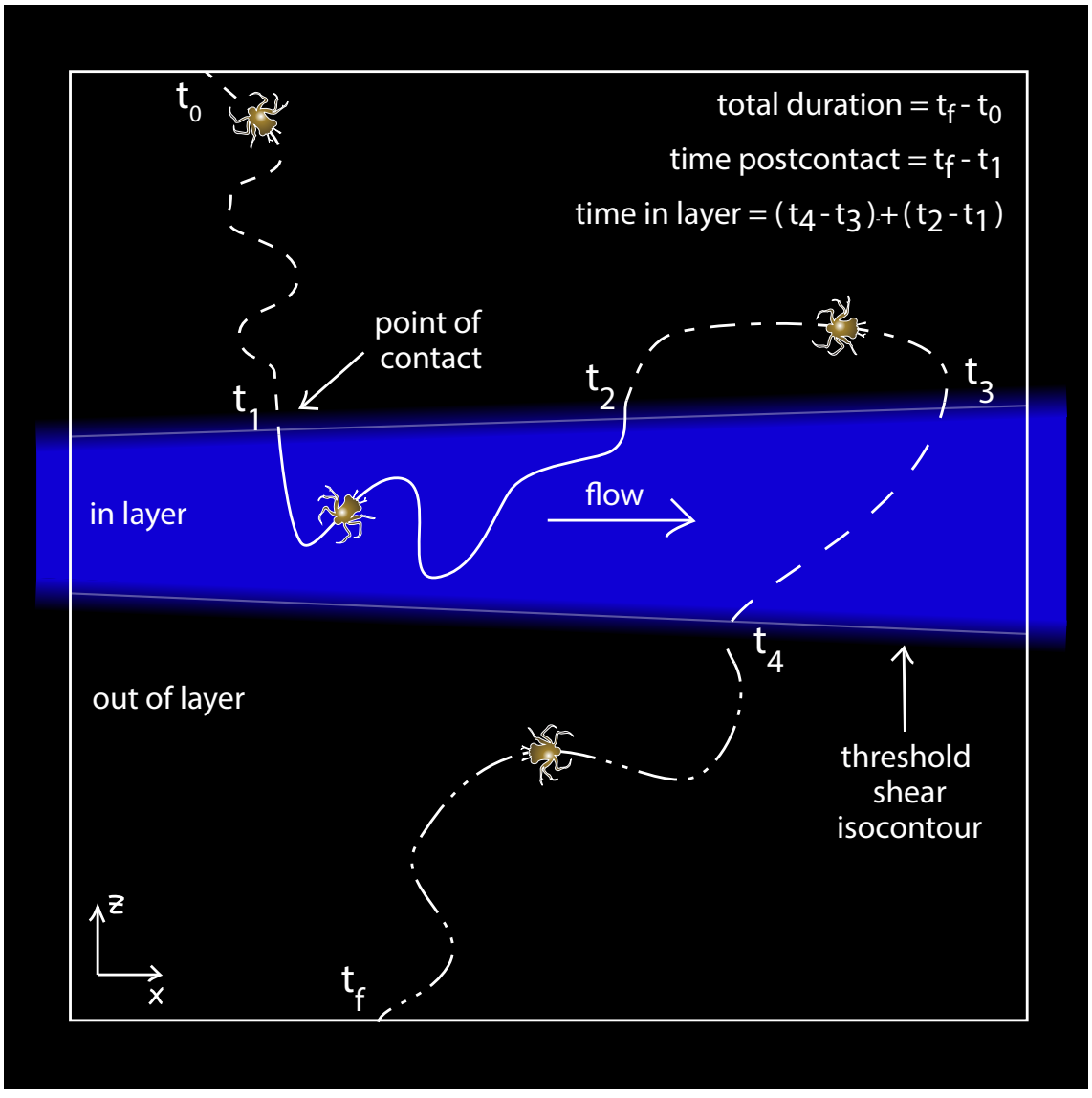

Figure 3.3: A hypothetical larval trajectory and visualization of the experimental domain.

In order to determine a threshold shear strain rate, we examined changes in relative swimming speed and directional heading to define the shear strain rate value that triggers the most significant and holistic change in larval behavior. The methodology used here is a refinement of similar techniques used in previous studies (Woodson et al. 2005; True 2011). For each trajectory, the mean and standard deviation of relative swimming speed and change in directional heading are computed for portions of the trajectory above and below a given shear strain rate value based on the physical location of the larvae. The absolute value of the difference between these values is plotted as a function of the particular shear strain rate value giving a measure of the change in the mean behavior and also the variability of behavior as a result of exposure to the given shear strain rate value. This process is repeated for each shear strain rate value a larva encounters along its trajectory. The behavioral response curves for all larvae are then ensemble averaged for each shear strain rate value after being normalized by the maximum response value for that particular response curve, which collapses all data to one response curve. This analysis is repeated for both behavioral parameters (relative speed, heading change) and all jet configurations (upwelling, downwelling, horizontal). A spline curve was then fit to the mean behavioral response for each jet layer configuration (i.e. the average of the relative speed and heading change responses) to aid in the selection of a threshold value for each shear flow orientation, indicated by a rapid change in the slope of the mean normalized response curve (spline curve). The benefit of completing analyses on individual paths and then ensemble averaging over the entire population is that it retains the variability of individual behavior while also revealing the population scale phenomena. Orientation-specific shear strain rate thresholds were defined for each shear flow orientation (see Results). Hhowever, a common threshold value of 0.1 s^{-1} (the greatest threshold) was used in order to define a common geometric treatment region (i.e. in-layer versus out-of-layer) among all shear flow treatments and thus to statistical compare larval

behavioral responses to different shear flow orientations.

3.3.2.3 Statistical Analyses

Statistical significance of larval behavioral responses was evaluated using one-way analysis of variance (ANOVA) models with slightly different designs for path kinematics and gross path parameters. The single factor (or treatment) is the treatment layer type, which has four levels: control, upwelling, downwelling, and horizontal. Changes in gross parameters (PRT, $NGDR$, and $VNGDR$) are evaluated via a one-way ANOVA on arcsine transformed data between control and treatment (upwelling, downwelling, horizontal jet layers) values. Arcsine transformation was warranted to alleviate known departures of proportional data (i.e. ranging from 0-1) from normality that is an underlying assumption of ANOVA (Zar 1999). Post-hoc Dunnett's Control (DC) tests are used to evaluate differences between control values and values for each jet layer configuration. Changes in path kinematics (relative swimming speed, turn frequency) were evaluated via a one-way, repeated measures ANOVA, with exposure (pre-contact versus post-contact) or location (in-layer versus out-of-layer) as the repeated measures variable for each individual path. The repeated measures aspect of the statistical analysis indicates that pre-contact versus post-contact or in-layer versus out-of-layer values are examined and compared for each individual larva, not simply the entire pre-contact (or in-layer) data set versus the entire post-contact (or out-of-layer) data set. This statistical design helps to account for individual variability in larval behavior. Experimental replicate (recall each treatment was replicated twice) is first nested as a "factor" inside treatment level for all analyses. The data are pooled if replicate effects are insignificant and the pooled error variance is used.

The fact that ANOVA does not require equal sample sizes across treatments makes it particularly useful in the present study in which animal availability and mortality are ever-present concerns. Assumptions inherent to the statistical validity of ANOVA

include the following: random sampling, normal distributions of independent samples, and treatment groups with the same variance (Zar 1999). Randomly selecting individuals from the same species and larval stage and ensuring that no larva was sampled more than once ensures these assumptions are valid for this study and thus that application of ANOVA is warranted to detect statistically significant changes in larval behavior. Additionally, all raw data distributions are examined for normality and equality of variances among experimental groups prior to statistical analyses.

3.4 Results

3.4.1 Laminar Jet Layer Characterization

Planar PIV results reveal that the flow fields produced by the laminar, planar free jet under all flow configurations quantitatively match the known analytical (steady) solution by Bickley (1937), with minor departures. Importantly, this indicates the steadiness, or time-invariance, of the flow fields and of all hydrodynamic signals contained in the flow fields (acceleration, rotation, deformation), which enables a robust method for correlating hydrodynamic signals with larval swimming behavior.

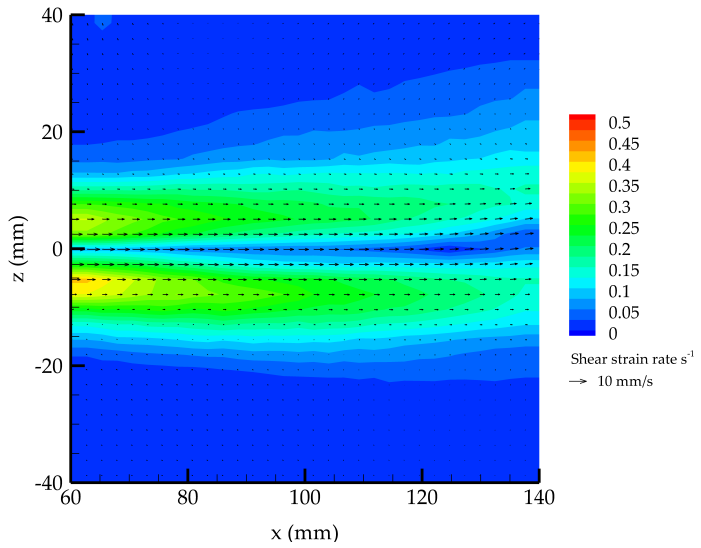

Figure 3.4: Time-averaged flow field in the laminar horizontal jet layer as measured using planar PIV ($Re_j \sim 50$). Vectors indicate fluid velocity and contours indicate fluid shear strain rate.

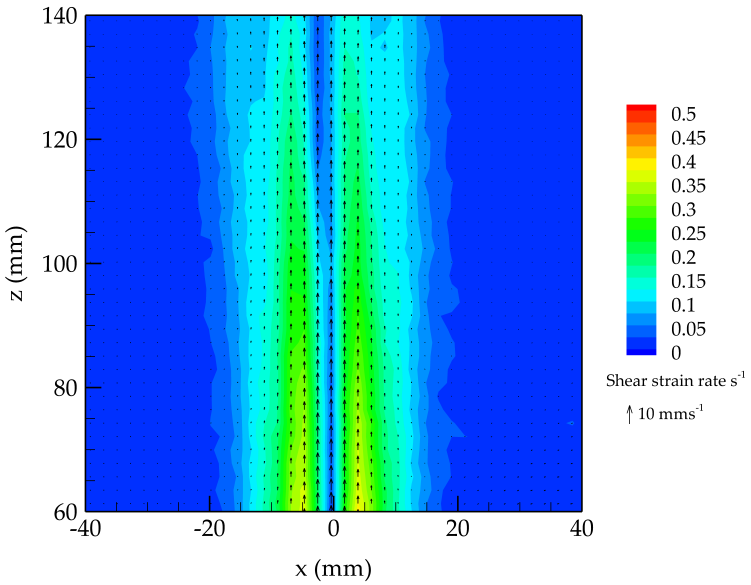

Figure 3.5: Time-averaged flow field in the laminar upwelling jet layer as measured using planar PIV ($Re_j \sim 50$). Vectors indicate fluid velocity and contours indicate fluid shear strain rate.

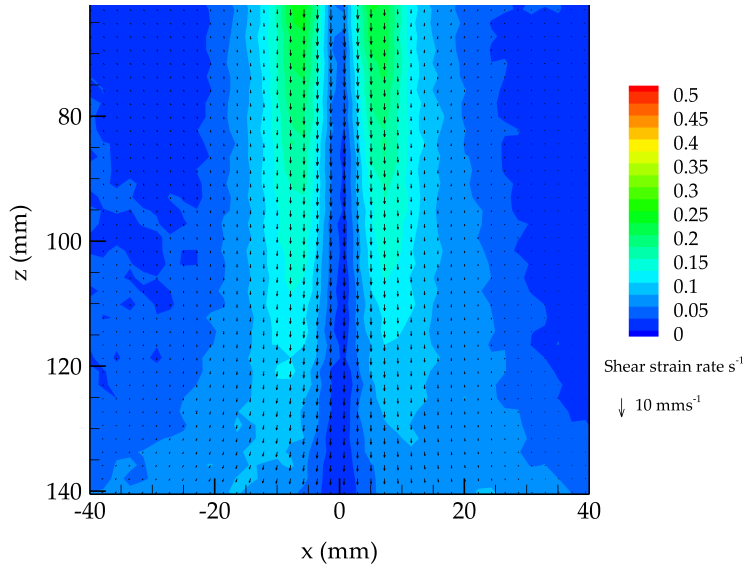

Figure 3.6: Time-averaged flow field in the laminar downwelling jet layer as measured using planar PIV ($Re_j \sim 50$). Vectors indicate fluid velocity and contours indicate fluid shear strain rate.

Figures 3.4, 3.5, and 3.6 show the time-averaged, two-dimensional velocity (vectors) and shear strain rate (contours) fields produced by the laminar jet layer under horizontal, upwelling, and downwelling flow configurations, respectively, for a jet Reynolds number of ~ 50. The maximum shear strain rate varies from approximately 0.35 s^{-1} to 0.12 s^{-1} with distance downstream from the jet exit (i.e., between x (or z) = 5 cm and x (or z) = 15 cm) due to the entrainment of low velocity fluid and the gradual broadening of the velocity profile due to the transverse diffusion of momentum. The maximum velocity along the jet centerline likewise varies from approximately 6 mm/s to 4.7 mm/s, and the velocity decreases in the transverse direction from a peak at the centerline. The range of maximum shear strain rate values and velocities throughout the observation window is nearly identical for all three jet layer configurations, as expected for dynamically-similar jets.

Extracting velocity and shear strain rate profiles at various streamwise locations downstream of the jet origin allows for closer comparison of the experimental (PIV) and analytical (Bickley 1937) flow fields. Figures 3.7 and 3.9 show comparisons of PIV and theoretical velocity and shear strain rate profiles extracted at various x locations from the horizontal laminar jet layer. Similarly, Figure 3.8 shows all velocity profiles extracted from each x location collapsed onto the self-similar profile in which the transverse coordinate is normalized by the jet half-width, δ_j, and the streamwise velocity, u, is normalized by the centerline velocity, U_o. There is strong agreement between the analytical and experimental flow fields throughout the observation window. Experimental centerline velocities typically are slightly lower and the overall velocity profile is slightly narrower (Figure 3.7)resulting in slightly elevated shear strain rate values when compared to analytical values for the horizontal jet layer (Figure 3.9). These departures likely are due to an unaccounted for momentum sink, such as a recirculation flow, which causes slight departure from the theoretical flow field. Velocity and shear strain rate profiles extracted from the upwelling and downwelling

flow fields (not shown) are nearly identical to those from the horizontal jet, with very minor departures from the analytical flow fields. Slight divergences from the analytical solution for the vertical jet layers were traced to a slight buoyancy effect due to a temperature difference of approximately 0.1 $^{\circ}C$ between the jet and the receiving fluid body. This effect was caused by slight heating of the recirculating fluid by the pump over time. Thus, buoyancy acted very slightly to accelerate (decelerate) the jet vertically upward (downward) for the upwelling (downwelling) case and inhibit (enhance) the diffusion of momentum in the transverse direction. Importantly, the slight buoyancy effect was constant over the course of an experiment and did not destabilize the jet.

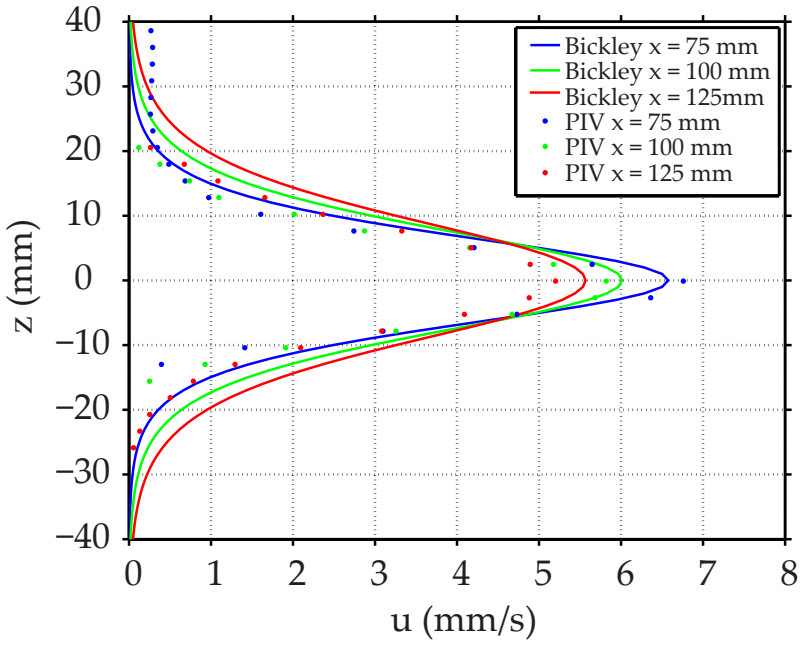

Figure 3.7: Comparison of analytical (Bickley) and experimental (PIV) velocity profiles in a horizontal laminar jet layer ($Re_j \sim 50$).

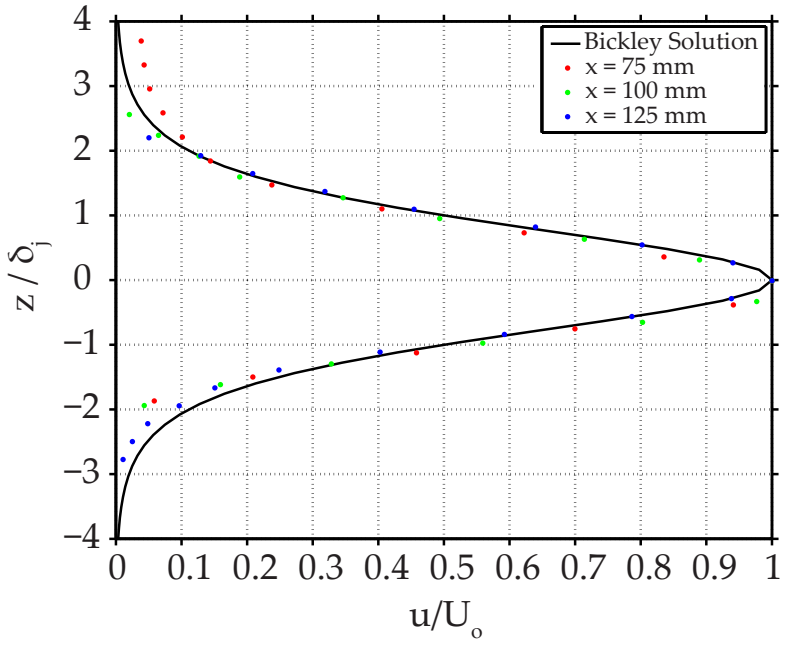

Figure 3.8: Comparison of analytical (Bickley) and experimental (PIV) self-similar velocity profiles in a horizontal laminar jet layer ($Re_j \sim 50$).

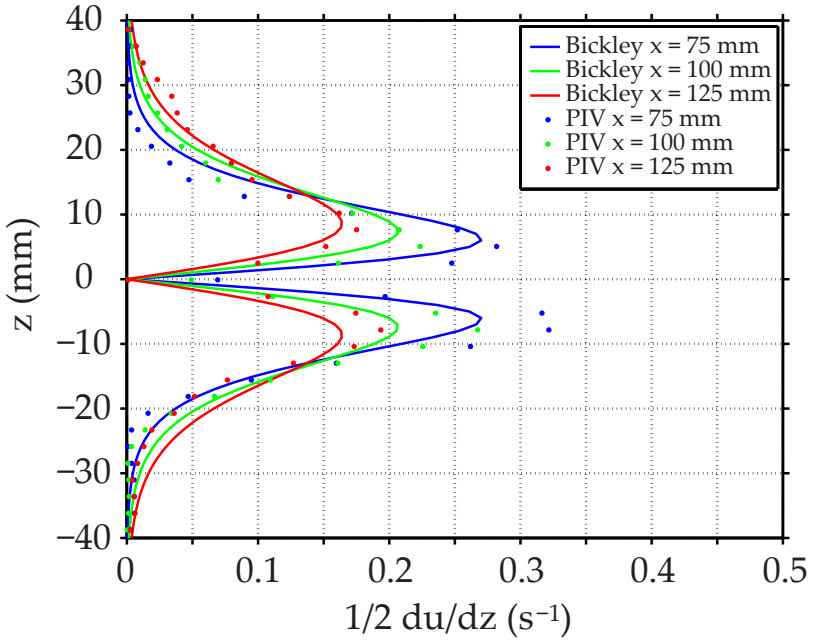

Figure 3.9: Comparison of analytical (Bickley) and experimental (PIV) shear strain rate profiles in a horizontal laminar jet layer ($Re_j \sim 50$).

The PIV flow characterization confirms that the flow field is steady (time-invariant), behaves dynamically as the theoretical solution predicts, and produces persistent and continuously-varying velocity and shear strain rate fields. All behavioral analyses make use of the experimental flow fields to compute relative swimming speed, shear strain rate thresholds, etc.

3.4.2 Larval Shear Strain Rate Threshold

Figures 3.10, 3.11, 3.12, and 3.13 show typical examples of digitized larval trajectories under various treatment conditions.

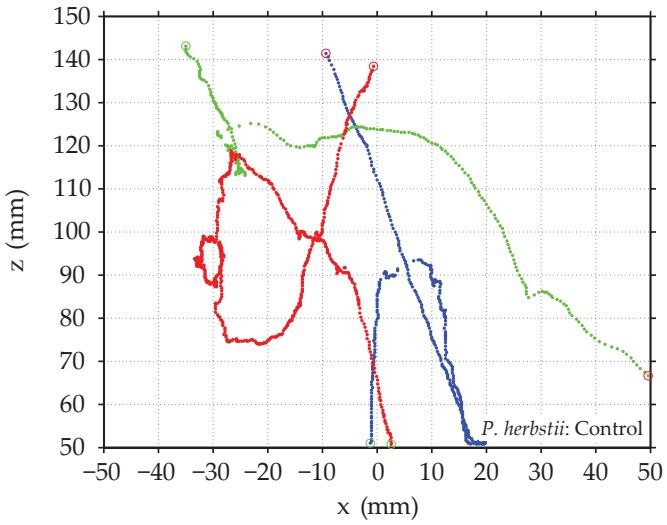

Figure 3.10: Sample trajectories in stagnant, filtered seawater (FSW). Start and end points are indicated by green and red circles, respectively.

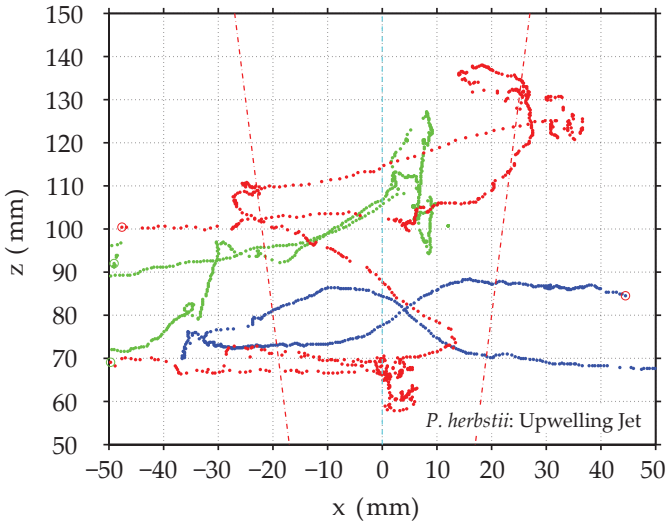

Figure 3.11: Sample trajectories in an upwelling jet layer. Jet centerline and edges, based on a shear strain rate threshold of 0.1 s^{-1}, are indicated by blue and red dashed lines, respectively. Start and end points are indicated by green and red circles, respectively.

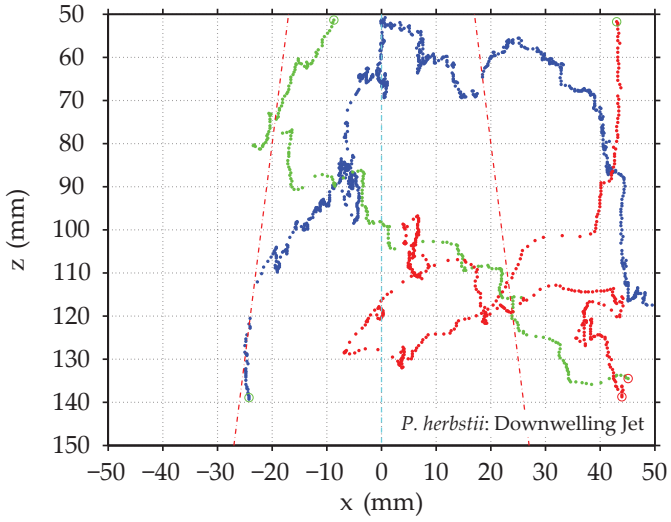

Figure 3.12: Sample trajectories in a downwelling jet layer. Jet centerline and edges, based on a shear strain rate threshold of 0.1 s^{-1}, are indicated by blue and red dashed lines, respectively. Start and end points are indicated by green and red circles, respectively.

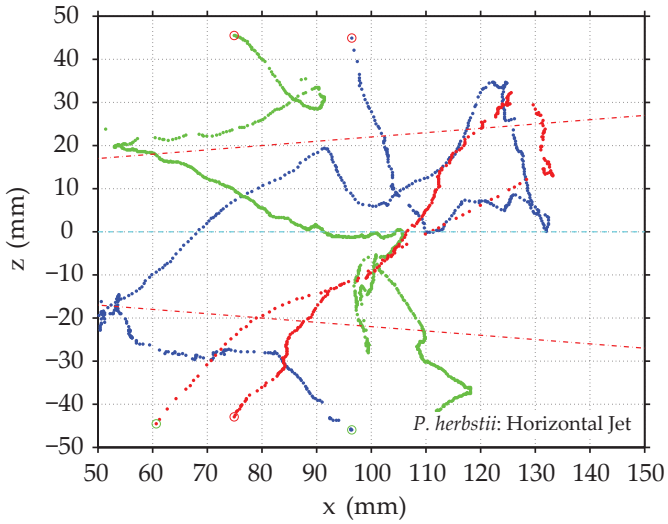

Figure 3.13: Sample trajectories in a horizontal jet layer. Jet centerline and edges, based on a shear strain rate threshold of 0.1 s^{-1}, are indicated by blue and red dashed lines, respectively. Start and end points are indicated by green and red circles, respectively.

Normalized shear threshold behavioral response curves generated for both behavioral parameters (relative speed, heading change) and all shear flow orientations (upwelling, downwelling, horizontal) are plotted as a function of shear strain rate in Figure 3.14. The left panel shows normalized change in mean larval behaviors, whereas the right panel shows normalized changes in larval behavioral variability. A spline curve was fit to the mean behavioral response for each jet layer configuration (i.e. the average of the relative speed and heading change responses, the black dashed lines) to aid in the selection of a threshold value, indicated by a rapid change in the slope of the mean normalized response curve (spline curve). The vertical dashed black line segments indicate the threshold shear strain rates for each shear flow orientation based on examination of individual spline curves for different orientations. As labeled in Figure 3.14, the behaviorally-defined threshold shear strain rate values defined for upwelling, downwelling, and horizontal shear flow orientations are 0.04 s^{-1}, 0.07 s^{-1}, and 0.10 s^{-1}, respectively.

3.4.3 Path Kinematics and Gross Path Parameters

As mentioned previously, a common threshold value of 0.1 s^{-1} (the highest threshold) was used in order to define a common geometric treatment region (i.e. in-layer versus out-of-layer) among all shear flow treatments and thus to statistically compare larval behavioral responses to different shear flow orientations. This shear strain rate value is used to divide the observation window into two geometric regions separated by the iso-contour of the threshold shear strain rate. In this way, the experimental domain is divided into the "in-layer" region (most shear strain rate values higher than threshold) and the "out-of-layer" region (all shear strain rate values lower than threshold). Using these definitions, individual larval trajectories can be analyzed by location (in-layer versus out-of-layer) as well as exposure (pre-contact versus post-contact). Relative swimming speed and turn frequency computed in-layer versus out-of-layer, as well as

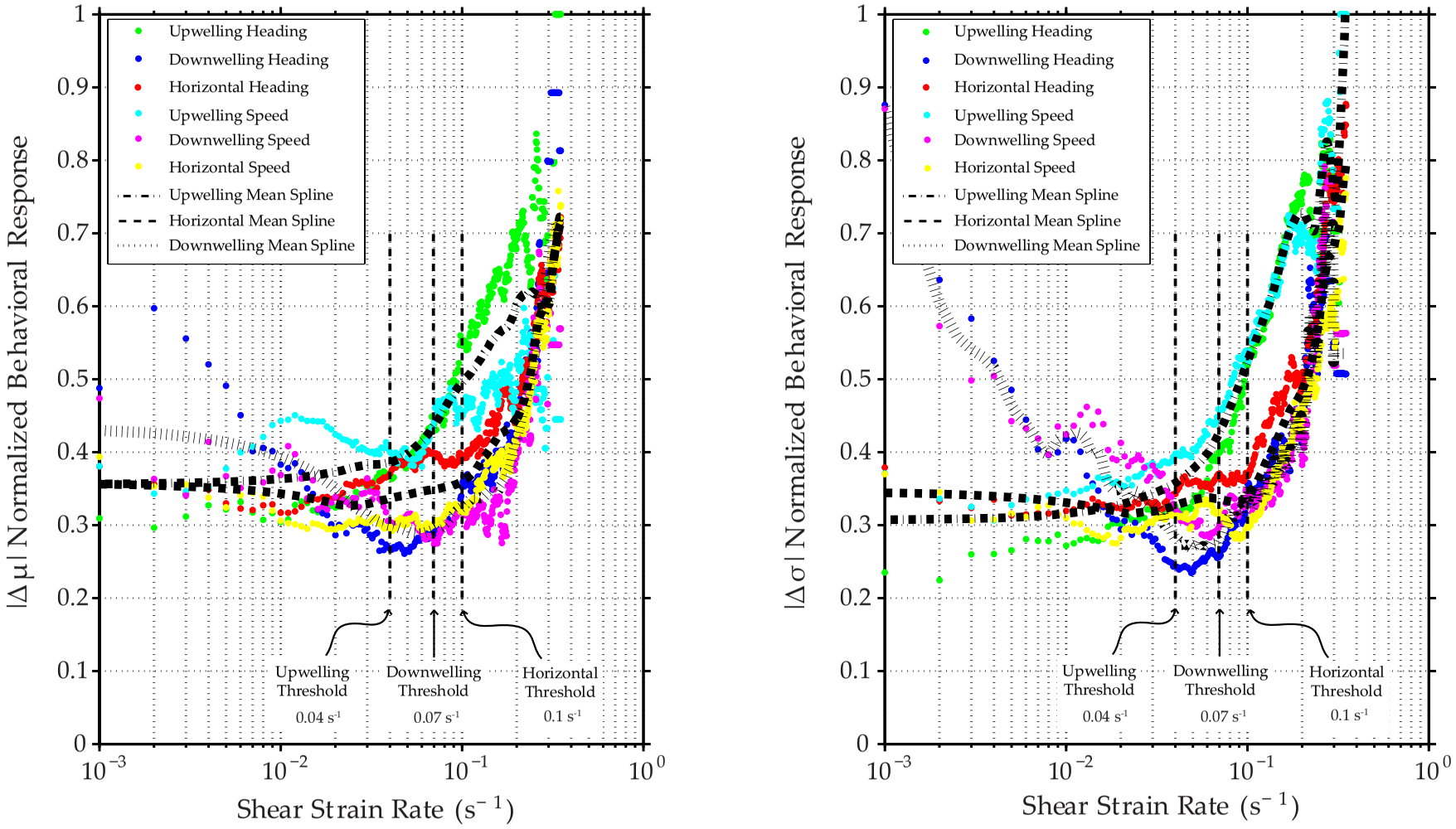

Figure 3.14: Larval shear strain rate threshold analysis. Left-panel: Normalized change in mean larval behavior. Right-panel: Normalized change in larval behavioral variability. The vertical dashed black lines indicate threshold shear strain rates for each shear flow orientation, as labeled.

pre-contact versus post-contact, are presented in Figures 3.15, 3.16, 3.17, and 3.18 for all flow configurations.

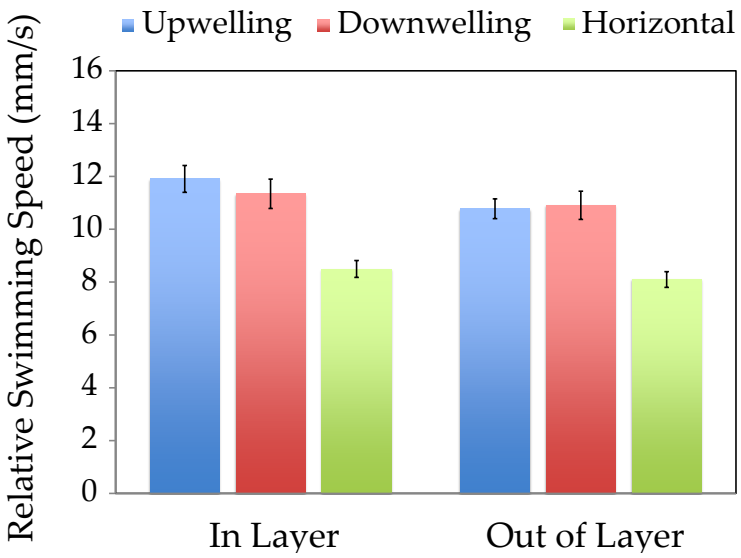

Figure 3.15: Relative swimming speeds in and out of the jet layer as defined by a shear strain rate threshold of 0.1 s^{-1}. Error bars are ± 1 SE.

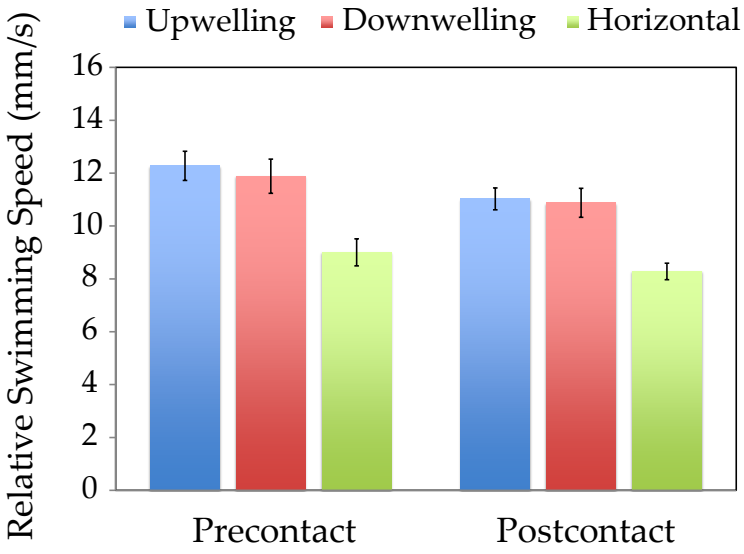

Figure 3.16: Relative swimming speeds pre- and postcontacting the jet layer as defined by a shear strain rate threshold of 0.1 s^{-1}. Error bars are ± 1 SE.

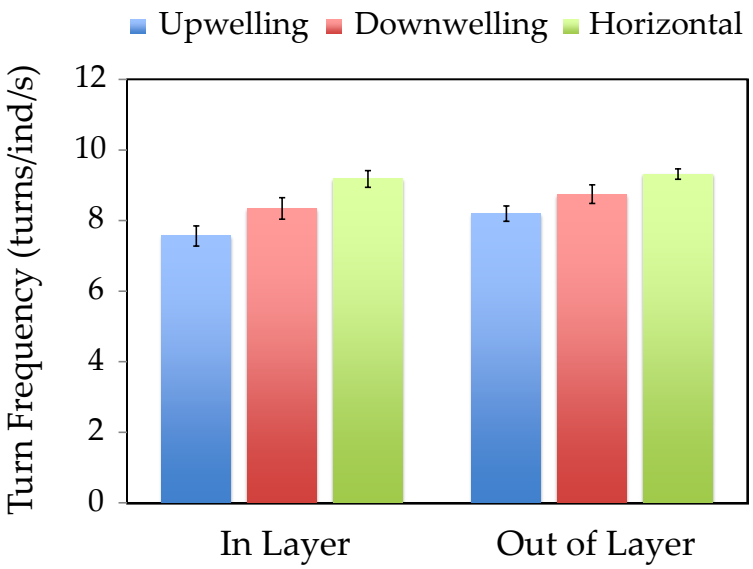

Figure 3.17: Turn frequency in and out of the jet layer as defined by a shear strain rate threshold of 0.1 s^{-1}. Error bars are ± 1 SE.

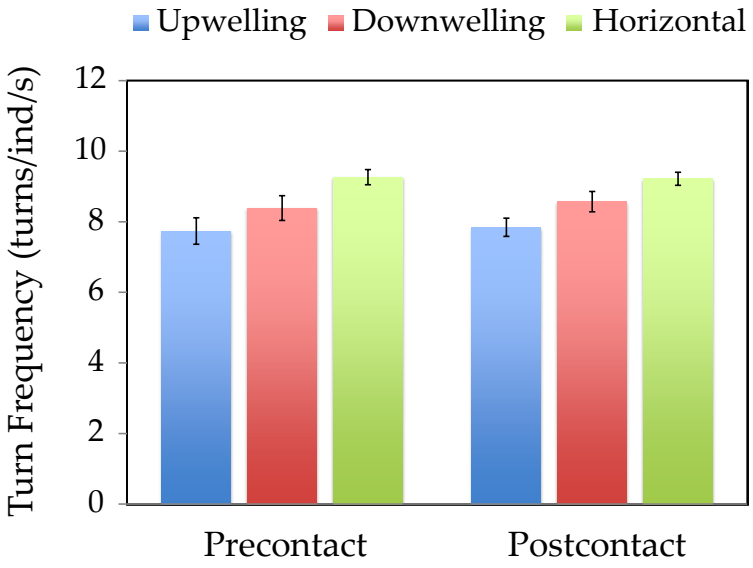

Figure 3.18: Turn frequency pre- and postcontacting the jet layer as defined by a shear strain rate threshold of 0.1 s^{-1}. Error bars are ± 1 SE.

The full summaries of the repeated measures ANOVA models for path kinematic parameters (relative swimming speed, turn frequency) are summarized in Tables 3.1,

3.2, 3.3, and 3.4. The first p-value labeled either "Location" (in-layer versus out-of-layer) or "Exposure" (pre-contact versus post-contact) evaluates the significance of behavioral differences due to an individual larva's presence in the laminar jet layer region versus outside of it, or pre-contact versus post-contact. The second p-value labeled "Treatment" indicates the significance of behavioral differences due to the effects of an upwelling versus downwelling versus horizontal laminar jet layer. Finally, the third p-value labeled "Location x Treatment" (in-layer versus out-of-layer) or "Exposure x Treatment" (pre-contact versus post-contact) is the interaction effect and evaluates whether or not behavioral differences for in-layer versus out-of-layer or pre-contact versus post-contact are contingent upon jet layer configuration (i.e. upwelling versus downwelling versus horizontal).

Table 3.1: Relative swimming speed (mm/s) (in-layer vs. out-of-layer), and summary of repeated measures ANOVA. Note that the Control values not analyzed in the ANOVA.

Treatment	n	Mean In-Layer (SE)	Mean Out-of-Layer (SE)
Control	40	9.462 (0.465)	
Upwelling	80	11.908 (0.506)	10.778 (0.375)
Downwelling	80	11.343 (0.557)	10.909 (0.535)
Horizontal	80	8.496 (0.319)	8.0978 (0.296)

DFE = 237	Location	Treatment	Location x Treatment
Num DF	1	2	2
Dem DF	237	237	237
F-value	8.7425	17.9952	1.1604
p-value	0.0034*	< 0.0001*	0.315

Table 3.2: Relative swimming speed (mm/s) (pre-contact vs. post-contact), and summary of repeated measures ANOVA. Note that the Control values not analyzed in the ANOVA.

Treatment	n	Mean Pre-contact (SE)	Mean Post-contact (SE)
Control	40	9.462 (0.465)	
Upwelling	65	12.274 (0.55)	11.029 (0.414)
Downwelling	64	11.883 (0.643)	10.878 (0.546)
Horizontal	71	9.002 (0.511)	8.280 (0.315)

DFE = 197	Exposure	Treatment	Exposure x Treatment
Num DF	1	2	2
Dem DF	197	197	197
F value	3.9576	16.6669	0.1899
p-value	0.048*	< 0.0001*	0.8272

Table 3.3: Turn frequency (turns/ind/s) (in-layer vs. out-of-layer), and summary of repeated measures ANOVA. Note that the Control values not analyzed in the ANOVA.

Treatment	n	Mean In-Layer (SE)	Mean Out-of-Layer (SE)
Control	40	7.518 (0.386)	
Upwelling	80	7.564 (0.287)	8.197 (0.216)
Downwelling	80	8.345 (0.305)	8.750 (0.262)
Horizontal	80	9.181 (0.238)	9.319 (0.146)

DFE=237	Location	Treatment	Location x Treatment
Num DF	1	2	2
Dem DF	237	237	237
F-value	8.0279	9.9734	1.0689
p-value	0.005*	< 0.0001*	0.345

Table 3.4: Turn frequency (turns/ind/s) (pre-contact vs. post-contact), and summary of repeated measures ANOVA. Note that the Control values not analyzed in the ANOVA.

Treatment	n	Mean Pre-contact (SE)	Mean Post-contact (SE)
Control	40	7.518 (0.386)	
Upwelling	65	7.739 (0.374)	7.844 (0.259)
Downwelling	64	8.387 (0.350)	8.569 (0.290)
Horizontal	71	9.266 (0.215)	9.216 (0.185)

DFE = 197	Exposure	Treatment	Exposure x Treatment
Num DF	1	2	2
Dem DF	197	197	197
F-value	0.3337	11.175	0.0928
p-value	0.5642	$< 0.0001^*$	0.9114

Examination of changes in path kinematic parameters reveals a consistency of larval behavioral responses to all three laminar jet layer orientations as evidenced by the lack of significance in the interaction effect for both relative swimming speed (In-Out: $p = 0.32$, Pre-Post: $p = 0.83$; Tables 3.1 and 3.2) and turn frequency (In-Out: $p = 0.35$, Pre-Post: $p = 0.91$; Tables 3.3 and 3.4). Relative swimming speeds are on average significantly smaller for the trials with the horizontal jet layer versus both vertical layers (significant treatment effect, In-Out: $p<0.0001^*$, Pre-Post: $p<0.0001^*$) regardless of position and are slightly smaller than the swimming speed for control ($\sim 9.5\ mm/s$). Swimming speeds in the vertical layers ($\sim 11.5\ mm/s$) are significantly higher. Turn frequency is on average significantly larger for the horizontal jet layer versus both vertical layer treatments (significant treatment effect, In-Out: $p<0.0001^*$, Pre-Post: $p<0.0001^*$) regardless of position or exposure. Turn frequency

in the horizontal layer ($\sim 9.25\ turns/ind/s$) is significantly elevated compared to control (stagnant) values ($\sim 7.5\ turns/ind/s$) whereas those in the vertical layers ($\sim 7.75 - 8.25\ turns/ind/s$) are only slightly larger than control values. For all jet layer configurations, relative swimming speeds are smaller post-contact (significant exposure effect, $p = 0.048^*$) and out-of-layer (significant location effect, $p = 0.0034^*$) and turn frequency increases out-of-layer (significant location effect, $p = 0.005^*$). Exposure and location effects are more pronounced for the vertical layer treatments for both path kinematic parameters (see significant Treatment effect; Tables 3.1 - 3.4).

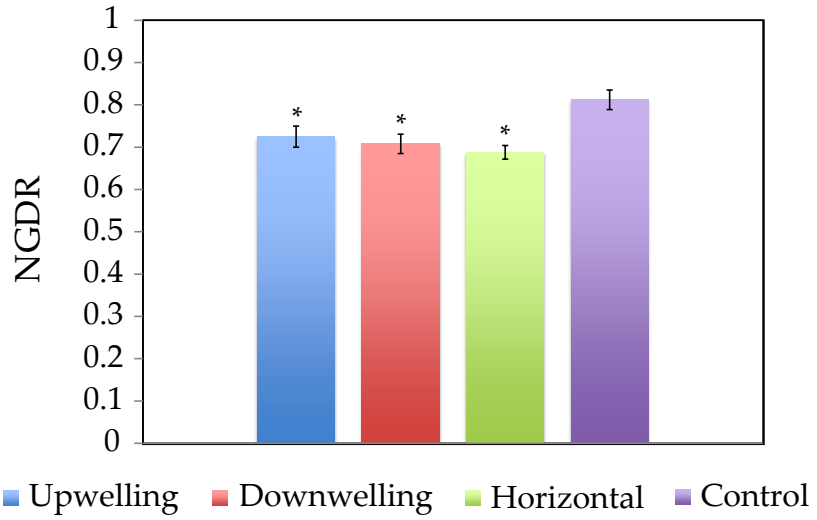

Figure 3.19: *NGDR* under control and jet layer flow configurations. * indicates significance of various jet layers as compared to control values via single-factor ANOVA and post-hoc Dunnett's Control tests (see Table 3.5).

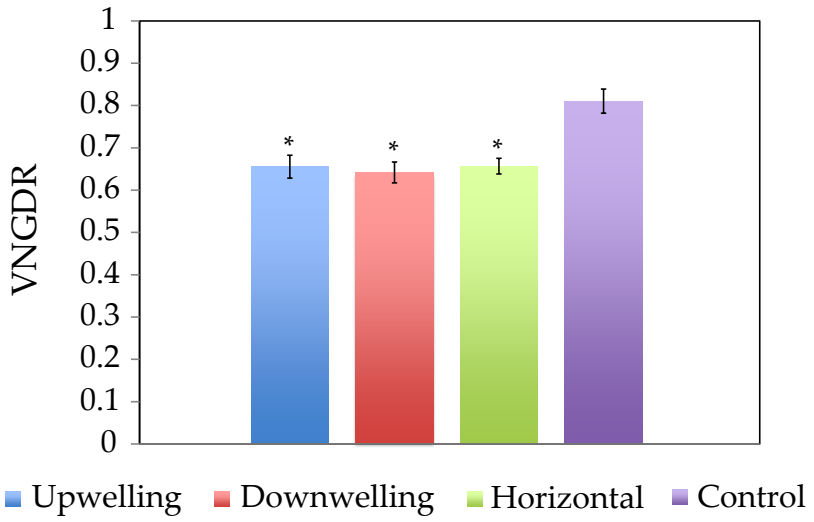

Figure 3.20: $VNGDR$ under control and jet layer flow configurations. * indicates significance of various jet layers as compared to control values via single-factor ANOVA and post-hoc Dunnett's Control tests (see Table 3.6).

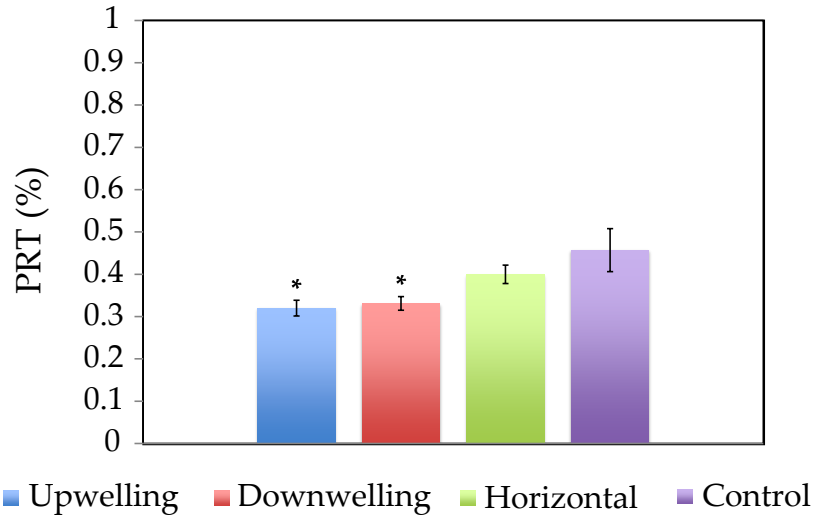

Figure 3.21: PRT under control and jet layer flow configurations. * indicates significance of various jet layers as compared to control values via single-factor ANOVA and post-hoc Dunnett's Control tests (see Table 3.7).

Significant reduction in $NGDR$ for all jet layer treatments (upwelling: $p = 0.0389^*$, downwelling: $p = 0.0119^*$, horizontal: $p = 0.0003^*$; Figure 3.19, Table 3.5) reveals the macroscale effects of increased turn frequencies, which is to make trajectories more sinuous ($NGDR \to 0$). Similarly, significant reductions in $VNGDR$ for all jet layers (upwelling: $p = 0.0001^*$, downwelling: $p<0.0001^*$, horizontal: $p<0.0001^*$; Figure 3.20, Table 3.6) reveals that larval trajectories are becoming less linear vertically, which yields low net vertical displacement. *P. herbstii* larvae are resisting vertical advection through depth-keeping behavior (i.e. decreased $VNGDR$ values), at least when velocity gradients are coherent and sensible and other sensory cues are absent. Finally, significant reductions in PRT for both vertical jet layers (upwelling: $p = 0.0018^*$, downwelling: $p = 0.0046^*$; Figure 3.21, Table 3.7) reveals explicit avoidance of the jet layer, likely as a means of avoiding vertical advection during depth-keeping behaviors. The lack of a significant change in PRT in the horizontal jet layer reveals that the jet layer is neither explicitly avoided nor sought after on the spatial scale of the layer itself (but not necessarily the vicinity of the layer).

Table 3.5: ANOVA and Dunnett's control test summary for net-to-gross displacement ratio (NGDR).

Treatment	n	Mean (SE)	DC Test
Control	40	0.812 (0.023)	
Upwelling	80	0.725 (0.025)	0.0389*
Downwelling	80	0.708 (0.023)	0.0119*
Horizontal	80	0.688 (0.016)	0.0003*
	SS	MS	DF
Error	14.427	0.052	276
Model	0.807	0.269	3
F-value	5.146	p-value	0.0018*

Table 3.6: ANOVA and Dunnett's control test summary for vertical net-to-gross displacement ratio (VNGDR).

Treatment	n	Mean (SE)	DC Test
Control	40	0.809 (0.029)	
Upwelling	80	0.654 (0.027)	0.0001*
Downwelling	80	0.64 (0.025)	< 0.0001*
Horizontal	80	0.656 (0.019)	< 0.0001*
	SS	MS	DF
Error	20.503	0.074	276
Model	1.95	0.65	3
F-value	8.750	p-value	< 0.0001*

Table 3.7: ANOVA and Dunnett's control test summary for proportional residence time (PRT).

Treatment	n	Mean (SE)	DC Test
Control	40	0.457 (0.051)	
Upwelling	80	0.320 (0.019)	0.0018*
Downwelling	80	0.331 (0.016)	0.0046*
Horizontal	80	0.400 (0.0218)	0.1996
	SS	MS	DF
Error	16.67	0.060	276
Model	0.919	0.306	3
F-value	5.072	p-value	0.002*

3.5 Discussion

Panopeus herbstii live in estuarine waters during both planktonic and adult life-stages (e.g. Dittel and Epifanio 1982). Dispersed larvae exhibit diel, tidal (endongenous), and ontogenetic (life-stage dependent) vertical migrations that have fundamental impacts on dispersal trajectories, benthic settlement, and population connectivity (Cronin and Forward 1979; Garrison 1999; Miller and Morgan 2013). Postlarval megalopae are in the dispersed (pelagic) larval phase directly preceding benthic settlement and exhibit a typical behavioral shift with respect to previous larval stages (zoeae) that cause them to aggregate at the surface or on the bottom depending on species and/or environmental cues. Megalopae typically aggregate near the surface at night, particularly during flood tide, reducing predation risk while also increasing the potential for flood tide transport (FTT) towards optimal benthic settlement sites (Queiroga and Blanton 2005). Periodic forays into the benthos also allow megalopae to sample benthic waters for chemical cues that may induce or delay benthic settlement (Rodriguez and Epifanio 2000; Lecchini et al. 2010). Thus, for imminently-settling megalopae we would expect to see behavioral processes consistent with FTT, specifically depth-keeping, and/or foraging and sampling depending on the presence, absence, or combination of sensory cues presented.

Hydrodynamics in Wassaw Sound are typical of many estuarine systems being tidally driven (tidal range $\sim 2-3\ m$) with extended periods of unidirectional flow and low wave action under normal conditions (Smee et al. 2010). Moderate current speeds ($\sim 0.5\ m/s$) and relatively shallow depths ($\sim 10-15\ m$) ensure that persistent tidally-modulated vertical shear structure is ever present and ideal for STST behaviors (e.g. Forward et al. 2001, Forward et al. 2003b) and/or habitat partitioning. Low freshwater input to the estuary ensures that the most persistent horizontal shear

structure is likely to be associated with estuarine fronts and channel sidewalls (i.e. salt marsh boundaries) separating water masses of differing hydrographic and biochemical properties (Largier 1993; O'Donnell 1993).

The results here are interpreted in the context of the behavioral goals of the megalopal stage with respect to a suite of sensory cues in which physical cues (light, pressure, salinity, hydrodynamics) are seen as base level cues upon which dissolved chemical cues act to stimulate behavioral processes on short time scale and fine spatial scales. The summation of all behavioral responses observed here indicates larval behavior that resists vertical advection ($\downarrow PRT$ in both vertical jet layers) through explicit depth-keeping behavior ($\downarrow VNGDR$) while remaining in the vicinity of all jet layers (though not in the layers themselves) through area-restricted search patterns ($\downarrow$ speed post-contact and $\uparrow$ turn frequency out-of-layer, $\downarrow NGDR$). It seems likely that larvae are optimizing long-term settlement goals with the short-term need to forage and sample local waters by exploiting the information contained in coherent shear flows. These behaviors are consistent with megalopal behavioral goals and illustrate the fundamental role that coherent, finescale hydrodynamic structure plays in triggering behavioral responses and structuring their environments.

3.5.1 Threshold-based, Shear-induced Behavioral Responses

The shear strain rate thresholds seen here (Figure 3.14) illustrate the fundamental role that coherent, finescale hydrodynamic structure plays in informing behavioral processes *in situ*. The fact that behavioral sensitivity depends on the orientation of the hydrodynamic cue with respect to gravity suggests megalopae have a keen awareness of both the temporal and spatial structure of hydrodynamic cues. The highest behavioral sensitivity exhibited was for upwelling conditions ($0.04\ s^{-1}$) with downwelling conditions producing the next highest sensitivity level ($0.07\ s^{-1}$). This is consistent with the excited changes in path kinematics ($\uparrow$ speed and turn frequency

on average) seen for both vertically-oriented shear layers (Tables 3.1 - 3.4) in which megalopae sweep around vertically advected waters while maintaining depth (Figure 3.20, Table 3.6). This behavior could allow larvae to gain useful information in the form of dissolved chemical cues about both surface (downwelling) and benthic (upwelling) waters in an efficient fashion. Finally, the lowest sensitivity exhibited was under horizontally-directed shear layer conditions (0.10 s^{-1}). These orientation-specific sensitivities are consistent with *in situ* hydrodynamic conditions that are likely to produce stronger horizontally-directed shear flows than vertically-directed shear flows (e.g. flow in the bottom boundary layer or in the shear layer in stratified tidal flows versus shear along channel sidewalls or estuarine fronts).

Collectively, the numerous physical and chemical cues influencing larval behavior compose a suite of sensory cues that may be additive or confounding at any particular time. Larval behavior at any point in time is a balance between the short-term need to forage and sample the local environment and the long-term need to find suitable settlement habitat. It is clear that the relative importance of any particular sensory cue may be trumped by another if the situation demands it. For example, a starved larva in the megalop stage (imminently-settling) that would normally respond to increasing pressure (Forward 1990), salinity (Queiroga and Blanton 2005), and turbulent kinetic energy (TKE, Welch et al. 1999) cues associated with a flood tide by swimming vertically up, may depart from expected FTT behaviors when presented with a thin planktonic layer containing enhanced concentrations of potential prey items and/or other dissolved chemical cues (Lindley et al. 1994). The intermittent injection of a dominating sensory cue, in the form here of a coherent shear flow, likely induces foraging/sampling behaviors and causes temporary departures from typical FTT behaviors that can significantly influence larval dispersal trajectories (Woodson and McManus 2007). For these imminently-settling *P. herbstii* megalopae, depth-keeping and large-scale sweeping in the region around persistent shear flows provides

the potential to sample various chemical cues being advected with frontal circulation while also avoiding direct vertical advection, possibly an energetically-favorable means of optimal site-selection for benthic settlement (e.g. Forward et al. 2001).

3.5.2 Vertical Migrations, Depth-regulation, and Departures from "Typical" Behaviors

Dispersed decapod larvae exhibit diel, tidal (endogenous), and ontogenetic (life-stage dependent) vertical migrations that require a well-developed behavioral basis for depth-regulation. The fundamental importance of vertical distribution of larval populations on horizontal transport and dispersal is well understood (Cronin and Forward 1986; Garrison 1999; Queiroga et al. 2002; Miller and Morgan 2013). Early studies by Sulkin (Sulkin 1973, 1975, 1984) established the behavioral basis of depth-regulation (the Negative Feedback model) whereby the interaction of larval orientation with respect to environmental cues (gravity, hydrostatic pressure) and locomotory activity produce stage-specific depth-regulation behaviors that are acutely developed in megalopae. Nevertheless, there is significant variability in depth-regulation and vertical migratory behaviors among species and by larval stage (e.g. Sulkin 1984). The results here show enhanced depth-keeping behaviors in the region near each shear flow treatment (in the absence of other sensory cues) (Figure 3.20, Table 3.6), which suggests coherent shear flows incentivize enhanced depth-keeping behaviors. We expect that this behavior is related to the enhanced concentrations of resources and information often contained in fronts and clines that are typically characterized by coherent hydrodynamic structure (see full discussion below).

Significant reductions in PRT for both vertically-directed layers (Figure 3.21, Table 3.7) reveal explicit avoidance of the jet layer, likely as a means of avoiding vertical advection during depth-keeping behaviors. Similarly, significant reductions in $VNGDR$ for each shear flow (Figure 3.20, Table 3.6) reveals changes in larval trajectories in which vertical displacement is likely to be retraced throughout the course

of the trajectory yielding low net vertical displacement. Recall that the $VNGDR$ can be viewed as a spectrum of depth-keeping behavior where low values ($\rightarrow 0$) indicate trajectories with low net vertical transport and thus strong depth-keeping behavior. Conversely, high $VNGDR$ values ($\rightarrow 1$) indicate trajectories with high net vertical transport and thus weak depth-keeping behavior. Megalopae can resist large scale net vertical advection by traversing "U-shaped" or "C-shaped" trajectories by actively changing path kinematics (speed, turn frequency) while also obtaining the maximum amount of information about the local environment by sweeping around coherent shear flows. Recall that in each shear flow treatment larval trajectories became more diffuse and sinuous ($\downarrow NGDR$, Figure 3.19, Table 3.5) and also exhibited area-restricted search behavior that would cause larvae to aggregate in the vicinity of the shear flows ($\downarrow$ speed post-contact and $\uparrow$ turn frequency out-of-layer), although not directly in the flow region ($\downarrow PRT$; Figure 3.21, Table 3.7).

A variety of factors are known to disrupt and/or modify "typical" vertical migratory behaviors (e.g. Lindley et al. 1994). We propose coherent shear flows not as a disrupter of vertical migratory behaviors, but as a modifier. Coherent shear flows can be uniquely exploited to accomplish short-term foraging/sampling behaviors while also maintaining depth, thus contributing positively to long-term FTT and benthic settlement goals. As modifiers of vertical migratory behaviors, coherent shear flows have the potential to significantly alter dispersal trajectories and population connectivity (Olmi 1994; Marta-Almeida et al. 2006). Short-term and long-term behavioral needs may often be in conflict; however, megalopae are seen here to modify behaviors in such a way as to optimize both by exploiting the information contained in coherent, multi-directional shear flows.

3.5.3 Larval Aggregations around Fronts and Clines

Fronts are known as regions of enhanced productivity that horizontally separate water masses of distinct hydrographic and biochemical properties (O'Donnell 1993; Largier 1993; Yoder et al. 1994). Similarly, clines, as regions of rapid vertical change in hydrographic and biochemical properties in the water column, have gained attention as ecological hot spots (particularly in association with thin planktonic layers) in which biomass can be several orders of magnitude higher than the surrounding waters (Haury and Wiebe 1982; McManus et al. 2003; Durham and Stocker 2012). Both fronts and clines have distinct hydrodynamic (e.g. vertical circulation cells, elevated shear) and biochemical signatures that can be exploited by competent plankters seeking to leverage the enhanced concentrations of resources (food, mates) and information (dissolved chemical cues) available. As such, fronts and clines are fundamentally linked to foraging and sampling behaviors and are often associated with high density plankton aggregations *in situ*, important mechanisms of biological patchiness (Tiselius 1992; Franks 1992; Epstein and Beardsley 2001; Simons et al. 2006; Benoit-Bird et al. 2009; Woodson et al. 2012).

Patchiness in planktonic decapod larvae populations has also been associated with fronts and clines. Eggleston et al. (1998) found significantly enhanced megalopae densities around a persistent front and proposed that estuarine fronts may act as conduits for larval transport. Garrison (1999) attributed finescale patchiness in brachyuran crab larvae populations to the interaction of behavioral processes and small scale hydrodynamic processes. Similarly, Natunewicz and Epifanio (2001) characterized the spatiotemporal characteristics of larval patches and proposed both behavior and physical forcing as potential mechanisms driving patch dynamics. Finally, Lindley et al. (1994) showed significant departures from expected diel vertical migratory behaviors in response to changing stratification and food patch dynamics in the water column producing vertical population distributions that were segregated according to larval

stage. Collectively, it is clear that 1.) planktonic decapod larvae populations exhibit considerable spatiotemporal patchiness, 2.) larval patchiness is often associated with both fronts and clines as regions of enhanced productivity and resources, and 3.) both behavior and physical forcing play important roles in driving larval patchiness.

The results here corroborate the importance of threshold-based behavioral processes, informed by fundamental hydrodynamic cues, in producing patchiness in larval populations. Examination of changes in path kinematics reveals a consistency of larval behavioral responses to each shear flow treatment as evidenced by the lack of significance in the interaction effect for both relative swimming speed and turn frequency computed by location (in-layer versus out-of-layer) and exposure (pre-contact versus post-contact) (Tables 3.1 - 3.4). Nuanced differences in average path kinematics revealed an area-restricted search behavior in the vicinity of horizontal shear flows (swimming slower on average (compared to control), swimming slower post-contact and out-of-layer, and greater turn frequency out-of-layer). Further, *P. herbstii* megalopae exhibit an excited area-restricted search behavior in the vicinity of both vertical shear flow treatments (swimming faster on average (compared to control), swimming slower post-contact and out-of-layer, and greater turn frequency out-of-layer). These behaviors are observed in the region surrounding the shear layer, but not directly in the shear layer. While all shear flows induce area-restricted search behaviors in the vicinity of the layers, the *excited* search behavior seen in both vertical layers is likely an artifact of larvae explicitly resisting vertical advection ($\downarrow PRT$, $VNGDR$) while also trying to remain in the vicinity of the layer. Significant reduction in $NGDR$ for all shear flow orientations reveals the macroscale effects of increased turn frequencies to make trajectories more sinuous and diffuse ($NGDR \rightarrow 0$). Collectively, these shear-induced behavioral responses are likely to produce megalopal aggregations in the vicinity of coherent shear flows. These behavioral responses are likely associated with foraging and sampling behaviors in which the coherent shear flow acts as an

initial cue to restrict search volume in hopes of exploiting some coincident or nearby cue and/or resource patch typical in fronts and clines.

3.5.4 Conclusion

P. herbstii megalopae, and likely many other Brachyuran crab species, can potentially optimize long-term settlement goals with the short-term need to forage and sample by exploiting the information contained in coherent shear flows which are often associated with fronts and clines, marine oases of enhanced productivity and resources. The findings here illustrate the fundamental role that coherent hydrodynamic cues plays in triggering behavioral responses and in structuring larval environments, likely causing periodic departures from "typical" behaviors and significantly altering dispersal trajectories and population connectivity.

CHAPTER IV

COPEPOD BEHAVIOR IN "CRYPTIC BLOOMS" OF TOXIC ALGAE

4.1 Abstract

Thin layers of toxic phytoplankton ("cryptic blooms") are modeled in a custom flume for behavioral assays with Calanoid copepods. *Acartia tonsa* and *Temora longicornis* are exposed to thin layers of algal exudates from the toxic dinoflagellate *Karenia brevis* (equivalent cell concentration: 1 - 10,000 $cells/mL$) to examine the effects of dissolved toxin levels and copepod species in behavioral response trends. Planar laser-induced fluorescence (LIF) is used to quantify the spatiotemporal structure of the chemical layers, ensuring a close match to *in situ* bloom conditions and allowing for quantitative correlation of copepod behavioral responses and dissolved toxin levels. Both copepod species display explicit avoidance of the toxic exudate layer and also the immediate vicinity of the layer. Measures of path kinematics (swimming speed, turn frequency) by location (in-layer versus out-of-layer) and exposure (pre-contact versus post-contact) reveal some similarities and also significant differences in behavioral response trends for the sympatric *A. tonsa* and the allopatric *T. longicornis*. *A. tonsa* significantly increases swimming speed and swimming speed variability in the exudate layer and post-contact, whereas *T. longicornis* slightly increases both in-layer and slightly reduces both post-contact. Both species increase turn frequency in-layer and post-contact with increasing *K. brevis* exudate concentration. These differences in path kinematic response trends produce differences in path fracticality ($F2D$ the two-dimensional path fractal dimension) in which *A. tonsa* trajectories likely become more diffuse and sinuous and *T. longicornis* trajectories likely become more linear

and ballistic (trending effects). Regression analyses of mean swimming speed and swimming speed variability by location and exposure reveal that the rate of change of behavior with increasing *K. brevis* exudate concentration is significantly higher for *A. tonsa*, ranging from thrice to fifty times the rate of change of *T. longicornis*. Thus, the sympatric *A. tonsa* appears to possess an adapted awareness of the toxic *K. brevis*, which is lacking for the allopatric *T. longicornis*. Regardless of the differences in response strategies, both species avoid the toxic exudate layer and its vicinity suggesting that *K. brevis* can potentially eliminate top-down grazer control entirely, another sinister mechanism by which it gains a competitive advantage over the local phytoplankton taxa.

4.2 Introduction

Harmful Algal Blooms (HABs) are associated with dense blooms of phytoplankton known to produce toxic compounds in both fresh and marine waters (Smayda 1997). HAB events are often associated with massive fish and marine mammal kills and human neurological poisoning by consumption of filter feeding shellfish, coral reef fishes, or even aerosol exposure in extreme events (Dolah 2000). The frequency, intensity, and geographic distribution of HAB events worldwide have been increasing in the past two decades, with associated adverse effects on human and economic health (Wang 2008, Anderson 1989, Smayda 1990, Hallegraeff 2005). Anthropogenic causes are often linked to HAB events due to injection of inorganic and organic nutrients into coastal marine ecosystems (coastal development, aquaculture, industrial waste, etc.) leading to eutrophication and monospecific domination (Verity 2010). The total estimated annual cost to the United States alone from HAB economic impact on commercial fisheries, public health, recreation/tourism, and monitoring/management is $87 million (Hoagland and Scatasta 2006).

In their role as trophic mediators, copepods link primary producers and higher

order trophic levels; thus they can significantly influence harmful algal bloom dynamics and modulate large-scale ecological effects through their interactions with toxic blooms. The effects of toxic phytoplankton blooms on copepod ecology range from the physiological (fecundity, overall fitness: Prince et al. 2006; Waggett et al. 2012) and behavioral (swimming speeds, fractal characteristics of trajectory, sampling, feeding and mating behaviors: Cohen et al. 2007; Breier and Buskey 2007; Schultz and Kiørboe 2009; Hong et al. 2012) to the evolutionary (species success: Jiang et al. 2011), spanning a wide spectrum of relevant spatiotemporal scales. There is a significant body of research on the physiological effects of toxic phytoplankton on copepod fitness, but relatively few studies have quantified fundamental behavioral responses, and fewer, if any, present ecologically-relevant toxic bloom conditions that give copepods a choice of dosed and undosed waters.

Many chemical compounds (e.g. domoic acid, paralytic shellfish poison, dimethyl sulfide: e.g. Prince et al. 2010) associated with toxic phytoplankton species are known to have deleterious effects on copepod fitness (Jiang et al. 2009) not only due to toxicity-related responses but also due to typical low nutritional values. Decreased grazing and fecundity are the most common results when copepod grazers are fed harmful alga, although the causes of decreased grazing (physiological incapacitation, behavioral avoidance or lack of stimulation) and/or decreased fecundity (toxic versus nutritional effect) vary among studies (Breier and Buskey 2007). Prince et al. (2006) found that on diets rich in *K. brevis*, *Acartia tonsa* experienced decreased survivorship and decreased egg production per female, but the percentage of eggs that hatched was unaffected. Similarly, egg production rates of *A. tonsa* fed toxic *K. brevis* strains were similar to those of starved copepods, whereas those of copepods fed non-toxic strains along with beneficial *Rhodomonas salina* were significantly higher (Waggett et al. 2012). Jiang et al. (2011) found an interesting physiological response with

adaptive implications in the copepod *A. tonsa* responding to the harmful dinoflagellate *Cochlodinium polykrikoides*: a rapid gain and loss of adaptive toxin resistance as a population. After four generations of chronic exposure to toxic phytoplankton, copepods had evolved toxin resistances 3 times higher than pre-exposure generations; all increased toxin resistance was lost within two generations lacking exposure. This suggests that copepods can rapidly adapt to dissolved toxic compounds and likely play a critical role in implementing some form of top-down grazer control on toxic phytoplankton blooms.

Algal toxins may influence copepod feeding behavior and alter top-down control exerted by copepod grazers. Waggett et al. (2012) showed that *K. brevis* can alter top-down grazer control of copepod grazers via multiple synergistic mechanism: (1) decreased ingestion rates, (2) decreased egg production, and (3) increased mortality of copepods through a combination of toxicity and nutritional inadequacy. Cohen et al. (2007) conducted grazing and mortality experiments with *K. brevis* cells and brevetoxins, establishing routes of toxicity for the copepods *A. tonsa*, *Temora turbinata* and *Centropages typicus*. *A. tonsa* exhibited minimal sublethal behavioral responses; however, there were significant effects on the swimming and photobehavior of *T. turbinata* and *C. typicus* at the lowest sublethal concentrations tested (105 *K. brevis* cells/L), suggesting very low behavioral response thresholds. Their data suggest that sublethal effects of *K. brevis* and its brevetoxins on copepod behavior occur on a species-specific basis. Similarly, Schultz and Kiørboe (2009) found that *A. tonsa* was capable of incredible selective feeding behaviors by remotely identifying and rejecting toxic cells based on associated hydrodynamic or chemical signatures. In contrast, Leandro et al. (2010) found that a lack of remote prey selection lead to the copepod *Calanus finmarchicus* becoming a preferential trophic vector for toxin accumulation, likely due to a lack of an ability to remotely characterize toxic cells. Recently, Hong et al. (2012) used digital holographic cinematography to compare feeding behavior of

free-swimming copepods, *A. tonsa*, on nutritional prey (*Storeatula major*) to that occurring during exposure to toxic and non-toxic strains of *K. brevis* and *Karlodinium veneficum*. They found two beating modes of the copepods feeding appendages, a "sampling beating" of short duration and a longer duration "grazing beating" that generates feeding currents, as well as a variety of behavioral regimes corresponding to the presence, absence, or combination of beneficial and harmful algal cells. Species-specific selective feeding behavior (or lack thereof) through active, remote prey selection can enhance or dampen bloom growth dynamics thus modulating ecological impacts on other trophic levels (Sole et al. 2006; Schultz and Kiørboe 2009).

HAB species employ various means to gain an initial competitive advantage and then proceed to dominate the local phytoplankton taxa. Kubanek et al. (2005) document the ability of a red tide dinoflagellate, *Karenia brevis*, to use allelopathy to outcompete other co-occuring non-toxic phytoplankton on a species-specific basis. This gives *K. brevis* a competitive advantage and could promote the onset of a monospecific HAB event. Following the onset of the bloom, toxic anti-grazing deterrents act to lower predation rates and sustain the bloom (Buskey and Hyatt 1995, Waggett et al. 2008, Graham and Strom 2010), whereas active remote prey-selection by chemical or fluid mechanical cues enhances or dampens the effect (Sole et al. 2006, Schultz and Kiørboe 2009). Turner et al. (2012) show that toxins accumulate disproportionately in the copepod *Calanus finmarchicus*, later shown by Leandro et al. (2010) to be due to a lack of active prey avoidance of toxic cells that are morphologically similar to non-toxic cells. Gannon et al. (2009) discuss the effect of HABs on nearshore fish communities through reduced fish abundance and health as well as changes in community structure. The effects may be due to neurotoxic influence that cause zooplankton to act erratically and thus become conspicuous prey items and preferential vectors for toxin trophic transfer. These factors, on a species-specific basis, can act in concert to produce preferential vectors by which toxins accumulate at higher and higher trophic

levels: the accumulation of toxicity.

An intriguing and relatively recent finding is the large number of toxic phytoplankton species recently identified in thin phytoplankton layers (Rines et al. 2002; McManus et al. 2008; Sullivan et al. 2010). Thin layers often function as marine oases with distinct hydrographic and biochemical signatures (e.g. McManus et al. 2003; Durham and Stocker 2012) that are often exploited by zooplankton populations to maximize foraging success (Tiselius 1992; Woodson et al. 2005). Hydrodynamic and chemical sensory cues associated with thin layers are sufficient to produce patchy aggregations in a variety of copepod species seeking to exploit the high densities of information and resources contained in the layer (e.g. Woodson et al. 2007). However, thin layers of toxic phytoplankton have also been shown to induce avoidance of the layer (Nielsen et al. 1990; Bjørnsen and Nielsen 1991). This, coupled with the often-elevated presence of predators (Benoit-Bird et al. 2009), suggests a dual nature for thin layers in the lives of copepod grazers in which abundant resources and sensory information are confounded by the potentially elevated predation risk and/or likelihood of exposure to toxic alga. More generally, this means that all of the biophysical mechanisms pertaining to thin layer formation, maintenance, and dispersal are equally applicable to HABs, which should be considered another biochemical effect in the dynamics and ecology of thin layers.

McManus et al. (2008) found enhanced concentrations of *Pseudo-nitzschia spp.* in a thin layer in Monterey Bay and proposed that thin layers may incubate and conceal a harmful algal bloom event until the effects are evident in massive fish kills: a "cryptic bloom". Elevated shear values in stably-stratified pycnoclines commonly associated with thin layers likely produce shear instabilities along the layer edges, which can produce chemical filaments emanating away from the layer, acting to effectively "diffuse" the chemical cues contained in the layer to a larger volume. This implies the possibility for distance detection and interaction by copepod grazers in the vicinity

of the layer, in sharp contrast to most physiological and behavioral studies to date that give copepods no choice of dosed or undosed waters.

In the present study, we assess behavioral responses of the sympatric hop-sinker *A. tonsa* and the allopatric cruiser *T. longicornis* to "cryptic blooms" of the toxic dinoflagellate *K. brevis* contained in finescale, sharp-edged layers spanning a range of bloom conditions from essentially non-bloom (1 cell/mL) to maximum bloom (10,000 cell/mL) densities. We hypothesize that the presence of toxic *K. brevis* exudate layers will likely induce direct avoidance behaviors of the layer, highly erratic swimming behaviors, and possibly fundamentally different behavioral responses between the sympatric *A. tonsa* and the allopatric *T. longicornis*.

4.3 Methods

A custom flume was fabricated to create fine-scale (4 *cm* thick), sharp-edged toxic phytoplankton exudate layers for copepod behavioral assays. The copepods *Acatia tonsa* and *Temora longicornis* were exposed to thin layers of extracellular exudates from the toxic dinoflagellate *Karenia brevis*, spanning an ecologically-relevant range of equivalent cell concentrations from $1 - 10,000$ $cells/mL$, conditions ranging from essentially non-bloom to maximum bloom densities (Gannon et al. 2009). The goal is to quantify toxin-induced copepod behavioral responses under established subsurface bloom conditions in an ecologically-relevant way, which, as detailed below, has important implications throughout the experimental design.

The decision to isolate and use only the exuded or extracellular toxins (as opposed to exuded toxins plus live cells) was made for multiple reasons. Primarily, we are interested in assessing the behavioral interactions of copepod grazers and "cryptic blooms", i.e. toxic phytoplankton contained in finescale, sharp-edged layers. This necessitates the potential for distance detection and thus interactions involving extracellular toxins. Second, Pierce et al. (2008) used liquid chromatography to identify

and quantify the most abundant brevetoxins present from the onset to the demise of a toxic *K. brevis* bloom event. They showed that the ratio of extracellular (PbTx-3) to intracellular (PbTx-2) toxins increased as the bloom age increased, showing that the dominant dissolved brevetoxin in an established *K. brevis* bloom is the extracellular PbTx-3 component. Finally, the presence of whole live cells, even toxic cells in certain species, induce direct grazing behaviors (e.g. Prince et al. 2006, Woodson et al. 2007), which would likely dominate and mask potential behavioral responses such as changes in kinematics or path fracticality. Again, in the present study we are interested in quantifying the behavioral responses of copepods to an established subsurface bloom event, which is why we chose to isolate only exuded extracellular toxins (predominantly PbTx-3) for behavioral assays.

4.3.1 Chemical Layer Flume and Physical Measurements

The custom built flume (Figure 4.1) was made of acrylic (1.905 cm thick) allowing for undistorted optical access and video observation of two-dimensional free-swimming copepod trajectories under infra-red illumination (CVI Melles Griot, 57 PNL 054/P4/S, >660 nm, 22 mW). The 10 cm x 10 cm observation window was centered in a 20 L volume; a custom baffle at one end of the volume (Figure 4.1, upper left panel) was designed to create thin chemical layers via weak density stratification ($\Delta\rho \leq 0.25\, ppt$) and low shear intrusions.

To create the appropriate thin chemical layer conditions, the flume was first filled to slightly below mid-depth with the lowest density, top layer, fluid. Next, the highest density bottom layer fluid was introduced from a slot located at the bottom of the tank. The tank was filled until the density interface between the top and bottom layers rested at the bottom edge of another slot located just below mid-depth in the tank. Finally, the chemical layer containing exuded *Karenia brevis* toxins at a desired concentration level was introduced via the slot located at mid-depth. The chemical

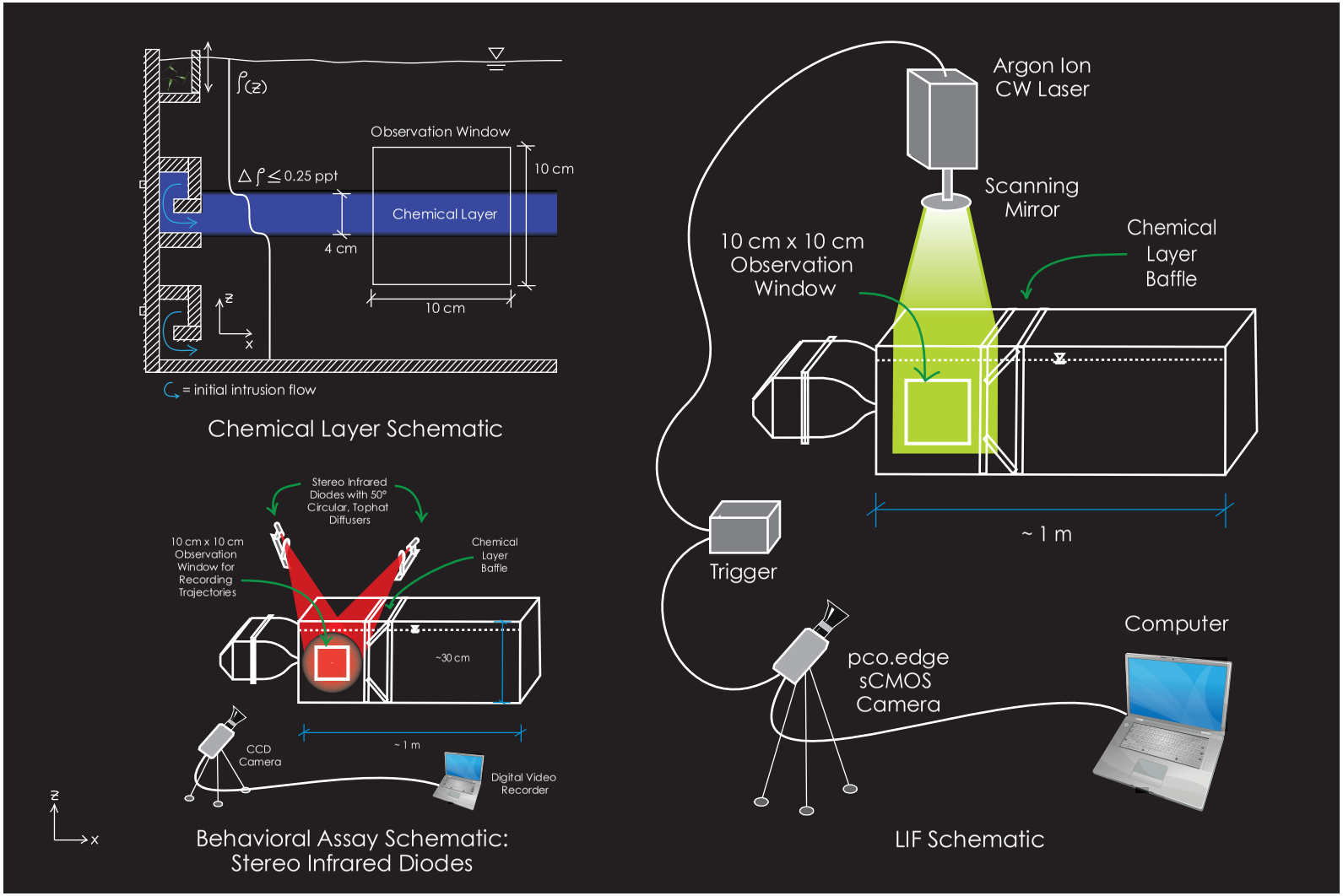

Figure 4.1: Experimental schematics for chemical layer creation (upper left panel), copepod behavioral assays (lower left panel), and LIF (right panel).

flow continued until a 4 cm chemical layer was created, centered in the observation window, at which point all flow was cut off and the layer was allowed to stabilize for $\sim$ 30 minutes before the start of behavioral assays. Once the chemical layer was stabilized, the long time scales associated with molecular diffusion ensure the steadiness of the layer structure over the course of the two hour behavioral assays. The flow of both the bottom and chemical layers was driven from elevated reservoirs at very low flow rates ($\sim 5\ L/hr$) so as not to introduce any buoyancy effects (via pump heating) or turbulent mixing (via unsteady pressure fluctuations, flow separation, etc.) and to minimize shear-induced mixing along the density interfaces. This experimental setup ensures sharp gradients at the edges of the chemical layer and a top hat chemical concentration profile over depth. A small amount of food coloring dye was added to the bottom and chemical layers ($\sim 2\ mL$ per 10 L) in order to visualize the density interfaces; *A. tonsa* and *T. longicornis* do not show any behavioral responses to the food-grade dyes used (personal correspondence Dr. Rachel Lasley-Rasher). The weak density stratification was necessary to "trap" the chemical layer at the desired location and avoid shear instabilities during set up. Density stratifications at this level ($\Delta\rho \leq 0.25\ ppt$) are well below threshold levels inducing behavioral responses for *A. tonsa* and *T. longicornis* (Woodson et al. 2007), ensuring that copepod behavioral responses are solely due to the presence of toxic exudates.

Quantification of the spatiotemporal structure of chemical concentration using planar laser-induced fluorescence (PLIF) validated that the apparatus produced a steady, sharp-edged chemical layer. PLIF is a widely-used, non-invasive technique for measuring scalar concentration fields in a variety of flow conditions. A planar light sheet was created by sweeping a continuous wave Argon ion laser (500 mW, 514 nm) through the observation region via a scanning mirror (Figure 4.1, right panel). The light sheet illuminates the chemical layer that was dosed with a photoreactive dye (Rhodamine 6G). A dedicated laptop PC (Dell Precision) running LabVIEW

(National Instruments) was used to create and synchronize the analog voltage signal controlling the scanning mirror and the digital pulse train controlling camera exposure through a USB-based DAQ Board (National Instruments). The beam was swept through the observation region one time per camera (Cooke Inc., pco.Edge, scientific CMOS, 5.5 MP, 16-bit, global shutter) exposure with images being recorded directly to the hard drive of a dedicated desktop PC running image acquisition software (CamWare64). An optical high-pass filter (Tiffen Orange 21) was used to isolate fluoresced light, ensuring the laser signal was not imaged. One minute image sequences were acquired at 5 Hz and post-processed using Lavision Inc. software (DaVis 8.1.6, LIF package). A concentration-intensity calibration curve was generated by imaging the observation volume at known dye concentrations of 0 - 50 $\mu g/L$ (in 5 $\mu g/L$ increments). Additionally, a darkfield image (with the lens cap on) was taken to correct for background camera noise. Crucially, the exact experimental configuration and settings (camera: lens, optical filter, position, f-stop, exposure time, frame rate; laser: power, sweep rate, geometry with respect to the imaging window) were used for both calibration and chemical layer imaging sequences. Post-processing algorithms used here correct raw images for laser light attenuation with depth, laser light absorption, non-uniformities in light sheet intensity, and background camera noise and produce an analytical relationship between pixel intensity and scalar concentration.

4.3.2 Plankton Collection, Care, and Culturing

A culture of *K. brevis* (strain No. 2228) was maintained (L1+Si growth media, 22 $^{\circ}C$ growth temperature, 12:12 light:dark) in the lab of Dr. Jeannette Yen (School of Biology, Georgia Institute of Technology) for several years. Culture growth phase curves were generated by counting cell densities using a Sedgewick rafter (standard hemacytometer practices) every other day. Cells were harvested only during the late exponential growth phase for copepod behavioral assays ensuring consistent toxicity

levels (which vary characteristically over the growth phase). An ELISA analysis was run on *K. brevis* cultures in the lab of Dr. Julia Kubanek (School of Biology, Georgia Institute of Technology) to quantify toxin types and levels. Brevetoxins were detected by the ELISA, with the predominant toxin being Type-2 brevetoxin, which accounts for 90 - 95 percent of the toxins produced in a typical bloom event (Naar et al. 2002). Computed Type-2 brevetoxin content per cell was between 8 - 12 pg/cell, a typical toxicity level for a mid-level algal bloom. To isolate extracellular dissolved toxins for copepod behavioral assays, *K. brevis* cultures were centrifuged at 1500 rpm for three minutes, settings observed to achieve minimal cell lysing and maximal aggregation of whole cells, thus isolating the dissolved extracellular toxins (PbTx-3) in the supernatant that was then isolated and diluted to the desired concentration level.

Acartia tonsa were collected in June - August 2012 at Priest Landing, Skidaway Island, Savannah, GA, USA using a plankton net deployed from the dock between 10 pm and midnight on the ebb or flood tide, depending. The net was deployed at a depth of $\sim 5\ m$ for 1 hour intervals after which the copepods were taken to the Priest Landing laboratory to be processed. The copepods were transferred to 20 L buckets of filtered seawater (FSW, 5 μm) at estuarine conditions (30 ppt, 28 $^{\circ}C$). They were kept under well-oxygenated conditions at low densities and fed a mixed diet of *Tetraselmis spp.* and *Rhodomonas lens*. Mixed-sex groups of ~ 60 copepods were sorted under a dissecting microscope prior to experimental trials.

T. longicornis were collected via net tows (250 μm mesh and cod end) at a depth of ~ 10 - 30 m in the Damariscotta River estuary at the Darling Maine Center, Walpole, Maine in the spring of 2012. Copepods were shipped overnight under temperature-controlled conditions to the Georgia Institute of Technology. Upon arrival, they were transferred to a temperature-controlled environmental room (32 ppt, 12 $^{\circ}C$) to acclimate, after which they were transferred to 20 L buckets of well-oxygenated

artificial seawater (Instant Ocean) at low densities and fed a mixed diet of *Tetraselmis spp.* and *Rhodomonas lens*. Mixed-sex groups of ~ 60 copepods were sorted under a dissecting microscope prior to experimental trials.

4.3.3 Behavioral Assays and Data Analysis

All behavioral assays were conducted in the same chemical layer flume and under identical conditions as for the LIF layer characterization, with the exception of the illumination source (Figure 4.1, lower left panel). All experiments were conducted in an environmental room at conditions (temperature and salinity) nearly identical to *in situ* conditions where each copepod species was collected (*T. longicornis*: 32 ppt, 12 $°C$, *A. tonsa*: 30 ppt, 28 $°C$). All behavioral assays were run in mixed-sex, species-specific trials, with $\sim$ 60 individuals. Two hour behavioral assays in toxic algal exudate layers were conducted under five concentration levels ranging from 1 - 10,000 cells/mL equivalent with two replicates of each species and treatment combination. One hour control experiments also were conducted for all species tested. The control experiments consisted of animals swimming freely in a stagnant tank with no chemical dosing. In all cases, animals were filmed in the 10 cm x 10 cm observation window.

A pair of infrared (IR) fiber-coupled diodes (CVI Melles Griot, 57 PNL 054/P4/S, >660 nm, 22 mW) were diffused via 50° circular, top hat diffusers (Thor Labs) providing backlit, stereo illumination. This method provides diffuse, effectively omni-directional illumination throughout the depth of the tank and eliminates potential phototactic effects. Copepod trajectories produced over the course of each two hour behavioral assay were recorded via a CCD video camera (Pulnix, 745i, 768 x 494 pixels) linked to a digital video recorder (Sony, mini dv tapes). All experiments were recorded at 30 frames per second (fps), which fully resolves all swimming behaviors of the species tested.

Mini dv tapes containing raw trajectory data were digitized as a series of uncompressed avi (Audio-Video Interleave) clips at 15 fps using iMovie HD (Apple Inc.). This frame rate is sufficient to resolve all copepod swimming behaviors. For example, maximum swimming speeds of *A. tonsa* reached up to 110 mm/s. This swimming speed results in a displacement of 550 $pixels/s$ at a typical magnification of 0.2 $mm/pixel$. Given a typical copepod body length of 1 mm (5 $pixels$), the corresponding displacement is 110 body lengths per second, or 7.33 body lengths per frame. Thus, 15 Hz is a sufficient temporal resolution to accurately resolve displacement of the body centroid for the maximum observed swimming speeds.

Free-swimming copepod trajectories were digitized in the x-z plane using DLTdv5, a MATLAB-based digitization software (Hedrick 2008). The resulting raw trajectory data sets (x, z, t) were analyzed using a suite of custom MATLAB codes. Path kinematic parameters were computed for portions of each trajectory inside and outside the algal exudate layer, as well as pre-contact and post-contact. The path kinematics computed in this study are swimming speed and turn frequency (TF, where a turn is defined as a change of direction of 15° or more). Additionally, the following gross trajectory parameters are computed and provide measures of the net effect of changes in copepod behavior on macroscale trajectory characteristics: the two-dimensional path fractal dimension ($F2D$), the proportional residence time (PRT = time spent in-layer/total time in observation window), and the proportional vicinity time (PVT = time in observation window post-contacting layer/total time in observation window). $F2D$ provides a scale invariant description of trajectory fracticality or self-similarity and provides useful insight into how changes in path kinematic parameters modify gross trajectory characteristics (see below for computation details). PRT and PVT answer aggregation and avoidance questions on the finescale (i.e. the scale of the layer) and macroscale (i.e. the scale of the vicinity of the layer/observation window), respectively, and are fundamentally linked to changes in path kinematics in-layer

versus out-of-layer (by location) and pre-contact versus post-contact (by exposure), respectively. Figure 4.2 shows a hypothetical copepod trajectory in the experimental domain as a useful visualization of PRT, PVT, the layer/treatment region, and the spatial scales of path kinematic responses by location (in-layer versus out-of-layer) and exposure (pre-contact versus post-contact) discussed below.

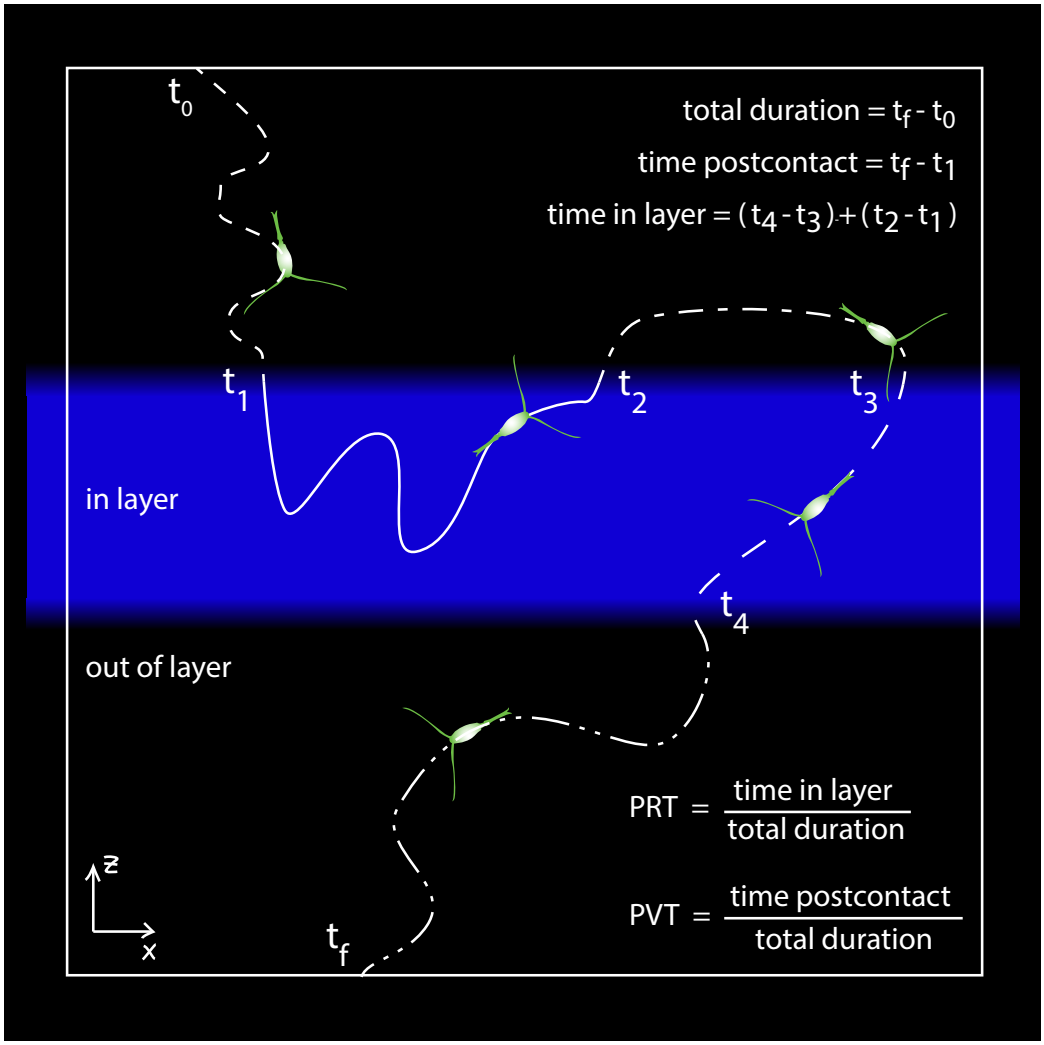

Figure 4.2: A hypothetical trajectory and the definition of the gross path parameters.

$F2D$ was computed using a custom box-count algorithm written in MATLAB (R2012b) following the recommendations of Liebovitch and Toth (1989), Buczkowski

et al. (1998), Uttieri et al. (2005), and Seuront (2009). Many factors affect the accuracy and statistical validity of fractal dimensions computed algorithmically, including the following that were addressed here: grid positioning with respect to the digitized trajectory data (i.e. origin location), the upper and lower limit of box sizes used as it relates to the overall resolution of the optical system, the mathematical sequence of box sizes, and the regression analyses used to extract $F2D$ as the slope of the resulting log-log plot of boxes occupied as a function of box size. Digitized trajectory data ($x,\ z,\ t$) were first shifted to a new origin located at the intersection of two tangent lines originating at the two trajectory points containing the minimum x and z values of the trajectory set, respectively (Buczkowski et al. 1998). Using a standardized grid origin with respect to the trajectory data ensures optimal embedding and alleviates the possibility of differing grid locations resulting in different computed fractal dimensions (Uttieri et al. 2005). Next, a dyadic sequence (2^n or powers of two) of box sizes was chosen, as this mathematical sequence always yields an integer number of boxes and alleviates potential border problems (Buczkowski et al. 1998). The lower cutoff for the box size sequence was chosen as 2^1 pixels to avoid saturation problems typical of single pixel box sizes, whereas the upper cutoff was taken as $2^8 = 256$, the power of 2 closest to half the minimum optical resolution of the system (e.g. for the camera used here, the CCD sensor is 480 x 720 pixels, $480/2 = 240 \rightarrow$ upper cutoff $= 256$). Finally, the digitized trajectory image was converted into a binary (or logical) array for each grid of box sizes and the sum of all nonzero elements (i.e. boxes occupied by the trajectory) is taken as the number of boxes occupied for that particular grid size. Lastly, linear least-squares regression analysis was used on the resulting data set to extract $F2D$. The R^2-SSR procedure (Seuront 2009) was employed to ensure a statistically valid and an accurate description of copepod path fractal characteristics. Validation and calibration of the algorithm were performed by computing fractal dimensions of two-dimensional linear motion (theoretical $F2D = 1$) and two-dimensional Brownian

motion, or random walk (theoretical $F2D = 2$). Values computed for each of these two cases were 0.9982 and 1.9982, respectively, revealing a constant correction factor of +0.0018, which was applied to all $F2D$ values computed here.

4.3.4 Statistical Analyses

All statistical analyses were executed using JMP Pro software (SAS). Analysis of covariance (ANCOVA) with three model effects (species, concentration, species x concentration interaction) were conducted on the mean behavioral responses (as opposed to the raw data consisting of ~ 80 observations per species at each concentration level). ANCOVA of the raw data revealed highly significant behavioral responses; however, low coefficients of determination (R^2), non-randomly distributed fit residuals, and significant lack of fit tests revealed that there was still a significant portion of the variability in the response data ($\sim 80\%$) that the model was unable to explain. Non-linear and generalized least square models did not significantly enhance the explanatory power as judged from the model R^2 and Akaike Information Criterion corrected (AICc) values. Thus, ANCOVA of the mean behavioral responses were conducted, yielding significant model effects and vastly improved coefficients of determination (R^2). This suggests that random effects such as copepod sex-ratios, slight deviations in experimental time-of-day, slight deviations in hunger-level, and potential dependence of response parameter distributions on *K. brevis* exudate concentration likely account for much of the unaccounted for variability. Performing regression analyses on the log-transformed concentration levels necessitated dropping the control (0 cell/mL equivalent) values from the regression analyses; however, control values are included in the scatterplots for reference.

4.4 Results

4.4.1 Chemical Layer Characterization

Figure 4.3 presents the chemical concentration field in which all concentrations have been normalized by the layer source concentration, C_o, of 20 $\mu g/L$ (Rhodamine 6G). Extracting vertical concentration profiles at various x locations (Figure 4.4) verifies the uniformity of the concentration field in the x direction, the sharpness and symmetry of gradients above and below the chemical layer in the z direction, and top-hat concentration profiles throughout the observation window. The 4 cm thick chemical layer features highly uniform concentrations above and below the layer ($\leq 2\%$ of C_o) and in the layer ($\geq 97\%$ of C_o), with a sharp gradient region (≤ 1 cm) joining maximum and minimum concentration zones. To take full advantage of the dynamic range of the camera, the non-layer region of the observation window was dosed a very low concentration of Rhodamine ($\sim$ 0.5 $\mu g/L$) as is seen in the vertical concentration profiles.

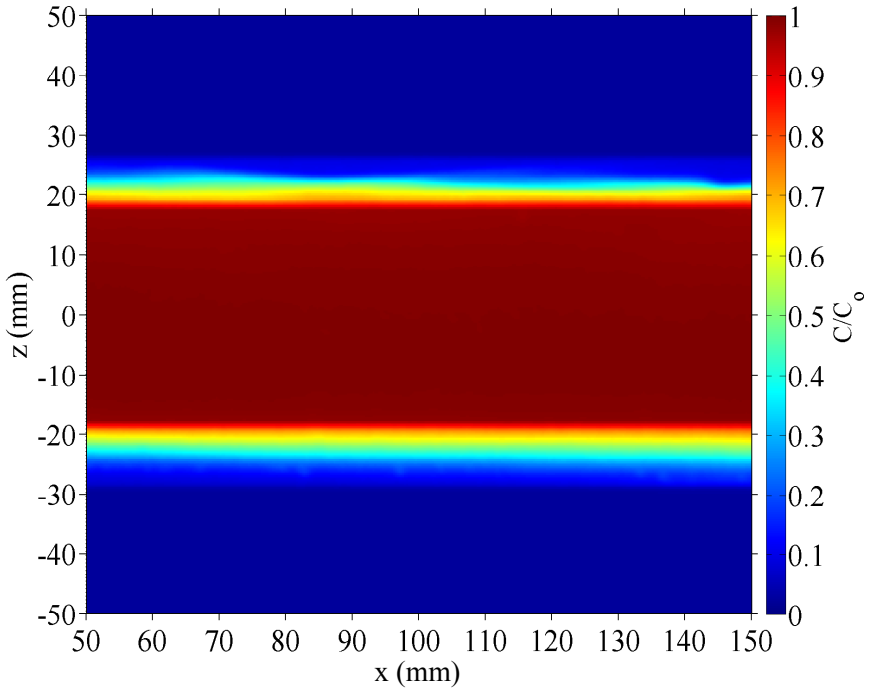

Figure 4.3: Concentration field (normalized by source concentration)in a chemical layer.

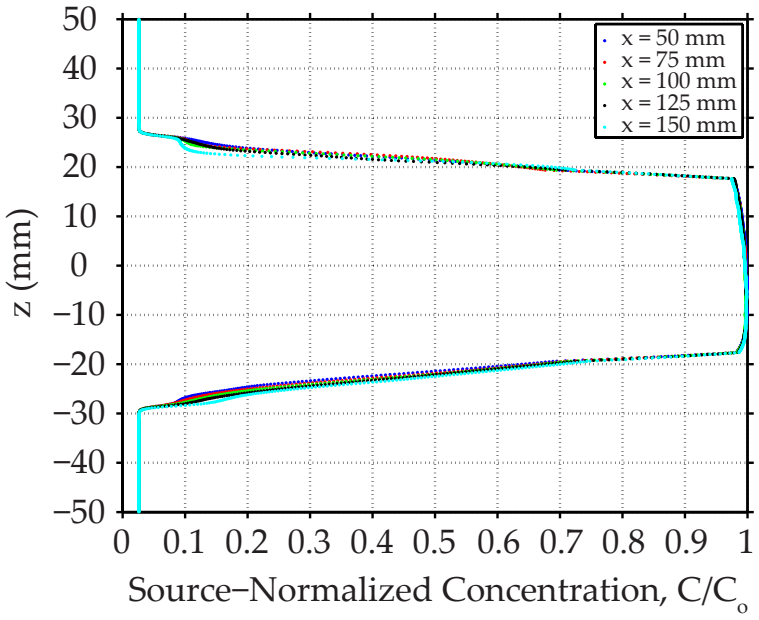

Figure 4.4: Vertical concentration profiles extracted at various horizontal positions in a chemical layer.

4.4.2 Path Kinematics and Gross Path Parameters

Figures 4.5 (*A. tonsa*) and 4.6 (*T. longicornis*) show all digitized trajectories for each *K. brevis* exudate layer concentration. An examination of these plots reveals the holistic, or population-level, behavior of both species due to increasing concentration of toxic algal exudates. Clearly, *A. tonsa* exhibits strong avoidance behaviors to increasing concentration levels. At the highest concentration of 10,000 cells/mL equivalent, only a handful of copepods are actually penetrating and/or crossing the exudate layer. *T. longicornis* shows a qualitatively similar increase in avoidance behavior to increasing concentration levels but appears more likely to penetrate and/or cross the exudate layer than *A. tonsa*. The mechanics behind the avoidance behaviors seen here are elucidated by quantifying path kinematics and gross path parameters as presented below.

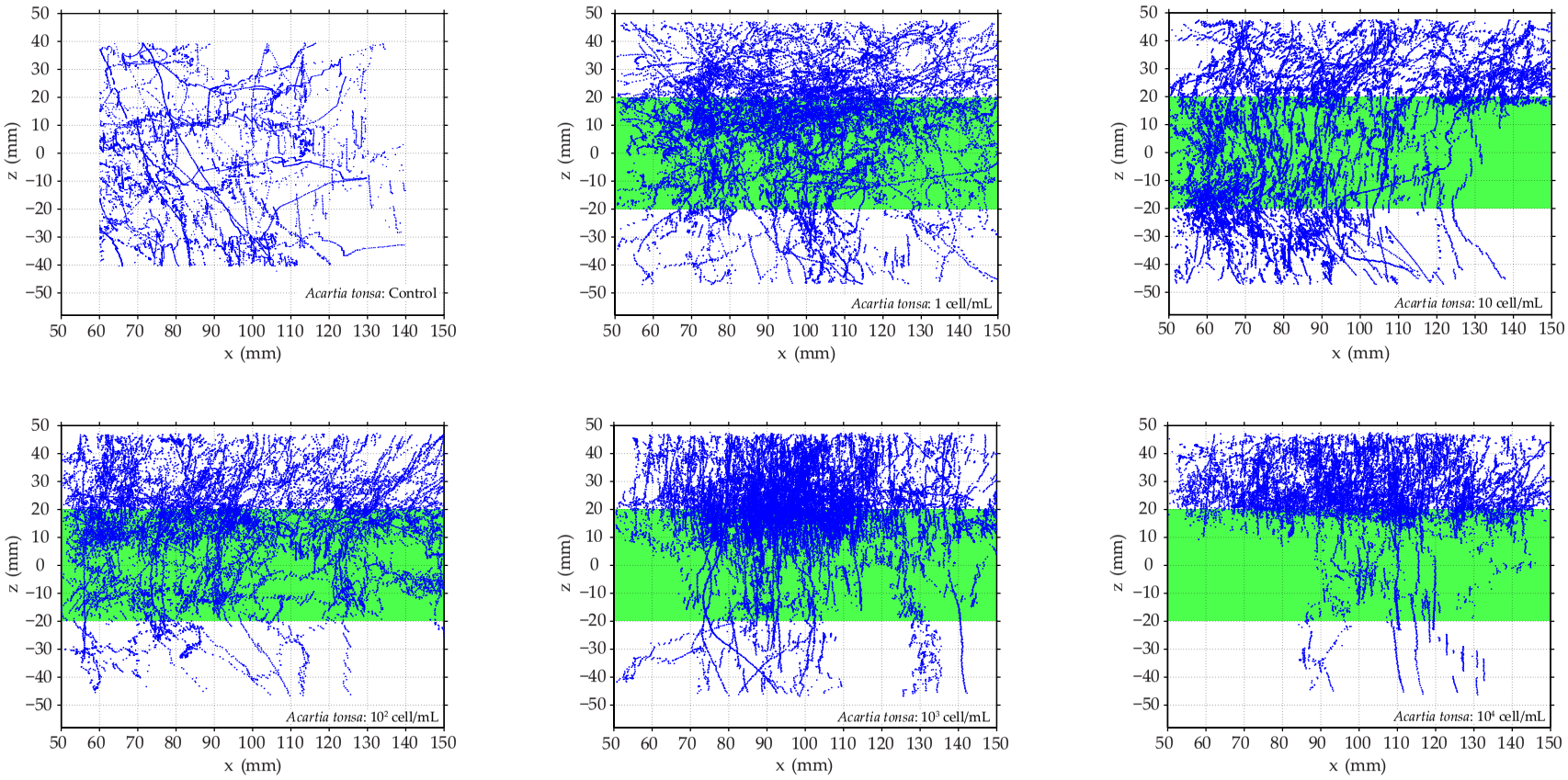

Figure 4.5: Digitized trajectories of *A. tonsa* in *K. brevis* exudate layers ranging from 0 (top left panel) to 10,000 (bottom right panel) cells/mL equivalent. The spatial location of the exudate layer is indicated by the green region.

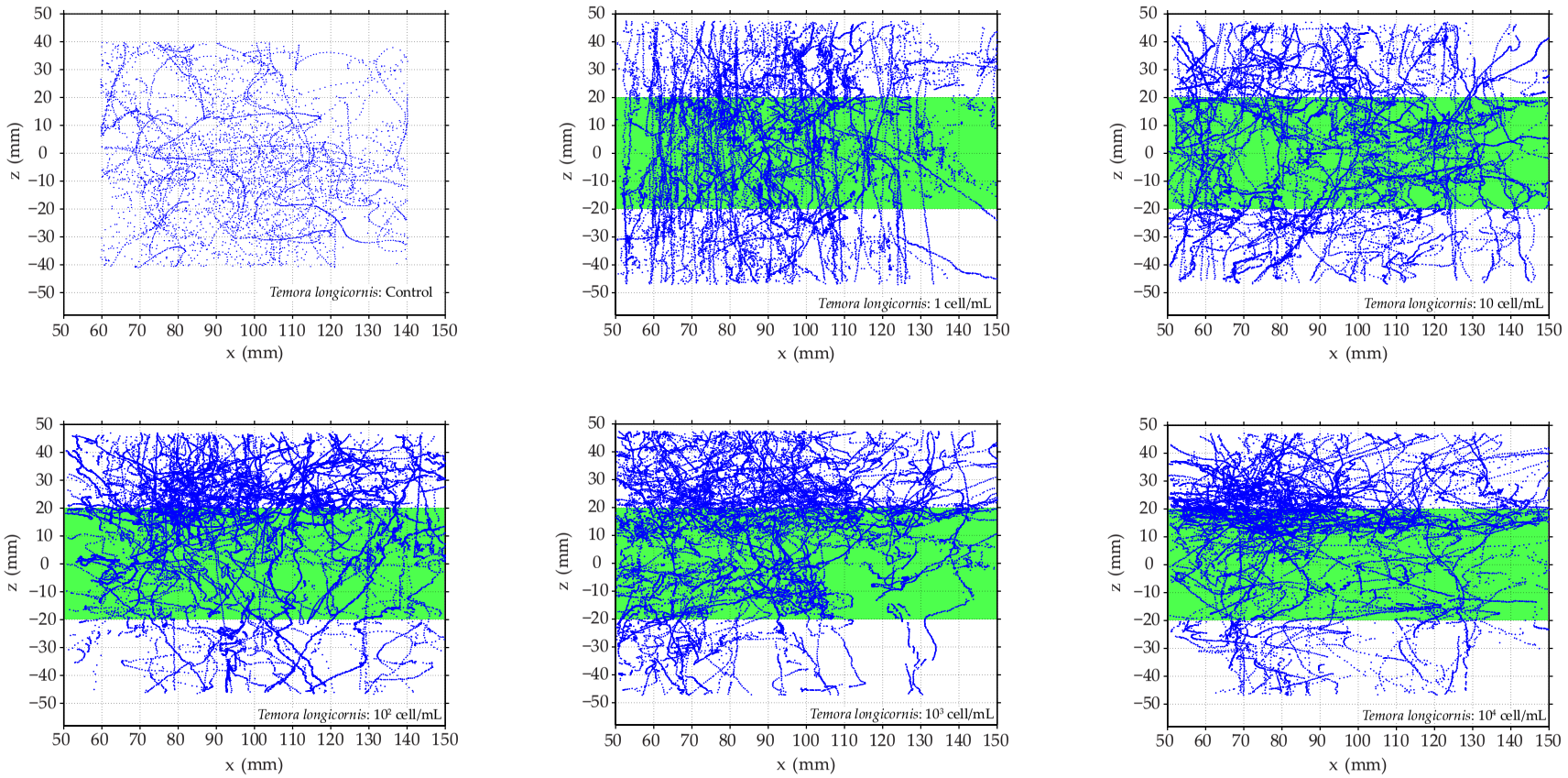

Figure 4.6: Digitized trajectories of *T. longicornis* in *K. brevis* exudate layers ranging from 0 (top left panel) to 10,000 (bottom right panel) cells/mL equivalent. The spatial location of the exudate layer is indicated by the green region.

Table 4.1 summarizes the analyses of covariance (ANCOVA) for various behavioral response parameters with three model effects (species, concentration, species x concentration interaction). The significance levels of each of the three model effects are summarized in the last three columns of Table 4.1, respectively. The ANOVA p-value indicates whether or the not the ANCOVA as constructed explains a significant amount of the variability in the response data and, similarly, the model coefficient of determination R^2 provides a measure of the percentage of variability in the response data explained by the ANCOVA. The species effect p-value indicates whether there is a significant difference between the mean response of all concentrations of each species (i.e. different fit line y-intercepts for each species). The concentration effect p-value indicates whether there is a significant dependence of the behavioral response parameter on *K. brevis* exudate concentration (i.e. non-zero fit line slope for the species-combined data set). Finally, the species x concentration interaction effect p-value indicates whether there is a significant difference between the slope of fit lines between species. The slope and y-intercept values in Table 4.1 linearly relate the behavioral response parameter (y) to the log-transformed concentration (x) for the ANCOVA (i.e. the regression that minimizes fit residuals of the combined behavioral response data of both species). In the scatterplots below, the ANCOVA regression is plotted unless the interaction effect is significant (or trending, $p < 0.2$), in which case the separate regression lines are plotted for each species for a quantitative discussion of trend differences between species.

Table 4.1: Summary of Analyses of Covariance Results

Behavioral Parameter	**n**	R^2	**Slope, y-intercept**	**F-value**	**ANOVA p-value**	**Species p-value**	**Conc. Level p-value**	**Interaction p-value**
PRT	10	0.885	-0.028, 0.4553	15.4581	0.0031*	0.048*	0.0009*	0.1219
PVT	10	0.867	-0.035, 0.7315	13.3744	0.0046*	0.1332	0.001*	0.3718
% Penetrating	10	0.9087	-0.051, 0.7868	19.928	0.0016*	0.0081*	0.0006*	0.4687
F2D	10	0.802	0.0024, 1.1001	8.1215	0.0156*	0.0048*	0.241	0.1024
μ **Speed (mm/s)**	10	0.465	-	1.7396	0.2581	0.2459	0.5915	0.1218
μ **Speed Post-Pre (mm/s)**	10	0.925	0.0645, -0.2022	24.7699	0.0009*	0.0027*	0.0044*	0.0015*
μ **Speed In-Out (mm/s)**	10	0.774	0.0698, -0.065	6.8576	0.0229*	0.0367*	0.0253*	0.0742**
σ **Speed (mm/s)**	10	0.898	0.0822, 3.152	17.6695	0.0022*	0.0006*	0.1016	0.05*
σ **Speed Post-Pre (mm/s)**	10	0.894	0.2387, -0.0636	16.9427	0.0025*	0.0065*	0.0068*	0.0056*
σ **Speed In-Out (mm/s)**	10	0.805	0.2103, -0.2098	8.2316	0.0151*	0.0206*	0.0117*	0.1901
Max Speed Post-Pre (mm/s)	10	0.643	3.1326, 16.754	3.5959	0.0854**	0.2043	0.031*	0.3808
μ **TF (turns/ind/sec)**	10	0.52	-	2.17	0.1926	0.2224	0.2745	0.1233
μ **TF Post-Pre (turns/ind/sec)**	10	0.662	0.0747, -0.2585	3.9105	0.0731**	0.2657	0.0221*	0.3948
μ **TF In-Out (turns/ind/sec)**	10	0.892	0.0504, -0.0993	16.6035	0.0026*	0.0722**	0.0005*	0.8058

As revealed in the digitized trajectory plots (Figures 4.5 and 4.6), explicit exudate layer avoidance behaviors are confirmed in trends of PRT, PVT, and the % penetrating greater than 25% of the exudate layer thickness (Figures 4.7 and 4.8, Table 4.1). Both species are significantly reducing the amount of time they spend directly in the layer (PRT) and its vicinity (PVT), and also exhibiting an increasing unwillingness to make excursions into the exudate layer (% Penetrating) with increasing *K. brevis* concentration (significant concentration effects, Table 4.1). PRT is trending towards a significant difference in the negative slope between species (i.e. significance in the species x concentration interaction effect, Table 4.1). The trending interaction effect suggests that *A. tonsa* could reduce PRT almost twice as fast as *T. longicornis* as evidenced by the regression slopes (m = -0.036 versus -0.019). This, in combination with the fact that *T. longicornis* is more likely to reside in and/or penetrate into the layer (significant species effect, PRT and % penetrating), seem to suggest a more acute avoidance response to the toxic layer for *A. tonsa*.

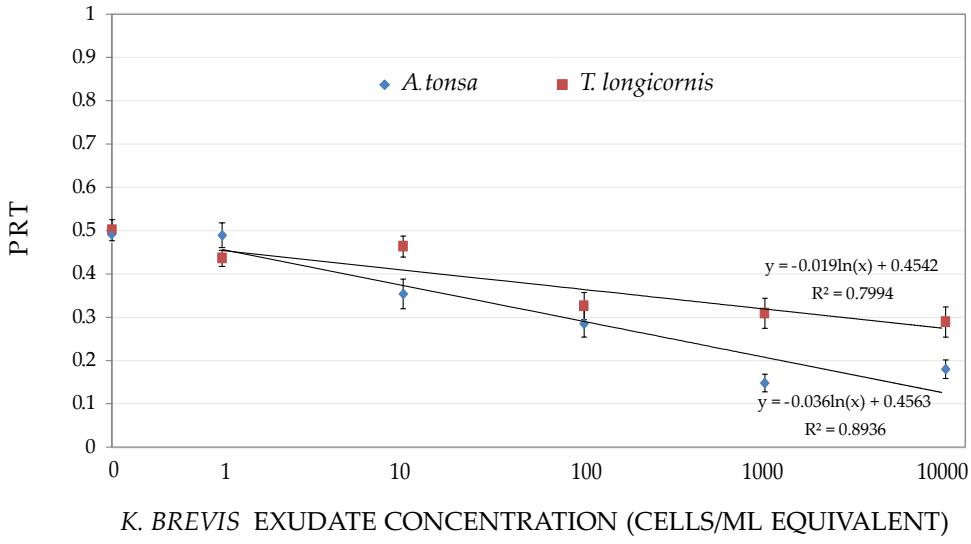

Figure 4.7: Proportional residence time (PRT) in *K. brevis* exudate layers. Linear regression lines using log-transformed concentration levels are displayed with fit equation. Error bars are ± 1 SE.

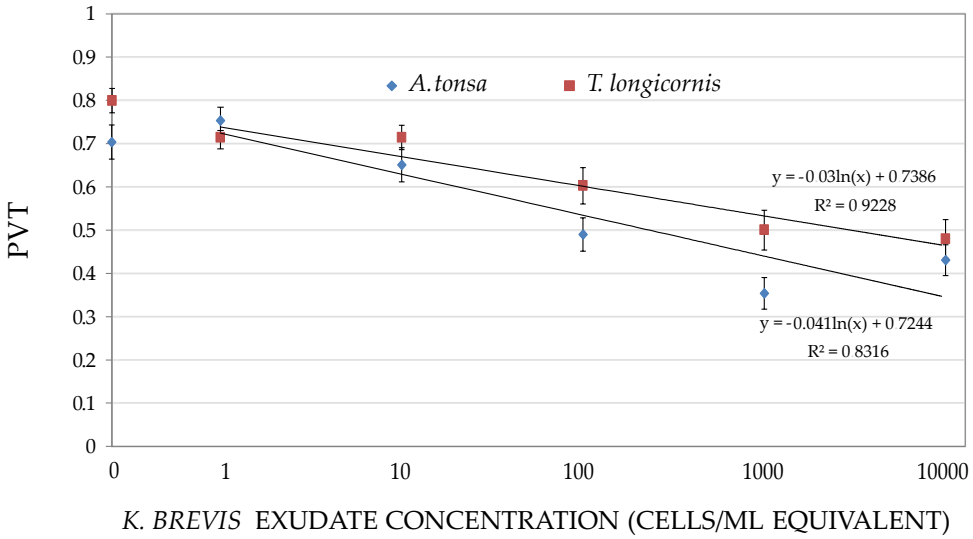

Figure 4.8: Proportional vicinity time (PVT) in *K. brevis* exudate layers. Linear regression lines using log-transformed concentration levels are displayed with fit equation. Error bars are $\pm$ 1 SE.

The regression analysis of the two-dimensional path fractal dimension, $F2D$, (Figure 4.9, Table 4.1) reveals significant differences in path diffusivity between species (significant species effects, Table 4.1) in which *A. tonsa* (hop-sinker) paths are on average more diffuse than those of *T. longcornis* (cruiser). While the concentration effect is not explicitly significant (Table 4.1), a trending interaction effect is likely confounding the main concentration effect; this is corroborated by examining $F2D$ trends with increasing *K. brevis* concentrations by species, as shown in Figure 4.9. Thus, it is likely that *A. tonsa* trajectories become more diffuse ($\uparrow F2D$) whereas *T. longicornis* trajectories become more linear and ballistic ($\downarrow F2D$) with increasing *K. brevis* concentrations. These changes in path fracticality are produced by changes in path kinematics (discussed below) and have important implications for predator prey-interactions via changes in encounter rates and also changes in hydrodynamic conspicuousness.

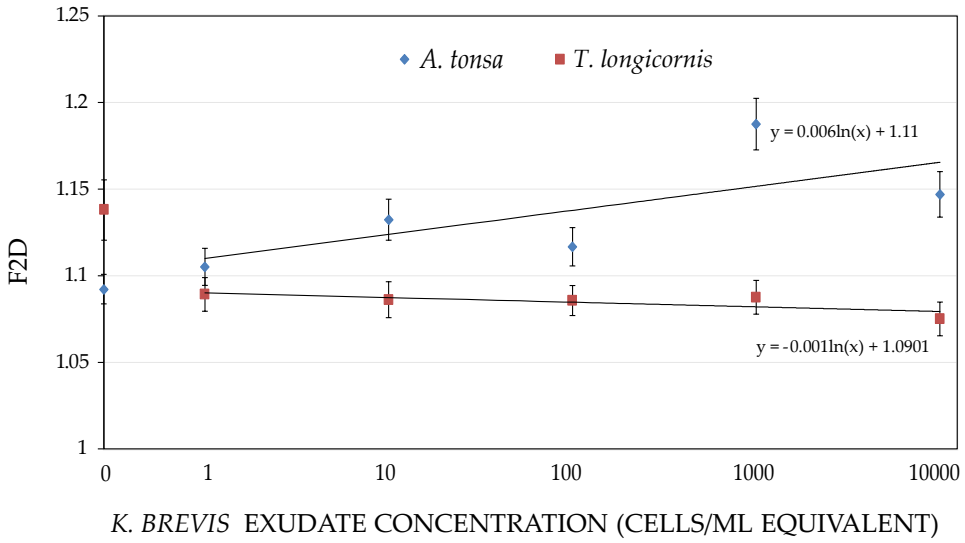

Figure 4.9: Two-dimensional path fractal dimension ($F2D$) in *K. brevis* exudate layers. Linear regression lines using log-transformed concentration levels are displayed with fit equation. Error bars are $\pm$ 1 SE.

Another reason for the obscured significance of $F2D$ trends is the lack of significance for regressions of *mean* kinematics (swimming speeds, turn frequency) that directly determine path fracticality ($F2D$). This lack of significance, coupled with significance of kinematics by location (in-layer versus out-of-layer) and exposure (pre-contact versus post-contact), reveals that behavioral responses elicited by *K. brevis* exudates are operating on higher frequencies and/or finer spatial scales that are not resolved in the average response (Table 4.1, recall Figure 4.2).

Regression analyses of swimming speed by exposure (post-contact - pre-contact) reveal significant responses to *K. brevis* exudates (concentration effect, Table 4.1) as well as differences in the rate of change of swimming speed with increasing concentration between species and in the directionality of the basic trends (positive versus negative slopes, significant interaction effect, Table 4.1). *A. tonsa* increases swimming speed post-contact nearly 9 times as fast as *T. longicornis* reduces swimming speed

post-contact (Figure 4.10, $m = 0.1448$ versus -0.0161). Similarly, regression analyses of swimming speed by location (in-layer - out-of-layer) reveal differences in the rate of change of swimming speed with increasing *K. brevis* concentrations between species (significant interaction effects, Table 4.1). *A. tonsa* increases swimming speed in-layer nearly 7 times as fast as *T. longicornis* increases swimming speed (Figure 4.11, $m = 0.1207$ versus 0.0188). Collectively, mean swimming speeds by exposure (Figure 4.10) and by location (Figure 4.11) reveal *A. tonsa* significantly increases swimming speed both post-contact and in-layer at a rate almost 10 times as fast as *T. longicornis* changes swimming speed. *T. longicornis*, on average, slightly reduces swimming speed post-contact and slightly increases swimming speed in-layer, a somewhat counter intuitive response given the strong avoidance behaviors exhibited ($\downarrow PRT,\ PVT$, etc.).

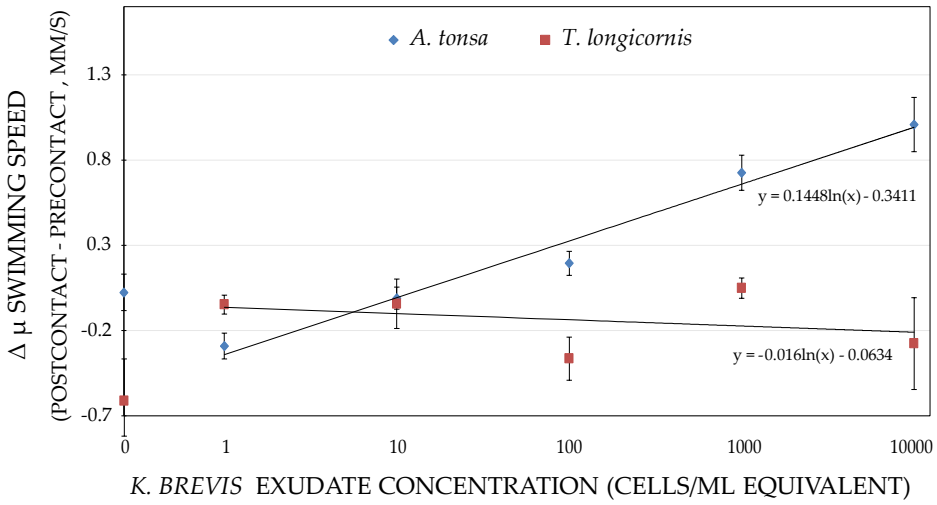

Figure 4.10: Difference between post-contact and pre-contact average ($\Delta\mu$) swimming speeds in *K. brevis* exudate layers. Linear regression lines using log-transformed concentration levels are displayed with fit equation. Error bars are ± 1 SE.

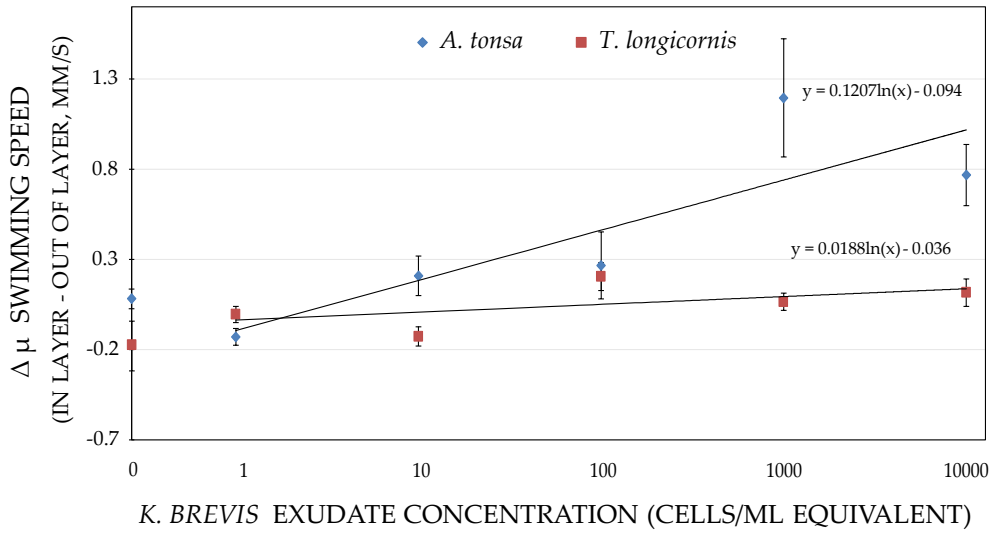

Figure 4.11: Difference between in-layer and out-of-layer average ($\Delta\mu$) swimming speeds in *K. brevis* exudate layers. Linear regression lines using log-transformed concentration levels are displayed with fit equation. Error bars are ± 1 SE.

It is useful to examine changes in not only the mean swimming speed but also trends of the standard deviation, or variability, of swimming speed. Regression of the standard deviation of swimming speeds (Figure 4.12) reveals significance differences not only in the rate of change of variability of swimming speed but also in the directionality of the basic trend (positive versus negative slopes, significant interaction effect, Table 4.1). *A. tonsa* increases swimming speed variability, on average, nearly 9 times as fast as *T. longicornis* reduces swimming speed variability ($m = 0.186$ versus -0.022, Figure 4.12).

Further examination of trends in swimming speed variability by exposure and location reveal subtleties in behavioral response strategies not seen in trends of overall speed variability. Figures 4.13 and 4.14 plot the difference in swimming speed variability by exposure and location, respectively, versus *K. brevis* exudate concentration. *A. tonsa* significantly increases swimming speed variability post-contact at

a rate almost 50 times as fast as *T. longicornis* reduces swimming speed variability post-contact (m = 0.4877 versus -0.01, Figure 4.13). The rate of change of swimming speed variability by location is much more comparable (trending interaction effect, Table 4.1), with *A. tonsa* likely increasing speed variability at a rate almost 3 times as fast as *T. longicornis* (m = 0.2972 versus 0.1234, Figure 4.14). Finally, examination of maximum swimming speeds achieved post-contact reveals that both species exhibit significantly higher maximum speeds post-contact and with increasing *K. brevis* concentration (Table 4.1).

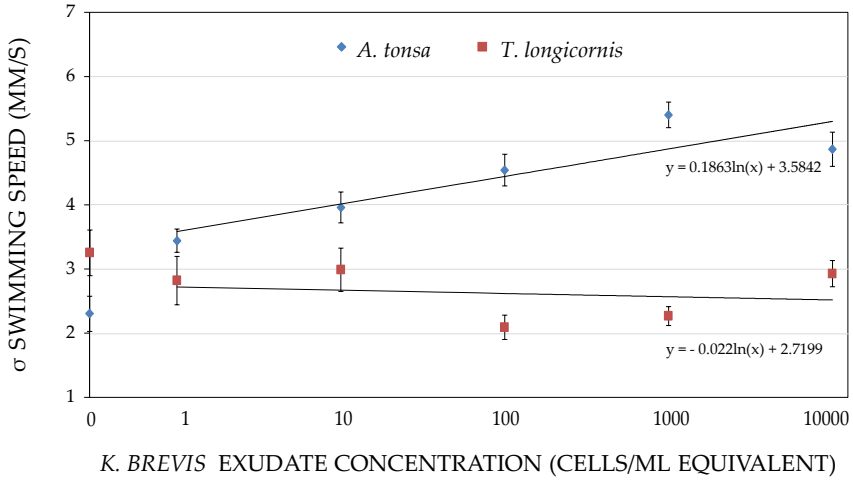

Figure 4.12: Standard deviation (σ) of swimming speed in *K. brevis* exudate layers. Linear regression lines using log-transformed concentration levels are displayed with fit equation. Error bars are ± 1 SE.

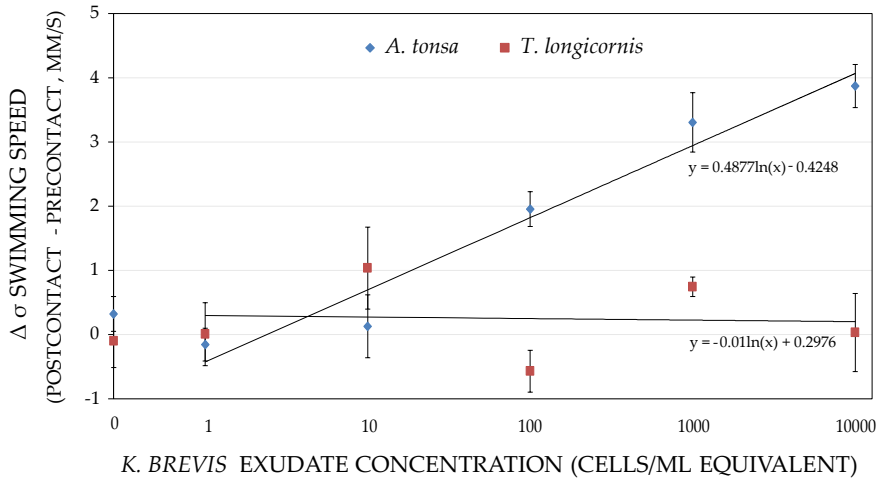

Figure 4.13: Difference between pre-contact and post-contact standard deviation ($\Delta\sigma$) of swimming speeds in *K. brevis* exudate layers. Linear regression lines using log-transformed concentration levels are displayed with fit equation. Error bars are $\pm$ 1 SE.

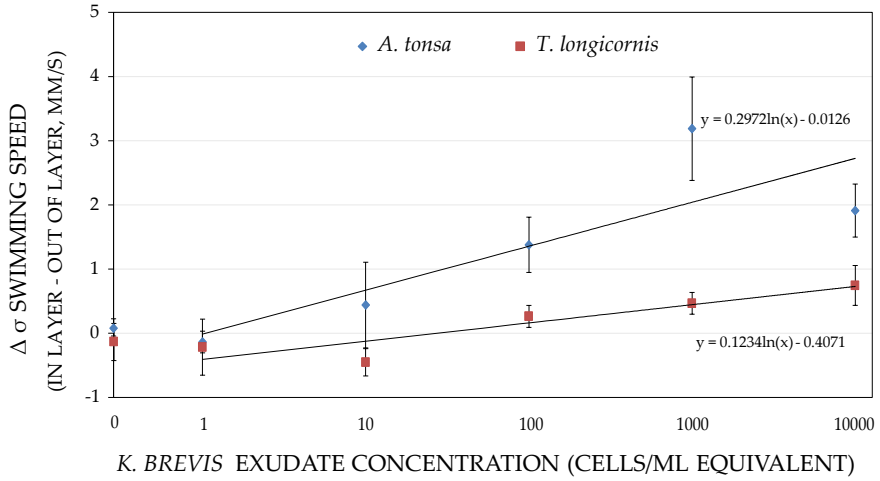

Figure 4.14: Difference between in-layer and out-of-layer standard deviation ($\Delta\sigma$) of swimming speeds in *K. brevis* exudate layers. Linear regression lines using log-transformed concentration levels are displayed with fit equation. Error bars are $\pm$ 1 SE.

Trends in turn frequency by exposure (Figure 4.15) and location (Figure 4.16) reveal that both species significantly increase turn frequency post-contact and in-layer, although there is no significant difference in the rate between species (Table 4.1). *T. longicornis* increases turn frequency post-contact and in-layer. When coupled with changes in swimming speed by location and exposure, this reveals a complex behavioral response in which trajectories are more linear and ballistic in the macro sense ($\downarrow F2D$) whereas increased turn frequencies post-contact and in-layer likely produce finescale portions of the trajectory that are actually more sinuous and diffuse. Conversely, *A. tonsa* exhibits a simpler response by increasing turn frequency post-contact and in-layer producing a more sinuous, diffuse trajectory in the macro sense ($\uparrow F2D$). As seen above, *A. tonsa* and *T. longicornis* employ significantly different behavioral strategies to achieve the same goals on the macroscale, although *A. tonsa* exhibits more sensitive, more rapid behavioral responses with increasing *K. brevis* concentrations.

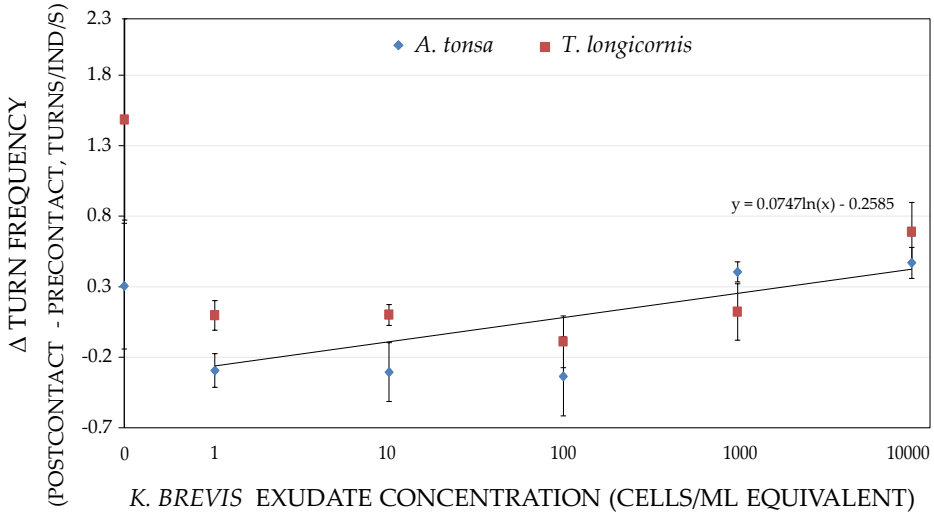

Figure 4.15: Difference between pre-contact and post-contact (Δ) turn frequency in *K. brevis* exudate layers. Linear regression lines using log-transformed concentration levels are displayed with fit equation. Error bars are $\pm$ 1 SE.

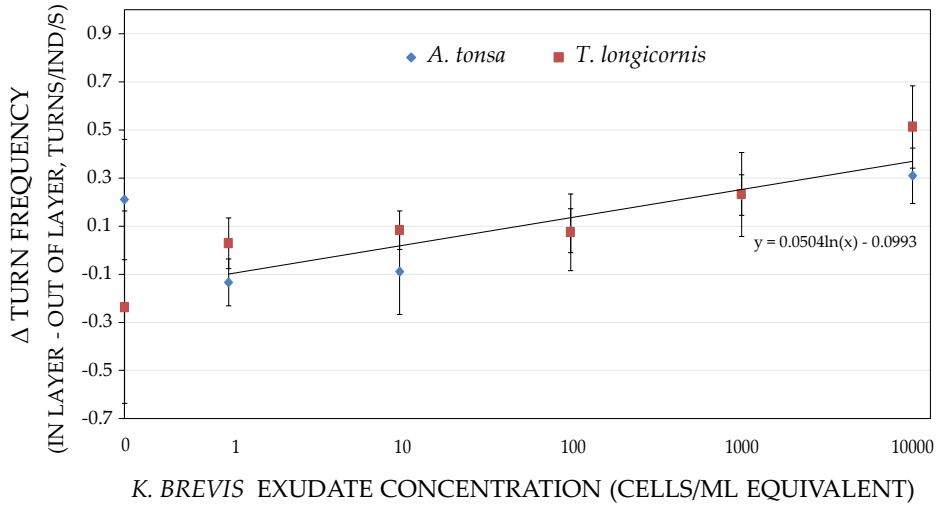

Figure 4.16: Difference between in-layer and out-of-layer (Δ) turn frequency in *K. brevis* exudate layers. Linear regression lines using log-transformed concentration levels are displayed with fit equation. Error bars are $\pm$ 1 SE.

4.5 Discussion

Strong avoidance behaviors and changes in path kinematics exhibited by both species here have important implications for HAB dynamics, predator-prey interactions, the bioaccumulation of toxicity via preferential predation, and overall ecological impacts. The results here corroborate some of what is known about the interactions of copepod grazers with toxic phytoplankton species and also offer new insight, particularly into behavioral interactions during the critical bloom incubation phase when toxic alga are often contained in thin layers. We have confirmed that even when given a choice between dosed or undosed waters, copepod behavioral responses produce highly erratic, hydrodynamically conspicuous swimming behaviors. As the direct trophic link between primary producers and high order trophic levels, copepods have the potential to significantly modulate the large scale ecological impacts of a harmful algal bloom event. Changes in individual copepod behaviors can produce population scale phenomena with important implications for harmful algal bloom dynamics (intensity/toxicity, duration, trophic transfers, etc.) and overall ecological impacts.

4.5.1 Implications for HAB Dynamics and Ecosystem Effects

There are multiple synergistic (and sinister) mechanisms that toxic phytoplankton species employ to gain an initial competitive advantage and then proceed to dominate local phytoplankton taxa. Toxic alga often produce anti-grazing compounds to modify top-down grazer control through (1) decreased ingestion rates, (2) decreased egg production, and (3) increased mortality of copepods through a combination of toxicity and nutritional inadequacy (Waggett et al. 2012). The data here elucidate another mechanism by which toxic phytoplankton may dominate planktonic ecosystems. Not only do they use toxic anti-grazing compounds to modify top-down grazer control and allelopathy to outcompete non-toxic phytoplankton taxa (Kubanek et al. 2005), but the very presence of toxic *K. brevis* exudates elicits explicit avoidance

of the layer and the surrounding volume ($\downarrow$ PRT, PVT, % $Penetrating$, Figures 4.7 and 4.8, Table 4.1). This implies that for *A. tonsa* and *T. longicornis* exudates from the toxic dinoflagellate *K. brevis* not only modify top-down grazer control, but eliminate it entirely by inducing strong avoidance behaviors, particularly when toxic alga are contained in thin layers (Rines et al. 2002, McManus et al. 2008, Sullivan et al. 2010) with sharp-gradients where copepods can detect and avoid the toxic layer. Thus, in the critical subsurface incubation phase (cryptic bloom) when copepods have a choice of dosed or undosed waters, explicit avoidance behaviors elicited by toxic phytoplankton likely act to protect and sustain new blooms until a critical mass is reached and other synergistic mechanisms act to sustain the bloom and enhance monospecific domination. Ecological scenarios in which copepods have a choice of toxic versus non-toxic waters (HAB incubation in subsurface cryptic blooms) and those in which they have no choice (mature and/or well-mixed blooms in which the physical scale of the layer exceeds copepod migratory and swimming capabilities) are both likely *in situ*. Quantifying the biophysical processes underlying HAB dynamics at both spatiotemporal scales is critical for predicting and modeling HAB incubation and overall ecological impacts. Cryptic blooms likely conceal a harmful algal bloom event until the effects are evident in massive fish kills and otherwise (McManus et al. 2008). Thus, sampling regimes aimed at early detection of HAB events must resolve thin layers at the appropriate temporal and spatial scales.

4.5.2 Potential for Preferential Predation and the Bioaccumulation of Toxicity

The net effect of changes in path kinematics (swimming speed, turn frequency) in response to increasing *K. brevis* exudate concentrations for *A. tonsa* is to produce trajectories that are highly erratic and hydrodynamically conspicuous everywhere ($\uparrow$ swimming speeds and speed variability by location and exposure, $\uparrow$ turn frequency by location and exposure, trending $\uparrow$ $F2D$, Table 4.1). Conversely, for *T. longicornis*

the net effect of changes in path kinematics produce trajectories that are highly erratic and hydrodynamically conspicuous only in the layer (↑ swimming speeds and speed variability by location, ↑ turn frequency by location, Table 4.1) and are more steady and inconspicuous post-contact and on average (↓ swimming speeds and speed variability by exposure, trending ↓ $F2D$, Table 4.1). Thus, the presence of thin layers of *K. brevis* exudates elicits erratic, hydrodynamically conspicuous swimming behaviors for at least some portion of the time for both species.

The excitation of erratic, hydrodynamically conspicuous swimming behaviors due to the presence of toxic algae has significant implications for predator-prey interactions (Visser and Kiørboe 2006), encounter rates (Kiørboe and Bagoien 2005), and importantly the bio-accumulation of toxicity into upper trophic levels (Tester et al. 2000). Erratic swimming behaviors produce not only large hydrodynamic signatures but also potential visual and chemical stimuli, thus increasing the conspicuousness of a copepod to a potential predator. For mechanosensitive predators, flow perturbations generated by highly unsteady, diffuse swimming behaviors seen here could lead to preferential predation of copepods dosed with toxic algal exudates, thus establishing a trophic vector by which toxins accumulate in upper trophic levels (Teegarden et al. 2003, Gannon et al. 2009).

4.5.3 Sympatry and Allopatry

The results herein provide potential insight into whether sympatric (geographically co-occurring) and allopatric (non-geographically co-occurring) copepods exhibit different behavioral strategies in response to thin layers of toxic algae. Sympatric species are known to gain adaptive resistance to toxic algae (Colin and Dam 2007, Jiang et al. 2011) whereas allopatric species likely lack an adapted awareness (Colin and Dam 2005, Turner et al. 2004). The known geographic distribution of many HAB species is expanding, including *K. brevis*, which is native to the Gulf of Mexico and

has bloomed as far north as North Carolina on the U.S. east coast (Tester et al. 1991, Glibert et al. 2005) suggesting increases in the degree of contact between naïve predators and HAB species.

Different behavioral response trends between species with increasing *K. brevis* concentration are explained not only by differences in morphology and swimming styles between the hop-sinking *A. tonsa* and the cruising *T. longicornis* (ANCOVA species p-value, Table 4.1) but also by a basic difference in response strategies for the sympatric *A. tonsa* and allopatric *T. longicornis* (ANCOVA species x concentration interaction p-value, Table 4.1). Regression analysis of swimming speed and swimming speed variability by location (in-layer versus out-of-layer) and exposure (pre-contact versus post-contact) reveal significant differences in behavioral response trends between species. *A. tonsa* significantly increases swimming speed and swimming speed variability in-layer and post-contact, whereas *T. longicornis* slightly increases both in-layer and slightly reduces both post-contact (Figures 4.10 - 4.14, Table 4.1). Not only do swimming speed response trends differ between species in terms of the directionality of the trend (i.e. positive versus negative slope of the fit lines), but the rate of change (i.e. the magnitude of the fit line slopes) of behavior for *A. tonsa* is significantly higher than that for *T. longicornis*, ranging from thrice to fifty times as large. Thus, it is clear that the sympatric *A. tonsa* possesses an adapted awareness of the toxic *K. brevis* lacking for the allopatric *T. longicornis* that is manifest as a more sensitive swimming behavior response with increasing *K. brevis* concentrations. This is further corroborated by the difference in PRT trends between species that would suggest that *A. tonsa* avoids the layer twice as likely as *T. longicornis*, as evidenced by the regression slopes (m = -0.036 versus -0.019, Figure 4.7). The similarity in trends of overall avoidance behaviors ($\downarrow PRT$, PVT) between species combined with the differences in trends of path diffusivity ($F2D$) signifies that while both species elicit increasing avoidance of the toxic layer and its vicinity with increasing toxin

concentration, there is a fundamental difference in not only the mechanisms by which the sympatric *A. tonsa* and allopatric *T. longicornis* modify swimming behaviors to achieve these ends but also the rate at which they do so.

4.5.4 Spatiotemporal Scales of Interaction: Elastic and Plastic Behavioral Responses

Computing behavioral responses by location (in-layer versus out-of-layer) provides a metric for behavioral *elasticity* and by exposure (pre-contact versus post-contact) for behavioral *plasticity* (recall Figure 4.2), describing responses that are ephemeral and enduring, respectively. A significant response by location signifies an elastic response; a copepod cruising around in a base behavioral state that comes into contact with a toxic algal exudate layer exhibits a behavioral response in-layer but quickly returns to its base state upon exiting the layer. In other words, the behavioral response is ephemeral and does not linger once out-of-layer. Conversely, a significant response by exposure signifies a plastic response; a copepod cruising around in a base behavioral state that comes into contact with a toxic algal layer exhibits a behavioral response upon contacting the layer and that response lingers post-contact, regardless of whether the copepod is in-layer or simply in the vicinity post-contacting the layer. Path kinematic responses by location in conjunction with PRT are associated with behavioral elasticity, finer spatial scales, and short time scales. Similarly, path kinematic responses by exposure and PVT are associated with behavioral plasticity, larger spatial scales, and longer time scales.

Significant behavioral responses in path kinematics (swimming speed, turn frequency) by location (in-layer versus out-of-layer) as well as exposure (pre-contact versus post-contact) (Table 4.1) suggest that there is both an elastic and plastic component of behavioral responses to toxic *K. brevis* exudate layers for both species. This, in combination with explicit reduction in both PRT and PVT, indicates that there are behavioral response processes relevant to not only the spatiotemporal scale

of the layer but also to that of the vicinity of the layer (i.e. the surrounding volume). Thus, this is likely a coupling mechanism between the spatiotemporal scale of the layer and that of the vicinity of the layer, a bridge between biophysical processes operating on fine spatial scales/short time scales and larger spatial scales/longer time scales. The combination of elastic and plastic behavioral responses induced by thin layers of toxic algal exudates produces a sort of behavioral hysteresis for both species in which toxin-induced behavioral responses linger and effectively diffuse into larger volumes on longer time scales.

CHAPTER V

ANTARCTIC KRILL AND THIN LAYER SENSORY CUES

5.1 Abstract

Finescale hydrodynamic and chemical cues commonly associated with thin planktonic layers are modeled to elucidate individual behavioral processes in Antarctic krill (*Euphausia superba*) on short time scales and fine spatial scales. The Bickley jet (planar free jet) is employed in a recirculating flume system to replicate ecologically-relevant thin shear ($Re_j \sim 100$) and phytoplankton (1000 cells/mL *Tetraselamis spp.*) layers for krill behavioral assays. Planar laser-induced fluorescence (LIF) and particle image velocimetry (PIV) measurements quantify the spatiotemporal structure of the phytoplankton and free shear layers, respectively, allowing for quantitative correlation of krill behavioral processes with coincident sensory cues. Analyses of digitized trajectories reveal a behavioral shear strain rate threshold of 0.02 s^{-1} that is seen to significantly influence behavior through changes in path kinematics. Decomposition of krill motion into translational and rotational components reveals statistically trending increases in the rotational component of motion after contacting both the free shear and phytoplankton layers. From a more macroscopic perspective, we observed a statistically trending increase in time spent in the vicinity of the free shear layer and significant increases in the time spent both within and in the vicinity of the phytoplankton layer. Finally, significant differences in distributions of body angle between all treatments indicate preferential orientations in the presence of hydrodynamic and chemical cues. We propose that thin layers, as regions of enhanced

productivity with distinct fluid mechanical and biochemical signatures, may be fundamentally important for krill populations seeking to aggregate or maximize foraging success.

5.2 Introduction

As direct consumers of primary producers and crucial prey for a variety of larger species, such as whales, seals, sea birds and squid, Antarctic krill (*Euphausia superba*) are a vital trophic link in the Southern Ocean food web (Everson 2000). They are also the subjects of a valuable commercial fishery (Nicol and Endo 1999) and are the focus of a significant body of literature (Siegel 2005). And yet, there are still significant holes in our basic understanding of krill ecology, particularly with respect to behavioral processes on short time scales and fine spatial scales (Nicol and Brierley 2010). It is reasonable to expect that finescale hydrodynamic and chemical cues commonly associated with thin planktonic layers (e.g., Dekshenieks et al. 2001) may be an integral component of krill ecology and could help explain higher frequency variability in population dynamics.

Patchiness of Antarctic krill populations is fundamentally linked to schooling dynamics and has long been recognized at a variety of scales (Murphy et al. 1998), though it was historically attributed to meso- and ocean scale circulation patterns (e.g. Fach et al. 2002; Hofmann and Murphy 2004). While this fundamental forcing mechanism can explain distributions and abundances on the subdecadal, ocean basin scale, it is clear that individual behavior that maximizes foraging success while minimizing predation risk (Daly and Macaulay 1991; Trathan et al. 1993; Cresswell et al. 2009) produces higher frequency variability and is necessary for life success.

Various mechanisms affecting patchiness of krill populations have been documented. Patches of algae induced changes in swimming behavior and increased population densities for the krill *Thysanoessa raschii* (Price 1989). Further, small-scale

shear associated with turbulent boundary layer flows was seen to generate aggregations of Pacific krill *Euphausia pacifica* (Ianson et al. 2011). Zhou and Dorland (2004) found a close correlation between the horizontal scale of Antarctic krill aggregations and that of local shear, with the relative magnitudes of current and swimming speeds being an important indicator of aggregation dynamics. Consistently, Nicol and Brierley (2010) show a close association between krill aggregations and local hydrography and have stressed the need for understanding aggregation dynamics on very small space and time scales. Individual behavioral processes on short time scales (and thus fine spatial scales) and behavioral flexibility are fundamental for optimizing foraging needs. In this note, Cresswell et al. (2007, 2009) predicted enhanced, patchy krill concentrations at the shelf break due to reduced swimming speeds and increased turn frequencies that cause krill to remain in these favorable zones, producing a distinct diel, cyclic pattern in population density.

One of the most ubiquitous mechanisms of patchiness and enhanced productivity in virtually all marine environments is thin layers (McManus et al. 2003). These spatially coherent plankton patches (marine snow, bacteria, phytoplankton, zooplankton, icthyoplankton) contain biomass that can be several orders of magnitude greater than the water column immediately above or below the layer, range in thickness from a few centimeters to a few meters vertically, span up to square kilometers horizontally, and can persist for days. Thin layers most often occur in stably-stratified waters and coincide with vertical gradients of physical and biochemical properties in the water column (Dekshenieks et al. 2001). The dense aggregation of biomass in thin layers acts as a biophysical coupling mechanism linking fine scale ($< 1\ m$) individual behavioral processes and submesoscale (10s to 100s m) processes underlying fishery productivity. Individual krill exploiting the highly concentrated, coincident sensory information contained in thin layers may be able to maximize foraging success, as many other plankters have been observed to do (e.g. Woodson et al. 2005, 2007;

Benoit-Bird et al. 2009). However, studies that link biological (growth, predation, cue sensing, foraging) and physical (thermocline and pycnocline dynamics, internal waves, vertical shear, turbulent mixing) processes in Antarctic krill at the correct and coincident spatial and temporal scales are largely lacking, as discussed by Nicol and Brierley (2010), although some are beginning to fill in these gaps (e.g. Wiebe et al. 2011). Further, there is a lack of laboratory studies that can extrapolate the ecological implications of thin layer phenomena to krill behavior and ecology.

There is compelling evidence that thin layers may be another mechanism that produces patchiness in krill populations and also may serve as marine oases that are critical for life success. Highly homogeneous and structured krill schools contrast sharply to well-mixed heterogeneous superswarms and layers (Watkins and Murray 1998), which often co-occur with hydrographic structure in the water column (Nicol and Brierley 2010 and/or in highly stratified waters (Wiebe et al. 2011). It seems likely that in the absence of some sensory stimulus or cue above a certain threshold (e.g. persistent shear structure or dissolved biochemicals), krill default to active-advection in mesoscale currents in highly homogeneous, well-structured schools in order to reap the associated fitness benefits (Grunbaum 1998): reduced predation rates (Burgess and Shaw 1979), increased foraging success (Baird et al. 1991, Foster et al. 2001) and reduced energy expenditures (Hamner and Parrish 1997, Ritz 2000). However, when presented with a sensory cue above some behavioral threshold it becomes advantageous to break formation and engage in area-restricted search behavior in order to locate and exploit resource patches. Given the fundamental importance of individual behavioral processes on short timescales and fine spatial scales, it is surprising that they remain remain relatively unquantified for this keystone species (e.g. Cresswell et al. 2009; Nicol and Brierley 2010). In the present study, we seek to quantify the behavioral response of *E. superba* to finescale hydrodynamic and chemical cues commonly associated with thin layers. We expect that the Antarctic krill will

aggregate about thin layer structure, as other zooplankton are known to do. Changes in individual krill behavior in response to ecologically-relevant sensory cues have the potential to produce population-scale phenomena, significantly affecting population dynamics with profound trophic implications in the Southern Ocean.

5.3 Methods

5.3.1 Thin Layer Flume and Layer Characterization

5.3.1.1 Planar Free Jet Layer

A planar free jet (the Bickley jet) was employed in a recirculating flume system to replicate ecologically-relevant thin shear layer for krill behavioral assays (Figure 5.1, left panel). The main flume (3 m x 50 cm x 50 cm) is constructed of clear acrylic (1.905 cm thick) for optical access. An elevated constant head tank (28 L, US Plastics) with a free surface overflow drives flow through a rotameter (Dwyer Instruments) that then passes through a slot jet nozzle (316 SS, jet opening 2.5 cm x 50 cm) to create a planar free jet in the main test section. A 12:1 area ratio contraction was employed with a 5^{th}-order polynomial shape to prevent flow separation and to minimize turbulent fluctuations in the upstream section. Stainless steel mesh (50% open area) and a layer of high porosity polypropylene sponge inside the main body of the nozzle further dampen turbulent fluctuations and create a uniform flow distribution across the width of the nozzle opening. These design features ensure a uniform (top-hat) velocity profile at the nozzle exit. The flow in the main test section passes through an acrylic flow conditioner to minimize recirculation, flow instability, and exit geometry effects. Finally, the flow passes a free surface overflow into the bottom reservoir (28 L, US Plastics) where it is pumped through a 4 diaphragm, positive displacement pump (JABSCO Model 31801-1305) to the constant head tank. In the test section, a coordinate system is defined such that x is the streamwise coordinate (as determined by the shear layer flow), z is the vertical coordinate (gradient direction), and y is the

transverse coordinate (i.e., across the flume).

Free shear flows were characterized with a planar particle image velocimetry (PIV) system. PIV is a non-intrusive flow characterization technique in which the flow of interest is seeded with neutrally-buoyant particles and illuminated with a sheet (in the planar case) of laser light. A series of images of the light scattered from seeding particles is post-processed to compute particle displacement fields between successive frames (e.g. Raffel et al. 1998). Here, a planar light sheet was created by sweeping a continuous-wave Argon ion laser (100 mW, 514 nm) beam (focused with a 1 m focal length spherical lens) through the observation region via a scanning mirror (Figure 5.1, right panel). The flow was seeded with 20 μm diameter hollow glass spherical particles to provide a strong light scattering signal in the imaging region (30 cm x 30 cm). A laptop PC running LabVIEW (National Instruments) was used to create and synchronize the analog voltage signal controlling the scanning mirror and the digital trigger to the camera through a USB-based DAQ module (National Instruments). The beam was swept through the observation region one time per camera (PCO-TECH Inc., pco.Edge, scientific CMOS, 5.5 MP, 16-bit, global shutter) exposure with images being recorded directly to the hard drive of a PC (64 Bit, Windows 7) running image acquisition software (CamWare64). Image sequences were acquired at 10 Hz for a period of one minute. All PIV analysis was performed using DaVis 8.1.6 software (LaVision Inc.). Images sequences were first postprocessed to enhance particle contrast and overall signal strength. Each image was then divided into 32 pixel square interrogation subwindows and a two-dimensional spatial cross-correlation was performed in wavenumber space between successive images for each interrogation subwindow. Particle displacement between successive frames was estimated by the location of the cross-correlation peak. A Gaussian peak fit analysis is employed to determine the displacement vector in each interrogation window to subpixel accuracy. The displacement vectors are then divided by the time delay between laser sweeps

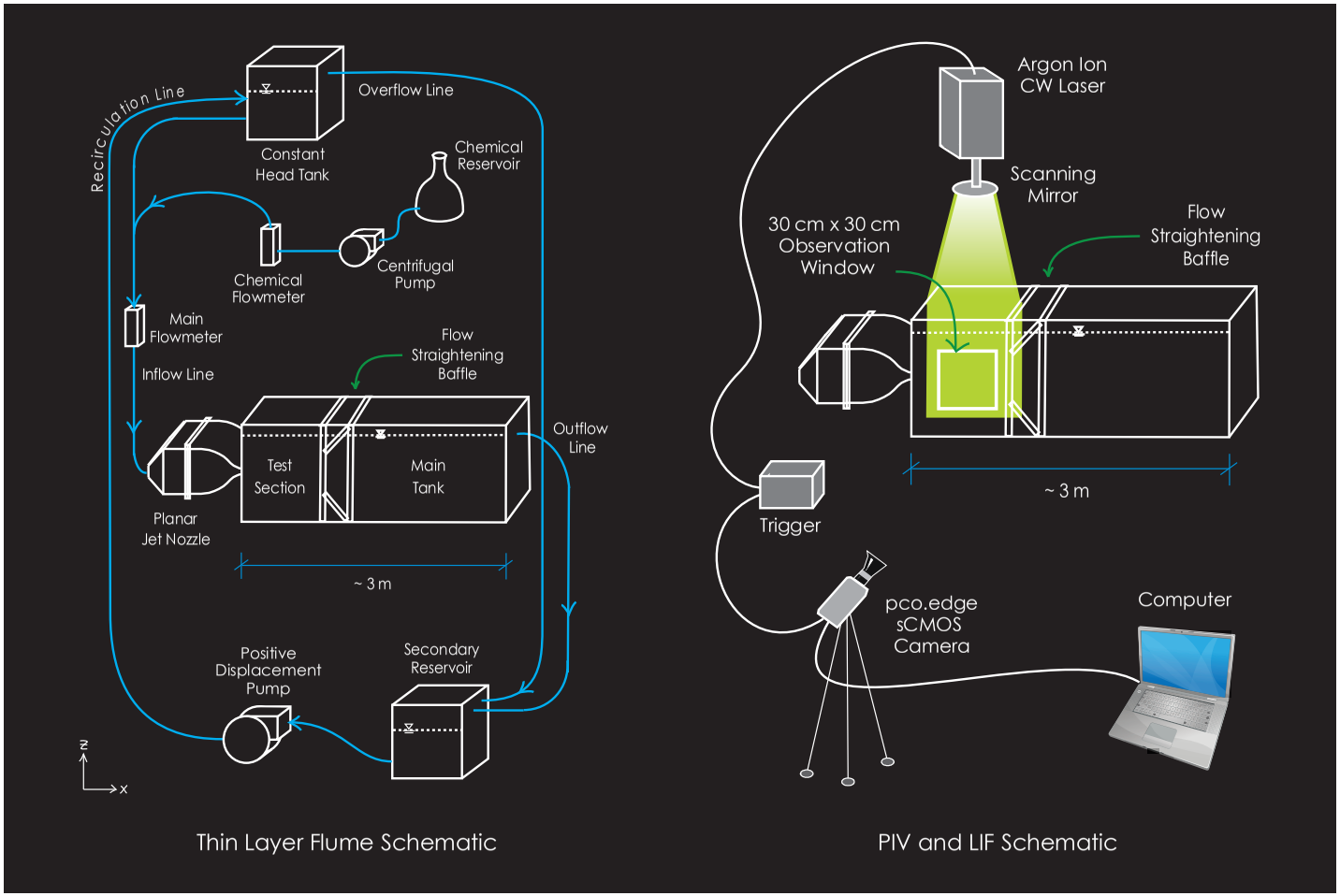

Figure 5.1: Experimental schematics for free jet and phytoplankton layer treatments (left panel) and for layer characterization via LIF and PIV (right panel).

(0.05 s) to produce the instantaneous two-dimensional velocity field, from which the shear strain rate field is computed (via central differences).

5.3.1.2 Phytoplankton Layer

Phytoplankton layer assays (1000 cells/mL *Tetraselmis spp.*) were conducted in the same flume and observation volume (Figure 5.1, left panel). A custom baffle at the downstream end of the observation volume was designed to create thin chemical layers via weak density stratification ($\Delta\rho \leq 0.25\ ppt$) and low shear intrusions.

The weak density stratification was necessary to overcome unavoidable shear instabilities present in free-shear flows and stabilize the chemical layer. First, the volume was filled to slightly below mid-depth with the lowest density (top layer) fluid. Next, the highest density (bottom layer) fluid was introduced via a slot located at the bottom of the tank. The tank was filled until the density interface between the top and bottom layers rested at the bottom edge of another slot located just below mid-depth in the tank. Finally, the chemical layer containing 1000 *cells/mL Tetraselmis spp.* was introduced via the slot located at mid-depth. The chemical flow continued until a 10 cm thick phytoplankton layer was created, centered in the observation window, at which point flow was stopped and the layer was allowed to stabilize for $\sim$ 30 minutes before the start of behavioral assays. The long-time scales associated with molecular diffusion ensure the steadiness of the layer structure over the course of the two hour behavioral assays. The flow of both the bottom and chemical layers was driven from elevated reservoirs at very low flow rates ($\sim$ 12 $L/2.5\ hr$) so as not to introduce any buoyancy effects (via pump heating) or turbulent mixing (via unsteady pressure fluctuations, flow separation, etc.) and to minimize shear-induced mixing along the density interfaces. A small amount of food coloring dye was added to the bottom and chemical layers ($\sim 2\ mL/10\ L$) in order to visualize the density interfaces.

Phytoplankton layers created using the methodologies described above were characterized with a planar laser-induced fluorescence (PLIF) system to ensure a steady, sharp-edged layer. PLIF is a non-invasive technique for measuring scalar concentration fields. The flow of interest is illuminated with a sheet of laser light (in the two dimensional or planar case), and a fluorescent dye (Rhodamine 6G) acting as a proxy for the scalar quantity is photoexcited to emit light of a longer wavelength. With proper system design and image post-processing techniques, the intensity of the fluoresced light is linearly proportional to the concentration field (Crimaldi 2008). Laser illumination is created in an identical manner as for the PIV system described above. The camera and timing control system are identical to the PIV system described above. An optical high-pass filter (Tiffen Orange 21) was used to isolate fluoresced light, ensuring the laser signal was not imaged. One minute image sequences were acquired at 5 Hz and postprocessed using DaVis 8.1.6 software (LaVision Inc.). A concentration-intensity calibration curve was generated by imaging the observation volume at known dye concentrations of 0 - 50 $\mu g/L$ (in 5 $\mu g/L$ increments). Additionally, a dark field image (with the lens cap on) was taken to correct for background camera noise. Crucially, the *exact* experimental configuration and settings (camera: lens, optical filter, position, f-stop, exposure time, frame rate; laser: power, sweep rate, geometry with respect to the imaging window) were used for both calibration and chemical layer imaging sequences. Postprocessing algorithms used here correct raw images for laser light attenuation with depth, laser light absorption, nonuniformities in light sheet intensity, and background camera noise and produce and analytical relationship between pixel intensity and scalar concentration. Note that during LIF experiments, a small amount of Rhodamine ($\sim$ 0.2 $\mu g/L$) was added to the top and bottom layers in order to provide a weak fluorescence signal and alleviate potential issues resulting from the finite dynamic range of the camera.

5.3.2 Behavioral Assays and Data Analysis

Euphausia superba were collected onboard the R.V. Laurence M. Gould in January 2012 ($64.98\,^{\circ}W - 64.48\,^{\circ}S$). A two-meter square frame net with a 700 mm mesh was towed obliquely from the surface to a depth of $\sim 120\ m$. Thirty krill were transferred to five, 4 L Nalgene bottles for transport to the Georgia Institute of Technology (Atlanta, Georgia, USA). Water temperature during transport was monitored via a data logger and did not exceed $2.7\,^{\circ}C$. Seven krill, ranging in length from $\sim 20\ mm$ to 43 mm (front edge of the eyeball to tip of telson), appeared healthy and active upon arrival. In Atlanta, krill were kept in well-oxygenated, 20 L buckets of artificial seawater (Instant Ocean, 35 *ppt*) in an environmental room at $0.1\,^{\circ}C$ and fed from a mixed diet of *Tetraselmis spp.* phytoplankton and brine shrimp (*Artemia salina*) nauplii.

Free-swimming krill trajectories were digitized under control (stagnant water), shear layer, and phytoplankton layer treatments. All behavioral assays were conducted in the same apparatus and under identical conditions as for the PIV (shear layer treatment) or LIF (*Tetraselmis spp.* layer treatment) layer characterizations. All experiments used artificial seawater (Instant Ocean) at *in situ* conditions, 35 ppt and $0.1\,^{\circ}C$. The same experimental group of seven adult, mixed-sex krill were exposed to each experimental treatment and recorded for one hour. In each case, krill were introduced to the tank and allowed to acclimate for one hour prior to the experiment. Using the threshold shear strain rate ($0.02\ s^{-1}$, see Results) and the vertical range of the phytoplankton layer (see Results), an "in-layer" region was defined as $-50\ mm \leq z \leq 50\ mm$. A 10 cm thick layer occupies 30 % of the observation window and is 2.5 times larger than the largest krill ($\sim 43\ mm$), making it unlikely that a krill could sense both edges of the layer simultaneously.

A pair of infrared (IR) fiber-coupled diodes (CVI Melles Griot, 57 PNL 054/P4/S, $>660\ nm$, 22 mW) were diffused via 50° circular, top hat diffusers (Thor Labs)

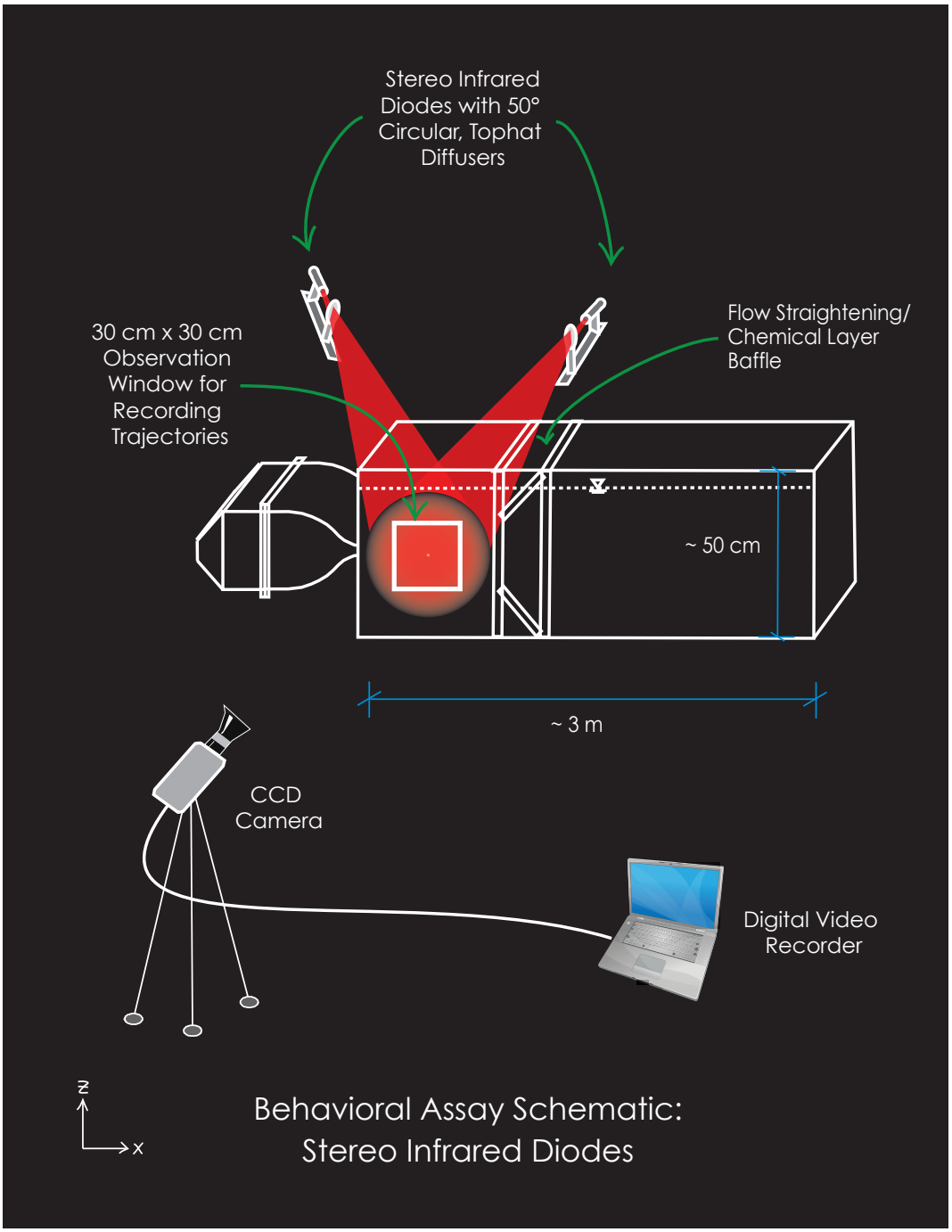

Figure 5.2: Experimental schematic for observation of krill behavioral assays. Illumination is provided by infrared diodes in stereo configuration.

providing backlit, illumination in stereo configuration (Figure 5.2). This method provides diffuse, effectively omni-directional illumination throughout the depth of the tank and eliminates potential photo-tactic effects. Two-dimensional krill trajectories in the x-z plane were recorded via a CCD video camera (Pulnix, 745i, 768 x 494 pixels) linked to a digital video recorder (Sony, mini dv tapes). All experiments were recorded at 30 frames per second (fps).

Mini dv tapes containing raw trajectory recordings were digitized as a series of uncompressed avi (Audio-Video Interleave) clips at 15 fps using iMovie HD (Apple Inc.). The reduction in temporal resolution is sufficient to resolve all krill swimming behaviors. For example, krill exhibited bouts of behavior with maximum swimming speeds of 150 mm/s. Hence, at a typical magnification of 0.8 $mm/pixel$, a swimming speed of 150 mm/s results in a displacement of 187.5 $pixels/s$. When considering an average krill body length of 30 mm (37.5 $pixels$), the corresponding displacement is 5 body lengths per second, or 1/3 body length per frame. Thus, 15 Hz is a sufficient temporal resolution to accurately resolve displacement of the body centroid for the maximum observed swimming speeds.

The head and tail points of free-swimming krill trajectories were digitized in the x-z plane using DLTdv5, a MATLAB-based digitization software (Hedrick 2008), and the "centroid" was located by interpolation. The resulting trajectory data sets (x_{head}, z_{head}, x_{tail}, z_{tail}, x_{cent}, z_{cent}, t) were analyzed using a suite of custom MATLAB codes.

Path kinematic parameters computed in this study are relative swimming speed (absolute velocity of krill's centroid - fluid velocity at centroid by spatial interpolation from the PIV data), turn frequency (where a turn is defined as a change of direction of the centroid heading of 15° or more), and the rotation-translation spectrum (RTS). The RTS is a measure of the relative translational and rotational components of the krill's motion, assuming rigid body motion. It is computed as the relative velocity of the head with respect to the tail divided by the maximum of either the head or tail

velocity:

$$RTS = \frac{|V_{head} - V_{tail}|}{max(V_{head}, V_{tail})} \tag{5.1}$$

RTS ranges from 0 - 2, with 0 corresponding to purely translational motion and the range of 1 - 2 corresponding to purely rotational motion about different centers of instantaneous rotation. These range from the head or tail (1) to the centroid (2). The RTS is a useful behavioral parameter to evaluate for krill because a complex morphology and propulsion system (drag-based propulsion through the metachronal beating of its pleopods) allows it to decouple its displacement vector (heading) from its body vector. In other words, there is potentially a non-zero angle of attack (difference between heading and body vector), and/or the krill is capable of manipulating the translational and rotational proportions of its motion. Note that the relative swimming speed and turn frequency relate to motion of the krill's centroid in x-z plane, i.e. the component of the krill's three-dimensional motion projected onto the plane of the camera (x-z plane). RTS and swimming mode analyses utilized a subset of trajectory data in which greater than 70% of the krill's motion was in the plane of the camera (i.e. the length of the body vector was $\geq$ 70% of the krill's total body length).

Gross trajectory parameters that provide measures of the net effect of changes in krill behavior on macroscale trajectory characteristics are: net-to-gross-displacement ratio ($NGDR$ = net displacement/gross displacement), proportional residence time (PRT = time spent in-layer/total time in observation window), and proportional vicinity time (PVT = time in observation window after contacting layer/total time in observation window).

Krill body angles with respect to the xy (BA_{xy}) and yz (BA_{yz}) planes were also

computed. BA_{xy} is defined as the angle between the body vector, originating at the tail and terminating at head, and the horizontal axis (line of constant z). BA_{yz} is defined as the angle between the body vector and the vertical axis (line of constant x). Both body angles range from $-90°$ to $+90°$, in which positive BA_{xy} indicates the head is above the tail and positive BA_{yz} indicates the head is facing downstream (positive x).

An analysis of krill swimming modes, as defined by Murphy et al. (2011), classified swimming behaviors as hovering (HOV), transition, or fast forward (FFW). These behavioral modes are defined by BA_{xy} and the normalized swimming speed (body length/s, BL/s) as follows: HOV - a normalized speed of <0.5 BL/s and BA_{xy} in the range of $25-50°$, transition - a normalized speed of 0.5 - 2 BL/s and BA_{xy} in the range of $10-50°$, and FFW - a normalized speed of >2 BL/s with no restriction on BA_{xy}. Using these behavioral classifications a time budget was generated to examine the percent of time spent in each swimming mode under various thin layer conditions.

A threshold shear strain rate value is defined to denote change in krill behavior by combining the shear strain rate data obtained using PIV and a careful point-by-point analysis of each krill trajectory in the velocity shear layer treatment. The benefit of completing analyses on individual paths and then ensemble averaging over the entire population is that it retains the variability of individual behavior while also revealing the population scale phenomena. The mean and standard deviation of all behavioral parameters are computed (for each trajectory) for portions of the trajectory above and below a given shear strain rate value based on the physical location of the krill head. The absolute value of the difference between these values is plotted as a function of the particular shear strain rate value giving a measure of the change in the mean behavior and also the variability of behavior as a result of exposure to the given shear strain rate value. This process is repeated for each shear strain rate value a krill encounters along its trajectory. The behavioral response curves for all krill are then

ensemble averaged (as a function shear strain rate) after being normalized by the maximum response value for that particular response curve. This procedure collapses all krill threshold curves for each behavioral parameter to a single plot.

5.3.3 Statistical Analyses

Throughout the course of a two-hour experiment, multiple trajectories of each krill were recorded. The four longest duration trajectories of each krill were extracted (as identified by differences in body length) and analyzed in a custom suite of MATLAB codes before being ensemble averaged to produce one average behavioral response data set per krill per treatment. A linear mixed model was run on the resulting data sets (JMP Pro software) in which the fixed effect was the treatment level (control, shear, phytoplankton) and the krill compose a randomized block effect; i.e., a repeated measures mixed model design. The restricted maximum likelihood (REML) analysis first uses a maximum likelihood estimation on a restricted likelihood function to estimate variance components using the random effect only (i.e. krill). The variance components are then used to estimate the significance of model fixed effects (treatment level). Post-hoc Tukey's Honest Significant Difference (HSD) tests were used to perform pairwise comparisons between treatments. Multiple comparisons of body angle histograms among treatments were conducted using the Wilcoxon Rank Sum Test after an initial Kruskal-Wallace test.

5.4 Results

5.4.1 Thin Layer Characterization

5.4.1.1 Velocity Shear Layer Treatment

A volumetric flowrate of 97.80 cm^3/s (1.55 gpm) was selected to produce a steady, transitionally-laminar flow field with 1 $^\circ C$, 35 ppt seawater. The result is a maximum jet exit velocity, U_j, of 7.7 mm/s and a jet Reynolds number($Re_j = U_j d/\nu$) of 107

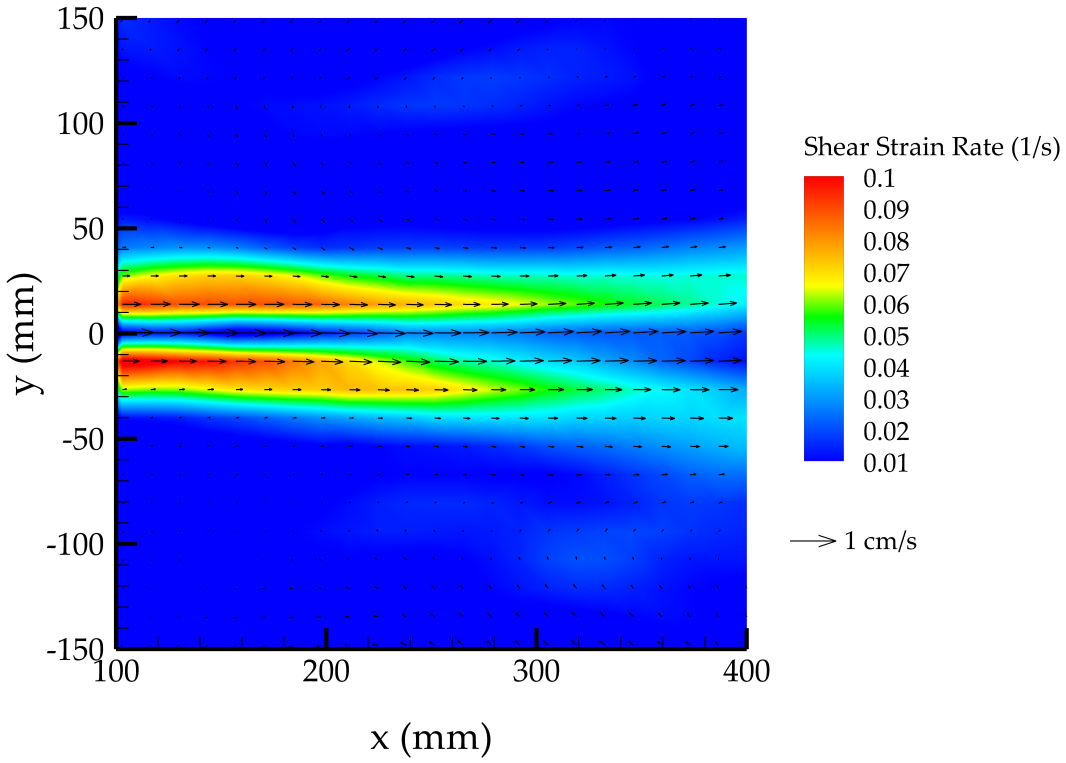

Figure 5.3: Time-averaged, planar PIV results in a planar free jet ($Re_j \sim 100$). Vectors indicate the fluid velocity, and contours indicate the fluid shear strain rate.

(Figure 5.3). The velocity and strain rate profiles vary continuously in the transverse directions producing ecologically-relevant velocity and shear strain rate fields throughout the experimental domain. As shown in Figure 5.3, the maximum shear strain rate varies from approximately 0.1 s^{-1} to 0.035 s^{-1} with distance downstream from the jet exit (i.e. between $x = 10$ cm and $x = 40$ cm) due to the entrainment of low velocity fluid and the gradual broadening of the velocity profile due to the transverse diffusion of momentum (Figure 5.3). The velocity along the jet centerline likewise varies from approximately 7 mm/s to 5 mm/s in the observation region (Figure 5.3).

Extracting velocity and shear strain rate profiles at various streamwise locations

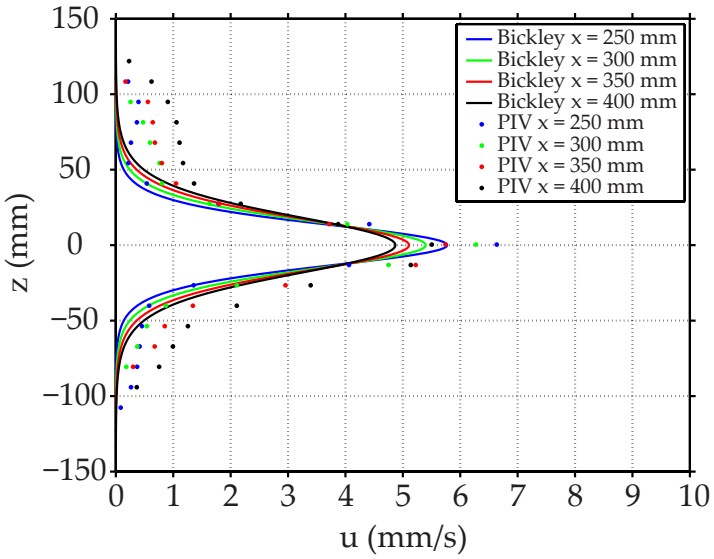

Figure 5.4: Comparison of analytical (Bickley) and experimental (PIV) velocity profiles in a planar free jet layer ($Re_j \sim 100$). The virtual origin correction has been applied, effectively shifting the analytical solution upstream by 100 mm.

allows for closer comparison of the experimental (PIV) and analytical (Bickley 1937) flow fields (Figures 5.4 and 5.5). Similarly, Figure 5.6 shows velocity profiles extracted from each x location collapsed onto the self-similar profile. When corrected for virtual origins effects, the data reveal very good agreement between the analytical and experimental flow fields near the jet centerline with departures further from the centerline throughout the observation region (see also Mehta and Bradshaw 1979, Hussein 1994, Woodson et al. 2005).

The analytical solution for the velocity field of a planar free jet as derived by Bickley (1937) is known to approach a self-similar solution in the far-field corresponding to the flow induced by a point source of momentum. However, the self-similar solution is singular near the jet origin and leads to discrepancies between experimental and analytical results in the far-field that are exacerbated with increasing jet Reynolds number, Re_j (Sato and Sakao 1964; Revuelta et al. 2002). The concept of a virtual origin was introduced in an effort to remedy the far-field discrepancies (Sato and

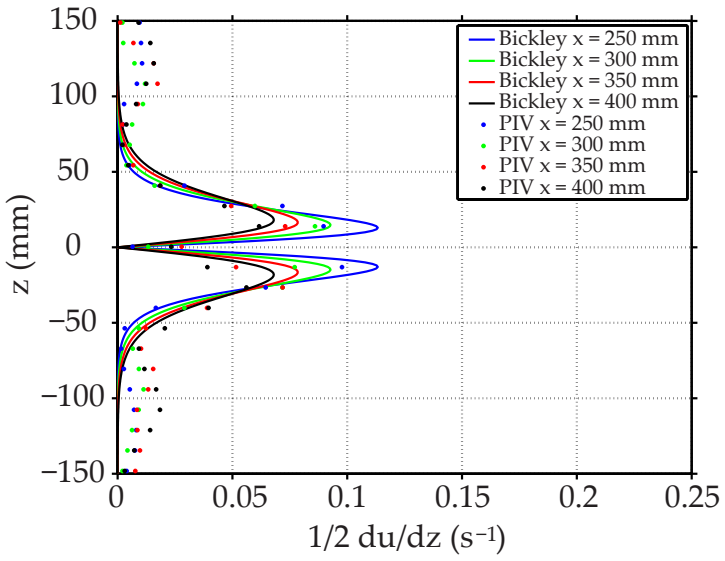

Figure 5.5: Comparison of analytical (Bickley) and experimental (PIV) shear strain rate profiles in a planar free jet layer ($Re_j \sim 100$). The virtual origin correction has been applied, effectively shifting the analytical solution upstream by 100 mm.

Sakao 1964) by accounting for the singular behavior of the self-similar solution near the jet origin. The virtual origin is the location where a point source of momentum would be located to produce the same jet characteristics as that originating from a nozzle of finite dimensions.

The location of the virtual origin can be found by plotting the streamwise variation in non-dimensional centerline velocities ($(U_j/U_o)^3$ versus x/D_j, Figure 5.7). Performing a linear least squares regression and extrapolating backwards to the x-intersect reveals the location of the virtual origin at x = -100 mm.

5.4.1.2 Phytoplankton Layer

Figure 5.8 presents the concentration field normalized by the layer source concentration, C_o, of 20 $\mu g/L$ (Rhodamine 6G). The resulting chemical layer features highly uniform concentrations above, below, and in the chemical layer, with a sharp gradient region $\leq$ 5 mm thick at the layer edge. Extracting vertical concentration profiles at various x locations (Figure 5.9) further verifies the uniformity of the concentration

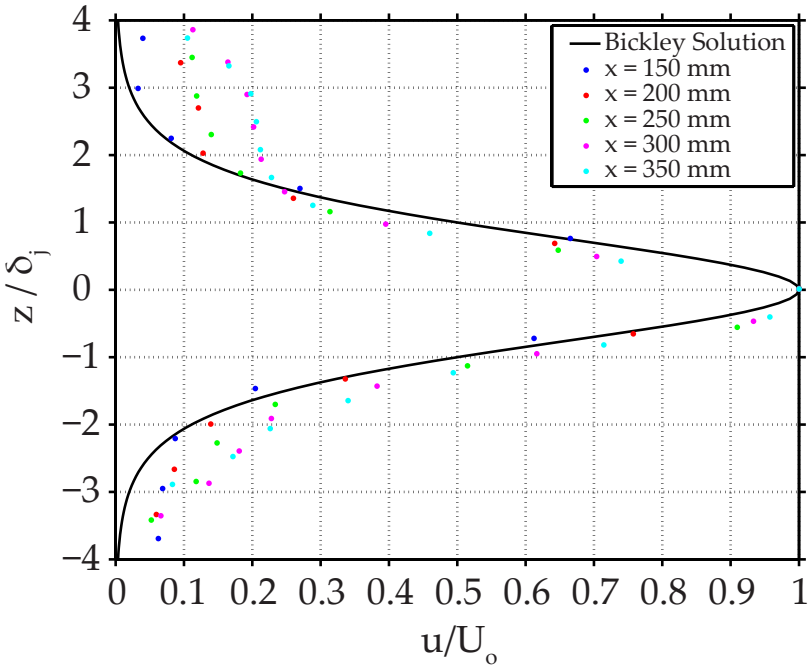

Figure 5.6: Comparison of analytical (Bickley) and experimental (PIV) self-similar velocity profiles in a planar free jet layer ($Re_j \sim 100$). The transverse coordinate is normalized by the jet half-width, δ_j, and the streamwise velocity, u, is normalized by the centerline velocity, U_o. The virtual origin correction has been applied, effectively shifting the analytical solution upstream by 100 mm.

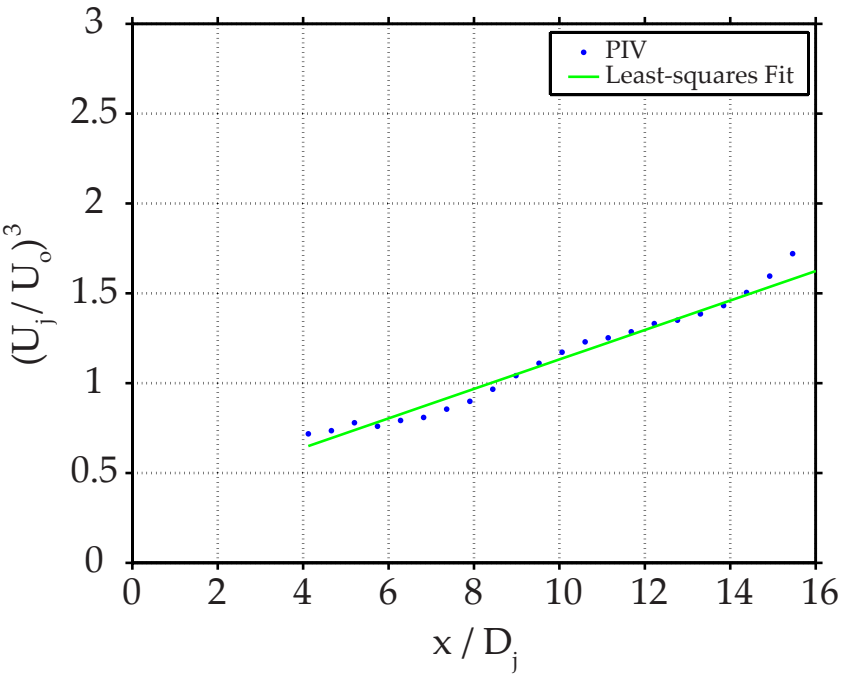

Figure 5.7: Streamwise variation in non-dimensional centerline velocities plotted to determine the virtual origin analysis of the jet.

field, the sharpness and symmetry of gradients at the edge of the chemical layer, and the top-hat concentration profiles.

5.4.2 Krill Shear Strain Rate Threshold

The shear strain rate threshold analysis based on the trajectories reveals a clear transition in behavior (Figures 5.10 and 5.11). The seven kinematics parameters collectively and consistently define the behavior transition threshold value, and the black dashed line is a spline fit to the average of all normalized response curves. Figure 5.11 reveals the threshold level identified in these analyses as 0.02 s^{-1}.

5.4.3 Path Kinematics and Gross Path Parameters

PRT and *PVT* significantly increase in the phytoplankton layer (Figure 5.12), Table 5.1). The slight increase in *PRT* and *PVT* for the velocity shear layer treatment is not statistically significant (Figure 5.12, Table 5.1), although the increase in *PVT*

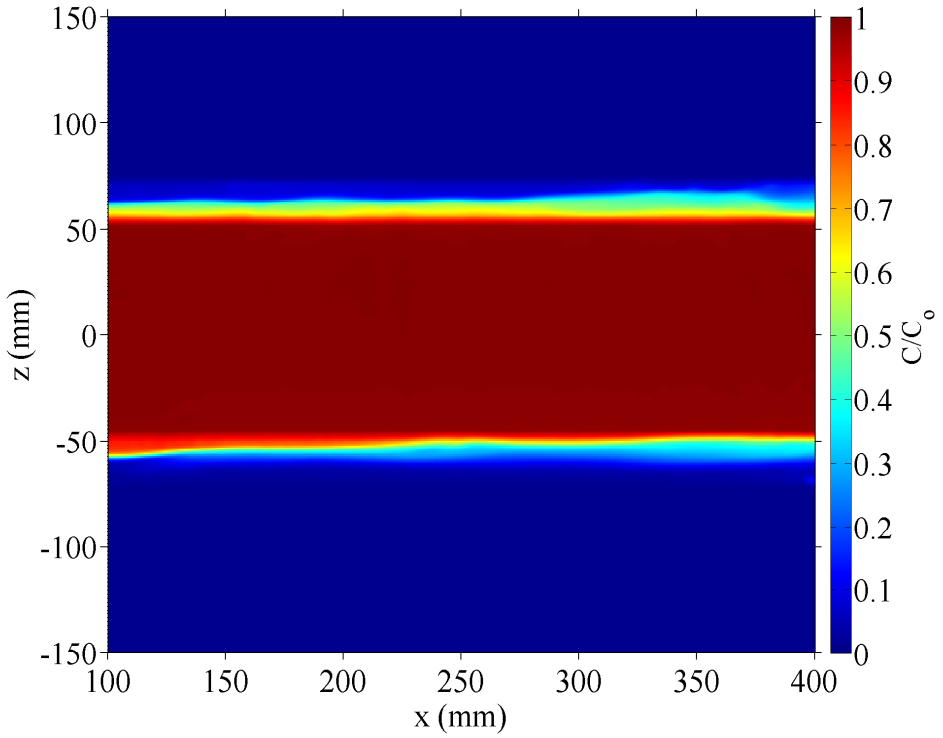

Figure 5.8: Concentration field (source-normalized) in a chemical layer.

is trending. Table 5.1 shows that there are no significant differences in average turn frequency, relative swimming speed, or RTS. Neither turn frequency nor relative swimming speed show any significant differences by location or exposure; however, changes in RTS show strongly trending increases postcontact with both the free shear and phytoplankton layers (Table 5.1). Finally, there were no significant changes in the overall diffusivity of trajectories ($NGDR$, Table 5.1).

Figure 5.13 shows the time budget including time spent hovering, in transition, and in fast forward swimming modes (Murphy et al. 2011) under control and thin layer treatments. Whereas there are subtle differences in the time budgets, the overall trend appears quite similar under control and treatments. Statistical analysis is consistent with no significant differences among the treatments (Table 5.2). Independent of control versus treatment, krill spend the greatest portion of time in the transition mode with time spent in the hovering and fast-forward swimming each corresponding

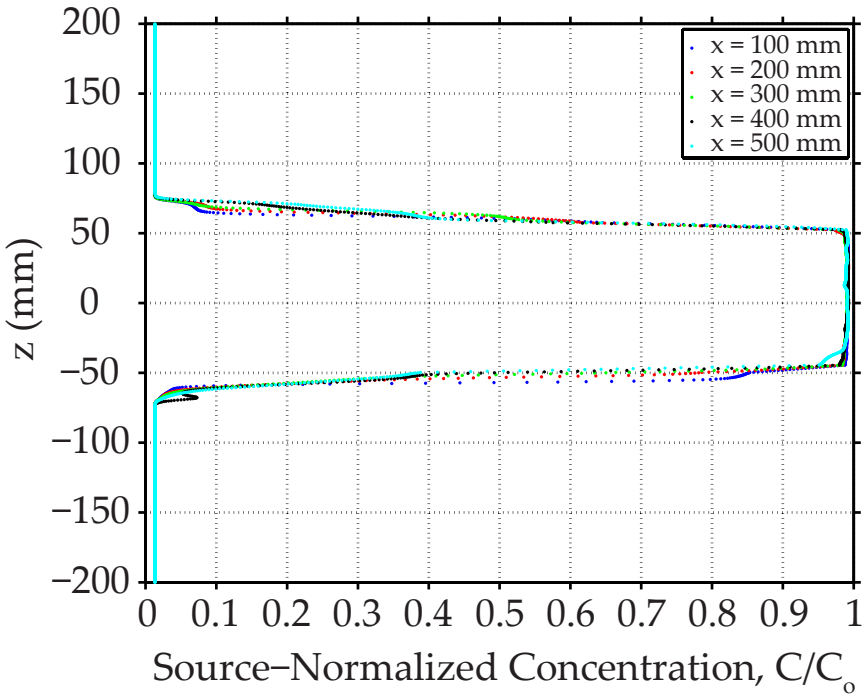

Figure 5.9: Vertical concentration profiles (source-normalized) extracted at various horizontal positions in a chemical layer.

to roughly half that in transition mode.

Figures 5.14 and 5.15 show body angle histograms. Distributions under all conditions reveal a strong preference for body orientations in which the head is above the tail (i.e., positive BA_{xy}). Interestingly, BA_{xy} distributions under shear and phytoplankton layers reveal shifting means in which krill are becoming more streamlined ($\downarrow BA_{xy}$) under shear layer conditions and more erect (vertical) under phytoplankton layer conditions ($\uparrow BA_{xy}$). BA_{xy} distributions under control and thin layer stimuli are all significantly different from each other via multiple comparisons (Wilcoxon Rank Sum Test, Table 5.3).

BA_{yz} distributions (Figure 5.15) reveal a fairly broad, uniform frequency distribution under control conditions. For the velocity shear layer treatment, the bimodal shear layer distribution reveals a preferential orientation of $25 - 30°$ (magnitude of BA_{yz}) with respect to the vertical and no strong preference for rheotactic behaviors

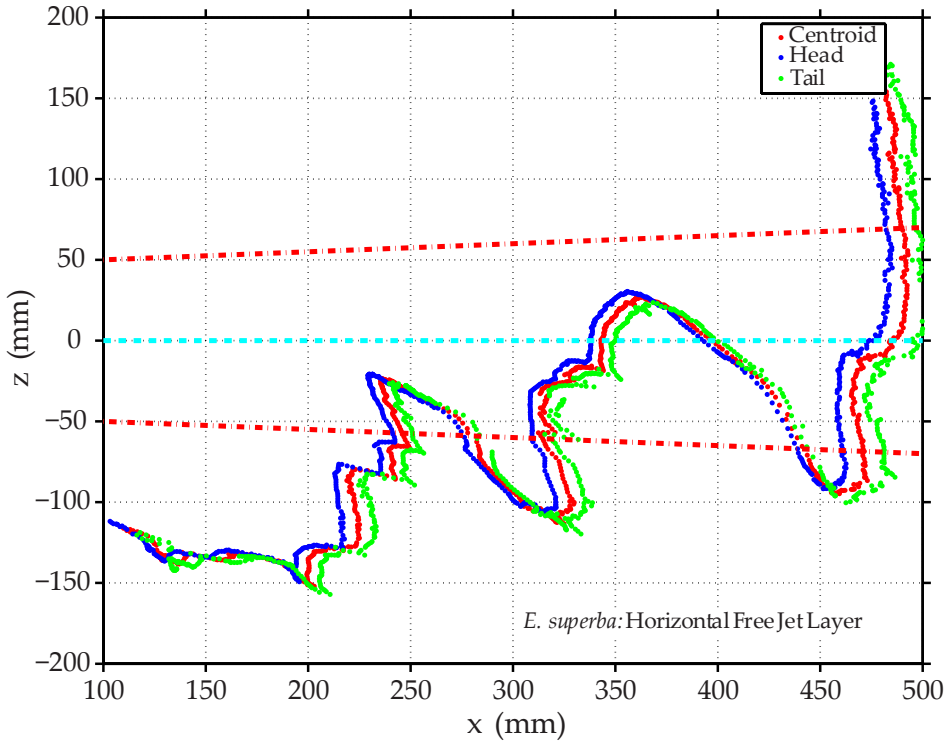

Figure 5.10: A sample krill trajectory in the velocity shear layer treatment showing the location of the head, tail, and centroid points digitized at 15 Hz. The jet centerline and edge location, based on a behavioral shear strain rate threshold of 0.02 s^{-1}, are indicated by blue and red dashed lines, respectively.

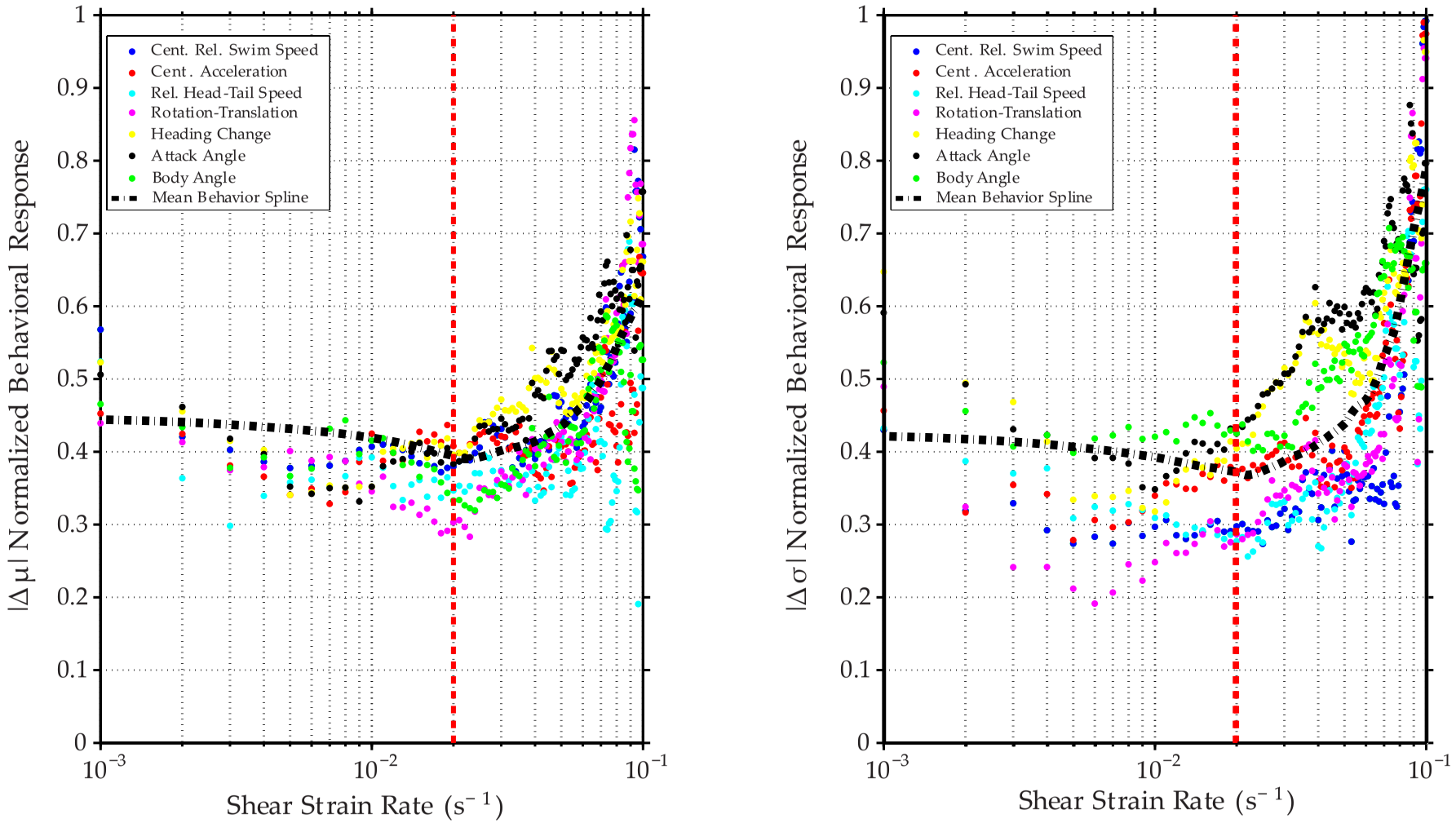

Figure 5.11: Krill shear strain rate threshold analysis. Left-panel: Normalized change in mean behavior. Right-panel: Normalized change in behavioral variability. The black dashed line is a spline curve fit to the average of all normalized response curves. The vertical red dashed line indicates the determined behaviorally-defined threshold shear strain rate value of 0.02 s^{-1}.

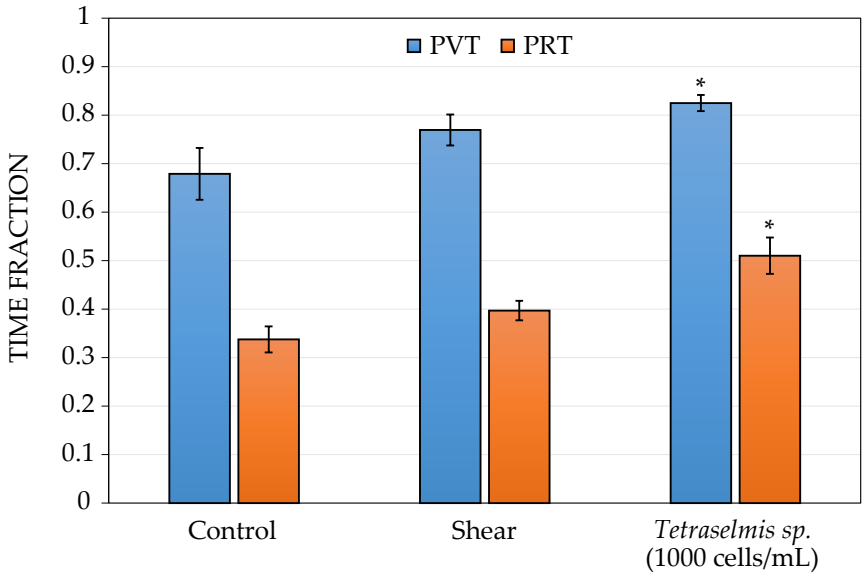

Figure 5.12: Proportional residence time (PRT) and proportional vicinity time (PVT) under control and thin layer treatments.

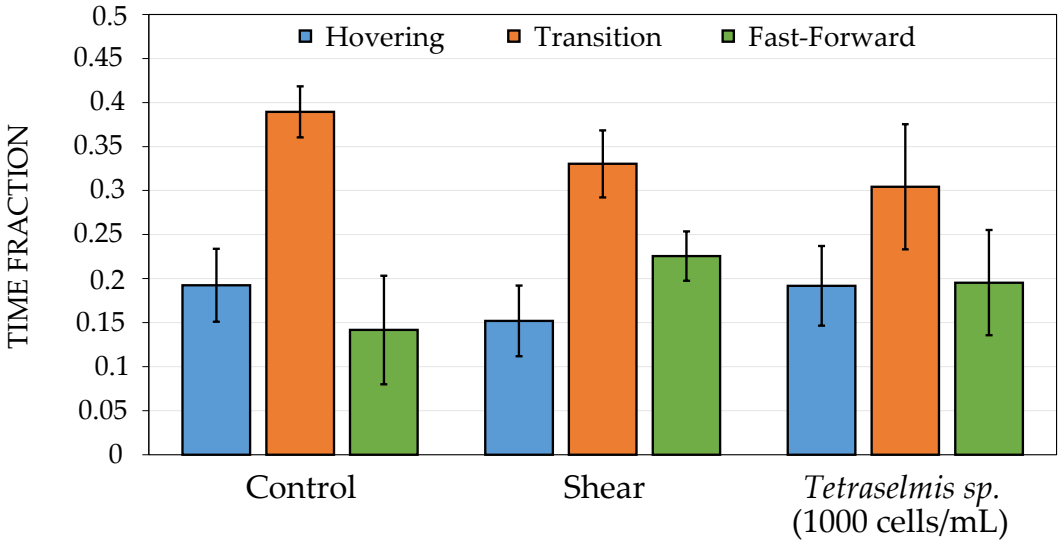

Figure 5.13: Fraction of time spent in various swimming modes as defined by Murphy et al. (2011). The time in unclassified swimming modes is not included, hence the total is not necessarily 100%.

(i.e. swimming against the flow by orienting upstream). There is a slight preference for alignment in the flow direction (i.e., peak for positive BA_{yz} mode). The addition of the phytoplankton ultimately focuses the broad control and the bimodal shear distributions into a unimodal distribution with a strong preference for orientations of $\sim 5^{\circ}$ with respect to the vertical. Distributions of BA_{yz} under control and thin layer stimuli are all significantly different from each other via multiple comparisons (Wilcoxon Rank Sum Test, Table 5.3).

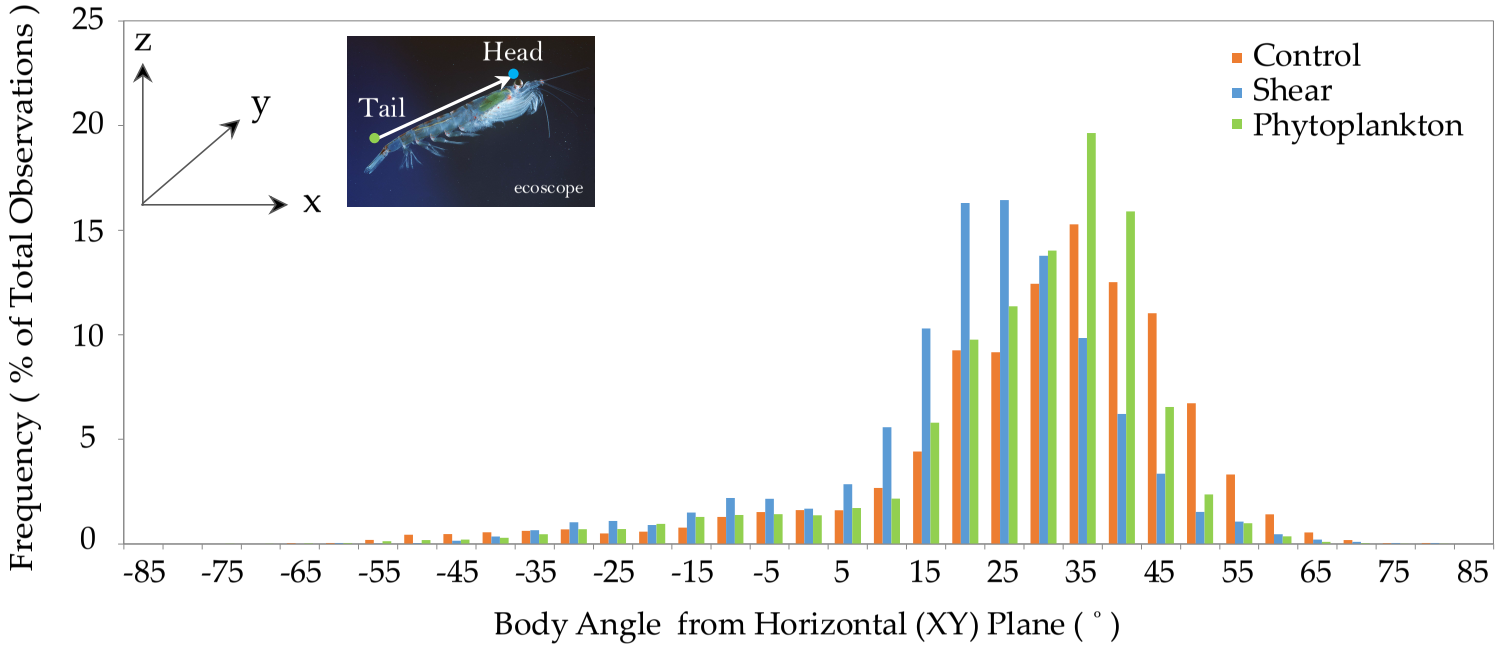

Figure 5.14: Frequency distribution of BA_{xy} under control and thin layer treatments. Body angle, BA_{xy}, is defined as the angle between the body vector, originating at the tail and terminating at head, and the horizontal (lines of constant z). Head above tail is defined as positive, and tail above head is defined as negative.

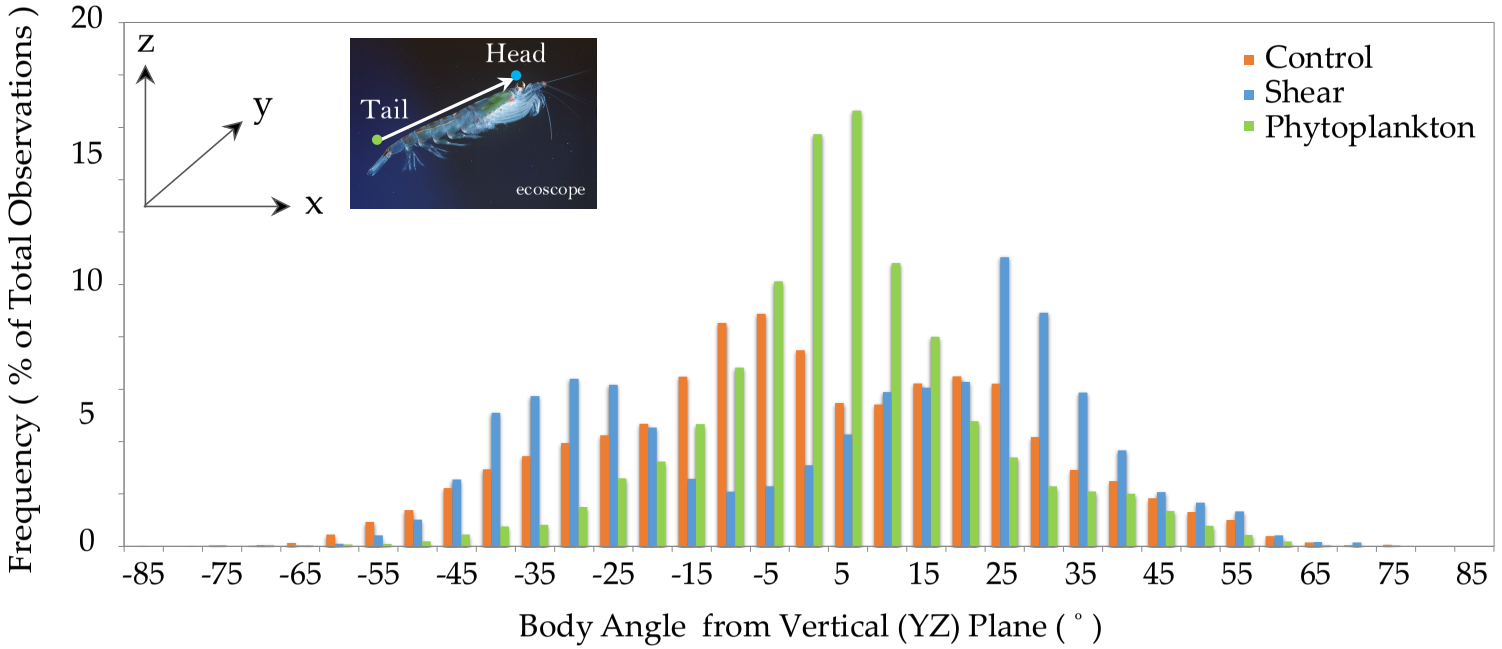

Figure 5.15: Frequency distribution of BA_{yz} under control and thin layer treatments. Body angle, BA_{yz}, is defined as the angle between the body vector, originating at the tail and terminating at head, and the vertical (lines of constant x). Facing downstream is defined as positive, upstream is defined as negative.

Table 5.1: Summary of restricted maximum likelihood (REML) analysis: Gross trajectory characteristics and average path kinematics. TF indicates turn frequency and RTS indicates rotation-translation spectrum. "RTS Post - Pre" indicates the difference between the post-contact (with the layer) value and the pre-contact value.

	Mean (SE)	**F-value**	**Layer Effect p-value**	**Tukey p-value (vs. Control)**
PRT				
Control	0.337 (0.027)			
Shear	0.397 (0.020)	4.0918	0.0046*	0.344
Phytoplankton	0.510 (0.037)			0.0038*
PVT				
Control	0.679 (0.053)			
Shear	0.769 (0.032)	4.8685	0.0283*	0.185
Phytoplankton	0.825 (0.017)			0.0233*
NGDR				
Control	0.764 (0.011)			
Shear	0.749 (0.021)	0.8197	0.4638	
Phytoplankton	0.702 (0.050)			
Average TF (turns/ind/s)				
Control	8.632 (0.374)			
Shear	8.047 (0.444)	0.6388	0.5449	
Phytoplankton	8.646 (0.479)			
Average Speed (mm/s)				
Control	33.469 (3.620)			
Shear	40.801 (5.332)	0.7851	0.4782	
Phytoplankton	37.781 (4.243)			
Average RTS				
Control	0.665 (0.026)			
Shear	0.068 (0.042)	1.2199	0.3294	
Phytoplankton	0.738 (0.047)			
RTS Post - Pre				
Control	0.058 (0.068)			
Shear	0.302 (0.101)	3.865	0.05*	0.0672**
Phytoplankton	0.283 (0.051)			0.0936**

Table 5.2: Summary of restricted maximum likelihood (REML) analysis: Fraction of time spent in each swimming mode. FFS indicates fast-forward swimming.

	Mean (SE)	**F-value**	**Layer Effect p-value**
Hovering			
Control	0.192 (0.041)		
Shear	0.152 (0.029)	0.6612	0.534
Phytoplankton	0.192 (0.062)		
Transition			
Control	0.389 (0.040)		
Shear	0.33 (0.038)	1.3729	0.2905
Phytoplankton	0.304 (0.028)		
FFS			
Control	0.142 (0.045)		
Shear	0.226 (0.071)	0.913	0.4275
Phytoplankton	0.195 (0.060)		

Table 5.3: Summary of Wilcoxon Rank Sum Test analysis: Multiple comparisons of body angle frequency distributions in xy and yz planes. Z is the standardized test statistic, which has an asymptotic standard normal deviation under the null hypothesis.

	Z	**p-value**
BA_{xy}		
Shear to Control	-42.316	< 0.0001*
Phytoplankton to Control	-15.3404	< 0.0001*
Phytoplankton to Shear	37.9579	< 0.0001*
BA_{yz}		
Shear to Control	12.4145	< 0.0001*
Phytoplankton to Control	15.0895	< 0.0001*
Phytoplankton to Shear	-8.8815	< 0.0001*

5.5 Discussion

5.5.1 Behavioral Response to Thin Layer Cues

Antarctic krill are highly competent, highly sensitive creatures with well-developed chemo- and mechano-sensory apparati. They are constantly sampling their local environments and exhibiting behavioral responses that have profound effects on their distributions and ultimately their abundances. Recent studies point towards thin layers as an important and fundamental factor influencing krill aggregation dynamics. Recall, thin layers are regions of enhanced productivity with distinct hydrodynamic and biochemical signatures that often co-occur with hydrographic structure (stably-stratified pycno-/thermocline, high shear, etc.) in the water column (e.g. Durham and Stocker 2012). Nicol and Brierley (2010) correlate the scale of patchiness in a krill aggregation directly to vertical shear, and Wiebe et al. (2011) report that maximum krill densities were consistently "related to features of the hydrographic structure of the water column" (i.e. a strong pycnocline). The data herein support these observations and for the first time quantify a behavior threshold value for shear strain rate of 0.02 s^{-1} (Figure 5.11). Further, significant changes in PRT and PVT (Table 5.1) observed here in response to chemical cues commonly associated with thin layers yielded distinct increases in the amount of time spent in the layer and also in the vicinity of the layer (Figure 5.12).

The findings here and the literature strongly imply that thin layers are an important factor influencing the patchiness of krill aggregations *in situ*. Zhou and Dorland (2004) showed an interesting vertical segregation of a nighttime, near-surface aggregation in which the upper part was swimming randomly at cruising speed and the lower part as a coherent school. Perhaps reduced predation risk from visual predators at night and the presence of a vertically-thin, high-resource patch (thin layer) made it beneficial to break formation and feed/forage while remaining in the proximity

of the school. Once satiated, individuals can quickly rejoin the school and state-dependent conspecific cues likely alert other krill to the presence of some nearby resource patch. Krill state and external stimuli influence pleopod beat frequency and amplitude (Johnson and Tarling 2008; Swadling et al. 2005). Thus hydrodynamic wake signatures (Catton et al. 2011; Murphy et al. 2013) could act as a feedback mechanism in which behavioral responses to finescale hydrodynamic and chemical cues influence swimming behaviors that in turn act as conspecific cues to other krill, alerting them to the presence of some resource/cue patch.

5.5.2 The Importance of Individual Behavioral Processes

Early experiments by Strand and Hamner (1990) evaluated the importance of various hydrodynamic, chemical, and visual cues in modifying schooling behaviors and often found effects that began as highly localized changes in individual behaviors that either propagated throughout the school or decayed locally. Similarly, field studies by Daly and Macaulay (1991) and Trathan et al. (1993) found that observed krill population distributions could not result simply as a function of physical forcing, stressing the importance of individual behaviors in influencing aggregation dynamics. Multiple studies have examined krill swimming behaviors under various hydrodynamic conditions such as varying current speeds (Swadling et al. 2005), small scale shear (*E. pacifica*, Ianson et al. 2011), and heterogeneous circulation fields (Zhou and Dorland 2004) and found in each case the importance of individual behaviors in modifying swimming behaviors and/or aggregation dynamics. The influence of individual krill state (sex, size, hunger level, stimuli, Swadling et al. 2005; Johnson and Tarling 2008) on swimming behaviors (pleopod beat rate, amplitude, etc.) and the corresponding changes in hydrodynamic wake signatures (Murphy et al. 2013) were found to be a viable conspecific cue for structuring krill aggregations (Catton et al. 2011) and elucidate yet another means by which individual behaviors form the basis of population

scale phenomena.

The important role of individual behavioral processes is clear. What remains unclear is the role of behavioral thresholds in response to finescale sensory cues that trigger changes in individual behaviors and the relative importance of various types of sensory cues in relation to one another (hydrodynamic, chemical, visual, etc.) in driving individual behavioral responses.

While Patria and Wiese (2004) established physiological thresholds for the northern Atlantic krill for detecting hydrodynamic perturbations, the authors are not aware of any studies that have quantified behavioral thresholds for any krill species. Various other studies have revealed the likelihood of behavioral sensitivity thresholds in hydrodynamic and chemical cues, but none have presented quantitative thresholds that trigger changes in individual behaviors. The highly localized changes in schooling behaviors induced by the presence of various sensory cues seen by Strand and Hamner (1990) indicate that behavioral response is triggered for only krill in the direct vicinity of the stimulus. Similarly, Hamner et al. (1983) found that presence of food exudates alone (not the cells themselves) was sufficient to trigger feeding behaviors, suggesting again that the chemical cue presented was strong enough to trigger a behavioral response. Establishing quantitative behavioral thresholds of relevant sensory cues (hydrodynamic, chemical, etc.) is of critical importance given the fundamental roles that mechano- and chemosensing play in predator/prey interactions, habitat partitioning, and schooling behaviors.

The behavioral shear strain rate threshold established here ($0.02\ s^{-1}$) is an important quantitative foundation for bio-physically coupled individual-based models (IBM) examining questions related to habitat partitioning, aggregations, and patchiness. Similarly, quantifying changes in path kinematics of individual krill in response to relevant, quantitative sensory cues is a substantial step towards understanding more fully the role of individual behavioral processes on fine spatial scales and short

time scales. Ultimately, this will shed light on the mechanisms by which changes in individual krill behavior influence aggregations around physical structure.

5.5.3 Energetics

The time budgets under ecologically-relevant conditions have important implications for krill energetics, swarm dynamics, and thus population dynamics. A schooling, foraging, or feeding Antarctic krill (away from sea ice) is likely to divide its time between hovering, fast-forward cruising, and the transitional mode between the two (Figure 5.13, Murphy et al. 2011). The data herein suggest that the percentage of time spent in each mode is similar among the control and thin layer treatments. As negatively buoyant nekton, a krill seeking to maintain station in the water column must constantly transfer downward momentum to the surrounding fluid in order to counteract body weight. Metachronal pleopod beating, optimal pleopod spacing, and the presence of lift-generating tip vortices on pleopod exopodites create efficient hovering behaviors (Alben et al. 2010; Murphy et al. 2013). Similarly, the generation of lift forces while cruising reduces the energy burden for maintaining depth in this swimming mode. Thus, it is likely that the transitional swimming mode between hovering and fast forward cruising is the most energetically expensive. However, it is a necessary cost for a foraging and/or feeding krill having to optimize the needs to sample/forage in large volumes via a more ballistic swimming mode (fast-forward) and to feed and/or incorporate sensory information more effectively while hovering in a localized volume. Even with an impressive suite of hydrodynamically efficient design features, krill are still faced with the prospect of spending up to 73 % of total daily metabolic expenditure on swimming behaviors (Swadling et al. 2005).

Findings here suggest a potential means by which krill can reduce energy expentures while still optimizing behavioral needs. The ability to manipulate the rotational and translational components of motion effectively decouples simple changes in path

(centroid) kinematics (speed, turn frequency) from changes in gross trajectory characteristics. For example, a mostly linear trajectory (high centroid $NGDR$) may actually feature a large rotational component such that the krill is able to effectively sweep/sample larger volumes without actually having to transverse a longer/more diffuse trajectory. Strongly trending increases in RTS postcontact with both the shear and phytoplankton layers (Table 5.1) indicate this could be an important means by which krill can reduce energy expenditures by exploiting the information contained in finescale hydrodynamic and chemical cues.

5.5.4 Body Orientation and Acoustic Biomass Estimates

Body angle distributions have been observed by various authors under stagnant water conditions (e.g. Kils 1981; Endo 1993; Miyashita et al. 1996) and the control distribution here is largely consistent with previous authors with a mean around 35°. Kils (1981) reported mean body angle of 45.3°, although with a slightly different definition of the body vector. In the velocity shear layer treatment, the distribution of BA_{xy} shifts to indicate a more streamlined body orientation aligned with flow perhaps to reduce drag (Figure 5.14). Conversely, in the phytoplankton layer treatment, the distribution of BA_{xy} shifts toward more vertical orientation, which seems likely to be related to feeding behaviors. For the phytoplankton layer, the distribution of BA_{yz} for the phytoplankton layer is consistent with a vertically-aligned preference.

The body angle also directly influences acoustic biomass estimates. Accurate and robust estimates of total krill biomass are fundamental to the sustainable management of the Southern Ocean fishery. The quantitative link between acoustic studies of krill populations and estimated biomass is the acoustic target strength (TS), the factor used to convert echo energy to abundances. TS is known to vary with body orientation (swimming angle) and body angle histograms have been generated for both Antarctic (Kils 1981; Endo 1993) and Pacific (Miyashita et al. 1996) krill with this end in mind.

The body angle histograms generated herein under hydrodynamic and biochemical conditions likely encountered *in situ* could lead to more accurate assessments of krill biomass when coupled with coincident hydrographic/biochemical data. Significant differences among body angle distributions under control, velocity shear layers, and phytoplankton layers (Figure 5.14, Table 5.3) should inform TS estimates that are specific to environmental conditions and yield more realistic estimates of krill biomass.

5.5.5 Free Shear Flows

Experimental centerline velocities are slightly greater and the overall velocity profile is broader with a distinct shoulder farther from the jet centerline compared to the analytical solution, likely associated with strong entrainment (Figure 5.4). This results in slightly reduced shear strain rate values when compared to analytical values and a smaller strain rate peak (Figure 5.5). These departures are likely due to an unaccounted for momentum sink (recirculation), exit geometry effects, and potential flow instability associated with intermediate Re_j effects. Linear stability analysis of the Bickley jet (Peacock et al. 2004) reveals two flow instability modes that manifest as velocity fluctuations that are symmetric and antisymmetric about the jet centerline, respectively. Both instability modes are sensitive to low frequency perturbations, but the symmetric mode is stable up to $Re_j \sim 100$ for most perturbation frequencies. Several experimental design measures were employed to dampen potential perturbations and the symmetry of flow fields produced here (Figures 5.4 and 5.5) implies that, if present, any flow instabilities are likely associated with the symmetric mode. These instabilities are transient and low frequency as revealed by the time-averaged flow field (Figure 5.3).

Importantly, it does not matter that we achieve a direct match to the theoretical flow field. What does matter, and has been confirmed by the PIV flow characterization, is that the flow field is steady, behaves dynamically similar to the theoretical

solution, and produces persistent and continuously-varying velocity and shear strain rate fields. All behavioral analyses make use of the experimental flow fields to compute relative swimming speed, shear strain rate thresholds, etc. and thus results are accurately quantify the sensory cues that krill experienced throughout the course of an assay.

CHAPTER VI

CONCLUSIONS AND CLOSING REMARKS

6.1 Conclusions

Finescale hydrodynamic and chemical cues commonly associated with thin layers and oceanographic fronts are fundamental in structuring nearshore ecosystems and act as highly patchy marine oases. Behavioral responses observed here by crustacean zooplankton with a variety of morphologies, ecologies, and life histories reveal that the sensory information and resources contained in finecale patches are fundamental to planktonic life success across a wide spectrum of ecological realities. From pelagic, vertically migrating copepods, to benthic, emerging mysids (True 2011), to schooling Antarctic krill, to dispersed crab larvae, all exhibit significant changes in behavior when presented with finescale hydrodynamic and/or chemical cues beyond behavioral thresholds. These thresholds trigger changes in behavior that allow zooplankton to exploit ephemeral resource patches, find mates, avoid predators, find suitable habitat, and escape potentially harmful environmental conditions.

In the first part of this study, we investigated how dispersed estuarine crab larvae can potentially optimize long term (habitat selection) and short term (foraging) behavioral needs by sensing and exploiting the information contained in multi-directional free shear flows, persistent hydrodynamic cues commonly associated with thin layers and oceanographic fronts. Analyses of digitized trajectories from free-swimming *Panopeus herbstii* (the Atlantic mud crab) megalopae established orientation-specific behavioral shear strain rate thresholds (0.04 s^{-1} upwelling flow, 0.07 s^{-1} downwelling flow, 0.1 s^{-1} horizontal flow) that are seen to significantly influence larval behavior through changes in path kinematics. Changes in path kinematic parameters

revealed a robust consistency of larval behavioral responses to all three laminar jet layer orientations, in layer versus out of layer as well as precontact versus postcontact. Relative swimming speeds were statistically smaller post-contact and out-of-layer and turn frequency was statistically larger out-of-layer. Differences in average path kinematics revealed an area-restricted search behavior in the vicinity of horizontal shear flows (swimming slower on average, swimming slower post-contact and out-of-layer, and greater turn frequency out-of-layer) and an excited area-restricted search behavior in the vicinity of both vertical shear flows (swimming faster on average, swimming slower post-contact and out-of-layer, and greater turn frequency out-of-layer), although not in the layers themselves. Significant reduction in the net-to-gross displacement ratio ($NGDR$) and the vertical-net-to-gross displacement ratio ($VNGDR$) with respect to control (stagnant) conditions indicate that larval trajectories become more sinuous and larvae enhance depth-keeping behaviors under all shear flow orientations. Collectively, these shear-induced behavioral responses are likely to produce megalopal aggregations in the vicinity of coherent shear flows, although there is explicit avoidance of both vertical layers themselves ($\downarrow$ proportional residence time). These responses are likely associated with foraging and sampling behaviors in which the coherent shear flow acts as a cue to restrict search volume in hopes of exploiting some coincident or nearby cue and/or resource patch that are typical in fronts and clines. The exploitation of sensory cues contained in finescale patches is likely an important means by which dispersed larvae can couple behavioral needs and processes operating on disparate time and space scales (i.e. foraging and finding suitable settlement habitat) and has important implications for structuring coastal marine ecosystems.

In the second part of this study, the sympatric *Acartia tonsa* and the allopatric *Temora longicornis* were exposed to thin layers of algal exudates from the toxic dinoflagellate *Karenia brevis* (equivalent cell concentration: 1 - 10,000 $cells/mL$). Both

copepod species display explicit avoidance of the toxic exudate layer and also the immediate vicinity of the layer. Measures of path kinematics (swimming speed, turn frequency) by location (in-layer versus out-of-layer) and exposure (pre-contact versus post-contact) reveal some similarities and also significant differences in behavioral response trends for the sympatric *A. tonsa* and the allopatric *T. longicornis*. *A. tonsa* significantly increases swimming speed and swimming speed variability in the exudate layer and post-contact, whereas *T. longicornis* slightly increases both in-layer and slightly reduces both post-contact. Both species increase turn frequency in-layer and post-contact with increasing *K. brevis* exudate concentration. These differences in path kinematic response trends produce differences in path fracticality ($F2D$ the two-dimensional path fractal dimension) in which *A. tonsa* trajectories likely become more diffuse and sinuous and *T. longicornis* trajectories likely become more linear and ballistic (trending effects). Regression analyses of mean swimming speed and swimming speed variability by location and exposure reveal that the rate of change of behavior with increasing *K. brevis* exudate concentration is significantly higher for *A. tonsa*, ranging from thrice to fifty times the rate of change of *T. longicornis*. Thus, the sympatric *A. tonsa* appears to possess an adapted awareness of the toxic *K. brevis*, which is lacking for the allopatric *T. longicornis*. Regardless of the differences in response strategies, both species avoid the toxic exudate layer and its vicinity suggesting that *K. brevis* can potentially eliminate top-down grazer control entirely, another sinister mechanism by which it gains a competitive advantage over the local phytoplankton taxa. The summation of all findings here corroborates some of what is known about the interactions of copepod grazers with HAB phytoplankton species but also offers critical new insight, particularly into behavioral interactions during the critical bloom incubation phase in subsurface thin layers. As trophic mediators linking primary producers and higher order consumers, copepods can significantly influence HAB dynamics and modulate large scale ecological effects through their

behavioral interactions with toxic blooms.

Finally, in the last part of this study, we investigated how finescale hydrodynamic and chemical cues commonly associated with thin planktonic layers affect individual behavioral processes in Antarctic krill (*Euphausia superba*) on short time scales and fine spatial scales. Analyses of digitized trajectories revealed a behavioral shear strain rate threshold of 0.02 s^{-1} that is seen to significantly influence krill behavior through changes in path kinematics. Decomposition of krill motion into translational and rotational components reveals statistically trending increases in the rotational component of motion after contacting both the free shear and phytoplankton layers, possibly an energetically-favorable way of sampling a larger volume without having to actually having to traverse a longer or more diffuse trajectory. We also observed a statistically trending increase in time spent in the vicinity of the free shear layer and significant increases in the time spent both within and in the vicinity of the phytoplankton layer, suggesting that finescale hydrodynamic and chemical cues could allow krill to hone in on resource patches with greater effectiveness. Finally, significant differences in distributions of body (swimming) angle between all treatments indicate preferential orientations in the presence of hydrodynamic and chemical cues. This could inform the use of acoustic target strength (TS) estimates which are specific to environmental conditions, thus improving krill biomass estimates when coupled with coincident hydrographic data. It is likely that thin layers (and/or frontal zones), as regions of enhanced productivity with distinct fluid mechanical and biochemical signatures, are fundamentally important for krill (and other obligate schoolers) populations seeking to maximize foraging success. Individual behavioral processes, in the context of obligate schooling behaviors and mesoscale circulation fields, likely explain much of the higher frequency variability in krill population dynamics.

6.2 Unique Contributions

The following are unique contributions of this study:

- Shown the ubiquity of behavioral shear strain rate thresholds as a fundamental influencer of individual behaviors in a variety of crustacean zooplankton species: an estuarine crab larvae (*P. herbstii*), 0.04/0.07/0.1 s^{-1}, Antarctic krill (*E. superba*), 0.02 s^{-1}, two tropical copepod species (*Acartia negligens* and *Clausocalanus furcatus*), 0.08 s^{-1} (True 2011), and an estaurine mysid (*Neomysis americana*), 0.065 s^{-1} (True 2011).

- Created and validated first laboratory model of thin layer conditions (hydrodynamic and chemical) for examining behavioral responses of larger zooplankton species, ichthyoplankton, and/or nekton.

- Established and quantified (PIV) steady (laminar to transitional), planar free shear flows at a variety of jet Reynold's numbers ($Re_j \sim 50 - 100$) and in multiple flow configurations (upwelling, downwelling, horizontal).

- Created and validated (LIF) the first laboratory model of a cryptic bloom, i.e. the subsurface incubation of a toxic phytoplankton bloom in a thin layer.

- Conducted the most extensive behavioral assays to date examining the behavioral interactions of copepod grazers and toxic phytoplankton, particularly in an ecologically-relevant scenario in which grazers have a choice of dosed and undosed waters.

- Elucidated the differences and similarities in behavioral response strategies for a sympatric (geographically co-occurring) and allopatric (geographically separate) copepod species in response to the toxic dinoflagellate *K. brevis*, providing important insights into potential future interactions in a changing seascape.

- Documented extreme avoidance of toxic algal exudate layers by copepod grazers, likely another mechanism by which toxic species gain an initial competitive advantage of local phytoplankton taxa and then proceed to monospecific domination to the detriment of the local ecosystem (and likely human population).

- Provided new insights into the potential role of foraging behaviors in selective tidal stream transport (STST) phenomena in *Panopeus herbstii* megalops: shear-induced depth-keeping behaviors in combination with area-restricted search behaviors.

- Provided evidence that Antarctic krill utilize finescale hydrodynamic and chemical cues associated with thin layers to hone in resource patches with greater effectiveness.

- Revealed an energetically-favorable behavior by which Antarctic krill can sweep/sample larger volumes by increasing the rotational component of motion.

- Revealed for the first time that Antarctic krill body angle histograms are significantly different under different environmental conditions, which could lead to condition-specific acoustic target strengths (TS) and thus improved biomass estimates.

- Provided significant quantitative information for ecosystem modelers examining the roles of individual plankton behaviors and physical forcing in producing spatiotemporal patchiness of productivity in marine ecosystems via biophysically coupled, individual-based models (IBM) by: the establishment of behavioral shear thresholds (a variety of species), the establishment of a sensory cue hierarchy quantifying the relative importance of different types of sensory cues (Antarctic krill), and behavioral response trends (regressions) for two copepod species in response to a common, toxic phytoplankton species.

6.3 Limitations and Challenges

One of the most prohibitive aspects of this study was the volume of data produced and the logistical challenges therein. Collecting raw (uncompressed) digital video of two hour behavioral assays, even at moderate frame rates (e.g. 15 Hz) and on a relatively low resolution camera (<1 MP), produces an exorbitant amount of data (as well as time required to digitize raw mini dv tapes). Then, of course, we are testing multiple species, under multiple conditions, and replicating experimental trials. Almost 10 TB of digital video data were generated throughout the course of this study, and that is without even having a backup of the raw data! Furthermore, many videos (all copepod assays) had to be digitally post processed to enhance contrast and increase signal-to-noise ratio (and thus digitization-ability) essentially multiplying the data volume. Transferring, post processing, and extracting the data contained in 10 TB of digital video creates incredible time, computational, and storage costs. Finally, another significant challenge here was the cost (money and time) associated with collecting, shipping, and caring for zooplankton used in these behavioral assays at Georgia Tech (Atlanta, Georgia). A vastly preferable scenario is to transport the experimental apparatus to coastal areas when possible where zooplankton are readily available.

6.4 Future Directions

Future studies and/or application of these findings may include:

- Development of a three-dimensional observation system to evaluate the potential importance of along-gradient (as opposed to purely across-gradient) behavioral processes.

- Application of a secondary, high-speed imaging system focusing on a smaller observation volume (e.g. the thin layer alone, the layer edge/gradient region, etc.)

to resolve higher frequency/smaller scale behavioral phenomena in important regions.

- Examination of trophic interactions in thin layer contexts; e.g. the interaction of copepods and ichthyoplankton in the presence of a thin algal layer.

- Application of simultaneous thin layer characterization (PIV and/or LIF) and behavioral assays to evaluate potential transient and/or unsteady phenomena.

- Evaluation of the influence of various internal waves processes on individual zooplankton behavior (Appendix C) through the use of simultaneous PIV and LIF.

- Application of the quantitative findings of this study to individual-based models (IBM) for these ecologically (and economically) important species, providing important tools for fisheries management.

APPENDIX A

HABS: SUPPLEMENTAL COPEPOD BEHAVIORAL RESPONSE SCATTERPLOTS

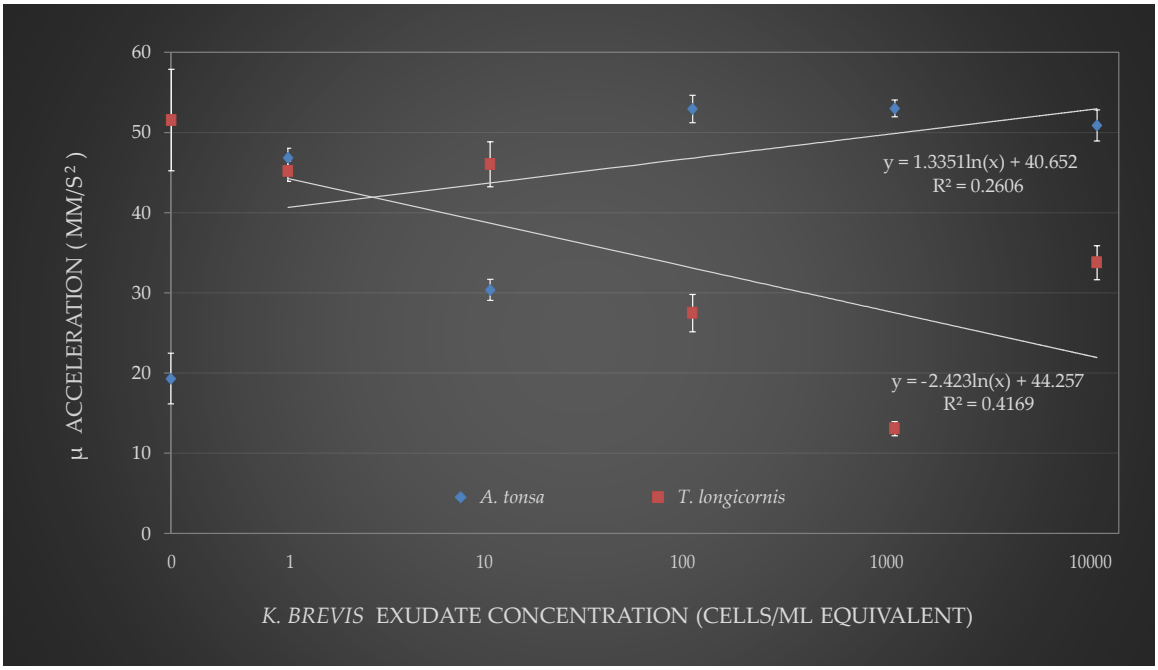

Figure A.1: Average Acceleration Under Various *K. brevis* Exudate Layer Concentrations. Linear regression lines using log-transformed concentration levels are displayed with corresponding fit equation and coefficient of determination.

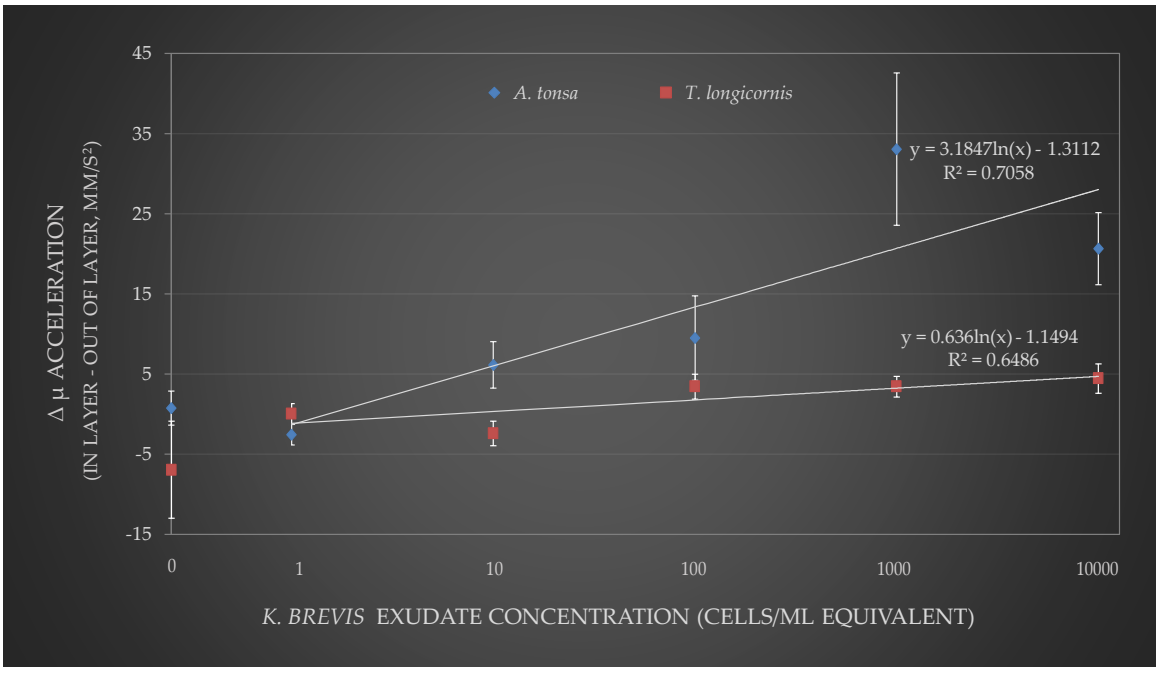

Figure A.2: Difference Between In Layer and Out of Layer Average Acceleration Under Various *K. brevis* Exudate Layer Concentrations. Linear regression lines using log-transformed concentration levels are displayed with corresponding fit equation and coefficient of determination.

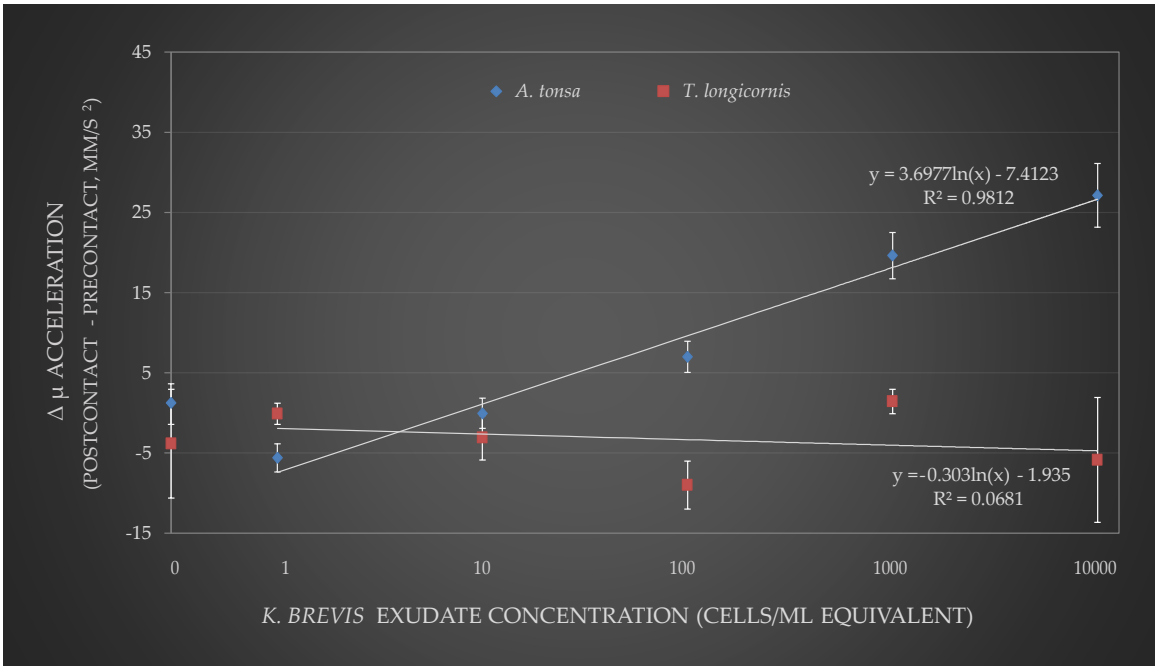

Figure A.3: Difference Between Precontact and Postcontact Average Acceleration Under Various *K. brevis* Exudate Layer Concentrations. Linear regression lines using log-transformed concentration levels are displayed with corresponding fit equation and coefficient of determination.

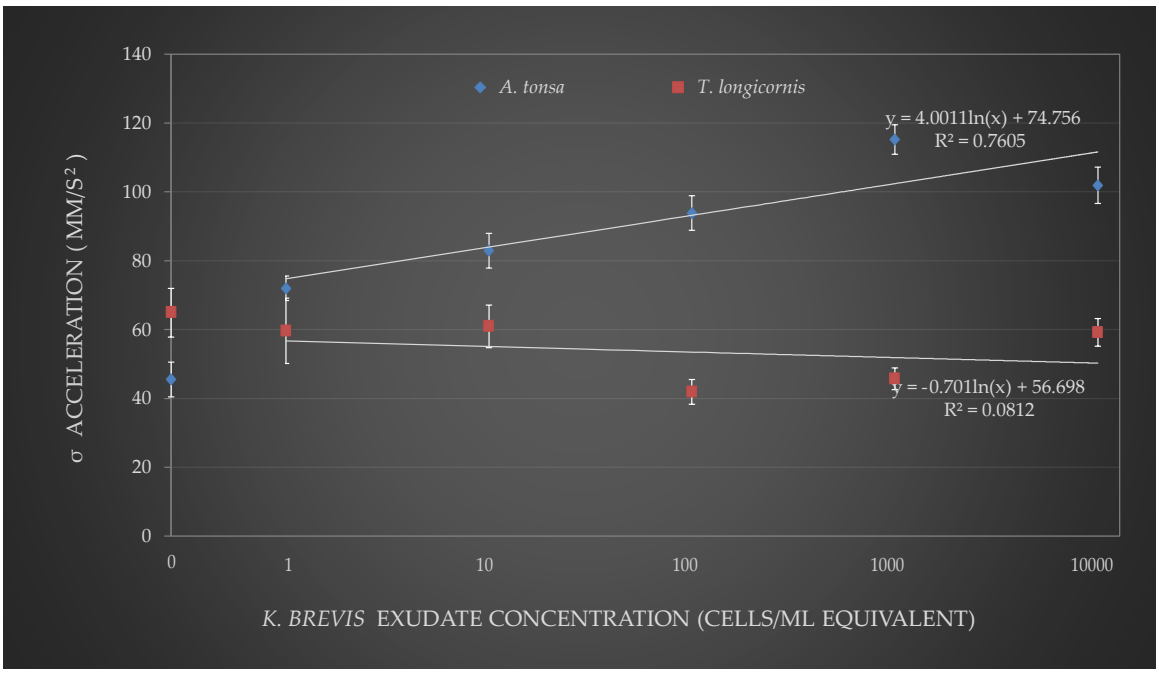

Figure A.4: Standard Deviation of Acceleration Under Various *K. brevis* Exudate Layer Concentrations. Linear regression lines using log-transformed concentration levels are displayed with corresponding fit equation and coefficient of determination.

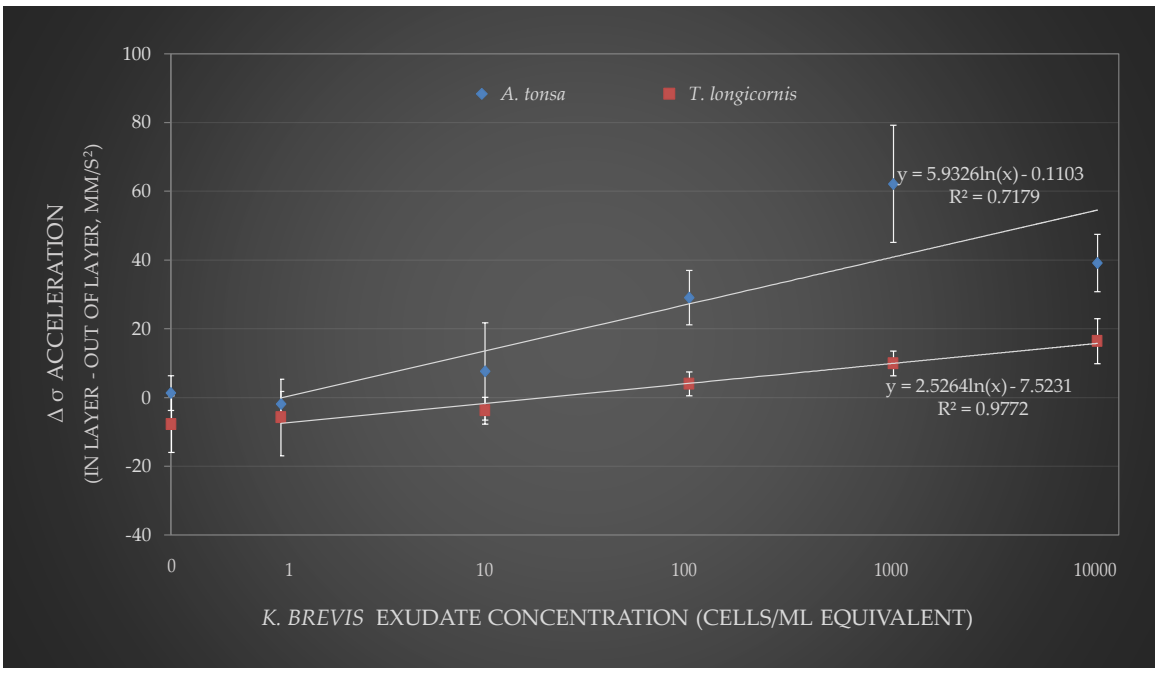

Figure A.5: Difference Between In Layer and Out of Layer Standard Deviation of Acceleration Under Various *K. brevis* Exudate Layer Concentrations. Linear regression lines using log-transformed concentration levels are displayed with corresponding fit equation and coefficient of determination.

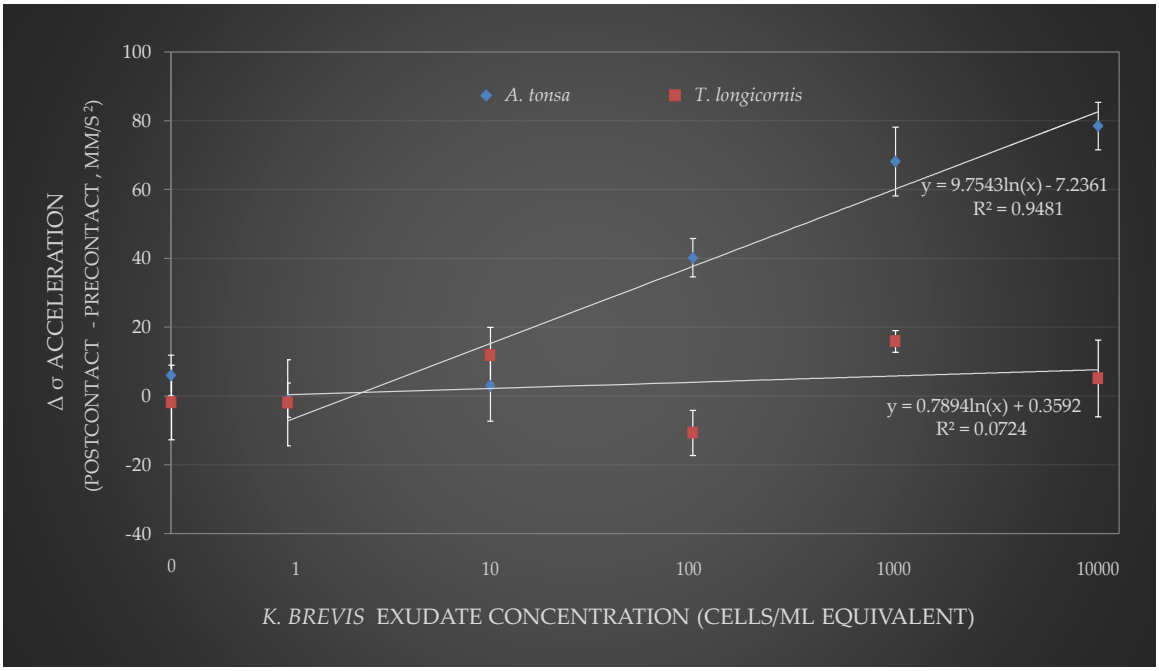

Figure A.6: Difference Between Precontact and Postcontact Standard Deviation of Acceleration Under Various *K. brevis* Exudate Layer Concentrations. Linear regression lines using log-transformed concentration levels are displayed with corresponding fit equation and coefficient of determination.

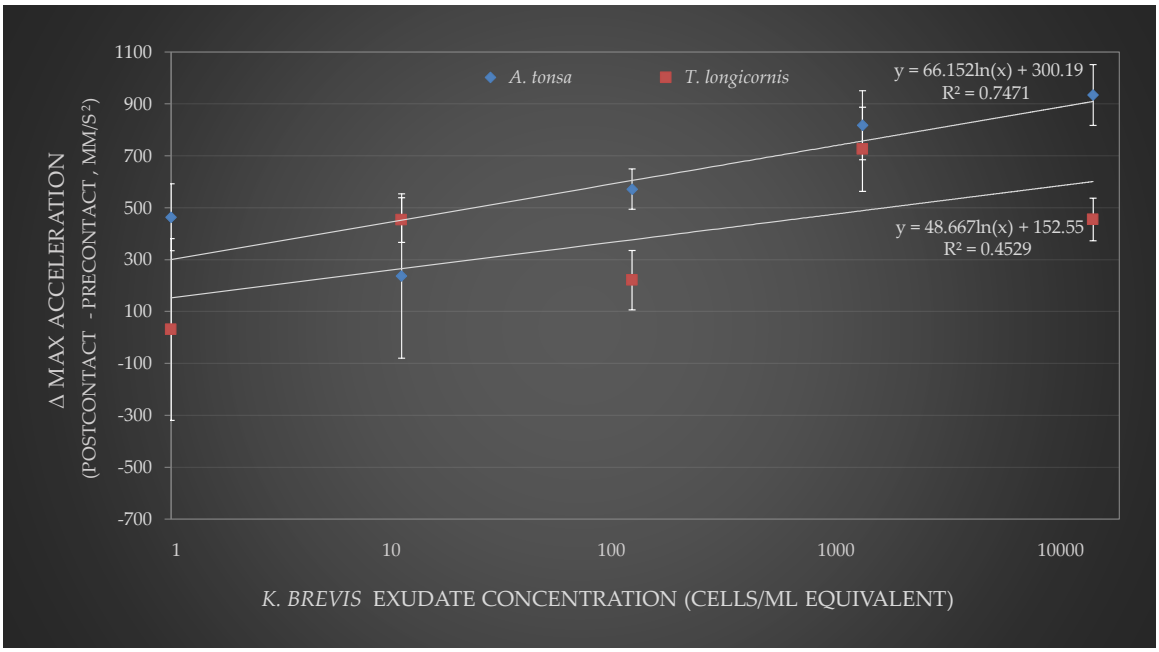

Figure A.7: Difference Between Precontact and Postcontact Maximum Acceleration Under Various *K. brevis* Exudate Layer Concentrations. Linear regression lines using log-transformed concentration levels are displayed with corresponding fit equation and coefficient of determination.

APPENDIX B

COPEPOD HUNGER LEVEL ANALYSIS: CONTROL AND LAMINAR JET LAYER

B.1 Summary of Behavioral Assays

Behavioral assays were conducted with the copepods *A. tonsa* and *T. longicornis* in which they were exposed to both stagnant (control) and horizontal free shear flows in two physiological conditions (starvation levels): 1) after being starved for 24 hours prior to the experiments and 2) after being fed mixed, beneficial phytoplankton directly prior to the experiment. The goal was to examine the effect of starvation levels on copepod behavioral responses to finescale hydrodynamic cues (free shear flow) associated with thin planktonic layers.

Free-swimming copepod trajectories were digitized in the x-z plane using DLTdv5, a MATLAB-based digitization software (Hedrick 2008). The resulting raw trajectory data sets (x, z, t) were analyzed using a suite of custom MATLAB codes. Path kinematic parameters were computed for portions of each trajectory in-layer and out-of-layer, as well as pre-contact and post-contact, with the layer treatment region being defined by a behavioral shear strain rate threshold of 0.025 s^{-1} (Woodson et al. 2005). The path kinematics computed were swimming speed and turn frequency (where a turn is defined as a change of direction of 15° or more). Additionally, the following gross trajectory parameters are computed and provide measures of the net effect of changes in copepod behavior on macroscale trajectory characteristics: the two-dimensional path fractal dimension ($F2D$), the proportional residence time (PRT = time spent in-layer/total time in observation window), and the net-to-gross displacement ratio ($NGDR$ = net displacement/gross displacement). To alleviate

potential dependence of $NGDR$ values on trajectory duration (Tiselius 1992), $NGDR$ was consistently computed for four second duration segments of a given trajectory and ensemble averaged. $F2D$ provides a scale invariant description of trajectory fracticality or self-similarity and provides useful insight into how changes in path kinematic parameters modify gross trajectory characteristics (see computation details in the Methods section of Chapter 4). Summaries of all raw kinematic and gross path parameter data are presented below in Tables B.1, B.3, and B.5.

B.2 Summary of Statistical Analyses

The effects of hunger level and experimental treatment on gross path parameters were analyzed separately for each species via a two-factor analysis of variance (ANOVA) including the following model effects: hunger level (starved versus fed), treatment (control versus jet), and hunger x treatment interaction. Changes in path kinematics (relative swimming speed, turn frequency) were analyzed separately for each species via a single-factor, repeated measures analysis of variance including the following model effects: hunger level (starved versus fed), location or exposure (repeated measures effect), and hunger x (location or exposure) interaction. Summaries of all statistical analyses are presented below in Tables B.2, B.4, and B.6.

Table B.1: Summary of gross path parameter data.

Species	**Hunger Level**	**Treatment**	**n**	**Mean PRT (SE)**	**Mean NGDR (SE)**	**Mean F2D (SE)**
A. tonsa	Fed	Control	40	0.563 (0.023)	0.338 (0.053)	1.070 (0.011)
A. tonsa	Starved	Control	33	0.662 (0.036)	0.650 (0.113)	1.079 (0.015)
A. tonsa	Fed	Jet	74	0.679 (0.030)	0.587 (0.068)	1.028 (0.001)
A. tonsa	Starved	Jet	66	0.565 (0.029)	0.488 (0.060)	1.058 (0.011)
T. longicornis	Fed	Control	38	0.523 (0.054)	0.472 (0.076)	1.085 (0.012)
T. longicornis	Starved	Control	39	0.619 (0.024)	0.736 (0.118)	1.129 (0.021)
T. longicornis	Fed	Jet	74	0.604 (0.028)	0.631 (0.073)	1.040 (0.008)
T. longicornis	Starved	Jet	63	0.633 (0.026)	0.535 (0.067)	1.057 (0.010)

Table B.2: Summary of two-factor ANOVA of gross path parameters. * indicates statistical significance to a 95 % confidence level ($p < 0.05$). ** indicates statistical significance to a 90 % confidence level (statistically trending, $p < 0.10$).

A. tonsa			
PRT			
DFE = 208	Hunger	Treatment	Hunger x Treatment
N param	1	1	1
DF	1	1	1
F-value	0.609	0.452	12.034
p-value	0.432	0.502	0.0006*
NGDR			
DFE = 208	Hunger	Treatment	Hunger x Treatment
N param	1	1	1
DF	1	1	1
F-value	24.742	3.921	92.296
p-value	<0.0001*	0.049*	<0.0001*
F2D			
DFE = 208	Hunger	Treatment	Hunger x Treatment
N param	1	1	1
DF	1	1	1
F-value	3.022	8.843	0.865
p-value	0.0836**	0.003*	0.353
T. longicornis			
PRT			
DFE = 209	Hunger	Treatment	Hunger x Treatment
N param	1	1	1
DF	1	1	1
F-value	1.677	2.977	0.887
p-value	0.197	0.086**	0.347
NGDR			
DFE = 209	Hunger	Treatment	Hunger x Treatment
N param	1	1	1
DF	1	1	1
F-value	15.404	1.293	62.442
p-value	<0.0001*	0.257	<0.0001*
F2D			
DFE = 209	Hunger	Treatment	Hunger x Treatment
N param	1	1	1
DF	1	1	1
F-value	5.796	23.559	1.356
p-value	0.0169*	<0.0001*	0.246

Table B.3: Summary of relative swimming speed data.

Species	Hunger Level	Treatment	n	Mean In-Layer (SE)	Mean Out-of-Layer (SE)
A. tonsa	Fed	Jet	54	4.101 (0.292)	2.754 (0.139)
A. tonsa	Starved	Jet	60	5.396 (0.384)	5.309 (0.613)
T. longicornis	Fed	Jet	64	2.916 (0.10)	2.868 (0.102)
T. longicornis	Starved	Jet	59	8.032 (0.579)	8.430 (0.635)
				Mean Pre-contact (SE)	**Mean Post-contact (SE)**
A. tonsa	Fed	Jet	24	2.945 (0.30)	3.889 (0.415)
A. tonsa	Starved	Jet	36	4.825 (0.789)	5.395 (0.535)
T. longicornis	Fed	Jet	38	2.799 (0.151)	2.896 (0.119)
T. longicornis	Starved	Jet	39	8.144 (0.875)	8.138 (0.708)
				Mean (SE)	
A. tonsa	Fed	Control	40	1.788 (0.087)	
A. tonsa	Starved	Control	33	1.904 (0.199)	
T. longicornis	Fed	Control	38	2.175 (0.058)	
T. longicornis	Starved	Control	39	5.554 (0.399)	

Table B.4: Summary of repeated-measures ANOVA of relative swimming speed. * indicates statistical significance to a 95 % confidence level ($p < 0.05$). ** indicates statistical significance to a 90 % confidence level (statistically trending, $p < 0.10$).

A. tonsa			
Speed In-Layer vs. Out-of-layer			
DFE = 110	Hunger	Location	Hunger x Location
Num DF	1	1	1
Den DF	110	110	110
F-value	21.988	0.838	2.441
p-values	<0.0001*	0.362	0.121
Speed Precontact vs. Postcontact			
DFE = 56	Hunger	Exposure	Hunger x Exposure
Num DF	1	1	1
Den DF	56	56	56
F-value	7.466	0.23	0.0139
p-values	0.0084*	0.633	0.9065
T. longicornis			
Speed In-Layer vs. Out-of-layer			
DFE = 119	Hunger	Location	Hunger x Location
Num DF	1	1	1
Den DF	119	119	119
F-value	113.875	0.663	1.132
p-values	<0.0001*	0.4173	0.289
Speed Precontact vs. Postcontact			
DFE = 73	Hunger	Exposure	Hunger x Exposure
Num DF	1	1	1
Den DF	73	73	73
F-value	56.327	1.603	1.318
p-values	<0.0001*	0.21	0.255

Table B.5: Summary of turn frequency data.

Species	Hunger Level	Treatment	n	Mean In-Layer (SE)	Mean Out-of-Layer (SE)
A. tonsa	Fed	Jet	54	12.252 (0.096)	12.503 (0.115)
A. tonsa	Starved	Jet	60	12.416 (0.208)	12.520 (0.183)
T. longicornis	Fed	Jet	64	11.916 (0.117)	12.20 (0.116)
T. longicornis	Starved	Jet	59	12.188 (0.188)	12.509 (0.176)
				Mean Pre-contact (SE)	**Mean Post-contact (SE)**
A. tonsa	Fed	Jet	24	13.847 (0.718)	12.220 (0.132)
A. tonsa	Starved	Jet	36	12.741 (0.195)	12.380 (0.252)
T. longicornis	Fed	Jet	38	12.341 (0.126)	11.924 (0.149)
T. longicornis	Starved	Jet	39	12.948 (0.228)	12.196 (0.233)
				Mean (SE)	
A. tonsa	Fed	Control	40	10.557 (0.183)	
A. tonsa	Starved	Control	33	7.128 (0.408)	
T. longicornis	Fed	Control	38	12.384 (0.073)	
T. longicornis	Starved	Control	39	5.120 (0.487)	

Table B.6: Summary of repeated-measures ANOVA of turn frequency . * indicates statistical significance to a 95 % confidence level ($p < 0.05$). ** indicates statistical significance to a 90 % confidence level (statistically trending, $p < 0.10$).

A. tonsa			
TF In-Layer vs. Out-of-layer			
DFE = 110	Hunger Level	Location	Hunger x Location
Num DF	1	1	1
Den DF	110	110	110
F-value	0.044	1.763	0.006
p-values	0.834	0.187	0.941
TF Precontact vs. Postcontact			
DFE = 56	Hunger Level	Exposure	Hunger x Exposure
Num DF	1	1	1
Den DF	56	56	56
F-value	3.902	11.028	3.336
p-values	0.05*	0.002*	0.073**
T. longicornis			
TF In-Layer vs. Out-of-layer			
DFE = 119	Hunger Level	Location	Hunger x Location
Num DF	1	1	1
Den DF	119	119	119
F-value	0.96	8.609	1.873
p-values	0.33	0.004*	0.174
TF Precontact vs. Postcontact			
DFE = 73	Hunger Level	Exposure	Hunger x Exposure
Num DF	1	1	1
Den DF	73	73	73
F-value	1.555	12.797	3.393
p-values	0.216	0.0006*	0.069**

APPENDIX C

INTERNAL WAVES

Internal waves are a ubiquitous feature in many coastal marine ecosystems and as such are important features to consider in the spatiotemporal dynamics of thin planktonic layers. Oscillations of the pycnocline in stratified waters due to internal wave propagation generate fluxes of quantities, such as fluid momentum, thermal energy, and chemical concentration. These fields compose a set of hydrodynamic and thermochemical sensory cues that are fundamental to many planktonic life processes, including prey and predator detection, mate-tracking, habitat partitioning, nutrient and waste transport processes, and chemical communications. Thus, we expect that internal waves generate sensory cues in the water column, influence many fundamental biological processes, and broadly affect spatiotemporal productivity dynamics through unique biophysical coupling over a wide range of relevant scales. We constructed an internal wave generator facility to mimic in situ characteristics that plankton observe. Simultaneous particle image velocimetry (PIV) and laser-induced fluorescence (LIF) are employed on internal waves generated in a two-layer stratification to quantify wave-induced scalar fluxes. Difficulties inherent in scaling down in situ conditions for laboratory-scale behavioral assays are discussed in the context of accurately matching spatiotemporal scales from a planktonic point of view. Finally, the results are interpreted in the context of zooplankton sensory ecology.

Internal waves are a ubiquitous feature of the world's atmosphere and oceans in which perturbations propagate along density interfaces in both two-layer and continuously stratified systems. Breaking internal waves are major contributors to the

vertical redistribution of mass and momentum in the world's lakes, oceans, and atmosphere (Staquet and Sommeria 2002, Troy and Koseff 2005) and have significant biological effects in many aquatic ecosystems from the accompanying vertical transport of nutrients and oxygen (Boegman et al. 2003). Lueck and Mudge (Lueck and Mudge 1997) argue that internal wave breaking in stratified oceanic systems is required to match the vertical heat flux from downwelling of cold, salty water in polar regions. Leichter et al. (Leichter et al. 1996) showed that breaking internal waves in coral reef systems can lead to dramatic changes in salinity, temperature and chlorophyll levels. Similarly, mean atmospheric circulation and pollutant transport have been linked to internal wave propagation and breaking events (Fritts 1989, Schilling and Etling 1996) as has sediment transport on the continental shelf (Bogucki et al. 1997, Troy and Koseff 2005). Thus, internal wave processes comprise foundational forcing mechanisms that drive a variety of effects on the spectrum from the purely physical to the purely biological. In order to gain a holistic understanding of thin layer dynamics, a quantification of the biophysical effects of internal wave processes is absolutely fundamental (Cheriton et al. 2009).

The review here will give a solid overview of the governing equations and solutions for infinitesimal perturbations (i.e. linear internal waves) in a two-layer stratification because of the dynamical relevance to documented thin layer structures *in situ*. Various engineering properties will also be considered not only for internal wavemaker design considerations but also for verification of experimental methods. Finally, a more detailed review of the relevance of internal waves in affecting biological processes associated with thin layer dynamics in highly stratified coastal marine ecosystems will be given.

C.1 Two-Layer Progressive Internal Waves: Governing Equations, Linear Solutions, and Engineering Properties

Following the analysis by Philips (Phillips 1966) for linear internal waves in the absence of Coriolis forcing, the Navier-Stokes equations to the Boussinesq approximation in differential form are given as

$$\frac{\partial u_i}{\partial t} + u_j \frac{\partial u_i}{\partial x_j} + \frac{1}{\rho_o}\frac{\partial p_i}{\partial x_i} + g m_i \frac{\rho}{\rho_o} = 0 \tag{C.1}$$

where i and j are the three coordinate directions, m is a unit vector vertically upwards, the density ρ is decomposed into the sum of the mean density as a function of depth $\rho(z)$ and perturbations about the mean, ρ'. The reference density, ρ_o , is usually taken as the mean density in the water column. Here, we have neglected density variations except in terms that are multiplied by the acceleration due to gravity, and the resulting governing equation shows that the total derivative of the fluid velocity field is simply the result of pressure gradient forces and buoyancy forces arising from fluid density variations in space. Similar, the flow is incompressible such that the divergence of the velocity field equals zero as

$$\frac{\partial u_i}{\partial x_i} = 0 \tag{C.2}$$

and the total derivative of the instantaneous density field, ρ, is given as the sum of the total derivative of density perturbations about the mean density, ρ', and changes in mean density with depth, $\rho(z)$, due to vertical advection given as

$$\frac{\partial \rho}{\partial t} = \frac{\partial \rho'}{\partial t} + u_j \frac{\partial \rho'}{\partial x_j} + w\frac{\partial \bar{\rho}}{\partial z} = 0 \tag{C.3}$$

If we consider the pressure, p, as the departure from hydrostatic pressure, combine separate equations for horizontal and vertical velocity vector components, differentiate with respect to time, and employ Equation C.3, we can eliminate the pressure gradient terms and arrive at a simple differential equation governing motion in a stratified fluid as

$$\frac{\partial^2}{\partial t^2}\left(\nabla^2 w\right) + N\left(z\right)^2 \nabla_h^2 w = Q\left(\mathbf{x}, t\right) \tag{C.4}$$

where the horizontal Laplacian $\nabla_h = \partial/\partial x + \partial/\partial y$, $Q(\mathbf{x}, t)$ is the sum of all non-linear terms, and the Brunt-Väisälä or buoyancy frequency $N(z)^2$ was previously given in Equation 2.2 and represents the theoretical maximum frequency limit for a propagating internal wave in a given stratification. In the absence of non-linearities (finite amplitude effects, the presence of mean shear in the flow field, etc.), the right-hand side of Equation C.4 is negligible and the linear governing equation is given as

$$\frac{\partial^2}{\partial t^2}\left(\nabla^2 w\right) + N\left(z\right)^2 \nabla_h^2 w = 0 \tag{C.5}$$

If we consider a velocity perturbation propagating in space and time the solution will take the form

$$w = W(z) e^{i(\mathbf{k}\cdot\mathbf{x} - \omega t)} \tag{C.6}$$

where $\mathbf{k}$ is the horizontal wavenumber vector and ω is the frequency of oscillation. Substituting this solution form into Equation C.5 yields a linear differential equation governing the vertical velocity perturbation $W(z)$ as

$$\frac{\partial^2 W}{\partial z^2} + \left[\frac{N(z)^2 - \omega^2}{\omega^2}\right] k^2 W = 0 \tag{C.7}$$

The perturbation eigenfunction $W(z)$ will be subjected to the dynamic free surface boundary condition at $z = 0$ of atmospheric pressure as

$$\omega^2 \frac{\partial W}{\partial z} g k^2 W = 0 \tag{C.8}$$

and the no penetration condition at an assumed horizontal, impermeable bed located at $z = -D$ as

$$W = 0 \tag{C.9}$$

For a given stratification $N(z)$, Equations C.7, C.8, and C.9 represent an eigenvalue problem in which the possible modes of motion for small disturbances at frequencies $\omega(k)$ can be found.

When the thermocline is fairly sharp and $N(z)$ reaches a maximum in this region (as in the vast majority of documented thin layers), the lowest internal wave mode dominates and higher modes dampen out, most likely from high shear associated with these modes, and ultimately degrade into turbulence. Thus, we will consider here the analytical solution and some engineering properties for the lowest mode internal wave in a two-layer stratification with a thin density interface, which presents itself as an

appropriate model for a laboratory investigation of internal wave effects in thin layer dynamics.

In a two layer density stratification (sharp thermocline between two homogeneous layers), $N(z)$ is only appreciable within a finite region of thickness ζ surrounding the density interface located at $z = -h_1$. Thus, outside the finite thickness interfacial region, Equation C.7 reduces to

$$\frac{\partial^2 W}{\partial z^2} - k^2 W = 0 \tag{C.10}$$

Additionally, for the lowest mode of motion the velocity perturbation changes little across a sharp interface such that

$$W\left(-h_{1+}\right) \approx W\left(-h_{1-}\right) \tag{C.11}$$

Furthermore, the change in $\partial W/\partial z$ across the density interface can be found by integrating Equation C.7 across the interfacial thickness ζ giving

$$\frac{\partial W}{\partial z}\left(-h_{1+}\right) - \frac{\partial W}{\partial z}\left(-h_{1-}\right) \approx k^2 W\left(-h_1\right)\left[\zeta - \frac{g}{\omega^2}\frac{\Delta\rho}{\rho_o}\right] \tag{C.12}$$

where $\Delta\rho$ is the magnitude of the density difference across the interface. Equations C.11 and C.12 provide continuity conditions for the solutions to Equation C.7 in the regions above and below the density interface. Finally, the solutions for the eigenvalue problem satisfying the appropriate boundary conditions in the regions above and below the density interface are given as

$$W(z) = A\sinh(kz) \qquad for\ -h_1 < z < 0 \tag{C.13}$$

$$= B\sinh[k(z+H)]) \quad for\ -H < z < -h_1 \tag{C.14}$$

in which the total depth H is the sum of the thicknesses of the upper and lower density layers, respectively, $h_1 + h_2$. The condition of continuity of the velocity field across the interface gives the ratio of the coefficients as

$$\frac{A}{B} = -\frac{\sinh(kh_2)}{\sinh(kh_1)} \tag{C.15}$$

This equation, when combined with Equation C.12, gives the two-layer, thin-interface dispersion relation for progressive internal waves as

$$\omega^2 = \frac{g'k}{k\zeta + \coth(kh_1) + \coth(kh_2)} \tag{C.16}$$

in which g', the modified acceleration due to gravity, has been defined as

$$g' = g\frac{\Delta\rho}{\rho_o} \tag{C.17}$$

Noting that most internal waves have wavelengths much greater than the interfacial thickness ζ such that $k\zeta << 1$, the dispersion relation reduces to

$$\omega^2 = \frac{g'k}{\coth(kh_1) + \coth(kh_2)} \tag{C.18}$$

Finally, the motion outside the thermocline region is irrotational and thus a convenient description of the motion is giving by the velocity potential in the upper and lower regions as

$$\Phi = \frac{ia\omega}{k}\frac{\cosh(kz)}{\sinh(kh_1)}e^{i(\mathbf{k}\cdot\mathbf{x}-\omega t)} \qquad for \ -h_1 < z < 0 \tag{C.19}$$

$$= -\frac{ia\omega}{k}\frac{\cosh[k(H+z)]}{\cosh(kh_2)}e^{i(\mathbf{k}\cdot\mathbf{x}-\omega t)} \quad for \ -H < z < -h_1 \tag{C.20}$$

where a is the amplitude of infinitesimal displacements in the thermocline given as

$$\eta = ae^{i(\mathbf{k}\cdot\mathbf{x}-\omega t)} \tag{C.21}$$

Some properties derivable from the linear solutions above are useful to consider for wavemaker design purposes and for zooplankton behavioral assays in which we desire to match fluid mechanical conditions common in documented thin layer structures. Namely, the shear strain rate field and the dynamic pressure field contain all of the sensory information likely to be employed by a zooplankter foraging in an internal wave field in the proximity of a well-defined thermocline. The following sets of equations summarize some useful parameters for planar internal wave induced flow fields in the upper and lower layers, respectively, computed readily from the velocity potential and horizontal momentum equations.

$$u(x,z,t) = -a\omega\frac{\cosh(kz)}{\sinh(kh_1)}e^{i(kx-\omega t)} \quad \text{(C.22)}$$

$$w(x,z,t) = ia\omega\frac{\sinh(kz)}{\sinh(kh_1)}e^{i(kx-\omega t)} \quad \text{(C.23)}$$

$$P(x,z,t) = -\frac{a\rho_o\omega^2}{k}\frac{\cosh(kz)}{\sinh(kh_1)}e^{i(kx-\omega t)} \quad \text{(C.24)}$$

$$\sigma(x,z,t) = -a\omega k\frac{\sinh(kz)}{\sinh(kh_1)}e^{i(kx-\omega t)} \quad \text{(C.25)}$$

$$u(x,z,t) = a\omega\frac{\cosh[k(H+z)]}{\sinh(kh_2)}e^{i(kx-\omega t)} \quad \text{(C.26)}$$

$$w(x,z,t) = -ia\omega\frac{\sinh[k(H+z)]}{\sinh(kh_2)}e^{i(kx-\omega t)} \quad \text{(C.27)}$$

$$P(x,z,t) = \frac{a\rho_o\omega^2}{k}\frac{\cosh[k(H+z)]}{\sinh(kh_2)}e^{i(kx-\omega t)} \quad \text{(C.28)}$$

$$\sigma(x,z,t) = a\omega k\frac{\sinh[k(H+z)]}{\sinh(kh_2)}e^{i(kx-\omega t)} \quad \text{(C.29)}$$

where u and w are the horizontal and vertical components of fluid velocity, respectively, and P and σ are the pressure and shear strain rate fields, respectively.

A number of other useful higher order properties such as energy density, energy flux, momentum, and radiation stresses can also be easily derived from the linear solutions presented above (Phillips 1966).

C.2 Biophysical Interactions in Internal Waves

Internal waves have the potential to influence biological processes in aquatic ecosystems in a variety of ways including the following: wave-breaking events transport nutrients and oxygen into the euphotic zone, wave-induced upwelling transports nutrient-rich waters to the surface in shallow coastal regions, shearing by progressive internal waves can aggregate various plankters into patchy distributions, and vertical advection can transport phytoplankton through photic gradients and potentially

enhance or impede photosynthesis (Evans et al. 2008). Furthermore, the existence of thin layer structures in highly stratified coastal environments (Cheriton et al. 2009, Velo-Suarez et al. 2010) indicates that quantifying the biophysical effects of internal wave propagation on thin layer dynamics is foundational. Undoubtedly, the magnitude of the effects will be dependent on the relevant biophysical variables such as hydrography and plankton motility, as well the relevant biological and physical spatiotemporal scales.

In a seminal paper, Franks (Franks 1995) built a simple model documenting how the interaction of vertical shear from vertically-propagating near-inertial internal waves and along-isopycnal (horizontal) phytoplankton patchiness can produce thin layers of phytoplankton on the order of 10s of centimeters. Importantly, the thickness of the thin layer is directly related to vertical shear and the scale of horizontal patchiness: smaller patchiness scales generate thinner vertical layers in a given vertical shear environment. A similar model by Lennert-Cody and Franks (Lennert-Cody and Franks 1999) explored changes in patch dynamics of swimming plankters in a two-layer stratification with both linear and weakly non-linear internal waves. They found that maximum increases in patchiness occur over the wave trough, that changes in concentration are opposite above and below the density interface, that changes in concentration increase linearly with wave amplitude and the swimming proficiency of the plankter, that maximum concentration increases occur in the upper layer and scale linearly with wave amplitude in a given stratification, and that maximum concentration increases are approximately twice the background concentration. Together, these models lay out two fundamental observations about the biophysical effects of internal waves: they have the capacity to produce vertically thin layers of phytoplankton and the magnitude of the effect is dependent upon the plankters involved. These model results open the door to extensive laboratory investigation of the underlying biophysical dynamics.

Rinke et al. (Rinke et al. 2007) utilized coincident acoustic hydrographic and biological data to document the effect of wind-induced downwelling that generated internal waves in the epilimnion on the spatial distribution zooplankters, predominately *Daphnia spp.*, in a reservoir in Germany. Internal wave generation and propagation was shown to laterally transport the zooplankton population, which led to higher abundances deeper in the water column. Evans et al. (Evans et al. 2008) used a combination of field data and modeling to analyze the photosynthetic effect of internal waves by advecting phytoplankton vertically through non-linear photic fields. They found that photosynthesis can be enhanced up to 200%, whereas it is potentially reduced by only 15%, with the results highly dependent on the matching of internal wave and photosynthetic time scales. Elsewhere, divergent processes from internal wave generation through the Strait of Gibraltar (Macias et al. 2010) were shown to cause reductions in zooplankton biomass. Taxonomically-specific alternating bands of high and low zooplankton abundance were consistent with internal wave induced flow patterns. The change in taxonomic composition within bands was traced directly to differences in swimming capabilities between zooplankters. Finally, several recent thin layer field studies (Cheriton et al. 2009, Velo-Suarez et al. 2010) have documented the effects of internal wave packets in vertically advecting existing thin layer structures and compressing or expanding layer thicknesses vertically.

These relatively recent studies collectively indicate that the biophysical effects of internal wave processes are both highly relevant and that the mechanisms are relatively unknown. The author knows of not a single laboratory investigation that has sought to isolate and quantify these mechanisms.

C.3 Internal Waves and Combined PIV and LIF

An ecologically-relevant (specifically to thin layer dynamics) set of behavioral assays would consist of exposing zooplankton to internal waves in a two-layer density stratification (Figure C.1). Formation of a thin interface between the two fluid layers can be created by slowly filling the flume with a lower density (salinity) fluid followed by a higher density fluid. Additionally, fluid that was undesirably mixed at the interface can be selectively withdrawn with an interface sharpening device. Additional care will be taken to ensure that animal behavioral responses to the density discontinuities will not override behavioral responses to the periodic velocity and pressure fluctuations associated with the internal waves. This will be accomplished by creating density differences that are below the response threshold reported by Woodson et al. (Woodson et al. 2007). A half-cylinder, plunger-type wavemaker oscillated about the interface can be used to generate lowest-mode, progressive internal waves for behavioral assays. Additional experimental equipment required includes a linear actuator and a data acquisition board on a PC to act as the analog position controller. Adequate flume length will ensure that high frequency evanescent modes decay before the observation section, and will also ensure monochromatic progressive waves can be dampened downstream via a horsehair beach and/or other flow baffling devices. Simultaneous PIV and PLIF (Figure C.2) will be used to generate stroke-to-amplitude ratios for the wavemaker and to compare experimental velocity and pressure fields to the theoretical lowest progressive mode fields.

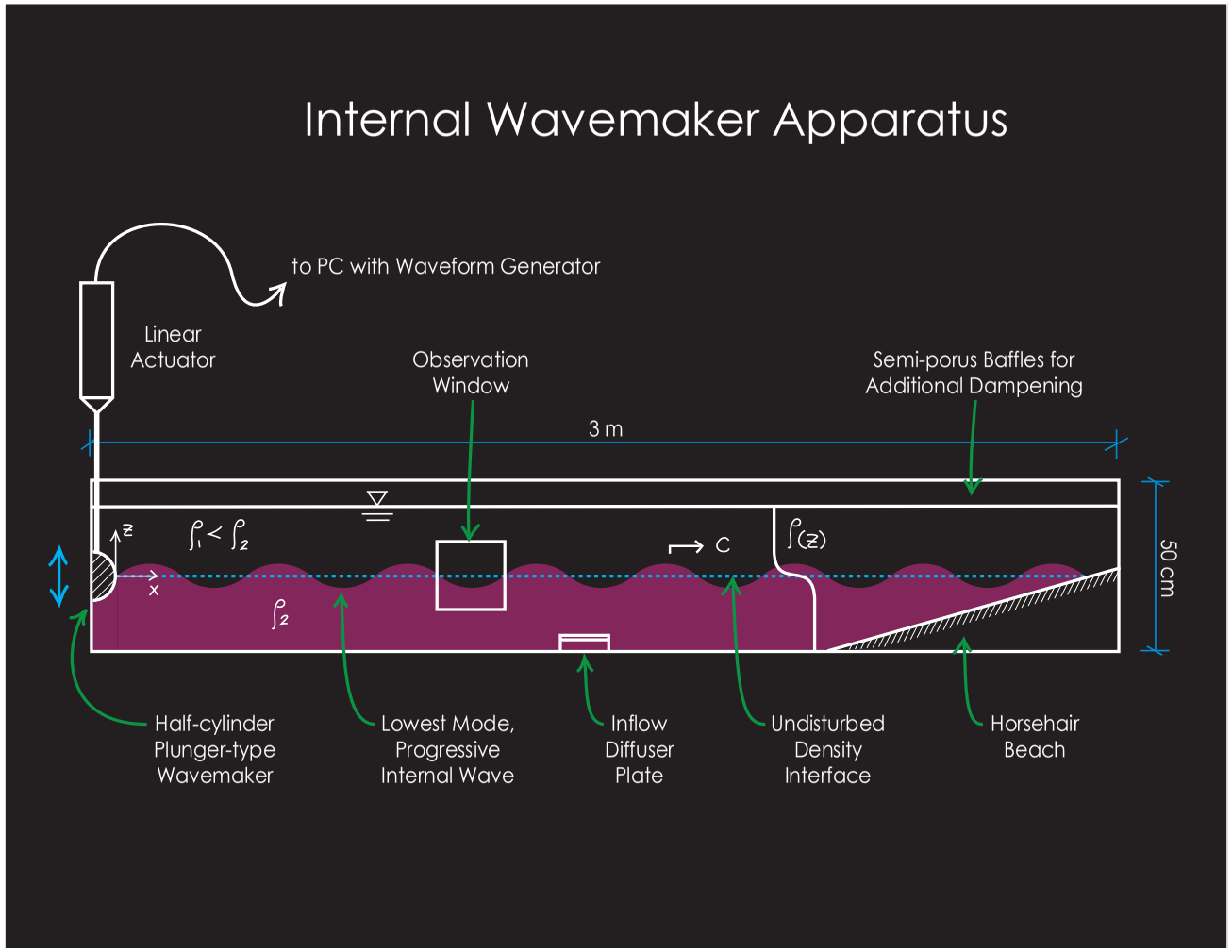

Figure C.1: Experimental schematic of an internal wave generator in a two-layer density stratification.

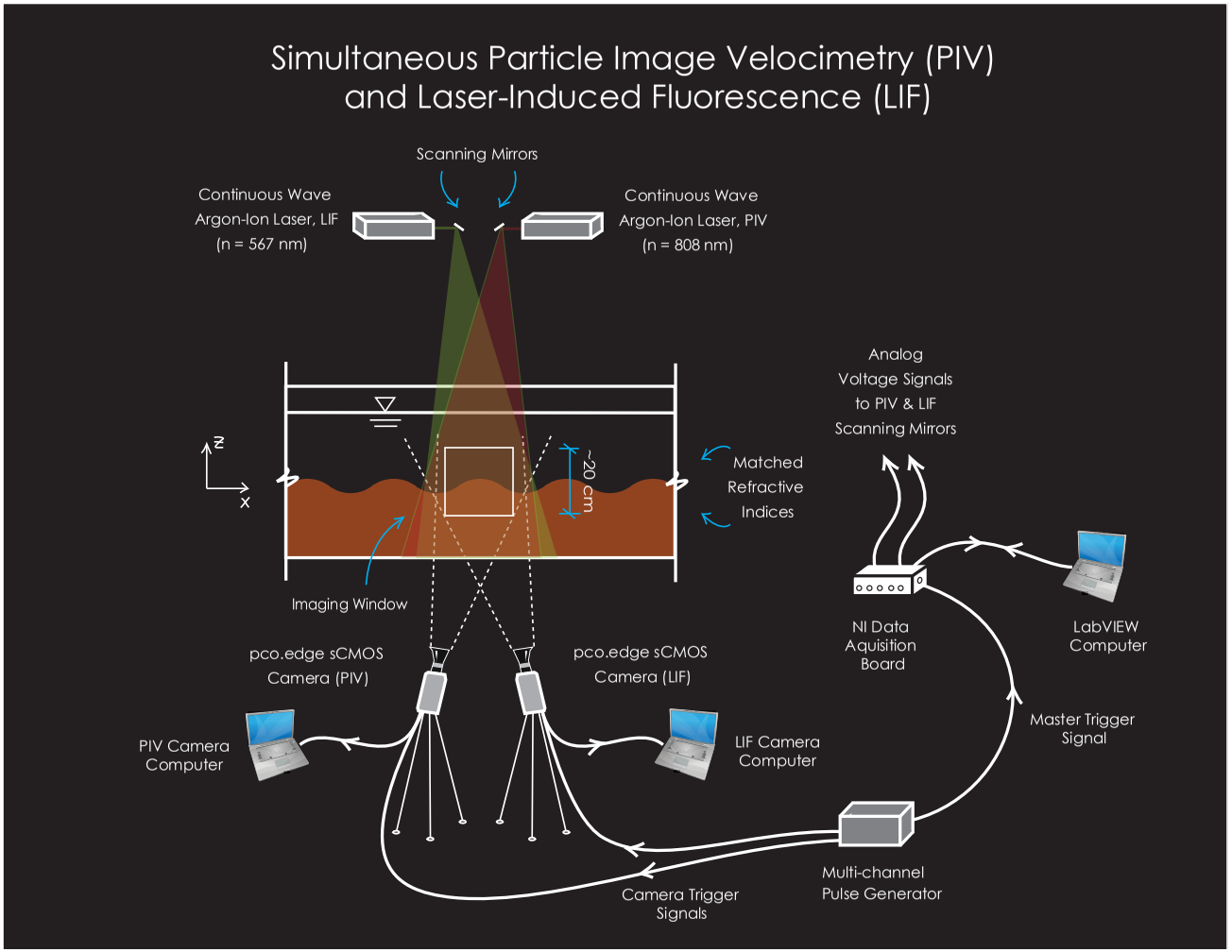

Figure C.2: Experimental schematic of simultaneous particle image velocimetry and laser-induced fluorescence characterization of an internal wave field.

Bibliography

S. Alben, K. Spears, S. Garth, D. Murphy, and J. Yen. Coordination of multiple appendages in drag-based swimming. *Journal of the Royal Society Interface*, 7: 1545–1557, 2010.

A. L. Alldredge, T. J. Cowles, S. MacIntyre, J. E. B. Rines, et al. Occurrence and mechanisms of formation of a dramatic thin layer of marine snow in a shallow Pacific fjord. *Marine Ecology Progress Series*, 233:1–12, 2002.

M. Alnahhal and Th. Panidis. The effect of sidewalls on rectangular jets. *Experimental Thermal and Fluid Science*, 33:838–851, 2009.

D. M. Anderson. Toxic algal blooms: A global perspective. *Red tides: Biology, environmental science, and toxicology*, pages 11–16, 1989.

E. C. Andrade. The velocity distribution in a liquid-into-liquid jet. part 2: The plane jet. *Proc Phys Soc*, 51:784–793, 1939.

W. R. Andrews, N. M. Targett, and C. E. Epifanio. Isolation and characterization of the metamorphic inducer of the common mud crab, *Panopeus herbstii*. *Journal of Experimental Marine Biology and Ecology*, 261:121–134, 2001.

E. Bagøien and T. Kiørboe. Blind dating - mate finding in planktonic copepod. iii. hydromechanical communication in *Acartia tonsa*. *Marine Ecology Progress Series*, 300:129–133, 2005a.

E. Bagøien and T. Kiørboe. Blind dating - mate finding in planktonic copepods. i. tracking the pheromone trail of *Centropages typicus*. *Marine Ecology Progress Series*, 300:105–115, 2005b.

T. A. Baird, C. H. Ryer, and B. L. Olla. Social enhancement of foraging on an ephemeral food source in juvenile walleye pollock, *Theragra chalcogramma*. *Environmenta Biology of Fishes*, 31:307–311, 1991.

K. J. Benoit-Bird, T. J. Cowles, and C. E. Wingard. Edge gradients provide evidence of ecological interactions in planktonic thin layers. *Limnology and Oceanography*, 54:1382–1392, 2009.

K. J. Benoit-Bird, M. A. Moline, C. M. Waluk, and I. C. Robbins. Integrated measurements of acoustical and optical thin layers i: Vertical scales of association. *Continental Shelf Research*, 30:17–28, 2010.

W. G. Bickley. The plane jet. *Philosophical Magazine*, 23:727–731, 1937.

D. A. Birch, W. R. Young, and P. J. S. Franks. Thin layers of plankton: Formation by shear and death by diffusion. *Deep-Sea Research Part I*, 55:277–295, 2008.

P. K. Bjørnsen and T. G. Nielsen. Decimeter scale heterogeneity in the plankton during a pycnocline bloom of *Gyrodinium aureolum*. *Marine Ecology Progress Series*, 73:263–267, 1991.

A. B. Bochdansky and S. M. Bollens. Relevant scales in zooplankton ecology: Distribution, feeding, and reproduction of the copepod *Acartia hudsonica* in response to thin layers of the diatom *Skeletonema costatum*. *Limnology and Oceanography*, 49:626–636, 2004.

L. Boegman, J. Imberger, and G. N. Ivey. High-frequency internal waves in large stratified lakes. *Limnology and Oceanography*, 48, 2003.

D. Bogucki, T. Dickey, and L.G. Redekopp. Sediment resuspension and mixing by resonantly generated internal solitary waves. *J. Phys. Ocean.*, 27, 1997.

S. M. Bollens, B. W. Frost, and J. R. Cordell. Chemical, mechanical and visual cues in the vertical migration behavior of the marine planktonic copepod *Acartia hudsonica*. *Journal of Plankton Research*, 16:555–564, 1994.

C. F. Breier and E. J. Buskey. Effects of the red tide dinoflagellate *Karenia brevis* on grazing and fecundity in the copepod *Acartia tonsa*. *Journal of Plankton Research*, 29:115–126, 2007.

S. Buczkowski, S. Kyriacos, F. Nekka, and L. Cartilier. The modified box-counting method: Analysis of some characteristic parameters. *Pattern Recognition*, 31:411–418, 1998.

J. W. Burgess and E. Shaw. Development and ecology of fish schooling. *Oceanus*, 22: 11–17, 1979.

E. J. Buskey. Swimming pattern as an indicator of the roles of copepod sensory systems in the recognition of food. *Marine Biology*, 79:165–175, 1984.

E. J. Buskey and C. J. Hyatt. Effects of the texas (USA) brown tide alga on planktonic grazers. *Marine Ecology Progress Series*, 126:285–292, 1995.

W. E. S. Carr. *Sensory Biology of Aquatic Animals*, chapter The molecular nature of chemical stimuli in the aquatic environment, pages 3–27. New York: Springer-Verlag, 1988.

W. A. Catterall, S. Cestele, V. Yarov-yarovoy, F. H. Yu, K. Konki, and T. Scheuer. Voltage-gated channels and gating modifier toxins. *Toxicon*, 49:124–141, 2007.

K. B. Catton, D. R. Webster, S. Kawaguchi, and J. Yen. The hydrodynamic disturbances of two species of krill: implications for aggregataion structure. *The Journal of Experimental Biology*, 214:1845–1856, 2011.

O. M. Cheriton, M. A. McManus, D. V. Holliday, C. F. Greenlaw, P. L. Donaghay, and T. J. Cowles. Effects of mesoscale physical processes on thin zooplankton layers at four sites along the west coast of the u.s. *Estuaries and Coasts*, 30:575–590, 2007.

O. M. Cheriton, M. A. McManus, M. T. Stacey, and J. V. Steinbuck. Physical and biological controls on the maintenance and dissipation of a thin phytoplankton layer. *Marine Ecology Progress Series*, 378:55–69, 2009.

F. S. Chia, J. Buckland-Nicks, and C. M. Young. Locomotion of marine invertebrate larvae: A review. *Canadian Journal of Zoology*, 62:1205–1222, 1984.

T. W. Clay, S. M. Bollens, A. B. Bochdansky, and T. R. Ignoffo. The effects of thin layers on the vertical distribution of larval pacific herring, *Clupea pallasi*. *Journal of Experimental Marine Biology and Ecology*, 305:171–189, 2004.

J.H. Cohen, P.A. Tester, and R. B. Forward, Jr. Sublethal effects of the toxic dinoflagellate *Karenia brevis* on marine copepod behavior. *Journal of Plankton Research*, 29:301–315, 2007.

S. P. Colin and H. G. Dam. Testing for resistance of pelagic marine copepods to a toxic dinoflagellate. *Evolutionary Ecology*, 18:355–377, 2005.

S. P. Colin and H. G. Dam. Comparison of the functional and numerical responses of resistant versus non-resistant populations of the copepod *Acartia hudsonica* fed the toxic dinoflagellate *Aleandrium tamarense*. *Harmful Algae*, 6:875–882, 2007.

E. A. Cowen and S. G. Monismith. A hybrid digital particle tracking velocimetry technique. *Experiments in Fluids*, 22:199–211, 1997.

T. Cowles, R. A. Desiderio, and M. E. Carr. Small-scale planktonic structure: persistence and trophic consequences. *Oceanography*, 11:4–9, 1998.

T. J. Cowles, R. A. Desiderio, and S. Neuer. *In situ* characterization of phytoplankton from vertical profiles of fluorescence emission spectra. *Mar. Biol.*, 115:217–222, 1993.

K. A. Cresswell, G. A. Tarling, and M. T. Burrows. Behaviour affects local-scale distributions of Antarctic krill around South Georgia. *Marine Ecology Progress Series*, 343:193–206, 2007.

K. A. Cresswell, G. A. Tarling, S. E. Thorpe, M. T. Burrows, J. Wiedenmann, and M. Mangel. Diel vertical migration of Antarctic krill (*Euphausia superba*) is flexible during advection across the Scotia Sea. *Journal of Plankton Research*, 31:1265–1281, 2009.

M. M. Criales, I. C. Zink, B. K. Haus, J. Wylie, and J. A. Browder. Effect of turbulence on the behavior of pink shrimp post larvae and implications for selective total stream transport behavior. *Marine Ecology Progress Series*, 477:161–176, 2013.

J. Crimaldi, M. Koehl, and J. Koseff. Effects of the resolution and kinematics of olfactory appendages on the interception of chemical signals in a turbulent odor plume. *Environ Fluid Mech*, 2:35–63, 2002.

J. P. Crimaldi. Planar laser induced fluorescence in aqueous flows. *Exp Fluids*, 44: 851–863, 2008.

J. P. Crimaldi and J. R. Koseff. High-resolution measurements of the spatial and temporal scalar structure of a turbulent plume. *Exp Fluids*, 31:90–102, 2001.

T. W. Cronin and R. B. Forward, Jr. Tidal vertical migration: An endogenous rhythm in estuarine crab larvae. *Science*, 205:1020–1022, 1979.

T. W. Cronin and R. B. Forward, Jr. Vertical migration cycles of crab larvae and their role in larval dispersal. *Bulletin of Marine Science*, 39:192–201, 1986.

K. L. Daly and M. C. Macaulay. Influence of physical and biological mesoscale dynamics on the seasonal distribution and behavior of *Euphausia superba* in the Antarctic marginal ice zone. *Marine Ecology Progress Series*, 79:37–66, 1991.

M. H. Daro. Migratory and grazing behavior of copepods and vertical distributions of phytoplankton. *Bull Mar Sci*, 43:710–729, 1988.

L. P. Dasi. *The small-scale structure of passive scalar mixing in turbulent boundary layers*. PhD thesis, Georgia Institute of Technology, Atlanta, GA, 2004.

G. J. Daviero, P. J. W. Roberts, and K. Maile. Refractive index matching in large-scale stratified experiments. *Exp Fluids*, 31:119–126, 2001.

M. M. Dekshenieks, P. L. Donaghay, J. M. Sullivan, J. E. B. Rines, T. R. Osborn, and M. S. Twardowski. Temporal and spatial occurrence of thin phytoplankton layers in relation to physical processes. *Marine Ecology Progress Series*, 223:61–71, 2001.

R. C. Deo, J. Mi, and G. J. Nathan. The influence of nozzle aspect ratio on plane jets. *Experimental Thermal and Fluid Science*, 31:825–838, 2007a.

R. C. Deo, J. Mi, and G. J. Nathan. The influence of nozzle-exit geometric profile on statistical properties of a turbulent plane jet. *Experimental Thermal and Fluid Science*, 32:545–559, 2007b.

J. B. Derenbach, H. Astheimer, H. P. Hansen, and H. Leach. Vertical microscale distribution of phytoplankton in relation to the thermocline. *Marine Ecology Progress Series*, 1:187–193, 1979.

A. I. Dittel and C. E. Epifanio. Seasonal abundance and vertical distribution of crab larvae in Delaware Bay. *Estuaries*, 5:197–202, 1982.

F. M. Van Dolah. Marine algal toxins: origins, health effects, and their increased occurrence. *Environ. Health. Persp.*, 108:133–141, 2000.

P. L. Donaghay and T. R. Osborn. Toward a theory of biological-physical control of harmful algal bloom dynamics and impacts. *Limnology and Oceanography*, 42: 1283–1296, 1997.

P. G. Drazin and W. H. Reid. *Hydrodynamic stability.* Cambridge University Press, United Kingdom, 1981.

W. M. Durham and R. Stocker. Thin phytoplankton layers: Characteristics, mechanisms, and consequences. *Ann. Rev. Marine Science*, 4:177–207, 2012.

W. M. Durham, J. O. Kessler, and R. Stocker. Disruption of vertical motility by shear triggers formation of thin phytoplankton layers. *Science*, 323:1067–1070, 2009.

D. B. Dusenbery. *Sensory Ecology: How Organisms Acquire and Respond to Information.* W. H. Freeman and Company, New York, 1992.

D. B. Eggleston, D. A. Armstrong, W. E. Elis, and W. S. Patton. Estuarine fronts as conduits for larval transport: hydrodynamics and spatial distribution of dungeness crab postlarvae. *Marine Ecology Progress Series*, 164:73–82, 1998.

Y. Endo. Orientation of Antarctic krill in an aquarium. *Bulletin of the Japanese Society of Scientific Fisheries*, 59:465–468, 1993.

J. T. Enright and W. M. Hamner. Vertical diurnal migration and endogenous rhythmicity. *Science*, 157:937–941, 1967.

A. W. Epstein and R. C. Beardsley. Flow-induced aggregation of plankton at a front: a 2-d Eulerian model study. *Deep Sea Research II*, 48:395–418, 2001.

M.A. Evans, S. MacIntyre, and G. W. King. Internal wave effects on photosynthesis: Experiments, theory, and modeling. *Limnology and Oceanography*, 53:339–353, 2008.

I. Everson. *Krill: Biology, Ecology and Fisheries.* Blackwell Science Ltd., 2000.

B. A. Fach, E. E. Hofmann, and E. J. Murphy. Modeling studies of Antacrtic krill *Euphausia superba* survival during transport across the Scotia Sea. *Marine Ecology Progress Series*, 231:187–203, 2002.

A. J. Ferrier, D. R. Funk, and P. J. W. Roberts. Application of optical techniques to the study of plumes in stratified fluids. *Dynamics of Atmospheres and Oceans*, 20: 155–183, 1993.

D. M. Fields. Orientation affects the sensitivity of *Acartia tonsa* to fluid mechanical signals. *Marine Biology*, 157:505–514, 2010.

D. M. Fields and J. Yen. The escape behavior of marine copepods in response to a quantifiable fluid mechanical disturbance. *Journal of Plankton Research*, 19: 1289–1304, 1997a.

D. M. Fields and J. Yen. Implications of the feeding current structure of *Euchaeta rimana*, a carnivorous pelagic copepod, on the spatial orientation of their prey. *Journal of Plankton Research*, 19:79–95, 1997b.

D. M. Fields, D. S. Shaeffer, and M. J. Weissburg. Mechanical and neural responses from the mechanosensory hairs on the antennule of *Gaussia princeps*. *Marine Ecology Progress Series*, 227:173–186, 2002.

R. B. Forward, Jr. Negative phototaxis in crustacean larvae: Possible functional significance. *J Exp. Mar. Bio. and Eco.*, 16:11–17, 1974.

R. B. Forward, Jr. Behavioural responses of crustacean larvae to rates of salinity change. *Biological Bulletin*, 176:229–238, 1989a.

R. B. Forward, Jr. Depth regulation of larval marine decapod crustaceans: Test of an hypothesis. *Marine Biology*, 176:229–238, 1989b.

R. B. Forward, Jr. Responses of crustacean larvae to hydrostatic pressure: behavioral basis of high barokinesis. *Mar Behav Physiol*, 17:223–232, 1990.

R. B. Forward, Jr, R. A. Tankersley, and D. Rittschof. Cues for metamorphosis of brachyuran crabs: An overview. *Amer Zool*, 41:1108–1122, 2001.

R. B. Forward, Jr, R. A. Tankersley, K. A. Smith, and J. M. Welch. Effects of chemical cues on orientation of blue crab, *Callinectes sapidus*, megalopae in flow: implications for location of nursery areas. *Marine Biology*, 142:747–756, 2003a.

R. B. Forward, Jr, R. A. Tankersley, and J. M. Welch. Selective tidal-stream transport of the blue crab *Callinectes sapidus*: an overview. *Bulletin of Marine Science*, 72: 347–365, 2003b.

R. B. Forward, Jr, N. B. Reyns, H. Diaz, J. H. Cohen, and D. B. Eggleston. Endogenous swimming rhythms of juvenile blue crabs, *Callinectes sapidus*, as related to horizontal transport. *Journal of Experimental Marine Biology and Ecology*, 229: 63–76, 2004.

E. G. Foster, D. A. Ritz, J. E. Osborn, and K. M. Swadling. Schooling affects the feeding success of Australian salmon *Arripis trutta* when preying on mysid swarms (*Paramesopodopsis rufa*). *Journal of Experimental Marine Biology and Ecology*, 261:93–106, 2001.

P. J. S. Franks. Sink or swim: accumulation of biomass at fronts. *Marine Ecology Progress Series*, 82:1–12, 1992.

P. J. S. Franks. Thin layers of phytoplankton: a model of formation by near-inertial wave shear. *Deep Sea Res I*, 42:75–91, 1995.

D.C. Fritts. A review of gravity wave saturation processes effects and variability in the middle atmosphere. *PAGEOPH*, 130, 1989.

S. M. Gallager, H. Yamazaki, and C. S. Davis. Contributions of fine-scale vertical structure and swimming behavior to formation of plankton layers on Georges Bank. *Marine Ecology Progress Series*, 267:27–43, 2004.

D. P. Gannon, E. J Berens McCabe, S. A. Camilleri, J. G. Gannon, M. K. Brueggen, A. A. Barleycorn, V. I. Palubok, G. J. Kirkpatrick, and R. S. Wells. Effects of *Karenia brevis* harmful algal blooms on nearshore fish communities in southwest Florida. *Marine Ecology Progress Series*, 378:171–186, 2009.

L. P. Garrison. Vertical migration behavior and larval transport in brachyuran crabs. *Marine Ecology Progress Series*, 176:103–113, 1999.

A. Genin, J. S. Jaffe, R. Reef, C. Richter, and P. J. S. Franks. Swimming against the flow: A mechanism of zooplankton aggregation. *Science*, 308:860–862, 2005.

P. M. Glibert, D. M. Anderson, P. Gentien, E. Granéli, and K. Seliner. The global, complex phenomena of harmful algal blooms. *Oceanography*, 18:136–147, 2005.

S. L. Graham and S. L. Strom. Growth and grazing of microzooplankton in response to the harmful alga *Heterosigma akashiwo* in prey mixtures. *Aquatic Microbial Ecology*, 59:111–124, 2010.

D. Grunbaum. Schooling as a strategy for taxis in a noisy environment. *Evolutionary Ecology*, 12:503–522, 1998.

L. Gui and S. T. Wereley. A correlation-based continuous window-shift technique to reduce the peak-locking effect in digital PIV image evaluation. *Exp Fluids*, 32: 506–517, 2002.

G. M. Hallegraeff. Harmful algal blooms: A global review. *UNESCO*, pages 25–49, 2005.

W. M. Hamner. Biomechanics of filter feeding in the Antarctic rill *Euphausia superba*: Review of past work and new observations. *Journal of Crustacean Builogy*, 8:149–163, 1988.

W. M. Hamner and P. P. Hamner. Behavior of Antarctic krill (*Euphausia superba*): schooling, foraging, and antipredatory behavior. *Canadian Journal of Fisheries and Aquatic Sciences*, 57:192–202, 2000.

W. M. Hamner and J. K. Parrish. *In Animal Groups in Three Dimensions: How Species Aggregate*, chapter Is the sum of the parts equal to the whole: the conflict between individuality and group membership, pages 165–173. Cambridge: Cambridge University Press, 1997.

W. M. Hamner, P. P. Hamner, S. W. Strand, and R. W. Gilmer. Behavior of Antarctic krill, *Euphausia superba*: Chemoreception, feeding, schooling, and molting. *Science*, 220:433–435, 1983.

W. Harder. Reactions of plankton organisms to water stratification. *Limnology and Oceanography*, 13:156–168, 1968.

L. R. Haury and P. H. Wiebe. Fine-scale multi-species aggregations of oceanic zooplankton. *Deep-Sea Research*, 29:915–921, 1982.

L. R. Haury, D. E. Kenyon, and Brooks. Experimental evaluation of the avoidance reaction of *Calanus finmarchicus*. *J Plankton Res*, 2:187–202, 1980.

T. L. Hedrick. Software techniques for two- and three-dimensional kinematic measurements of biological and biomimetic systems. *Bioinspiration and Biomimetics*, 3:1–6, 2008.

A. E. Hill. A mechanism for horizontal zooplankton transport by vertical migration in tidal currents. *Marine Biology*, 111:485–492, 1991a.

A. E. Hill. Vertical migration in tidal currents. *Marine Ecology Progress Series*, 75: 39–54, 1991b.

P. Hoagland and S. Scatasta. *Ecology of Harmful Algae: The economic effects of Harmful Algal Blooms*. Springer-Verlag, 2006.

R. C. Hobbs and L. W. Botsford. Diel vertical migration and timing of metamorphosis of larvae of the dungeness crab *Cancer magister*. *Marine Biology*, 112:417–428, 1992.

E. E. Hofmann and E. J. Murphy. Advection, krill, and Antarctic marine ecosystems. *Antarctic Science*, 16:487–499, 2004.

D. V. Holliday, P. L. Donaghay, C. F. Greenlaw, D. E. McGehee, M. M. McManus, J. M. Sullivan, and J. L. Miksis. Advances in defining fine- and micro-scale pattern in marine plankton. *Aquatic Living Resources*, 16:131–136, 2003.

R. Holzman and P. C. Wainwright. How to surprise a copepod: Strike kinematics reduce hydrodynamic disturbance and increase stealth of suction-feeding fish. *Limnology and Oceanography*, 54:2201–2212, 2009.

J. Hong, S. Talapatra, J. Katz, P.A. Tester, and R.J. Waggett. Algal toxins alter copepod feeding behavior. *PLoS One*, 7:e36845, 2012.

L. T. Houser and C. E. Epifanio. Impacts of biochemical cues on horizontal swimming behavior of individual crab larvae. *Marine and Freshwater Behaviour and Physiology*, 42:249–264, 2009.

H. J. Hussein. Evidence of local axisymmetry in the small scales of a turbulent planar jet. *Phys Fluids*, 6:2058–2070, 1994.

G. E. Hutchison. The paradox of the plankton. *Am Nat*, 95:137–145, 1961.

D. Ianson, S. E. Allen, D. L. Mackas, M. V. Trevorrow, and M. C. Benfield. Response of *Euphausia pacifica* to small-scale shear in turbulent flow over a sill in a fjord. *Journal of Plankton Research*, 33:1679–1695, 2011.

T. R. Ignoffo, S. M. Bollens, and A. B. Bochdansky. The effects of thin layers on the vertical distribution of the rotifer, *Brachionus plicatilis*. *Journal of Experimental Marine Biology and Ecology*, 316:167–181, 2005.

J. S. Jaffe, P. J. S. Franks, and A. W. Leising. Simultaneous imaging of phytoplankton and zooplankton distributions. *Oceanography*, 11:24–29, 1998.

G. S. Jamieson and A. C. Phillips. Occurrence of *Cancer spp.* crab megalopae off the west coast of Vancouver Island, British Columbia. *US Fishery Bulletin*, 86: 525–542, 1988.

G. S. Janowitz, D. Kamykowski, and G. Liu. A three-dimensional wind and behaviorally driven population dynamics model for *Karenia brevis*. *Continental Shelf Research*, 28:177–188, 2008.

H. Jiang, T. R. Osborn, and C. Meneveau. Chemoreception and the deformation of the active space in freely swimming copepods: A numerical study. *J Plankton Res*, 24:495–510, 2002.

X. Jiang, Y. Tang, D.J. Lonsdale, and C.J. Gobler. Deleterious consequences of a red tide dinoflagellate *Cochlodinium polykrikoides* for the calanoid copepod *Acartia tonsa*. *Marine Ecology Progress Series*, 390:105–116, 2009.

X. Jiang, D.J. Lonsdale, and C.J. Gobler. Rapid gain and loss of evolutionary resistance to the harmful dinoflagellate *Cochlodinium polykrikoides* in the copepod *Acartia tonsa*. *Limnology and Oceanography*, 56:947 – 954, 2011.

M. L. Johnson and G. A. Tarling. Influence of individual state on swimming capacity and behaviour of Antarctic krill *Euphausia superba*. *Marine Ecology Progress Series*, 366:99–110, 2008.

P. S. Karasso and M. G. Mungal. Scalar mixing and reaction in plane liquid shear layers. *J Fluid Mech*, 323:1412–1426, 1996.

P. S. Karasso and M. G. Mungal. PLIF measurements in aqueous flows using the Nd:YAG laser. *Experiments in Fluids*, 23:382–387, 1997.

U. Kils. The swimming behavior, swimming performance and energy balance of Antarctic krill, *Euphausia superba*. *BIOMASS Science Series 3*, pages 1–127, 1981.

T. Kiørboe. How zooplankton feed: mechanisms, traits and trade-offs. *Biological Reviews*, 86:311–339, 2011.

T. Kiørboe and E. Bagoien. Motility patterns and mate encounter rates in planktonic copepods. *Limnology and Oceanography*, 50:1999–2007, 2005.

T. Kiørboe and A. W. Visser. Predator and prey perception in copepods due to hydromechanical signals. *Marine Ecology Progress Series*, 179:81–95, 1999.

T. Kiørboe, E. Saiz, and A. W. Visser. Hydrodynamic signal perception in the copepod *Acartia tonsa*. *Marine Ecology Progress Series*, 179:97–111, 1999.

K. L. Kirk and J. J. Gilbert. Escape behaviour of *Polyathra* in response to artificial flow stimuli. *Bull Mar Sci*, 53:96–105, 1988.

M. A. R. Koehl, J. R. Koseff, and J. P. Crimaldi. Lobster sniffing: antennule design and hydrodynamic filtering of information in an odor plume. *Science*, 294:1948–1951, 2001.

E. S. Kornienko, O. M. Korn, and S. D. Kashenko. Comparative morphology of larvae of coastal crabs (crustacea: Decapoda: Varunidae). *Russian Journal of Marine Biology*, 34:77–93, 2008.

B. A. Krafft, G. Skaret, T. Knutsen, W. Melle, T. Klevjer, and H. Soiland. Antarctic krill swarm characteristics in the southeast atlantic sector of the southern ocean. *Marine Ecology Progress Series*, 465:69–83, 2012.

J. Kubanek, M. K. Hicks, J. Naar, and T. A. Villareal. Does the red tide dinoflagellate *Karenia brevis* use allelopathy to outcompete other phytoplankton? *Limnology and Oceanography*, 50:883–895, 2005.

P. K. Kundu and I. M. Cohen. *Fluid Mechanics*. Elsevier Academic Press, 2004.

J. Largier. Estuarine fronts: How important are they? *Estuaries*, 16:1–11, 1993.

L. G. Larsen and J. P. Crimaldi. The effect of photobleaching on plif. *Exp Fluids*, 41:803–812, 2006.

G. L. Lawson, P. H. Wiebe, C. J. Ashjian, and T. K. Stanton. Euphausiid distribution along the western antarctic peninsula - part b: Distribution of euphausiid aggregations and biomass, and associations with environmental features. *Deep-Sea Research II*, 55:432–454, 2008.

L. F. Leandro, G. J. Teegarden, P. B. Roth, Z. Wang, and G. J. Doucette. The copepod *Calanus finmarchicus*: A potential vector for trophic transfer of the marine algal biotoxin, domoic acid. *Journal of Experimental Marine Biology and Ecology*, 382:88–95, 2010.

D. Lecchini, S. C. Mills, C. Brie, R. Maurin, and B. Banaigs. Ecological determinants and sensory mechanisms in habitat selection of crustacean postlarvae. *Behavioral Ecology*, 17:599–607, 2010.

J. J. Leichter, S. R. Wing, S. L. Miller, and M. W. Denny. Pulsed delivery of subthermocline water to Conch Reef (Florida Keys) by internal tidal bores. *Limnol. and Ocean.*, 41:1490–1501, 1996.

A. W. Leising. Copepod foraging in patchy habitats and thin layers using a 2-d individual-based model. *Marine Ecology Progress Series*, 216:167–179, 2001.

A. W. Leising and P. J. S. Franks. Copepod vertical distribution within a spatially variable food source: A simple foraging-strategy model. *J Plankton Res*, 22:999–1024, 2000.

A. W. Leising and P. J. S. Franks. Does *Acartia clausi* (copepoda: Calanoida) use an area-restricted search foraging strategy to find food? *Hydrobiologia*, 480:193–207, 2002.

A. W. Leising, J. J. Pierson, S. Cary, and B. W. Frost. Copepod foraging and predation risk within the surface layer during night-time feeding forays. *Journal of Plankton Research*, 27:987–1001, 2005.

C. E. Lennert-Cody and P. J. S. Franks. Plankton patchiness in high-frequency internal waves. *Marine Ecology Progress Series*, 186:59–66, 1999.

D. R. Lide, editor. *CRC Handbook of Chemistry and Physics*, volume 88. CRC, Boca Raton, Florida, 2008.

L.S. Liebovitch and T. Toth. A fast algorithm to determine fractal dimension. *Physics Letters A*, 141:386–390, 1989.

J. A. Lindley, R. Williams, and D. V. P. Conway. Variability in dry weight and vertical distributions of decapod larvae in the Irish Sea and North Sea during the spring. *Marine Biology*, 120:385–395, 1994.

R. G. Lueck and T. D. Mudge. Topographically induced mixing around a shallow seamount. *Science*, 276:1831–1833, 1997.

D. Macias, R. Somavilla, J. I. Gonzalez-Gordillo, and F. Echevarria. Physical control of zooplankton distribution at the Strait of Gibraltar during an episode of internal wave generation. *Marine Ecology Progress Series*, 408:79–95, 2010.

D. L. Mackas, H. Sefton, C. B. Miller, and A. Raich. Vertical habitat partitioning by large calanoid copepods in the oceanic sub-arctic Pacific during spring. *Progress in Oceanography*, 32:259–294, 1993.

E. Malkiel, J. Sheng, J. Katz, and J. R. Strickler. The three-dimensional flow field generated by a feeding calanoid copepod measured using digital holography. *The Journal of Experimental Biology*, 206:3657–3666, 2003.

B. B. Mandelbrot. *Fractals: Form, Chance, and Dimension*. W. H. Freeman and Company, 1977.

B. B. Mandelbrot. *The Fractal Geometry of Nature*. W. H. Freeman and Company, 1982.

K. H. Mann and J. R. N. Lazier. *Dynamics of Marine Ecosystems: Biological-Physical Interactions in the Oceans*. 3rd edition, 2006.

M. Marta-Almeida, J. Dubert, A. Peliz, and H. Queiroga. Influence of vertical migration pattern on retention of crab larvae in a seasonal upwelling system. *MEPS*, 307:1–19, 2006.

J. Mauchline. *The Biology of Calanoid Copepods*. San Diego: Elsevier Academic Press, 1998.

M. A. McManus, A. L. Alldredge, A. H. Barnard, E. Boss, et al. Characteristics, distribution and persistence of thin layers over a 48 hour period. *Marine Ecology Progress Series*, 261:1–19, 2003.

M. A. McManus, R. M. Kudela, M. V. Silver, G. F. Steward, J. M. Sullivan, and P. L. Donaghay. Cryptic blooms: Are thin layers the missing connection? *Estuar Coast*, 31:396–401, 2008.

K. Mead, M. Wiley, M. Koehl, and J. Koseff. Fine-scale patterns of odor encounter by the antennules of mantis shrimp tracking turbulent plumes in wave-affected and unidirectional flow. *J Exp Biol*, 206:181–193, 2003.

R. D. Mehta and P. Bradshaw. Design rules for small low speed wind tunnels. *Aeronautical Journal*, 83:443–449, 1979.

L. A. Melton and C. W. Lipp. Criteria for quantitative PLIF experiments using high-power lasers. *Exp Fluids*, 35:310–316, 2003.

S. A. Mileikovsky. Speed of active movement of pelagic larvae of marine bottom invertebrates and their ability to regulate their vertical position. *Marine Biology*, 23:11–17, 1973.

C. B. Miller. *Biological Oceanography*. Blackwell Publishing, 2004.

S. H. Miller and S. G. Morgan. Interspecific differences in depth preference: regulation of larval transport in an upwelling system. *Marine Ecology Progress Series*, 476: 301–306, 2013.

S. P. Milroy, D. A. Dieterle, R. He, G. J. Kirkpatrick, K. M. Lester, K. A. Steidinger, G. A. Vargo, J. J. Walsh, and R. H. Weisberg. A three-dimensional biophysical model of *Karenia brevis* dynamics on the west Florida shelf: A look at physical transport and potential zooplankton grazing controls. *Continental Shelf Research*, 28:112–136, 2008.

K. Miyashita, I Aoki, and T. Inagaki. Swimming behaviour and target strength of isada krill (*Euphausia pacifica*). *ICES Journal of Marine Science*, 53:303–308, 1996.

M. A. Moline, K. J. Benoit-Bird, I. C. Robbins, M. Schroth-Miller, C. M. Waluk, and B. Zelenke. Integrated measurements of acoustical and optical thin layers ii: Horizontal length scales. *Continental Shelf Research*, 30:29–38, 2010.

S. G. Monismith, J. R. Koseff, J. K. Thompson, C. A. Oriordan, and H. M. Nepf. A study of model bivalve siphonal currents. *Limnology and Oceanography*, 35: 680–696, 1990.

M. M. Mullin and E. R. Brooks. Some consequences of distributional heterogeneity of phytoplankton and zooplankton. *Limnology and Oceanography*, 21:784–796, 1976.

D. W. Murphy, D. R. Webster, S. Kawaguchi, R. King, and J. Yen. Metachronal swimming in Antarctic krill: Gait kinematics and system design. *Marine Biology*, 158:2541–2554, 2011.

D. W. Murphy, D. R. Webster, and J. Yen. The hydrodynamics of hovering in Antarctic krill. *Limnology and Oceanography: Fluids and Environments*, 3:240–255, 2013.

E. J. Murphy, J. L. Watkins, K. Reid, P. N. Trathan, I. Everson, J. P. Croxall, J. Priddle, M. A. Brandon, A. S. Brierley, and E. Hofmann. Interannual variability of the South Georgia marine ecosystem: biological and physical sources of variation in the abundance of krill. *Fisheries Oceanography*, 7:381–390, 1998.

J. Naar, A. Bourdelais, C. Tomas, J. Kubanek, P. L. Whitney, L. Flewelling, K. Steidinger, J. Lancaster, and D. G. Baden. A competitive elisa to detect brevetoxins from *Karenia brevis* (formerly *Gymnodinium breve*) in seawater, shellfish, and mammalian body fluid. *Environmental Health Perspectives*, 110:179–185, 2002.

C. C. Natunewicz and C. E. Epifanio. Spatial and temporal scales of patches of crab larvae in coastal waters. *Marine Ecology Progress Series*, 212:217–222, 2001.

S. Nicol. Krill, currents, and sea ice: *Euphasia superba* and its changing environment. *BioScience*, 56:111–120, 2006.

S. Nicol and A. S. Brierley. Through a glass less darkly - new approaches for studying the distribution, abundance and biology of euphusiids. *Deep-Sea Research II*, 57: 496–507, 2010.

S. Nicol and Y. Endo. Krill fisheries: Development, management and ecosystem implications. *Aquatic Living Resources*, 12:105–120, 1999.

T. G. Nielsen, T. Kiørboe, and P. K. Bjørnsen. Effects of a *Chrysochromulina polylepis* subsurface bloom on the planktonic community. *Mar. Ecol. Prog. Ser.*, 62:21–35, 1990.

D. P. Nowacek, A. S. Friedlaender, P. N. Halpin, E. L. Hazen, D. W. Johnston, A. J. Read, B. Espinasse, M. Zhou, and Y zhu. Super-aggregations of krill and humpback whales in Wilhelmina Bay, Antarctic Peninsula. *PLoS ONE*, 6:e19173, 2011.

J. O'Donnell. Surface fronts in estuaries: a review. *Estuaries*, 16:12–39, 1993.

C. B. Officer. *Physical Oceanography of Estuaries (and Associated Coastal Waters)*. John Wiley and Sons, 1976.

E. J. Olmi. Vertical migration of blue crab *Callinectes sapidus* megalopae: Implications for transport in estuaries. *Marine Ecology Progress Series*, 113:39–54, 1994.

F. S. Ott and R. B. Forward, Jr. The effect of temperature on phototaxis and geotaxis by larvae of the crab *Rhithropanopeus harrisii* (gould). *Journal of Experimental Marine Biology*, 23:97–107, 1976.

G. A. Paffenhöfer. On the relation of structure, perception and activity in marine planktonic copepods. *Journal of Marine Systems*, 15:457–473, 1998.

M. P. Patria and K. Wiese. Swimming in a formation in krill (euphausiacea), a hypothesis: dynamics of the flow field, properties of antennular sensor systems and a sensory-motor link. *Journal of Plankton Research*, 26:1315–1325, 2004.

T. Peacock, E. Bradley, J. Hertzberg, and Y. Lee. Forcing a planar jet flow using mems. *Experiments in Fluids*, 37:22–28, 2004.

O. M. Phillips. *The Dynamics of the Upper Ocean*. Cambridge University Press, 1966.

R. Pierce, M. Henry, and P. Blum. Brevetoxin abundance and composition during ECOHAB-florida field monitoring cruises in the Gulf of Mexico. *Continental Shelf Research*, 28:45–58, 2008.

J. J. Pierson, B. W. Frost, D. Thoreson, A. W. Leising, J. R. Postel, and M. Nuwer. Trapping migrating zooplankton. *Limnology Oceanography: Methods*, 7:334–346, 2009.

G. C. Pitcher, F. G. Figueiras, B. M. Hickey, and M. T. Moita. The physical oceanography of upwelling systems and the development of harmful algal blooms. *Progress in Oceanography*, 85:5–32, 2010.

S. A. Poulet and G. Ouellet. The role of amino acids in the chemosensory swarming and feeding of marine copepods. *J Plankton Res*, 4:341–361, 1982.

K. L. Poulson, R. D. Sieg, and J. Kubanek. Chemical ecology of the marine plankton. *Natural Product Reports*, 26:729–745, 2009.

H. J. Price. Swimming behavior of krill in response to algal patches: A mesocosm study. *Limnology and Oceanography*, 34:649–659, 1989.

E. K. Prince, L. Lettieri, K. J. McCurdy, and J. Kubanek. Fitness consequences for copepods feeding on a red tide dinoflagellate: deciphering the effects of nutritional value, toxicity, and feeding behavior. *Oecologia*, 147:479–488, 2006.

E. K. Prince, K. L. Poulson, T. L. Myers, R. D. Sieg, and J. Kubanek. Characterization of allelopathic compounds from the red tide dinoflagellate *Karenia brevis*. *Harmful Algae*, 10:39–48, 2010.

H. Queiroga. Vertical migration and selective tidal stream transport in the megalopa of the crab *Carcinus maenas*. *Hydrobiologia*, 375/376:137–149, 1998.

H. Queiroga and J. Blanton. Interactions between behaviour and physical forcing in the control of horizontal transport of decapod crustacean larvae. *Advances in Marine Biology*, 47:107–214, 2005.

H. Queiroga, P. Moksnes, and S. Meireles. Vertical migration behaviour in the larvae of the shore crab *Carcinus maenas* from a microtidal system (Gullmarsfjord, Sweden). *Marine Ecology Progress Series*, 237:195–207, 2002.

M. Raffel, C. Wilbert, and J. Kompenhans. *Particle Image Velocimetry: A Practical Guide*. Berlin: Springer, 1998.

A. Revuelta, A. L. Sanchez, and A. Linan. The virtual origin as a first-order correction for the far-field description of laminar jets. *Phys Fluids*, 14:1821–1824, 2002.

J. E. B. Rines, P. L. Donaghay, M. M. Dekshenieks, J. M. Sullivan, and M. S. Twardowski. Thin layers and camouflage: hidden *Pseudo-nitzschia* spp. (bacillariophyceae) populations in a fjord in the San Juan Islands, Washington, USA. *Mar Ecol Prog Ser*, 225:123–137, 2002.

K. Rinke, I. Hubner, T. Petzoldt, S. Rolinski, M. Konig-Finke, J. Post, A. Lorke, and J. Benndorf. How internal waves influence the vertical distribution of zooplankton. *Freshwater Biology*, 52:137–144, 2007.

D.A. Ritz. Is social aggregation in aquatic crustaceans a strategy to conserve energy? *Canadian Journal of Fisheries and Aquatic Sciences*, 57:59–67, 2000.

R. A. Rodriguez and C. E. Epifanio. Multiple cues for induction of metamorphosis in larvae of the common mud crab *Panopeus herbstii*. *Marine Ecology Progress Series*, 195:221–229, 2000.

J. P. Ryan, M. A. McManus, J. D. Paduan, and F. P. Chavez. Phytoplankton thin layers caused by shear in frontal zones of a coastal upwelling system. *Mar Ecol Prog Ser*, 354:21–34, 2008.

J. P. Ryan, A. M. Fischer, R. M. Kudela, J. F. R. Gower, S. A. King, R. Marin III, and F. P. Chavez. Influences of upwelling and downwelling winds on red tide bloom dynamics in Monterey Bay, California. *Continental Shelf Research*, 29:785–795, 2009.

W. Santana, G. Pohle, and F. Marques. Larval development of *Apiomithrax violaceus* (a. milne edwards, 1868) (decapoda: Brachyura: Majoidea: Pisidae) reared in laboratory conditions, and a review of larval characters of pisidae. *Journal of Natural History*, 38:1773–1797, 2004.

H. Sato. The stability and transition of a two-dimensional jet. *J Fluid Mech*, 7:53–80, 1960.

H. Sato and F. Sakao. An experimental investigation of the instability of a two-dimensional jet at low Reynolds numbers. *J Fluid Mech*, 20:337–352, 1964.

V. Schilling and D. Etling. Vertical mixing of passive scalars owing to breaking gravity waves. *Dyn. of Atmos. Oceans*, 23, 1996.

H. Schlichting. Laminare strahlausbreitung. *ZAMM*, 8:260–263, 1933.

M. Schultz and T. Kiørboe. Active prey selection in two pelagic copepods feeding on potentially toxic and non-toxic dinoflagellates. *Journal of Plankton Research*, 31: 553–561, 2009.

L. Seuront. *Fractals and Multifractals in Ecology and Aquatic Science*. CRC Press, 2009.

L. Seuront. Zooplankton avoidance behavior as a response to point sources of hydrocarbon-contaminated water. *Marine and Freshwater Research*, 61:263–270, 2010.

L. Seuront. Behavioral fracticality in marine copepods: Endogenous rhythm versus exogenous stressors. *Physica A*, 390:250–256, 2011.

L. Seuront, J. Hwang, L. Tseng, F.G. Schmitt, S. Souissi, and C. Wong. Individual variability in the swimming behavior of the sub-tropical copepod *Oncaea venusta* (copepoda: Poecilostomatoida). *Marine Ecology Progress Series*, 283:199–217, 2004.

J. W. Shan, D. B. Lang, and P. E. Dimotakis. Scalar concentration measurements in liquid-phase flows with pulsed lasers. *Experiments in Fluids*, 36:268–273, 2004.

A. L. Shanks. Vertical migration and cross-shelf dispersal of larval *Cancer spp.* and *Randallia ornata* (crustacea:brachyura) off the coast of southern California. *Marine Biology*, 92:189–199, 1986.

V. Siegel. Distribution and population dynamics of *Euphausia superba*: summary of recent findings. *Polar Biology*, 29:1–22, 2005.

R. D. Simons, S. G. Monismith, L. E. Johnson, G. Winkler, and F. J. Saucier. Zooplankton retention in the estuarine transition zone of the St. Lawrence Estuary. *Limnology and Oceanography*, 51:2621–2631, 2006.

T. J. Smayda. Harmful algal blooms: their ecophysiology and general relevance to phytoplankton blooms in the sea. *Limnology and Oceanography*, 42:1137–1153, 1997.

T.J. Smayda. Novel and nuisance phytoplankton blooms in the sea - evidence for a global epidemic. *Toxic Marine Phytoplankton*, pages 29–40, 1990.

D.L. Smee, M.C. Ferner, and M.J. Weissburg. Hydrodynamic sensory stressors produce nonlinear predation patterns. *Ecology*, 91:1391–1400, 2010.

J. Sole, E. Garcia-Ladona, and M. Estrada. The role of selective predation in harmful algal blooms. *Journal of Marine Systems*, 62:46–54, 2006.

M. T. Stacey, M. A. McManus, and J. V. Steinbuck. Convergences and divergences and thin layer formation and maintenance. *Limnology and Oceanography*, 52:1523–1532, 2007.

C. Staquet and J. Sommeria. Internal gravity waves: from instabilities to turbulence. *Ann. Rev. Fluid Mech.*, 34:559–593, 2002.

J. V. Steinbuck, M. T. Stacey, M. A. McManus, O. M. Cheriton, and J. P. Ryan. Observations of turbulent mixing in a phytoplankton thin layer: Implications for formation, maintenance, and breakdown. *Limnology and Oceanography*, 54:1353–1368, 2009.

S. Strand and W. Hamner. Schooling behavior of Antarctic krill (*Euphausia superb*) in laboratory aquaria: reactions to chemical and visual stimuli. *Marine Biology*, 106:355–359, 1990.

J. R. Strickler and G. Balazsi. Planktonic copepods reacting selectively to hydrodynamic disturbances. *Phil Trans R Soc*, 362:1947–1958, 2007.

R. P. Stumpf, R. W. Litaker, L. Lanerolle, and P. A. Tester. Hydrodynamic accumulation of *Karenia* off the west coast of florida. *Continental Shelf Research*, 28: 189–213, 2008.

S. D. Sulkin. Depth regulation of crab larvae in the absence of light. *J Exp Mar Biol Ecol*, 13:73–82, 1973.

S. D. Sulkin. The influence of light in the depth regulation of crab larvae. *Biol Bull*, 148:33–343, 1975.

S. D. Sulkin. Behavioral basis of depth regulation in the larvae of brachyuran crabs. *Marine Ecology Progress Series*, 15:181–205, 1984.

S. D. Sulkin, I. Phillips, and W. van Heukelem. On the locomotory rhythm of brachyuran crab larvae and its significance in vertical migration. *Marine Ecology Progress Series*, 1:331–335, 1979.

S. D. Sulkin, W. van Heukelem, P. Kelly, and L. van Heukelem. The behavioral basis of larval recruitment in the crab *Callinectes sapidus* Rathbun: a laboratory investigation of ontogenetic changes in geotaxis and barokinesis. *Biol Bull*, 159: 402–417, 1980.

J. M. Sullivan et al. Layered organization in the coastal ocean: An introduction to planktonic thin layers and the LOCO project. *Continental Shelf Research*, 30:1–6, 2010.

M. M. Sutor, T. J. Cowles, W. T. Peterson, and S. D. Pierce. Acoustic observations of finescale zooplankton distributions in the Oregon upwelling region. *Deep Sea Research*, 52:109–121, 2005.

K. M. Swadling, D. A. Ritz, S. Nicol, J. E. Osborn, and L. J. Gurney. Respiration rate and cost of swimming for Antarctic krill, *Euphausia superba*, in large groups in the laboratory. *Marine Biology*, 146:1169–1175, 2005.

R. A. Tankersley, L. M. McKelvey, and R. B. Forward, Jr. Responses of estuarine crab megalopae to pressure, salinity and light: Implications for flood-tide transport. *Marine Biology*, 122:391–400, 1995.

S. Tapia-Lewin and L. M. Pardo. Field assessment of the predation risk - food availability trade-off in crab megalopae settlement. *PLOS ONE*, 9:e95335, 2014.

G. A. Tarling, T. Klevjer S. Fielding, J. Watkins, A. Atkinson, E. Murphy, R. Korb, M. Whitehouse, and R. Leaper. Variability and predictability of Antarctic krill swarm structure. *Deep-Sea Research I*, 2009:1994–2012, 2009.

T. Tatsumi and T. Kakutani. The stability of a two-dimensional laminar jet. *Journal of Fluid Mechanics*, 4:261–75, 1958.

G. J. Teegarden, A. D. Cembella, C. L. Capuano, S. H. Barron, and E. G. Durbin. Phycotoxin accumulation in zooplankton feeding on *Alexandrium fundyense* - vector or sink? *Journal of Plankton research*, 25:429–443, 2003.

P. A. Tester, R. P. Stumpf, F. M. Vukovich, P. A. Fowler, and J. T. Turner. An expatriate red tide bloom: Transport, distribution, and persistence. *Limnology and Oceanography*, 36:1053–1061, 1991.

P. A. Tester, J. T. Turner, and D. Shea. Vectorial transport of toxins from the dinoflagellate *Gymnodinium breve* through copepods to fish. *Journal of Plankton Research*, 22:47–61, 2000.

N. Tinbergen, M. Impekoven, and D. Franck. An experiment on spacing-out as a defense against predation. *Behavior*, 28:307–321, 1967.

P. Tiselius. Behavior of *Acartia tonsa* in patchy food environments. *Limnology and Oceanography*, 37:1640–1651, 1992.

P. Tiselius and P. R. Jonsson. Foraging behavior of six calanoid copepods: observations and hydrodynamic analysis. *Marine Ecology Progress Series*, 168:119–126, 1990.

J. Titelman. Swimming and escape behavior of copepod nauplii: implications for predator-prey interactions among copepods. *Marine Ecology Progress Series*, 213: 203–213, 2001.

J. Titelman and T. Kiørboe. Motility of copepods nauplii and implications for food encounter. *Marine Ecology Progress Series*, 247:123–135, 2003.

P. N. Trathan, J. Priddle, J. L. Watkins, D. G. M. Miller, and A. W. A. Murray. Spatial variability of antarctic krill in relation to mesoscale hydrography. *Marine Ecology Progress Series*, 98:61–71, 1993.

C. D. Troy and J. R. Koseff. The generation and quantitative visualization of breaking internal waves. *Experiments in Fluids*, 38:549–562, 2005.

A. C. True. Patchiness: Zooplankton behavior in finescale vertical shear layers. Master's thesis, Georgia Institute of Technology, Atlanta, GA, 2011.

J. H. Tumlinson, W. J. Lewis, and L. E. M. Vet. How parasitic wasps find their hosts. *Sci Am*, 268:100–106, 1993.

J. T. Turner and P. A. Tester. Toxic marine phytoplankton, zooplankton grazers, and pelagic food webs. *Limnology and Oceanography*, 42:1203–1214, 1997.

J. T. Turner, V. Roncalli, P. Ciminiello, C. D. Aversano, E. Fattorusso, L. Tartaglione, Y. Carotenuto, G. Romano, F. Esposito, A. Miralto, and A. Ianora. The importance of small planktonic copepods and their roles in pelagic marine food webs. *Zool Stud*, 43:255–266, 2004.

J. T. Turner, G. J. Doucette, C. L. Powell, D. M. Kulis, B. A. Keafer, and D. M. Anderson. Biogeographic effects of the Gulf of Mexico red tide dinoflagellate *Karenia brevis* on Mediterranean copepods. *Harmful Algae*, 16:63–73, 2012.

D. R. Unger and F. J. Muzzio. Laser-induced fluorescence technique for the quantification of mixing in impinging jets. *AICHE J*, 45:2477–2486, 1999.

M. Uttieri, E. Zambianchi, J.R. Strickler, and M.G. Mazzocchi. Fractal characterization of three-dimensional zooplankton swimming trajectories. *Ecological Modeling*, 185:51–63, 2005.

L. Velo-Suarez, L. Fernand, P. Gentien, and B. Reguera. Hydrodynamic conditions associated with the formation, maintenance and dissipation of a phytoplankton thin layer in a coastal upwelling system. *Continental Shelf Research*, 30:193–202, 2010.

P. G. Verity. Expansion of potentially harmful algal taxa in a Georgia estuary (USA). *Harmful Algae*, 9:144–152, 2010.

L. E. M. Vet. From chemical to population ecology: Infochemical use in an evolutionary context. *J Chem Ecol*, 25:31–49, 1999.

M. Viitasalo, T. Kiørboe, J. Flinkman, L. W. Pedersen, and A. W. Visser. Predation vulnerability of planktonic copepods: consequences of predator foraging strategies and prey sensory abilities. *Marine Ecology Progress Series*, 175:129–142, 1998.

A. W. Visser and T. Kiørboe. Plankton motility patterns and encounter rates. *Oecologia*, 148:538–546, 2006.

R. J. Waggett, P. A. Tester, and A. R. Place. Anti-grazing properties of the toxic dinoflagellates *Karlodinium veneficum* during predator-prey interactions with the copepod *Acartia tonsa*. *Marine Ecology Progress Series*, 366:31–42, 2008.

R. J. Waggett, D. R. Hardison, and P. A. Tester. Toxicity and nutritional inadequacy of *Karenia brevis*: synergistic mechanisms disrupt top-down grazer control. *Marine Ecology Progress Series*, 444:15–30, 2012.

D. Walker. A fluorescence technique for measurement of concentration in mixing liquids. *J Phys E Sci Instrum*, 20:217–224, 1987.

D. Wang. Neurotoxins from marine dinoflagellates: A brief review. *Marine Drugs*, 6: 349–371, 2008.

P. Ward, M. Whitehouse, M. Meredith, E. Murphy, R. Shreeve, R. Korb, J. Watkins, S. Thorpe, R. Woodd-Walker, A. Brierley, N. Cunningham, S. Grant, and D. Bone. The southern Antarctic circumpolar current front: physical and biological coupling at South Georgia. *Deep-Sea Research I*, 49:2183–2202, 2002.

J. L. Watkins and A. W. A. Murray. Layers of Antarctic krill, *Euphausia superba*: are they just long krill swarms? *Marine Biology*, 131:237–247, 1998.

D. R. Webster and M. J. Weissburg. The hydrodynamics of chemical cues among aquatic organisms. *Annu Rev Fluid Mech*, 41:73–90, 2009.

D. R. Webster, S. Rahman, and L. P. Dasi. Laser-induced fluorescence measurements of a turbulent plume. *J Eng Mech*, 129:1130–1137, 2003.

J. M. Welch, R. B. Forward, Jr, and P. A. Howd. Behavioural responses of blue crab *Callinectes sapidus* larvae to turbulence: implications for selective tidal stream transport. *Marine Ecology Procress Series*, 179:135–143, 1999.

S. T. Wereley and C. D. Meinhart. Second-order accurate particle image velocimetry. *Exp Fluids*, 31:258–268, 2001.

P. H. Wiebe, C. J. Ashjian, G. L. Lawson, A. Piñones, and N. J. Copley. Horizontal and vertical distribution of euphausiid species on the Western Antarctic Peninsula U.S. GLOBEC Southern Ocean study site. *Deep-Sea Research II*, 58:1630–1651, 2011.

C. B. Woodson. *Thin layers: Physical and chemical cues contributing to observed copepod aggregations*. PhD thesis, Georgia Institute of Technology, Atlanta, GA, 2005.

C. B. Woodson and M. A. McManus. Foraging behavior can influence dispersal of marine organisms. *Limnology and Oceanography*, 52:2701–2709, 2007.

C. B. Woodson, D. R. Webster, M. J. Weissburg, and J. Yen. Response of copepods to physical gradients associated with structure in the ocean. *Limnology and Oceanography*, 50, 2005.

C. B. Woodson, D. R. Webster, M. J. Weissburg, and J. Yen. Cue hierarchy and foraging in calanoid copepods: ecological implications of oceanographic structure. *Marine Ecology Progress Series*, 330:163–177, 2007.

C. B. Woodson, M. A. McManus, J. A. Tyburczy, J. A. Barth, L. Washburn, J. E. Caselle, M. H. Carr, D. P. Malone, P. T. Raimondi, B. A. Menge, and S. R. Palumbi. Coastal fronts set recruitment and connectivity patterns across multiple taxa. *Limnology and Oceanography*, 57:582–596, 2012.

J. Yen and D. M. Fields. Escape responses of *Acartia hudsonica* (copepoda) nauplii from the flow field of *Temora longicornis* (copepoda). *Archive Hydrobiol*, 36:123–134, 1992.

J. Yen, P. H. Lenz, D. V. Gassie, and D. K. Hartline. Mechanoreception in marine copepods: electrophysiological studies on the first antennae. *Journal of Plankton Research*, 14:495–512, 1992.

J. Yen, M. J. Weissburg, and M. H. Doall. The fluid physics of signal perception by mate-tracking copepods. *Philosophical Transactions of the Royal Society of London*, 353:787–804, 1998.

J. A. Yoder, S. G. Ackleson, R. T. Barber, P. Flament, and W. M. Balch. A line in the sea. *Nature*, 371:689–692, 1994.

C. M. Young. *Ecology of Marine Invertebrate Larvae*, chapter Behaviour and locomotion during the dispersal phase of larval life, pages 249–277. CRC Press, Boca Raton, FL, 1995.

J. H. Zar. *Biostatistical Analysis*. Upper Saddle Hall, NJ: Prentice Hall, 4th edition, 1999.

M. Zhou and R. D. Dorland. Aggregation and vertical migration behavior of *Euphausia superba*. *Deep-Sea Research II*, 51:2119–2137, 2004.

R. K. Zimmer and C. A. Butman. Chemical signaling processes in the marine environment. *Biol Bull*, 198:168–187, 2000.